



Development of electrostrictive P(VDF-TrFE-CTFE) terpolymer for inkjet printed electromechanical devices

Qing Liu

► To cite this version:

Qing Liu. Development of electrostrictive P(VDF-TrFE-CTFE) terpolymer for inkjet printed electromechanical devices. Electronics. Université de Lyon, 2016. English. NNT : 2016LYSEI126 . tel-02063349

HAL Id: tel-02063349

<https://theses.hal.science/tel-02063349>

Submitted on 11 Mar 2019

HAL is a multi-disciplinary open access archive for the deposit and dissemination of scientific research documents, whether they are published or not. The documents may come from teaching and research institutions in France or abroad, or from public or private research centers.

L'archive ouverte pluridisciplinaire **HAL**, est destinée au dépôt et à la diffusion de documents scientifiques de niveau recherche, publiés ou non, émanant des établissements d'enseignement et de recherche français ou étrangers, des laboratoires publics ou privés.



N°d'ordre NNT : 2016LYSEI126

THESE de DOCTORAT DE L'UNIVERSITE DE LYON

opérée au sein de

L'Institut National des Sciences Appliquées de Lyon

Ecole Doctorale N°162

Mécanique, Energétique, Génie Civil, Acoustique

Spécialité de doctorat : Génie Mécanique

Soutenue publiquement le 29/11/2016, par:

Qing LIU

Development of Electrostrictive P(VDF-TrFE-CTFE) Terpolymer for Inkjet Printed Electromechanical Devices

Devant le jury composé de :

LIANG, Zhiyong
DANTRAS, Eric

Professeur
Professeur

HMPI, Florida State Univ.
CIRIMAT, Univ. Toulouse

Rapporteur
Rapporteur

BODDAERT, Xavier
MILLION, Antoine
ZHANG, Qiuyu
CAPSAL, Jean-Fabien

Professeur
Professeur
Professeur
Maître de Conférences

CMP, Mines Saint-Etienne
Hospices Civiles de Lyon
Northwestern Polytech. Univ.
LGEF, INSA Lyon

Président
Examinateur
Examinatrice
Co-directeur de thèse

RICHARD, Claude
COTTINET, Pierre-Jean

Professeur
Maître de Conférences

LGEF, INSA Lyon
LGEF, INSA Lyon

Directeur de thèse
Examinateur

Development of Electrostrictive P(VDF-TrFE-CTFE) Terpolymer for Inkjet Printed Electromechanical Devices

Département FEDORA – INSA Lyon - Ecoles Doctorales – Quinquennal 2016-2020

SIGLE	ECOLE DOCTORALE	NOM ET COORDONNEES DU RESPONSABLE
CHIMIE	CHIMIE DE LYON http://www.edchimie-lyon.fr Sec : Renée EL MELHEM Bat Blaise Pascal 3 ^e etage secretariat@edchimie-lyon.fr Insa : R. GOURDON	M. Stéphane DANIELE Institut de Recherches sur la Catalyse et l'Environnement de Lyon IRCELYON-UMR 5256 Équipe CDFA 2 avenue Albert Einstein 69626 Villeurbanne cedex directeur@edchimie-lyon.fr
E.E.A.	ELECTRONIQUE, ELECTROTECHNIQUE, AUTOMATIQUE http://edeea.ec-lyon.fr Sec : M.C. HAVGOUDOUKIAN Ecole-Doctorale.eea@ec-lyon.fr	M. Gérard SCORLETTI Ecole Centrale de Lyon 36 avenue Guy de Collongue 69134 ECULLY Tél : 04.72.18 60.97 Fax : 04 78 43 37 17 Gerard.scorletti@ec-lyon.fr
E2M2	EVOLUTION, ECOSYSTEME, MICROBIOLOGIE, MODELISATION http://e2m2.universite-lyon.fr Sec : Sylvie ROBERJOT Bat Atrium - UCB Lyon 1 04.72.44.83.62 Insa : H. CHARLES secretariat.e2m2@univ-lyon1.fr	M. Fabrice CORDEY CNRS UMR 5276 Lab. de géologie de Lyon Université Claude Bernard Lyon 1 Bât Géode 2 rue Raphaël Dubois 69622 VILLEURBANNE Cédex Tél : 06.07.53.89.13 cordey@univ-lyon1.fr
EDISS	INTERDISCIPLINAIRE SCIENCES-SANTE http://www.ediss-lyon.fr Sec : Sylvie ROBERJOT Bat Atrium - UCB Lyon 1 04.72.44.83.62 Insa : M. LAGARDE secretariat.ediss@univ-lyon1.fr	Mme Emmanuelle CANET-SOULAS INSERM U1060, CarMeN lab, Univ. Lyon 1 Bâtiment IMBL 11 avenue Jean Capelle INSA de Lyon 696621 Villeurbanne Tél : 04.72.68.49.09 Fax : 04 72 68 49 16 Emmanuelle.canet@univ-lyon1.fr
INFOMATHS	INFORMATIQUE ET MATHEMATIQUES http://infomaths.univ-lyon1.fr Sec : Renée EL MELHEM Bat Blaise Pascal 3 ^e etage infomaths@univ-lyon1.fr	Mme Sylvie CALABRETTO LIRIS – INSA de Lyon Bat Blaise Pascal 7 avenue Jean Capelle 69622 VILLEURBANNE Cedex Tél : 04.72. 43. 80. 46 Fax 04 72 43 16 87 Sylvie.calabretto@insa-lyon.fr
Matériaux	MATERIAUX DE LYON http://ed34.universite-lyon.fr Sec : M. LABOUNE PM : 71.70 –Fax : 87.12 Bat. Direction Ed.materiaux@insa-lyon.fr	M. Jean-Yves BUFFIERE INSA de Lyon MATEIS Bâtiment Saint Exupéry 7 avenue Jean Capelle 69621 VILLEURBANNE Cedex Tél : 04.72.43 71.70 Fax 04 72 43 85 28 jean-yves.buffiere@insa-lyon.fr
MEGA	MECANIQUE, ENERGETIQUE, GENIE CIVIL, ACOUSTIQUE http://mega.universite-lyon.fr Sec : M. LABOUNE PM : 71.70 –Fax : 87.12 Bat. Direction mega@insa-lyon.fr	M. Philippe BOISSE INSA de Lyon Laboratoire LAMCOS Bâtiment Jacquard 25 bis avenue Jean Capelle 69621 VILLEURBANNE Cedex Tél : 04.72 .43.71.70 Fax : 04 72 43 72 37 Philippe.boisse@insa-lyon.fr
ScSo	ScSo* http://recherche.univ-lyon2.fr/scso/ Sec : Viviane POLSINELLI Brigitte DUBOIS Insa : J.Y. TOUSSAINT Tél : 04 78 69 72 76 viviane.polsinelli@univ-lyon2.fr	M. Christian MONTES Université Lyon 2 86 rue Pasteur 69365 LYON Cedex 07 Christian.montes@univ-lyon2.fr

*ScSo : Histoire, Géographie, Aménagement, Urbanisme, Archéologie, Science politique, Sociologie, Anthropologie

111

Abstract

Ferroelectric materials have attracted an emerging attention due to their capability of converting external electric excitation into other accessible energy forms such as mechanical force, heat (electrocaloric effect), and magnetoelectric field and vice versa. Thanks to their flexibility, light weight, relatively low mechanical strength, ease of processability into large-area films, polymers materials which possess ferroelectric behavior have been booming recently. Amongst all the ferroelectric polymers, specific interests have been given to PVDF-based copolymers and terpolymers due to their high electromechanical response. P(VDF-TrFE) copolymer has been extensively and fully investigated from the physico-chemical aspect, which are frequently employed in non-volatile memory, sensor and actuator devices, owing to its large ferroelectricity and piezoelectric coefficient. Aiming at improving the global electrostrictive properties, bulk defects were introduced into the PVDF-based copolymer whereby micrometer-sized ferroelectric domains broke into nano-sized crystal domains. Its ferro-paraelectric transition behavior consequently depended on the external excitation frequency. Therefore, P(VDF-TrFE-CTFE) terpolymer is more likely to be defined as a ferroelectric polymer with a relaxor behavior, exhibiting the outstanding electrostrictive response upon the electric excitation. The electromechanical behavior is closely related to several physical and electric parameters such as dielectric permittivity ϵ' and mechanical strength Y , all of which heavily rely on the polymer microstructure. This thesis aims to systematically determine how these variables influence the electromechanical behavior of the as-cast terpolymers by means of temperature annealing treatment and plasticization approaches. Additionally, inkjet printed sensors and electronic devices over flexible substrates are of significant interest due to its less production complexity, high throughput and cost-effective characteristics. During this work, inkjet printing technology is considered to be employed for manufacturing flexible large-area sensor networks. The feasibility and maneuverability of the P(VDF-TrFE) copolymer and terpolymer were carefully carried out for a piezoelectric force sensor implementation.

Firstly the influence of the polymer processing on the microstructure-electromechanical properties of the P(VDF-TrFE-CTFE) terpolymers were investigated. The variations of the Curie transition and melting regions were investigated as a function of the annealing temperature and time duration. Crystallinity fraction was shown to increase monotonically with the increase of the annealing temperature. It is not the case for the melting temperature for the corresponding terpolymers which exhibits a two stepwise decrease with a cross point at 90 °C. Annealing above 90 °C caused crystal stacks thickening and a narrow distribution of crystal size. This was evidenced by a remarkably decrease of the FWHM values from ca. 15 °C to around 8 °C. With the help of Atomic Force Microscopy profiles, worm-like crystal nanodomains were observed in terpolymers. Coarse and loose bumpy-like topographic morphology witnessed for the pristine was due to the heterogeneous morphology and flat-on oriented crystal lamellae. Regular needle-like nanometer-sized crystallites and distinct phase boundary suggested the edge-on oriented crystal lamellae in intermediate terpolymers induced by temperature annealing process. Additionally, the dielectric behaviors were studied with the help of broadband dielectric

spectroscopy and reliably linked to the fraction of interphase region. Electric breakdown failure was examined by applying a high field to the films. Increasing crystal content enhanced the electric breakdown strength. Electromechanical response was finally evaluated with a bilaminar unimorph cantilever beam bender. The tip displacement δ and transverse strain s_{31} for each annealed terpolymer followed a quadratic-type variation with the applied electric field. δ maximized at a 37.6% crystal content whilst S_{31} values showed an exponential decay function of increase of crystal fraction.

Besides the electromechanical properties, the dynamics of semi-crystalline (P(VDF-TrFE-CTFE) terpolymers were fully investigated as a function of temperature and frequency, by means of broadband dielectric spectroscopy (BDS) technique. Four types of relaxation regimes were observed over the full dielectric spectroscopy, namely β (second) relaxation in the sub-glass state, α (segmental dynamics) in the rubbery state, the Curie transition and space charge carrier motions at high temperatures. Constrained segmental dynamics were observed in the terpolymer containing the higher crystal fraction for which a narrow relaxation time distribution was found. These results indicate an increasing average size of the cooperative rearranging region over the crystalline fraction. A decrease of the strength index values also implied a more fragile behavior for terpolymers with a higher degree of crystallinity. An exceptional increase in dielectric strength $\Delta\epsilon_\alpha$ was found as the crystallinity increased. This behavior could be explained by an enhanced interphase region (rigid amorphous phase). The Curie transition showed an accelerating relaxation rate for a more fragile terpolymer. Moreover, a motion of the space charge carrier ions was observed in the higher temperature range. Finally, there was evidence that the segmental dynamics in the amorphous phase was responsible for the motion of the space charge carrier ions.

In addition, dielectric and electromechanical response of DEHP-plasticized terpolymer blend were several orders of magnitude enhancement compared to the neat one. An interpretation of this fundamental trend is given on a molecular level by means of BDS technique. In contrast to the negative influence of recrystallization on molecular mobility, introduction of DEHP tends to accelerate the relaxation time and monotonically lower the glass transition temperature, with a rather good consistency with the Fox model. In this case, charge carrier ions translational motion was consequently accelerated and transferred across the phase boundary of the mobile and rigid amorphous phase where the ions piled, rising a huge local interfacial polarization. Therefore, addition of the DEHP plasticizer eventually led to larger dielectric permittivity at low frequency due to the enhancement of interfacial polarization (MWS) and its relaxation peak drifted towards the higher frequency by almost one decade, compared with pure terpolymer matrix.

Inkjet printed electromechanical devices based on terpolymers are an alternative way to fabricate force sensor networks. The ink jettable parameters were firstly adapted to the rheological behavior of the polymer solution ink. The inkjet printing protocol for ferroelectric P(VDF-TrFE) copolymer and electrostrictive P(VDF-TrFE-CTFE) terpolymer were then carefully optimized. The piezoelectric copolymer force sensor has to be poled prior to its calibration or its application as an impact force sensor device. A large remnant polarization P_r is obtained, resulting in the excellent piezoelectric behavior. Inversely, a force sensor device made

with an electrostrictive terpolymer is neither necessary to be poled and nor exhibit large remnant polarization. In this regard, an indispensable electric field bias is compulsory to induce the polarization. It is remarkable that for a given electromechanical performance the bias electric field for an electrostrictive terpolymer is much lower than the corresponding poling electric field for a copolymer. It is also observed that the properties equivalent to the corresponding ferroelectric copolymer can be obtained for a bias electric field as low as $7.5\text{V}/\mu\text{m}$.

These results show definitely the feasibility of low cost printed terpolymer electromechanical devices with performances comparable to the ferroelectric copolymer once at the expense of only a fairly low electric field bias. These findings are rather promising for the moment, although future work goes to the fully printed and multi-stack structured large area polymer electronic device networks with the aim of the enhanced mechanical energy density.

Keywords: *Crystallinity; Molecular mobility; Plasticized terpolymer blends, Interfacial polarization; Inkjet printing technique; Piezoelectric force sensor.*

Acknowledgement

This PhD work has been carried out in lab of Laboratoire de Génie Electrique et Ferroélectricité (LGEF) of Université de Lyon, INSA Lyon under supervisions of Dr. Jean-Fabien CAPSAL and Prof. Claude Richard. I would like to borrow this opportunity to express my deep gratitude to the PhD defense committee and all jury members defending president Prof. Xavier BODDAERT, Prof. Zhiyong LIANG, Prof. Qiuyu ZHANG, Dr. Eric DANTRAS, Prof. Antoine Million for accepting and examining the PhD manuscript and comment feedbacks. Without these valuable remarks, this PhD thesis would not be that good.

Working as a PhD staff in LGEF can be described as tough, franking in particular a place being far away from the place I used to be. Since the first moment I made my mind to dedicate myself to be a PhD researcher, I have to cope with complex and obscure physical theory, stubborn machines, tight deadline, unwanted experimental data and endless reading and writing. Finally these challenges deserve a reward of perfect end in current stage of my entire research career. Here I would like to mention all the members who provided me help during my entire life as of now, to whom I would like to give all my sincere gratitude. Without your offer of help, this thesis is not possible.

First of all my deepest gratitude goes to Prof. Claude Richard and Dr. Jean-Fabien Capsal, giving me this precious opportunity to be academic member and making the successful continuation of my research career in LGEF, an environmental-kindly place where the staffs are trying to create a friendly atmosphere and do the highest level of researches covering the interdisciplinary scientific and technological domains. Frankly Prof. Claude Richard is always patient, supporting, professionalism and warm kindness in the last three years, especially in the last stage of my PhD stay in LGEF. His advices and suggestions are extremely valuable and wide scope whatever the academic or professional. Specific thanks should be given to Dr. Jean-Fabien Capsal for transferring all his knowledge to me and bringing me into the new fields I never touched. He is smart, curious and creative, always being ready to find something interesting and new.

Secondly, I would like to acknowledge Prof. Laurent Lebrun, a very talkative and nice director of the laboratory, and Prof. Daniel Guyomar for their daily conversation and fruitful discussions, making the working atmosphere very relaxing and friendly in LGEF. Many thanks goes to Mme Laurence Seveyrat and Mme Veronique Perrin for all the great technical and scientific supports as well as interactions. And I would also like to thank Mr. Frederic Defromerie for his supports on realization of the experimental setups and black humor jokes. A big thank

should be given to my colleagues, Bin Bao, Tomas Huguet, Kritsadi Thetraphi and Bhaawan Gupta for their unconditional supports. I would also give the indispensable appreciation to the lab. members Yang Li, Xunqian Yin and Bin Zhang for their kind help during the PhD stay.

I oblige to express my innumerable gratitude to Mme Evelyne Dorieux for her unstopped, patient and kind help with all the PhD administration of living and working in LGEF, Lyon France.

I could not forget the valuable advices my master director Prof. Qiuyu Zhang gave in NPU, Xi'an China, who has brought me into an amazing polymer world. Her kindness, warm-heartedness and professionalism, responsibility and ever availability make her as one of the best mentors for my academic career. I thank her again for her as a PhD defense committee member and valuable comments on the PhD work.

My life in Lyon, France would not have been fun and pleasant without my intimate friends off the lab. work. Many specific thanks goes to my compatriots Xiaolu Jiang, Jinjiang Guo, Jingping Li, Wenjun Hao, Xichen Yuan, etc. Here although I could not name all these lovely guys, without your standing and warm encouragement, I would not have imaged such a memorable and dynamic life in France.

Finally, I feel like expressing all infinite gratitude to my parents and family members from whom I received innumerable, unconditional and ever-continuous supports. My mom always taught me with her examples, giving me the best family education ever which still kept with me today. She also transmitted her endless love and effort to me, making me always encouraged!

I thank all you for your indulgence!

Table of Contents

Abstract	iii
Acknowledgement	ix
Nomenclatures and Abbreviations	1
Chapter I	
Force Sensor and Inkjet Printing Functional Layers: the-state-of-the-art	5
I Introduction	6
II Force Sensor Mode (<i>Transduction Principle</i>).....	6
II. 1 General Overview	6
II. 2 Piezoresistive Effect Based Sensor (active sensor)	8
II. 3 Capacitive Sensor (active sensor)	13
II. 4 Piezoelectric Effect Based Sensor (passive sensor)	16
II. 5 Summary.....	20
III Printed Electronics Technologies	20
IV Inkjet Printing Technologies	26
IV. 1 Ink Ejection	26
IV.1.1 Continuous Inkjet Printing.....	26
IV.1.2 Drop-on-demand (DoD) Inkjet Printing.....	27
IV.1.3 Piezoelectric DoD Inkjet Printing Process	29
IV. 2 Ink Jettability	30
IV. 3 Drop Impact.....	33
IV .4 Flexible Substrate and Surface Treatment	34
IV. 5 Dropped Ink Drying	36
V Fluorinated Electrostrictive Polymers	38
VI Objective of This Work	41
References	43
Chapter II	
Control of Recrystallization and its Effect on Electromechanical Performances of Electrostrictive P(VDF-TrFE-CTFE) Terpolymer	51
I Introduction	52

II Experimental Section.....	54
II. 1 Materials and Sample Elaboration	54
II. 2 Device Fabrication and Characterization Techniques	55
II.2.1 Differential Scanning Calorimetry (DSC).....	55
II.2.2 Atomic Force Microscopy (AFM)	56
II.2.3 Mechanical Strength Properties	56
II.2.4 Dielectric Properties	57
II.2.5 Electric Breakdown Strength	57
II.2.5 Field-induced Electrostrictive Strain.....	58
III Results and Discussions	59
III. 1 Thermal Data Analysis and Crystalline Properties.....	59
III.1.1 Temperature Dependence of Isothermal Crystallization	59
III.1.2 Temperature Dependence of Isothermal Crystallization	64
III. 2 Surface Topography.....	66
III. 3 Dielectric Permittivity and Breakdown Strength	68
III.3.1 Dielectric Behavior under a Low Electric Field	68
III.3.2 Breakdown Strength under High Electric Field.....	72
III. 4 Electromechanical Properties.....	75
III.4.1 Mechanical Behaviors.....	75
III.4.2 Electromechanical Behaviors	76
IV Conclusions.....	81
References	83

Chapter III

Influence of the Crystallization on the Molecular Mobility and Ionic DC Conductivity Behaviors of Relaxor Ferroelectric P(VDF-TrFE-CTFE) Terpolymers89

I Introduction.....	90
II Experimental Section.....	93
II. 1 Materials and Isothermal Crystallization.....	93
II. 2 Device Fabrication and Characterization Techniques	93
II.2.1 Dielectric Data Acquisition.	93
II.2.2 Dielectric Data Analysis	94
III Results and Discussions	94
III. 1 Broadband Dielectric loss spectra and Tan δ	94
III.1.1 Dielectric Loss Spectra.....	94

III.1.2 Dielectric Relaxation Behavior.....	96
III. 2 Segmental Dynamics of Semicrystalline Terpolymers.....	98
III. 3 Influence of segmental dynamics on the Curie transition behavior	104
III. 4 Sub-glass β -relaxation mode.....	109
III. 5 Mobility of Space Charges during High-Temperature processing.....	110
IV Conclusions.....	114
References	116

Chapter IV

Plasticization Effects on Relaxor Ferroelectric P(VDF-TrFE-CTFE) Terpolymers: Mechanical Behavior, Morphology and Molecular Mobility 123

I Introduction.....	124
II Experimental Section.....	125
II. 1 Materials and Elaboration	125
II. 2 Methods and Techniques	127
II.2.1 Characterization Technique.....	127
II.2.2 Device Fabrication and Characterization.....	127
III Results and Discussions	129
III. 1 Miscibility and Effects of plasticizer on thermal behaviors of terpolymers	129
III. 2 Surface Morphology	134
III. 3 Tensile Test	136
III. 4 Influence of DEHP Plasticizer on Molecular Mobility	137
III.4.1 Segmental Relaxation- α Process.....	142
III.4.2 Strength & Fragility Index.....	153
III.4.3 Plasticizing Effect on the Sub-glass Relaxation Process- β Relaxation.....	154
III. 5 Mobility of Space Charge Carriers at High Temperature.....	157
III. 6 Interfacial polarization and primary relaxation in constrained amorphous phase	162
IV Conclusions.....	170
References	172

Chapter V

Enhanced Inkjet Printed Pseudo-piezoelectric Force Sensors based on Electrostrictive P(VDF-TrFE-CTFE) Terpolymer and Ferroelectric P(VDF-TrFE) Copolymer 179

I Introduction.....	180
---------------------	-----

II Working Principle and Theoretical Consideration.....	180
III Experimental Section.....	182
III. 1 Chemicals and Materials.....	182
III. 2 Inkjet Printing Process and Device Fabrication	183
III. 3 Characterization	184
IV Result and Discussion.....	185
IV. 1 Design and Inkjet Printing of Two Types of Force Sensors.....	185
IV. 4 Ferroelectric Characteristics of Inkjet Printed Sensors	197
IV. 5 Electromechanical Coupling Behavior of Printed Electrostrictive Terpolymer	201
IV. 5 Piezoelectric Behavior of Ferroelectric Inkjet Printed Sensor.....	202
IV. 6 Pseudo-piezoelectric Behavior of Electrostrictive Terpolymer	207
V Conclusions.....	210
References	211
Chapter VI	
General Conclusions and Perspectives.....	217
VI. 1 Conclusions.....	218
VI. 2 Future Work and Perspectives	223
Appendix:.....	225
Surface Energy Measurement	225
Owens-Wendt-Kaelble Method.....	225
List of Figures	227
List of Tables	237

Nomenclatures and Abbreviations

Nomenclatures

Symbols	Full description
ΔR	Change of specific resistance
R	Specific resistance
d_i	Piezoresistive coefficient
T_i	external force excitation
Y_i	Young's modulus of piezoresistor
s_i	Strain induced by mechanical stress
V_{out}	Voltage output
V_{in}	Voltage input
I	Current output
V^+, V^-	Potential of positive/negative ends
$C_{I,P}$	Capacitance
t_i	Thickness
A_i	Area of the electrode overlapping
$\varepsilon_{i,r}, \varepsilon'$	Dielectric permittivity
ε''	Dielectric loss
ε_0	Permittivity in vacuum
ΔS_A	Surface area variation
$\frac{\partial S_1}{\partial t}$	Change rate of the force-induced strain in plane direction
Re	Reynolds number
We	Weber number
Oh	Ohnesorge number
Ca	Capillary number
ρ	Density
σ	Surface tension/surface free energy
v	Velocity
η	Viscosity
d	Diameter
β^*	Ratio of drop diameter before impact to the droplet diameter wetted on substrate
γ_{gs}	Surface tension at interface of gas and solid
γ_{sl}	Surface tension at interface of solid and liquid
γ_{gl}	Surface tension at interface of gas and liquid
θ	Contact angle
Y	Young's Modulus
δ	Tip displacement of the uimorph actuator
χ_c	Crystalline fraction
T_g	Glass transition temperature

BOPVDF	Biaxially oriented PVDF films
D	Electric displacement
S_M	Maxwell strain
S_E	Real electrostrictive strain
Q	Intrinsic electrostrictive coefficient
M_{3i}	Global electrostrictive coefficient
E_μ	Elastic mechanical energy density
$\Delta\epsilon_\alpha$	Dielectric strength of α re
σ	Conductivity
KWW	Kohlrausch-Williams-Watts (KWW) function
β_{KWW}	Stretched exponential factor of KWW
f	Electric frequency
D	Strength index
$T_{g.diel}$	Glass transition defined by BDS
T_{me}	Merging temperature
B	Apparent activation energy of α relaxation
R	Gas constant ($8.3144598 \text{ J mol}^{-1} \text{ K}^{-1}$)
T	Temperature
E_β	Activation energy of sub-glass relaxation
M^*	Complex electric modulus
ϵ''_{der}	Kramers-Kronig dielectric loss derivatives
δ	Solubility parameter
E_A	Apparent activation energy
σ	DC Conductivity
U	Electric energy density
α'	Primary relaxation of constrained amorphous
U	Electric energy density
M_{33}	Global electrostrictive coefficient
η	Viscosity
Q	Intrinsic electrostrictive coefficient
d_{33eq}	Pseudo-piezoelectric coefficient

Abbreviations

Symbols	Full description
nN	NanoNewton
ZnO	Zinc Oxide
MEMS	Microelectromechanical system
AFM	Atomic Force Microscopy
mN	MilliNewton
LTCC	Low-temperature Co-fired Circuits
Al_2O_3	Aluminum Oxide
ssDNA	Two single-stranded Deoxyribonucleic acid
F_i	Force component
PDMS	Poly(dimethylsiloxane)

nA, mA	Nanoampere, Milliampere
PZT	Lead Zirconate Titanate ceramics
MOSFETs	metal oxide semiconductor field effect transistors
PVDF	Poly(vinylidene fluoride)
NiTi	Nickel and Titanium alloy
P(VDF-TrFE)	Poly(vinylidene fluoride-trifluoroethylene)
P(VDF-TrFE-CTFE)	Poly(vinylidene fluoride-trifluoroethylene-chlorotrifluoroethylene)
RFIDs	Radio-frequency Identifications
R2R	Roll-to-Roll
CNTs	Carbon Nanotubes
PEDOT:PSS	Poly(3,4-ethylenedioxythiophene): Polystyrene sulfonate
CIJ	Continuous inkjet printing
DoD	Drop-on-demand inkjet printing
pl	Picoliter
CTE	Coefficient of thermal expansion
PET	Polyethylene terephthalate
PAcryn.	Polyacrylate
PEN	Polyethylene naphthalate
PC	Polycarbonate
PS	Polystyrene
PI	Polyimide
PEGMA	Poly(ethylene glycol) monomethyl ether methacrylate
PEG/PEO	Poly(ethylene glycol)/Poly(ethylene oxide)
SEM	Scanning electronic microscopy
OFET	Organic field-effect transistor
LED	Light-emitting diode
SLR	Super-cooled liquid region
DSC	Differential scanning calorimetry
RT	Room temperature
FWHM	Full width at high maximal
BDS	Broadband dielectric spectroscopy
HHTT	head-to-head and tail-to-tail
PPT	poly(pentamethylene terephthalate)
PLLA	poly(L-lactic acid)
PET	poly(ethylene terephthalate)
P(VDF-HFP)	Poly(vinylidene fluoride-hexafluoropropylene)
PP	Polypropylene
DMA	Dynamic mechanical analysis
<i>T, G</i>	<i>Trans, Gauche</i> molecular Conformation
P(VDF-CTFE)	Poly(vinylidene chlorotrifluoroethylene)
MWS	Maxwell-Wagner-Sillars
CL	Coherent length
CRR	Cooperative Rearranging Region
RAP	Rigid amorphous phase
MAP	Mobile amorphous phase

DC	Direct Current
PBAC	Poly(bisphenol A carbonate)
PMMA	Poly(methyl methacrylate)
DEHP	Di-2-ethylhexyl phthalate
MEK	Meth Ethyl Ketone
DEP	Diethyl phthalate
PVC	Poly(vinyl chloride)
TMBPA-PC/ TEHP	Tetramethyl bisphenol A polycarbonate/Tris(2-ethylhexyl) phosphate
KWW	Kohlrausch-Williams-Watts function
PLA/ATBC	Acetyltributylcitrate doped poly(lactic acid) blend
P(VDF-TrFE-CFE)	Poly(vinylidene fluoride-trifluoroethylene-chlorofluoroethylene)
DBP	Di- <i>n</i> -butyl phthalate
VFT	Vogel-Fulcher-Tammann
CuPc	Copper phthalocyanine
DMF	Dimethylformamide
cP	Centipoise
PTFE	Poly(tetrafluoroethylene)

Chapter I

Force Sensor and Inkjet Printing Functional Layers: the-state-of-the-art

I Introduction

Force sensing element plays an important role in the fields where the response has to be reacted in real world. Thanks to the nature even small living creatures are capable of perceiving the external wide range scale magnitude of force owing to their large numbers of mechanoreceptors. So are human beings which respond to an external stimulus and react with corresponding manipulation with the help of force sensing system embedded in our skins. Inspired by the nature, extensive researches have been carried out by pioneers to understand the underlying working principles and further fabricate several sensor prototypes depending on the potential end implementation so far. In parallel the stimuli output actuators which behaves the reversible functionality than force sensors are also being addressed, mostly known as the artificial muscle. Recently, specific characteristic demands such as sensitivity (nN), accuracy, power-to-weight to some pitch quality are required [1, 2], to fulfill the requirements in application fields of robotics [3, 4], electrotiles [5-7], minimally invasive surgery [8, 9] in clinical treatment and so forth, which literally act as a driving force to the sensor technologies.

In this chapter the author provides an overview of force sensor technology, concerning the fundamental consideration of a force sensor design and its working principle, accompanying with the description of advantages and demerits of each concept and the state of the art of force sensor researches all walks of life, with the primary emphasis on piezoelectricity based force sensor as basic principle employed in our present mechanical sensor device.

II Force Sensor Mode (*Transduction Principles*)

II. 1 General Overview

A sensor is defined as a device that is able to respond to some kinds of input physical stimulus and convert this stimulus into unique output signals, compatible with signal processing circuits which ensure the signal readability. Here it should be noted that the physical sensory inputs are not only confined as mechanical stimulations, but also heat change (pyroelectric) [10], chemical oxidation-reduction [11], phototronics (ZnO) [12] and so forth. Compared with these sensory input stimulations, force sensor is more likely to function in a contact sensing mode. For example, the complex mechanical force such as the vibration is usually characterized with specific frequency, amplitude and phase as the identified information. The sensory components, acted as an intrinsic sensor, should be embedded or attached to the vibration body seamlessly in order to *in situ* or real-time monitor the mechanical information carried by the vibration, in particular in field of microelectronic packaging industry [13]. Such intrinsic force sensors were also utilized in field of nondestructive component detection or noncontact interface, for instance acceleration and motion control. On the other hand, extrinsic sensors appear to be mounted the contact interface sites and engage with touching incident. On basis of these purposes, force

sensors are designed taking into consideration of “the values” and give rise to some key specific interests of sensor characteristics, declared as sensitivity, accuracy, resolution, response time, full-scale application span, etc to evaluate the sensor performance. And these characteristics strongly determine the selectivity of sensing materials by the physical nature or configuration of a sensor, which in turn affect the reliability of the sensor performance. For instance, the MEMS cantilever force sensor harnessed for Atomic Force Microscopy (AFM) profile acquisition can measure the finest atomic scale force of several nanoNewton while the reliability of mechanical structure of an aircraft or space station can also be manifested by the giant measurement scope of force sensors.

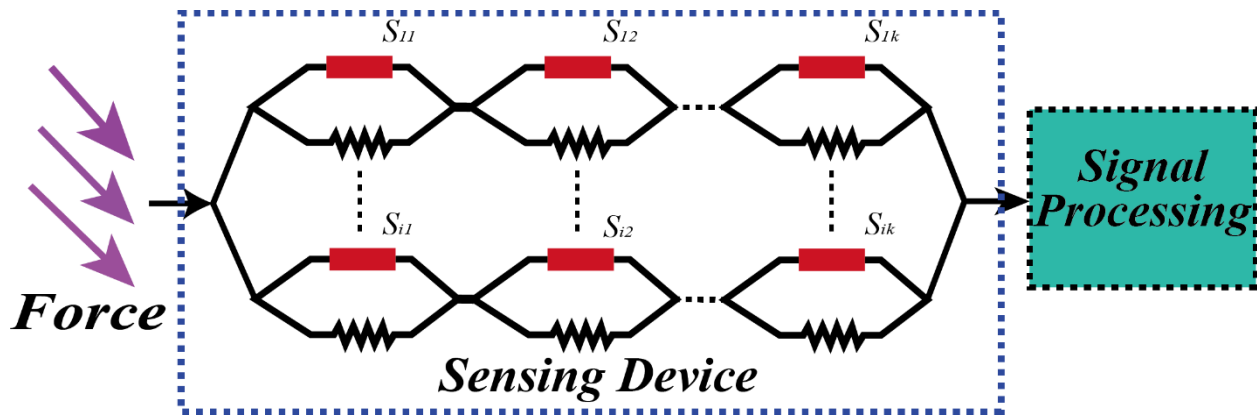


Figure I. 1 Schematic of a force system comprising sensing component array and signal processing circuit for readout.

Generally, the sensor working as an energy transducer consists of three main subdivisions, namely stimulus (excitation), transducer and signal processing sections as presented in Figure I. 1. The force simulations, behaving similarly to the heat, optic, electric and magnetic stimuli, carry the information as an example of mechanical vibration mentioned previously. It should be noted that the sensors family were categorized according to these external simulations and so as for the force sensors. The latter ones mainly are the acceleration, torque and pressure sensors. Normally, the feedback signal reflects the characteristics of the force applied, but sometimes this is not necessary. In such circumstance, Force sensors could be classified as two groups, quantitative sensor and qualitative one [1]. The Quantitative sensors give the full information in term of the electric signal output in most cases whereas the qualitative sensors function as the output signal surpassed the predetermined percolation threshold values, for example, the haptic sensing device mounted on touch screen portables where the accurate force values were not indispensable [14]. Moreover, a constant force applied is barely routine, far less than the varying frequency and amplitude coexisted. And recently force sensors do not serve the sensory device solely, but they usually coupled with the thermal and humidity [15-17]. A rather good examples of tactile sensing system of human fingertips presents the force and thermal perceptible capability simultaneously.

As motivated by human skin, specific interest is given to the humanoid robotic gears, such as medical treatment, rehabilitation involving prosthetic limbs and implantation of artificial organs. More recently, anthropomorphic robot arms for surgical operation were developed which can perceive the biomechanics and tissue disease [18-20].

Since a sensor is a converter capable of transforming the nonelectric energy into an electric signal, one even multiple transformation or change steps were required prior to an electric signal output. This converting process can be direct or indirect. The passive sensors are defined as a direct convertor which can generate the induced charges underlying specific physic effects such as pyroelectric, photoelectric and piezoelectric sensors and do not rely on the external power supply. Nonetheless, the active force sensors perform with the requirements of external power alimentation as a necessity. The inherent parameter of the sensors was modified in response to the external excitation. And these physical properties can be subsequently switched to the readable electrical signal. The output electric signal is supposed to be the values which are encoded in an algorithmic approach. The data processing part will be discussed later on. For example, a strain gauge force sensor can measure the tensile strength based on the resistance-modulate behavior. The resistance of sensors changed upon the sensor deformation and led to the variation feedback of electric current of external power source. Apart from active force sensor based on resistance, the sensors in response to the force excitation rely other transduction principles such as capacitive, resonant frequency, optical and electromagnetic methods. In following chapter, the most commonly employed transduction principles in force sensor systems were described. Meanwhile, the state of the art of each method was also summarized.

II. 2 Piezoresistive Effect Based Sensor (active sensor)

Generally, electric resistance is determined by the materials in nature and its dimension regardless the flow of charges in conductive materials. When a mechanical stimuli was applied upon the conductive material, its dimension changes and assists to counteract the geometric deformation apparently. And its electric resistance varied due to the change of flow of charge which is responsible for the variation of specific of resistance [1]. Having the quite similar behavior as cardiovascular circulation of human body, blood flow was blocked and weakened if there occurs an aneurysm [21]. Charge flow was to some patch modified upon the deformation of a conductor induced by external force application. Subsequently, the electric resistance variation ΔR can be detected being related to the applied force according to a piezoresistive or elastoresistive effects [22, 23]:

$$\frac{\Delta R}{R} = \sum d_i T_i = \sum d_i Y_i S_i \quad \text{I.1}$$

where R and ΔR are the original resistivity of resistor and variation of specific resistance respectively; d_i is assigned to piezoresistive coefficient and T_i represents the external force

(stress) applied. Y_i and s_i are the Young's modulus of piezoresistor and strain induced by stress for each component, respectively. Piezoresistive effect of monolithic metal wire was firstly reported in year 1895 and later was used for force sensor since the giant piezoresistive effect in silicon and germanium was discovered in year 1954 [24]. Materials for force induced resistor were classified in nature as metal, semiconductor and elastic polymers. Piezoresistive effect could be employed to fabricate the force sensor depending on a functional relationship between the induced strain (or geometric deformation) and applied force.

The performance of a piezoresistive sensor can be determined by the sensitivity, referring to the variation of the specific resistance to the force induced strain s_i and also rely on the shape of piezoresistor. It has been reported that the gauge factor ($\frac{\Delta R}{R}/s_i$) of metallic filaments as a piezoresistor ranges from 2 to 6. For example, Copper (Cu) and Nickel (Ni) alloy presented a constant sensitivity value of 2 over wide range of strain within limited temperature range, while platinum alloys possess a higher sensitivity of ~ 5 under rather high temperature environment. Silicon, a typical representative of semi-conductive materials shows ultrahigh sensitivity up to 150 [25]. Higher sensitivity gives better accuracy in theory only in case of good design concept. Aiming to obtain good sensitivity, a strain gauge like alloys piezoresistor were designed firstly in 1938 and has been fundamental sensing elements for many applications involving pressure sensor, load cells and torque sensor, etc. As presented in Figure I. 2, piezoresistor is attached to the

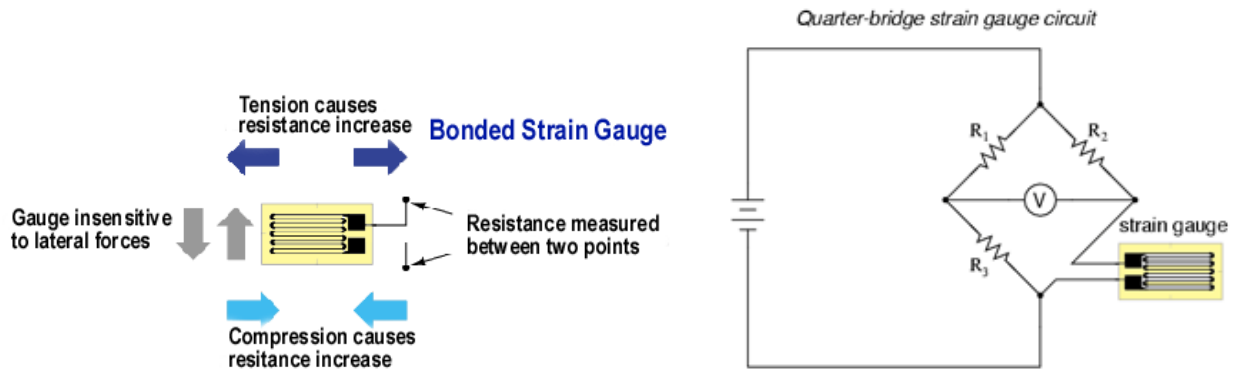


Figure I. 2 Schematic of piezoresistive force sensor based on a strain gauge, showing the alloy wires bond to the plastic backing. Force normally was applied in aligned with longitudinal direction (a). Quarter wheatstone bridge circuit for precisely measuring resistance of the strain.

plastic backing and is quite long in longitudinal while short in transverse direction. The elastic backing is electrically orthogonal with piezoresistor and carries the force, the scope of which scaled strongly depending on the tensile strength behaviors of elastic backing materials thanks to the constant Young's modulus upon the elongation before reaching the yield state. The strain gauge force sensors were stuck to the object and ensure absence of displacement between sensor and object. Since alloys have been used for the piezoresistor, there rises a challenge that the

temperature would change the resistance values of a fabricated pieoresistor force sensor. And the variation of resistance upon force can be precisely evaluated by quarter Wheatstone bridge circuit [26, 27]:

$$V_{out} = A(V^+ - V^-) = AV_{in} \frac{\Delta R}{4R + 2\Delta R} \approx AV_{in} \frac{\Delta R}{4R} \quad \text{I. 2}$$

despite the surrounding temperature, metal resister could generate current induced heat flow which might change the electric behavior of piezoresistor and plastic backing. Therefore in practical application, specific temperature compensation circuit was used to counteract the negative influence of the thermal flow to the sensitivity of force sensor.

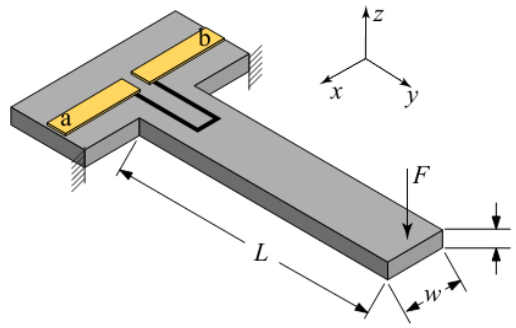


Figure I. 3 A schematic diagram of cantilever beam with strain gauge piezoresistor mounted. Force F was applied upon its free end perpendicular to beam in-plane. The range of gauge force is associated with size and shape of cantilever for a given beam material. The electrodes a and b were connected to the Wheatstone bridge circuit for measurement.

Compared to a stretch mode along with the longitudinal direction, milliNewton (mN) force can be measured more precisely by a cantilever beam mode with the help of piezoresistive force sensor mounted. The basic structure of force sensor system is presented in Figure I. 3. A high sensitive piezoresistor with its end was mounted onto a cantilever beam. In order to ensure good adhesion, varying materials deposition methods were carefully chosen. When a force is applied normal to the beam, the longitudinal length of piezoresistor is forced to be enhanced because of a stretch mode. Meanwhile, the length was compressed as cantilever beam was tilt due to an upturn applying force. By optimizing the beam materials (plastic, ceramic, Al, etc) and dimension thereof, wide range of force values can be measured. Hansu Birol et al. [28] introduced a cantilever force sensor with a single belt resistor attached as sensing element. 200 μm -thick dielectric ceramic thin-layer was coated on the Alumina substrate in a Low-temperature co-fired circuits (LTCC) method. Such cantilever force sensor has a sensitivity of hundreds of millinowton scale. Riadh Lakhmi et al. [29] further developed a millinewton force sensor based on Hansu Birol's cantilever force sensor. The glass-ceramic ink was chosen as a beam materials which was firstly screen-printed on the Al_2O_3 substrate. Piezoresistor inks was then printed on the

beam and followed a sintering process at 850 °C. The piezoresistive strain gauge was finalized by an etching step to the screen-printed shape-integrated piezoresistors. The novel fabricated sensor turns out to possess a greatly enhanced sensitivity of several millinewton (mN), with detectable force range of 0.1-4.3 mN.

Another screen-printed millinewton piezoresistive force sensors were fabricated in a simple and low cost way by Xinyu Liu et al [30]. The manufacturing process and the sensor prototypes were presented in Figure I. 4. The conductive carbon inks was printed onto the paper based hydrophobic cantilever beams. The novel MEMS force sensor can be folded into 3D dimension with high stiffness and anisotropic responses but lightweight. The force sensor was used to measure the mechanical behavior of soft materials such as polymers also demonstrated a surprisingly high sensitivity. The tunability of the sensitivity was closely dependent upon the dimension of paper beams which can be shaped arbitrarily. However, its drawbacks narrowed its application filed since the resonant frequency is quite lower to the kilo-scale Hertz of silicon-based cantilever beams.

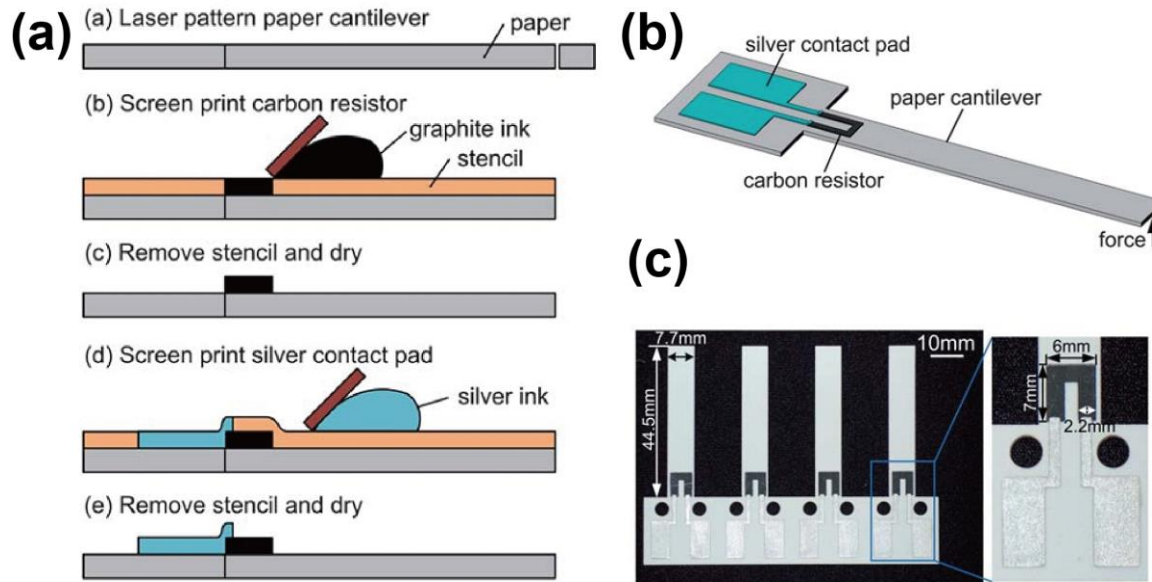


Figure I. 4 Schematic of cantilever beam integrated with the piezoresistor. (a) Fabrication process of paper based piezoresistive cantilever force sensor using a screen printing technique. (b) A diagram of paper cantilever beam mounted with a silver metalized carbon piezoresistor. (c) Dimensions of printed cantilever force sensor array.

High force sensitivity can be also achieved by using an ultrathin strain gauge piezoresistive force sensor. M. Gel and I. Shimoyama proposed an ultrathin piezoresistor based on the submicrometer-thick cantilever beam using a micromachining technology [31]. The multilayer cantilever beam consists of self-sensing silicon piezoresistive cantilever and insulator backing materials. A piconewton force was applied by using a piezoelectric actuator and the resistance of

the self-sensing beam was monitored by lock-in amplifier, corresponding to nanometer scaled displacement. Such ultrathin cantilever beam sensor was potentially used for biomedical application. R. Mukhopadhyay et al [32] also developed a feasibility of the piezoresistive cantilever force biosensor. The commercially available cantilever beam, with a piezoresistive sensor in-built embedded, was functionalized with 12-nucleotide ss-DNA sensor (S) probes by a robust inkjet printing technology. The cantilever sensor assay can measure the nanomechanical response of the DNA hybridization process according to a drift electric voltage of the embedded piezoresistor (see quarter Wheatstone bridge circuit).

Multiple-axial force sensor were designed and fabricated based on the piezoresistor by Lucia Beccai et al. [19]. The piezoresistors consists of four-axial p-type silicon based resistor units which are perpendicular each other in a cross-shape. Each with its one end was tethered to a high aspect-ratio cross-shape flexible element equipped with a $525\ \mu\text{m}$ high silicon mesa as presented in Figure I. 5a. The external applying force can be resolved into three decoupled force components F_x , F_y and F_n by analyzing the fractional change of resistance $\Delta R/R$ for each piezoresistor unit. The four-axial sensor shows rather good linear dependent upon the shear and

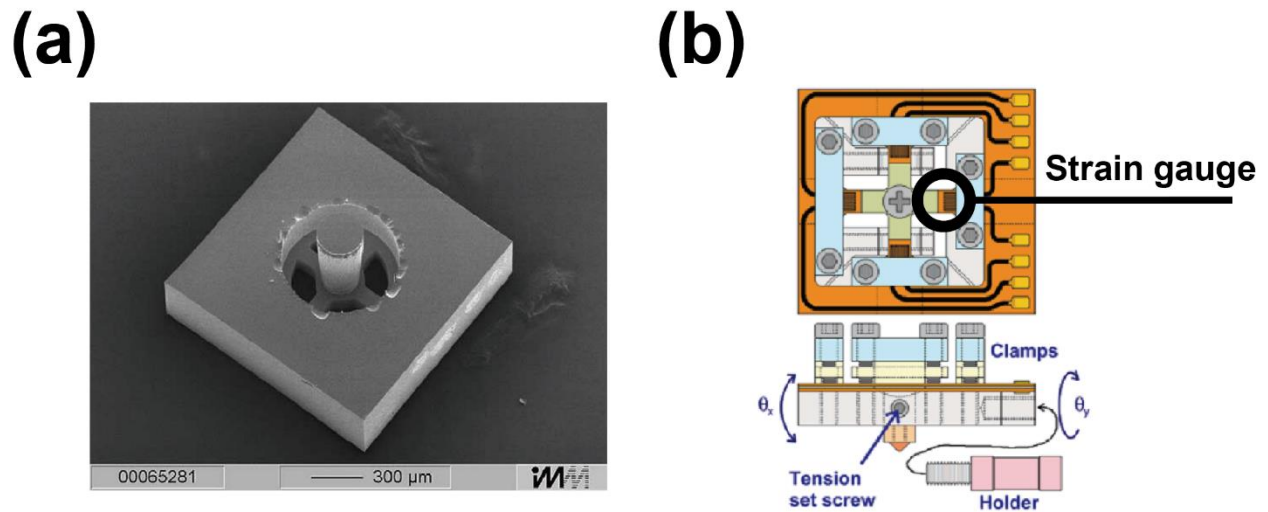


Figure I. 5 Scanning electronic microscopy (SEM) graphic of a four-axial piezoresistive force sensor tethered on flexible platform[19] (a). Intact 3D piezoresistive force sensor prototype where the strain gauge mounted onto the Ti-foil cantilever beam. The schematics also show two rotational degrees of freedom of the device for eliminating cross-talk [33].

normal force and high sensitivity of $0.032 \pm 0.001\ \text{N}^{-1}$ was achieved. Finally, elastic polyurethane polymer has been used to micro-force sensor packaging to obtain a smart interface in biomechanical measurement. Kai Kristiansen et al [33] proposed a novel 3D sensor device for AFM profiles. The piezoresistor consisted of a probe centrally located in a spring shaped like a symmetric cross, corresponding to four symmetrical Ti-foil cantilevers having a common probe tip as shown in Figure I. 5b. The four piezoresistive strain gauge elements were placed close to

the clamps of the fixed ends of the spring cantilever beam and are able to simultaneously and linearly measure both normal (out-of-plane) and lateral (in-plane) forces orthogonally with wide force range of <1 nN, ~ 10 μ m and ~ 1 mN for micro-, meso- and macroscale force sensor, respectively. The force sensor was examined by measuring the storage modulus of cross-linked polymer P(dimethylsiloxane) (PDMS) and the measured storage values was consistent with the values found by other characteristic technique.

Besides, other models have also been reported using the piezoresistive rubber force sensor transduction method. Liyun Guan et al. [34] developed a novel force sensor mode. The feasibility and realization of stretchable sensor based on conductive ionic liquids deposited onto two horizontal rubber fibers have been investigated. The ionic liquid wetted amid the rubber fibers shows the strain dependence of specific resistance, which making it possibility to act as a high sensitive force sensor even down to 1% strain. Subsequently, the qualitative force sensors were adapted to monitor the human-motion to diagnose the Parkinson's disease and potentially could serve the sport aspect. A piezoresistor tactile force sensor array involving cross-sectional warp and weft yarn metallic wires (rows and columns) were reported by Makoto Shimojo et al. [35]. The metallic cables were stitched into conductive rubber which separated the cables at their cross point. The tactile force sensor array textile, attached to the humanoid robotics, were calibrated and showed rather good performance in response to pressure/force in the range of 0-200 kPa. However, the readout resistance signal was 1 millisecond (ms) phase delay to the applying force, while this must be due to the viscoelasticity of the rubber in nature.

II. 3 Capacitive Sensor (active sensor)

Capacitor generally consists of two conductive electrodes which are isolated by insulators such as flexible silicone, dielectric polymers or commonly-used millimeter-scale air gap layer. And it can be recharged and stock a quantity of charges on which its capacitive performance is strongly dependent. For a given capacitor, the capacitance value is described as a function of variables, those are, the gap width between two adjacent electrodes d , total effective electrode area A , dielectric constant of insulator ϵ_i and number of capacitor elements n , etc [1, 36]:

$$C_I = f(t_i, A_i, \epsilon_i, n) \quad \text{I. 3}$$

In most cases, the electrodes of capacitive force sensors are in parallel dimension whatever plate or cylinder shaped. A capacitance of an absolutely parallel-plate capacitor can be termed as $C_p = 4\pi\epsilon_r\epsilon_0 \frac{A}{t}$, where ϵ_r is the relative permittivity of space filler amid the both electrodes and ϵ_0 is permittivity in vacuum; t represents the distance between two electrode plates; here the electrode edge effect is negligible since the overlapping area of electrode $A \gg t^2$. The distance t between the electrodes is usually lower, as the inverse relation between capacitance and gap

between electrodes is highly non-linear and the sensitivity drops significantly with larger gaps. An applied force which is normal or lateral can cause somewhat variation or displacement of conductive electrodes and the capacitor responds with a change in its capacitance. The schematics of capacitor on each status were presented in Figure I. 6. Such capacitance drift makes a capacitor element possible to be employed as a force sensor in theory. Technically, the normal force tends to alter the distance between the parallel electrode plates while the tangential force changes the overlapping electrode surface area.

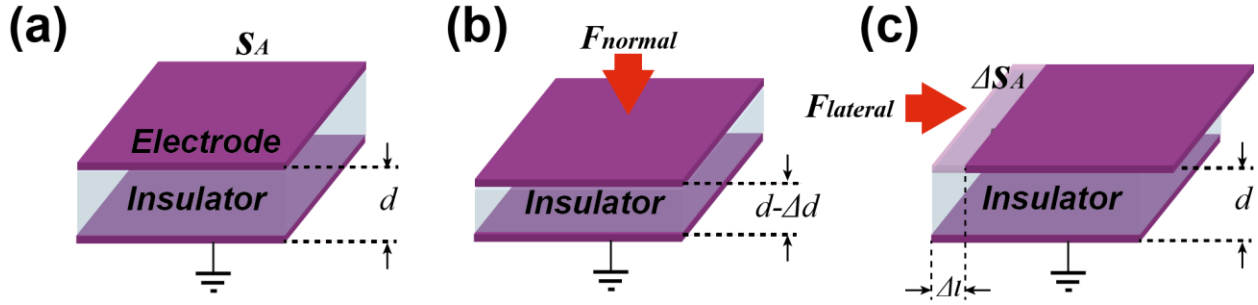


Figure I. 6 Parallel-plate capacitor with insulator gap sandwiched by two conductive electrodes (a); gap between two electrodes was compressed by Δd due to an applying normal force F_{normal} (b); ΔS_A surface area variation when a lateral force $F_{lateral}$ is applied to a plate capacitor (c).

The force sensing principle will be described following. The force induced changes of capacitance value were usually not measured directly. Instead, the displacement or deflection of capacitor conductive plate caused by applying force gives the capacitive contrast of the electric elements, which is eventually converted into an electric signal in a much more accessible measurement mode, that is, output voltage $V_{out} = V_{ref} \sum \frac{\Delta C_p}{C_p}$, where V_{ref} is the voltage supply for capacitance measurement[37]. It has also been well-known that capacitance and gap between electrodes is highly non-linear and the sensitivity drops significantly with larger gaps. However, induced capacitance is more likely to be linearly dependent on in-plane force.

Self-capacitance force sensing devices were designed as a qualitative tactile touch force sensor with only one conductive plate serving into the capacitance measurement circuit. The naked or metallic plate exposing to the surroundings were taken another electrode. When a conductive object touches the capacitive force sensor, the capacitance difference relative to the ground values was measured. Such capacitor is easy to design and fabricate, although their drawbacks are pronounced, such as nonstable reference capacitance value, non-directional electric field leakage, tremendous parasitic noise, etc. More capacitive force sensor modalities were based on the mutual capacitor. Lucie Viry et al. [38] proposed a simple capacitive 3D force sensor prototype. The force sensor consists of the sole shared top electrode and four metallic square bottom electrodes which were arranged similar to the square individually, having the identical distance mutually. The electrodes were both embedded into the flexible PDMS

micrometer layer and was separated by both $150\ \mu\text{m}$ air gap and fluorosilicone dielectric insulators stacks. The out-of-plane component F_z of the three-axial applying force was evaluated readily according to a conventional approach (Figure I. 7a) while the on plane components F_x and F_y caused a horizontal slip of top electrode and yielded a variation of overlapping area of top and bottom parallel-plates which gave rise to the capacitance discrepancies. As expected, the nonlinear plot of normalized capacitance variation against normal component of applying force values was obtained, the segment of which presented a strong force dependence of sensitivity. An excellent linear relationship between tangential force and the force induced capacitance change was observed although a somewhat initial force need to be applied in order to overcome the static force due to capacitor structure. Rachid Bekhti et al [39] reported a compact and cost-effective 3D force sensor based on the almost the similar concept as Lucie Viry's except an optimal space filler materials as presented in Figure I. 7b. The reliability of the three-axial force sensor was realized by applying a low-magnitude force of different directions. A good linearity of capacitance to versus force applied was a result according to standard linear least-squares method. In addition, the sensitivity and sensor resolution smoothly depended on the dielectric behavior of the insulator layer.

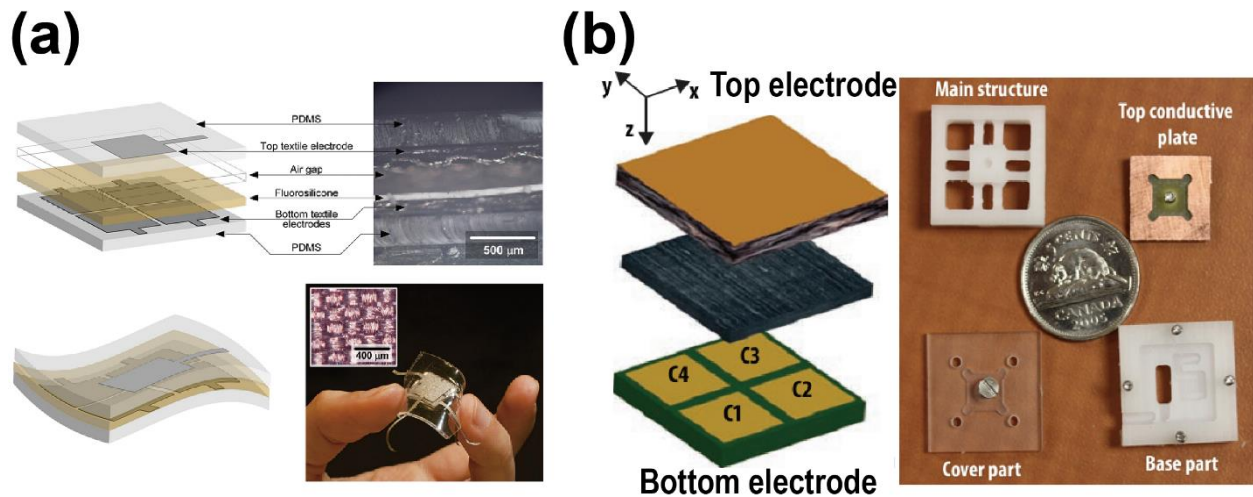


Figure I. 7 (a) Diagram of capacitive force sensor structure and monolithically fabricated element with cross-sectional view [38]. (b) Simplified illustration of three-axial capacitive force sensor and the components in reality.

Keekyoung Kim et al. [40] reported a capacitive strategy to the monolithic MEMS-based microgripper with integrated force feedback along two axes. The motions of gripper arm, with movable one, were handled by V-beam electro-thermal actuator in millimeter sensitivity. The contact force of microgripper was monitored by the longitudinal capacitive force sensor with comb-like parallel-plate metallic electrodes while gripping force was measured by an altitudinal comb-like force sensor. After sensor calibration using a precision microbalance, the resolution of

contact force between the microgripper and substrate is turned out to reach a high level of 39.5 nN with seconds. Meanwhile, the gripping arm in altitudinal direction was also calibrated. Finally, the feasibility of microgripper implementation on micromanipulation of micrometer-sized porcine cells was presented and the validation experiments resulted in a high level of sensitivity of nanonewton (nN) force scale. Xu et al. [41] designed and fabricated a microgripper with dual-axis force sensing ability based on a comb tooth like capacitive force sensors. Compliant rotatory and linear guiding flexures were the basic working principle of such microgripper. The sensors proposed were capable of gripping force sensing and environmental interaction ability upon each orthogonal force direction. Prior to practical implementation, its performance and effectiveness were verified by precisely calibrated. Feasibility of the developed gripper device are validated through the experimental investigations on gripping a human hair eventually.

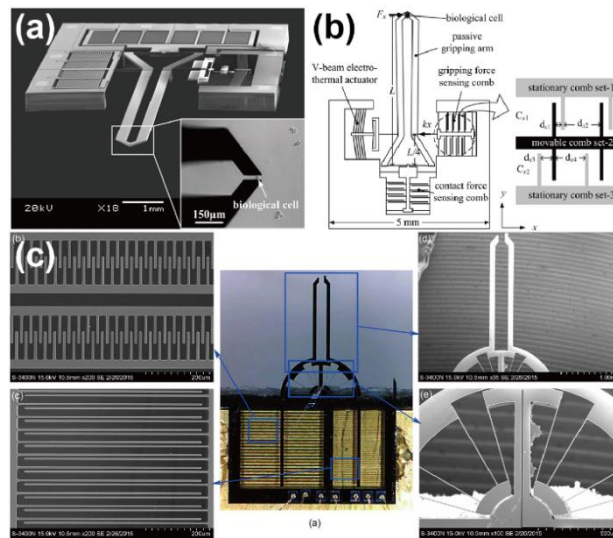


Figure I. 8 Schematics and microscopies of MEMS-based capacitive force sensors. (a) and (b) Microgripper with dual-axial force sensor using two orthogonal comb-like electrode capacitors; (c) photographic of developed microtweezer bearing the compliant rotatory structure and linear guiding flexure joint with two comb-like capacitive force sensors. Adapted from the illustration provided by literature [40, 41].

II. 4 Piezoelectric Effect Based Sensor (passive sensor)

In previously section (PVDF-based polymers), we summarized that piezoelectric effect has been used to describe the phenomenon which possesses an electric and mechanical transduction method in many material kinds. This coupling effect was firstly found for the natural crystal such as quartz and potassium sodium tartrate tetrahydrate, the latter also known as Rochelle salt. These materials are able to yield the internal electric displacement or surface charge in response to the external applied mechanical stress. Over the decades, ceramics, polymers and liquid crystals have been successively unveiled and presented rather strong electromechanical transduction behavior due to a large piezoelectric effect, which is also defined as the well-known inversely piezoelectric

coupling effect if a material is mechanically actuated under the application of the electric field E . The materials which coupled with electric field are likely to serve as an actuator potentially. Likewise, the piezoelectric effect confers materials the possibility of design and fabrication of a force or pressure sensor. And the sensing elements are in theory passive. That means the external power supply is not mandatory to operate the function of the piezoelectric force sensor, rather than the elements based on the piezoresistive and capacitive transduction methods [1, 2, 15]. This passive feature makes the force sensor reliability and high efficiency due to no depletion of ponderous power supply system. This gives tremendous advantages to miniaturize the microelectromechanical system such as portable and wearable equipment.

In most cases, piezoelectric force sensor is capacitor-like transducer with sensing layers sandwiched between two conductive electrodes. The mechanically induced electric displacement (charge or voltage changes) can be measured in two accessible ways: real-time output current I and voltage V . The latter in correlation with applied force F can be given as following expression [14, 21]:

$$V = \frac{Q}{C} \approx \frac{d_{ij}t}{4\pi\epsilon_0\epsilon_r A} F \quad 1.4$$

where Q is the charges yield; C is the capacitance of parallel-plate piezoelectric device; d_{ij} represents the piezoelectric coefficient along or normal to the piezoelectric force sensor in-plane; t and A are the respective thickness and overlapping surface area of electrodes of a capacitor. For a given material, the sensitivity of piezoelectric force sensor is determined by t/ϵ_r cluster. Aiming at achieving high sensitivity, the layer thickness value t should be desirable thick which highly relies on the fabrication process. In some cases, force sensor was used at limited place where small size of force sensor was demanded such as tactile sensing of robotic fingertips. ϵ_r is wanted large enough, originating from the dielectric material in nature. The indicative parameter, piezoelectric coefficient d_{ij} , contributes much to the sensitivity and must be as large as possible. Previous section described that when a stress was subjected to the piezoelectric materials in thickness mode (d_{33}), the short circuit leakage current I is simplified as $I = d_{33}YA \frac{\partial S_1}{\partial t}$ [42]. The output current is detectable if the differential of the mechanical strain of capacitor like force sensor is not equal to 0. So the piezoelectric force sensor only functions when there is a dynamic force. If the applying force maintains constant value, the charge or current returns to the reference value of zero.

To ensure high sensitivity, specific interest has been given to the materials with high d_{33} and ϵ_r . Crystals, semiconductive compound have been widely used as a sensing material due to high dielectric permittivity and piezoelectric coefficient d_{33} value [43-46]. The first piezoelectric force sensor was based on quartz crystals element. Because of its stiffness and high Young's modulus,

the quartz crystal sensing element was used where large strength of force applied. However, dielectric and piezoelectric behavior of quartz were not so high enough that high force sensitivity could not be achieved. Thus, ceramic perovskite has attracted much attention, in particular Lead Zirconate Titanate (PZT) which has a utmost large dielectric constant of ca. 10^4 at room temperature [47]. Moreover, this output signal (I or V) has always been quite small value with nanoampere (nA) or microampere (mA) for certain microelectromechanical device. Therefore, electric amplifier was aligned with sensing elements optionally so as to improve the linearity, reliability and high signal-to-noise ratio.

A large number of force or pressure sensor prototypes based on perovskite ceramics were proposed. Canan Dagdeviren et al. [47] introduced a conformal amplified force sensor array using PZT ferroelectric ceramics integrated with a construction of silicon metal oxide semiconductor field effect transistors (MOSFETs) on the flexible elastomer silicone. PZT sensing layers were connected to the gate of transistor which allows feedback signal processing. The piezoelectric pressure sensor was employed to measure the subtle changes in arterial pressure using devices mounted on the skin which is valuable for monitoring vital signs in emergency care, detecting the early onset of cardiovascular disease and continuously assessing health status. Ultrathin inorganic

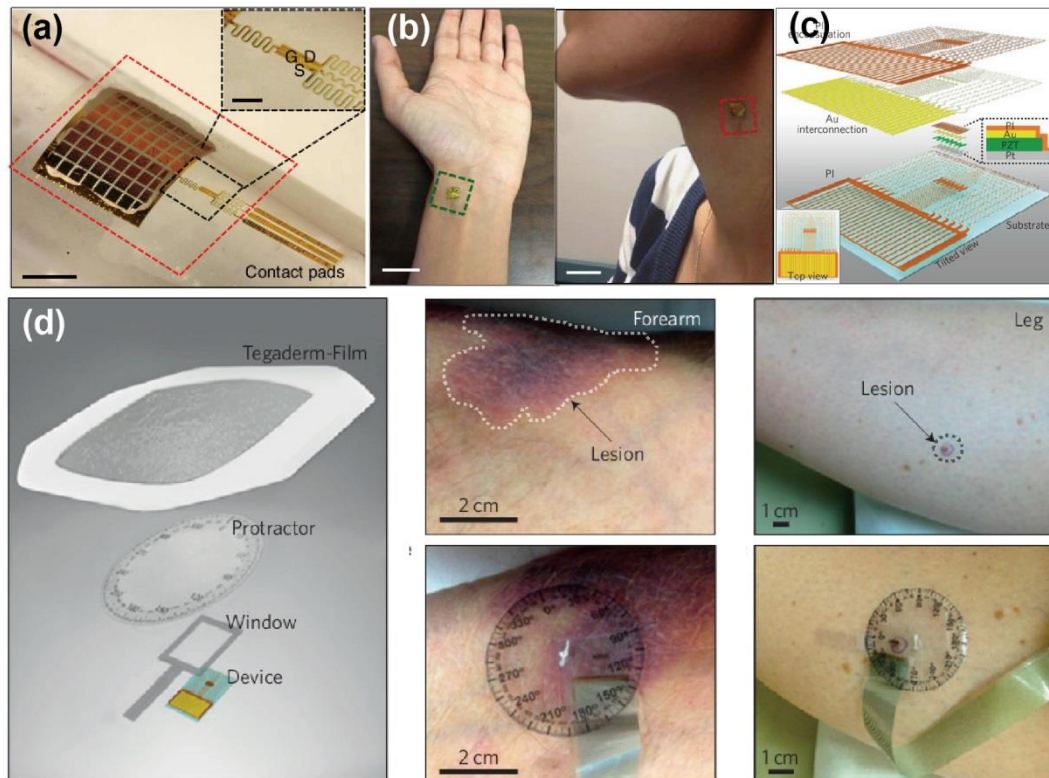


Figure I. 9 (a) Photographic of encapsulated PZT piezoelectric force sensing elements device wrapped on a cylindrical support. Square-like force sensor array was collectively integrated with silicon metal oxide semiconductor field effect transistor. (b) Photographs of representative application of the piezoelectric force sensor mounted on human wrist and neck for monitoring the

transient blood pressure waves. (c) Schematic illustration in tilted overview of soft tissue biomechanical force sensor. (d) Schematics of force sensor system in leftmost graphic [47]; figure in middle showing the large area of lesion of human skin with (lower) or without (upper) a mounted biomechanical force sensor device; a small lesion spot mounted with or without a nanoribbon force sensor system [48].

piezoelectric and semiconductor materials on elastomer substrates enable amplified, low hysteresis measurements of pressure on the skin, with high levels of sensitivity (~ 0.005 Pa) and fast response times (~ 0.1 ms). Recently, the same authors [48] proposed a series of materials and design concepts that allows for *in vivo* measurements of viscoelasticity in the near-surface regions of the epidermis through the use of ultrathin, stretchable networks of mechanical actuators and sensors constructed with nanoribbons of PZT ceramics. Soft, reversible lamination onto the skin enables rapid, quantitative assessment of vis-coelastic moduli, with the ability for spatial mapping. The newly fabricated force sensor systems can provide precise and reproducible evaluation of mechanic behavior for wide range of bottom materials and conditions. Applications *in vitro* with mock and *ex-vivo* skin preparations under varying conditions and *in vivo* on human subjects, collected at various locations over all main regions of body, under both normal conditions and following administration of pharmacological and cosmetic (moisturizing) agents, demonstrate the capabilities. Experimental validation for biomechanical inspection was extended to the general organs of living bodies, exhibiting the broad applicability and adaptability to all parts of body. The schematic representations and experimental photographics were shown in Figure I. 9.

The supports of force sensor have not always been flat and stiff in reality. Although large amount of outperformed force sensor prototypes were constructed using the stiff PZT sensing elements, there rises challenges if the supports of the sensing system have the more complex surface characteristics, such as human fingertips. Deformation of the supports also might cause dysfunction of the sensing elements during in case of motion, even though the soft and flexible polymer foils were used as a force sensor substrate. Thanks to its flexibility, fast response and ease of processibility, PVDF-based fluorinated polymers enable to give special advantages in flexible force sensor implementation and can be compatible with signal processing integrated circuit. Deok-Ho Kim et al. [49] presented a superelastic alloy (NiTi) microgripper with integrated electromagnetic actuator. Ability to measure the millinewton (mN) scale force was realized by an integrated PVDF piezoelectric force sensor. The beam of the microgripper with one end for manipulation of the object, was connected an electromagnetic actuator and operated by compliant configuration. Biocompatible Parylene layers PVDF force sensing elements were mounted to the beam tips, which gives the microgripper capability of manipulation of biological cell. Prior to the integration of the microgripper, the actuator and force sensor system were calibrated and high sensitivity of hundreds of millinewton (mN) was achieved consequently. Ravinder S. Dahiya et al. [50] reported a piezoelectric tactile force sensor integrated with oxide semiconductor FET using P(VDF-TrFE) copolymer as gate insulator layers. This device was electromechanically coupled with tactile force via an integrated field effect transistor which served as a signal-modulator as shown in Figure I. 10. The compact tactile force sensor could be embedded in soft and compliant elastomers for human-machine interface sensing elements.

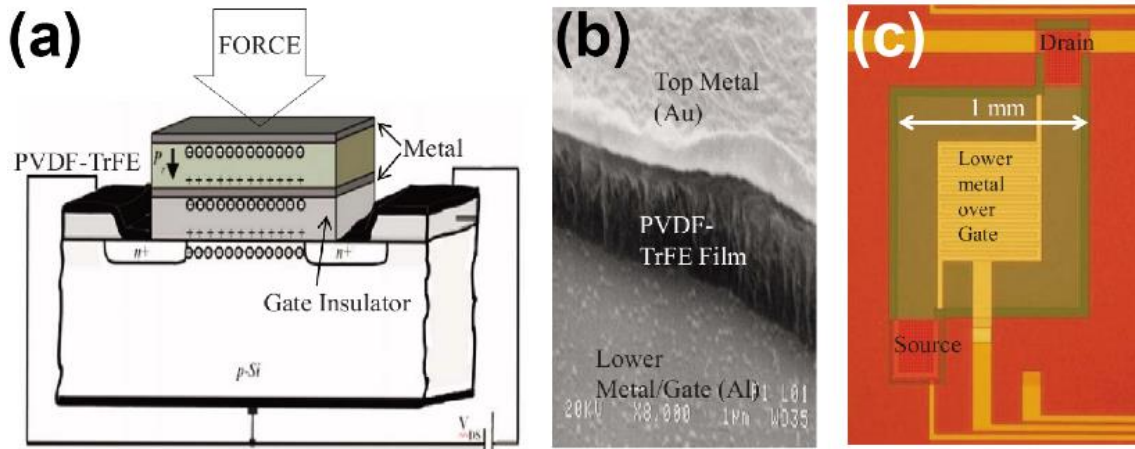


Figure I. 10 Schematic (a), microscopy (b) and photographic (c) of tactile piezoelectric force sensor integrated with metal oxide semiconductor field effect transistor.

II. 5 Summary

In this section we described the three mainly available transduction methods functioning on the force feedback sensor device and reviewed the state of the art progress of these conversion forms on the microscale newton characterizing in microelectromechanical, microelectronics, biological and medical device application fields as summarized in Table 1. However, specific characteristics upon the sensor device were demanded to fulfill the harsh requirement, such as high sensitivity, fast response, flexibility, reliability and ease of manufacturing, etc. Thus, the printing technologies have been adapted, aiding and revolutionizing the burgeoning field of flexible/bendable sensor devices. In this current study, inkjet printing, one of the emerging and promising sensor manufacturing techniques was employed. Next section will give an overview of inkjet printing technology and its printing counterparts.

III Printed Electronics Technologies

Printing is defined as a reproduction process in which printing ink is applied to a printing substrate in order to transmit information (patterns, graphics, texts, etc) in repeatable forms using an image-carrying medium. This sophisticated technique has been extensively developed for the media products and packaging industries over more than one hundred years. Recent years saw a specific interest given to the printed electronic devices as well as force sensor, which raised the challenges and problems for manufacturing and fabricating field. Due to its simplified processing procedures, fast prototyping, low volume materials using, ease of pattern transferring principle, printing technologies provides an alternative manufacturing route to low-cost and large area printed electronic devices and transducers, such as organic thin film solar cell [51, 52], transistor [53, 54], sensors [55, 56], light emitting diodes [57] and RFID tags [58, 59].

Table I. 1 Comparison of force sensor technologies based on three mainly reviewed transduction principles

Transduction Technologies	Materials		Configuration	Gauge Range	Resolution	Merits & Demerits	Sensitivity	Applications	Ref.
Piezoresistive Force Sensor	Bulk Metal (Copper, Ag)		Straight/meandered wire	0%-300% strain	1 mN, 1 μ N	Advantages --Low cost, good sensitivity, low noise, simple electronics, flexible and stretchable,	1.0-2.0	Tactile sensing,	[1], [2] [22]-[36]
	Metal Nanoparticles, alloy (Ag Nps, Pt NPs)						4.0-6.0 (alloy)		
	Carbon derivatives (CNTs, Graphene, Fabres)		Woven & yarn textile	128 Pa	--		100-400		
	Semi-conductor					± 150			
	Conductive Polymers & Composites, Ionic Liquids		Cantilever, MEMS	nN, μ N, mN	5 nN 10.36 μ NV ⁻¹	25-50	Microscopic acquisition,		
	Printed Circuits (Ag NPs, PEDOT:PSS)					4.0-12.0	RFIDs		
Capacitive Force Sensor	Air gaps Ceramics		Parallel-plate capacitor array	130 kPa	6.6E-4 kPa ⁻¹ 2.3E-4 kPa ⁻¹	Advantages -- high sensitivity, Feasibility, immune to temperature change, robust, multicontact sensing, productivity	3%/mN 14.22 N ⁻¹	Tactile sensing,	[1] [2] [37]-[42]
	PDMS		Interdigitated electrodes,	5 mN (PDMS)	--			Accelerometer,	
	High Dielectrics Polymers (PS, PP, PA, PI, PVDF)		Woven & yarn textile;	1 mN	--	Demerits Stray and hysteresis, High Voltage supply, nonlinearity	1.14 kPa ⁻¹	Medical device, imaging	
	Ceramics		MEMS,	65 nN, $\pm 144 \mu$ N	0.61 μ N		6%/ μ N		
Piezoelectric Force Sensor	Materials	Dielectric Constant	Parallel-plate Capacitor-like sensor array	18 mN	39.5 mN V ⁻¹	Advantages --High sensitivity and output, resolution Linearity, High SNR Robotics, Dynamic force sense, No voltage supply	39.5mNV ⁻¹ 0.05 V N ⁻¹	Tactile sensing	[14], [21], [43]-[50]
	Oxide and nitride (Quartz, ZnO, AlN)	<10		0-10 N	--			Accelerometer	
	Piezoelectric Ceramics (PZT, BaTiO3. etc)	>100	POSFET (Piezoelectric oxide semiconduct or field effect transistor)	25 N	50 mV N ⁻¹	Demerits --Pyroelectric Integrated, Temperature variation	500 mV N ⁻¹	Dynamics motion,	
	Ferroelectric Polymer (PVDF, P(VDF-TrFE)), P(VDF-TrFE-CTFE)	10~100		Cardiovascular sensing	--		2 μ A Pa ⁻¹	Internet Things identifier	

On one hand, printing electronics simulated the specific demanding in advancement of bandwidth of information carrier materials, paving the way to explore large area multifunctional printed electronic devices, seemingly depending on the aim of end applications. This could also give the numerous possibilities and complimentary materials for their deposition. On the other hand, various printing techniques have also offered a plenty of opportunities and roadmap for a selected functional materials such as unique flatbed patterns, 2D and 3D micromachining electronic devices. Fortunately, a number of printing technologies have been developed to deposit a wide range of materials on versatile substrate which are ubiquitously non-planar and flexible.

Generally, for a typical process of printing electronics, printed material was firstly treated and modulated with digital information, and then delivered upon the desired position on the substrate by various printing technologies. According to the materials transferring process, printing techniques could be classified into two main groups: contact and non-contact printing. In a contact printing technique, digitalized materials carrier or distributor system was in physical contact with the flexible substrate to afford the realization of materials transportation. Several prevalent printing technologies with regard to the contact principles involve the gravure printing, flexographic printing, lithography/offset printing, microcontact, etc [51, 60, 61].

The distinctive feature of gravure printing technology is that the information elements are engraved on the surface of the functional inks delivery system like the rotary metallic cylinder by employing the electromechanical gear. The information inks were then trapped in the engraved microcells and reproduced to the substrate as presented in Figure I. 11b. Fast and high throughput production are highlighted for gravure printing in a roll-to-roll (R2R) extended streamline mode [62]. However, the main limitation is also manifested. Engraved module is forced to be compressed against the auxiliary rotary cylinder and might give damage to the substrate and engraved information carrier, resulting in low resolution and incomplete patterns. Inversely, flexographic printing technologies employed an embossed information carrier layer [60, 63]. This relief elastomer (e.g. rubber and PDMS) layer is usually prepared by the lithographic etching method. When the printing proceeds, an auxiliary ink delivery system is engraved microcell arrays allowing a reliable transfer of the functional inks to the digital embossment on the cylinder surface. Last printing step shares the similar ink delivery system with the gravure printing technology and schematic representation is presented in Figure I. 11a. Such printing technology is compatible with a wide range of the inks and therefore results in the uniform thin ink layers, offering the improved pattern reliability and sharp edges than gravure printing features. Moreover, lithography technology is also a robust and deeply developed printing technique [51, 64]. The pattern to print is transfer to the plate cylinder by complex and successive surface micromachining technologies, which also rise out of the pristine printing plate. Meanwhile, blank ink spots were offset by orthogonal aqueous dampening solution or waterless silicone system.

Besides as stated classic contact printing technologies, some emerging inks transfer techniques such as micro-contact [36], nano-imprinting [65] and transfer printing [66] technique are developed for the future trend of successfully and fully flexible printed electronic device.

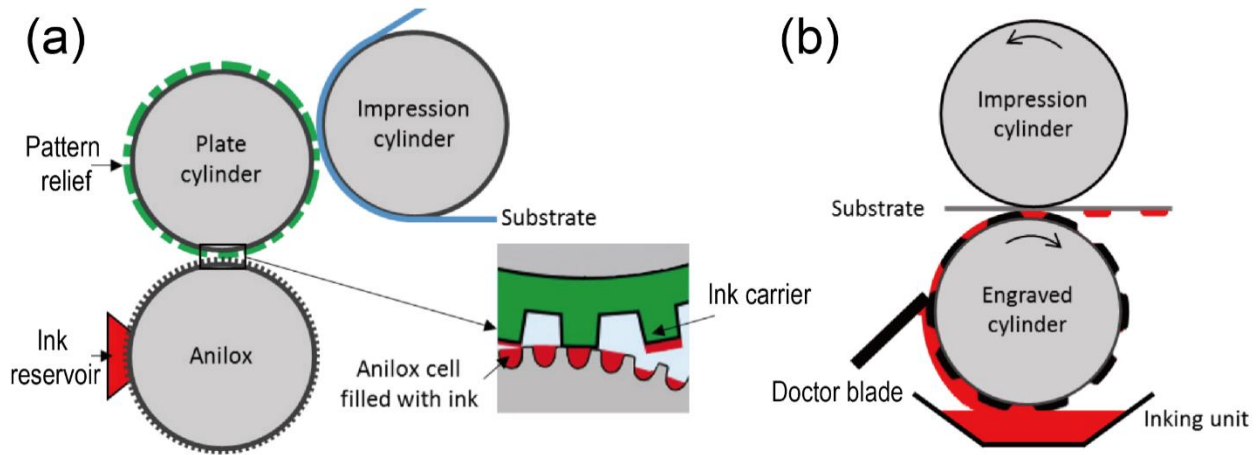


Figure I. 11 Schematics of typical flexographic printing (a) and gravure printing technologies (b). Gear-like ink transfer system was zoomed. Adapted from the illustration provided by the literature [60].

The non-contact printing processes could be explained by two means. The first one which differs from the contact printing technologies describes that the inks delivery system does not touch with the substrate. The most popular and matured non-contact printing technique is screen-printing. In Figure I. 12, the basic principle of this printing is based on a screen stencil, allowing viscous or colloidal inks pass through, whatever in a flatbed or high throughput sheet-to-sheet or roll-to-roll processes. Ink poured inside the stencil was squeezed and forced to transfer through the screen to the beneath substrate supports. This printing technique also deals with high viscosity ink solution, making it very step-consuming and expensive for maintenance and clean. Additionally, although less capital was invested into the screen stencil printing, the print quality and characteristics were closely depending on a plenty of factors during pre-patterned and printing step, such as high resolution screen pattern, mesh size of stencil, printing force and speed, etc. The second one is an emerging direct patterning technology. The materials are deposited through a print head which is able to transpose the digital information into program controlled human-machine interface platform. This direct patterning also gives possibility of drop-on-demand materials deposition, affording more complicated and miniaturized electric devices. Amongst all the direct patterning techniques, contact free inkjet printing has undergone the rapid development in printed electronics. Such technique uniquely copes with liquid ink solution, firstly transported and stocked in the microchamber. Ink solutions, often as a train of droplets, were expelled out of printing nozzle by thermal or electromechanical actuators at precisely controlled location. The droplets then detached with nozzle orifice and hit the substrate in a stable

trajectory. A successful inkjet printed pattern was the result of compatibilization of ink rheological parameters with drop ejection system and wettable substrate.

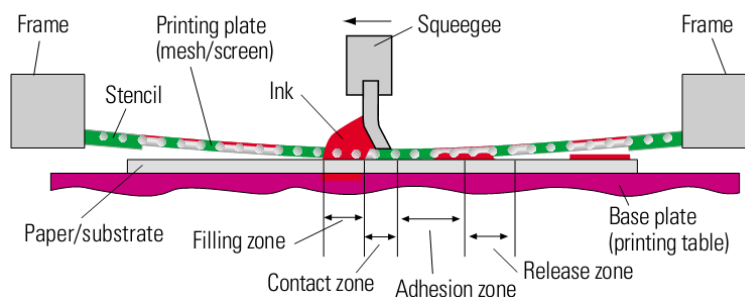


Figure I. 12 Schematic of a flatbed screen printing process. Inks poured on the upper side of stencil, beneath which was placed the substrate. The inks (red) were squeegeed to pass through blanket mesh which carries the pattern information. Figure adapted from the illustration provided in the literature [60].

Having described each printing techniques, it is a critical issue to develop the printed materials in terms of excellent specific rheological behavior and physical nature point of view. Potentially printable materials employed in printing process can be divided into three large group of families involving conductor, semiconductor and dielectric insulator based ink solutions. Each family can be categorized as ink solutions and suspensions, depending on the printing technologies and low-cost and long life-time of printed electronics. Single compound ink formulations are not always suitable for printing manipulations. Hence, chemical and physical modifications of the ink formulations have been made in order to fulfill the requirement of stability and high quality of printing patterns. For example, cosolvent system is able to minimize the coffee-ring effect in the printed patterns, which is the common problematic issue in the ink solution-based printing technologies. Besides, hybrid ink materials have also been developed in an attempt to compensate the dwarfed electrical property. Printed electronic circuits using carbon nanotubes (CNTs) doped PEDOT:PSS inks presented the orders of magnitude increasing electrical conductivity.

Amongst the different printing technique as stated above, inkjet printing technology is carefully selected as the main materials deposition method because this technique has been highlighted as a high throughput, cost-effective, low materials wastage and step-saving printing approach. Hence, the forthcoming part will give an overview of this robust and rapid prototyping technology in terms of ejection principle, ink physics, drop morphology, drying dynamics and versatile substrate.

IV Inkjet Printing Technologies

In previous section, the advantages of non-contact inkjet printing technology have been highlighted. High reliability and reproducibility make this printing technique compatible with wide range of materials to deposit. Up to date, many researchers have reported prominent contribution in printed sensor and electronics over large flexible substrate by inkjet printing technique. In the framework of this thesis, we employed this advanced materials deposition approach to achieve our desirable sensor application.

A successful inkjet printed pattern relies on the combination of physico-chemical properties of ink solution, corresponding characteristics of drop formation system and wettability of the substrate. Several successive process steps can be highlighted during printing and without any perfect patterns could be impossible.

IV.1 Ink Ejection

Stable and reliable ink ejection is a quite crucial specific interest for inkjet printing technologies. According to the print head technologies, inkjet printing process can be divided into two main families, continuous inkjet printing (CIJ) and drop-on-demand (DoD) printing, both of which used different types of transduction principle. Figure I. 13 summarized the diagram of continuous and drop-on-demand types of droplet ejection and the most commonly adopted transduction methods. CIJ and DoD printing technologies can further be subdivided into several items, critically depending on the ink ejection and droplet positioning methods. These methods are adapted for the arbitrary geometry of the printhead and the nozzles which can yield microscale diameter of drops equivalent to the volume of ~100 picoliter.

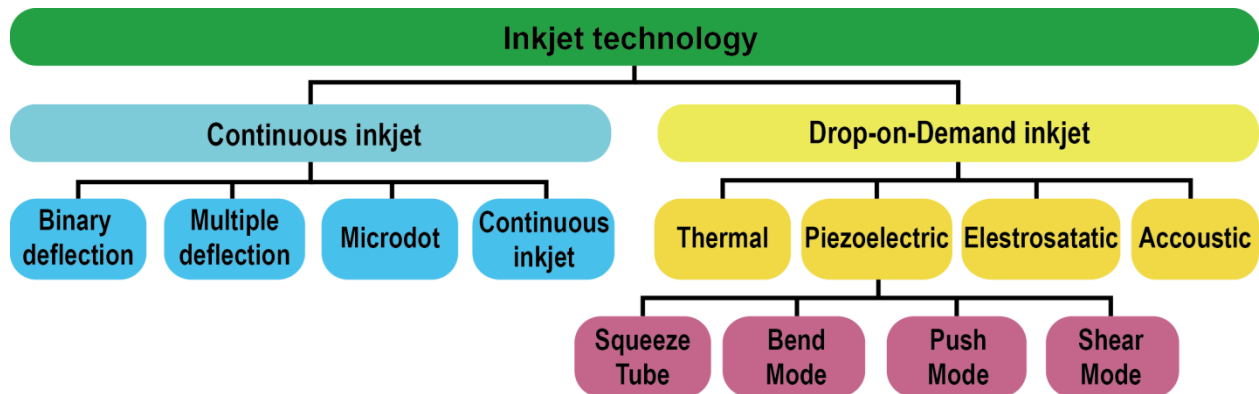


Figure I. 13 Road-mapping of two main kinds of inkjet printing technologies

IV.1.1 Continuous Inkjet Printing

Through a number of transduction principles can be used for droplet formation in continuous inkjet mode, the inks were delivered from the reservoir and expelled out of the nozzle by a

continuous and regular electric driven mechanical actuation. The ink flow filament breaks into a stream of droplets at the nozzle boundary at very high frequency actuation. The droplet morphology which was closely consistent with Rayleigh-Tomotika instability in theory evolves during the flying trajectory [67]. As depicted in Figure I. 14, the completely metamorphic drop formation travelling through the first parallel plate where drops were charged selectively corresponding to the pattern to print. The charged droplets were deflected under an electrostatic field and were caught by the suspended gutter beneath the substrate. Uncharged droplets continue to hit the wanted location. Continuous drop ejection enable the high throughput manufacturing and the application field where high-volume production and long distance droplet travel riding were needed, could benefit. However, relatively high printing quality and resolution could not be guaranteed because of the long flying trajectory of the ink droplets between printhead and substrate.

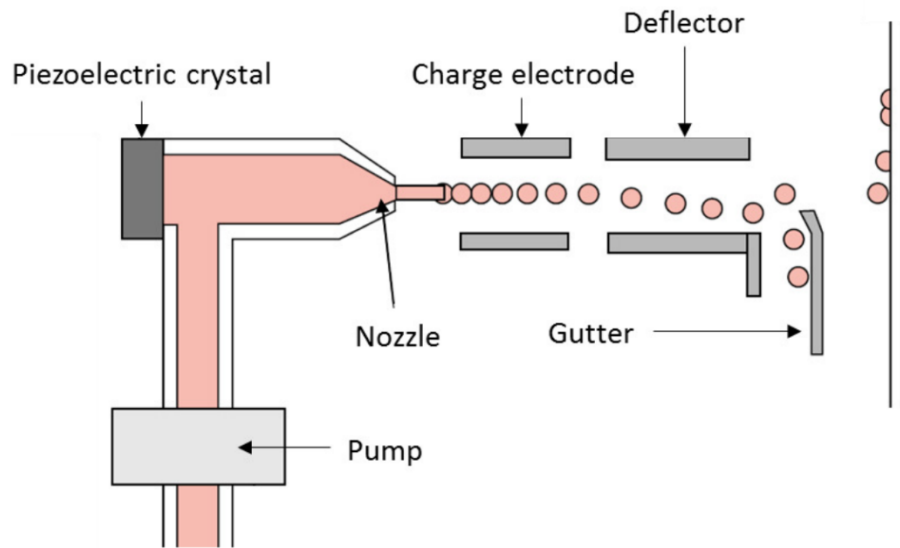


Figure I. 14 Process flow of continuous inkjet printing technique, using a piezoelectric crystal electromechanical actuator. Adapted from illustration provided by Brian Derby [68].

IV.1.2 Drop-on-demand (DoD) Inkjet Printing

Drop-on-demand inkjet printing technique does not need continuous ink ejection, only where there is the pattern information carried upon the requirement. The motion of dynamic printhead should be either three-axial direction, or compensated by the movement of substrate platform in certain direction. The commercially available inkjet printing system was based on different transduction principles in the scenario of ink ejection (recall Figure I. 3) up to now and the most widely used transduction methods are thermal and piezoelectric. Figure I. 15a present the configuration of a thermal actuator inducer ink ejection nozzle. A heating resistor mounted close to the nozzle was heated by electric imaging signal and triggered the vaporization of the volatile

solvent into bubbles subsequently. This leads to jump of the gas pressure in the capillary tube, resulting in the ink ejection. In case of piezoelectric actuation mechanism (in Figure I. 15b), the capillary, serving as an ink reservoir, was surrounded by a tubular piezoelectric ceramics actuator. When the electric impulse was applied, the actuator was mechanically deformed, leading to the positive pressure propagating through the ink reservoir chamber. The incompressible inks, rather than reflowing back due to the mitral valve, are accelerated and flow out of the nozzle orifice at high ejection frequency. The ink vacancy is refilled by aspiration of reservoir via applying a negative pressure successively.

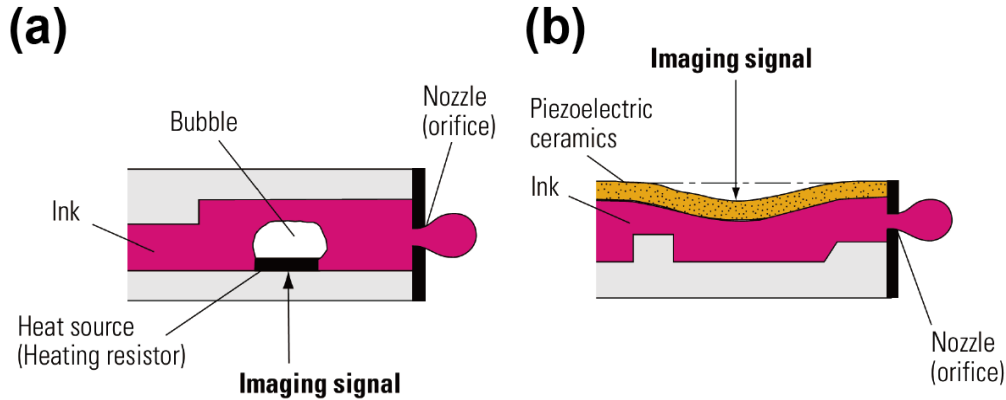


Figure I. 15 Two main kinds of transduction principles for drop-on-demand inkjet printing ejection: thermal (a) and piezoelectric actuation (b). Figure adapted from illustration provided by Khan [60].

The printhead based on the thermal actuator is of great simplicity and cost efficiency. High vapor pressure solvent to create the bubbles under low temperature atmosphere limits the manipulation of the wide range of fluids. The field where high precise ink volume demanded could not be benefitted such as commercially desktop and domestic printer. In piezoelectric printing system, piezoelectric actuators behind nozzles are used instead of the heating elements. Piezoelectric inkjet printing is more sophisticated, reliable and reproducible, popular employed either in industrial areas or academic researches. Piezoelectric actuation behavior could be readily controlled by the electric signal impulse whereby the drop quantity and velocity could be precisely modulated for a given ink solution. Besides, DoD printing operates at typical acoustic frequencies in the wide range of 1~20 kHz and generates in order of decimal picoliter droplets. Although pulse amplitude and width contribute much to the drop ejection, the printable droplet morphology is more likely linked to the rheological and physico-chemical properties of the ink solutions. In this present work, lab scale piezoelectric ink ejection mode is harnessed and detailed description of piezoelectric actuation process will be discussed.

IV.1.3 Piezoelectric DoD Inkjet Printing Process

Understanding the piezoelectric actuation in response to the electric pulse is an essential step to master the emerging inkjet printing technology. Figure I. 16 depicted the main four steps of actuation processes of a certain nozzle for the cross-section of the nozzle device during droplet formation and ejection. The printhead unite including a nozzle consists of the core tubular capillary ink reservoir chamber and shape-adaptable piezoelectric actuator. The initial stage sees free deformation on the piezoelectric actuator with absence of rectangular voltage (Figure I. 16a). And the piezoelectric element is contracted upwards under applied unipolar voltage in figure 5b, during which the ink fluid was aspirated by the negative pressure induced by the contraction of piezoelectric element. Subsequently, the voltage is switched off and the piezoelectric element relaxes to its normal status, applying the pressure wave which propagates through the ink reservoir chamber to the nozzle. In this regard, the inks fluid near the nozzle orifice is squeezed and jetted in a quantity-modulated mode as presented in Figure I. 16c. The ink fluid motion at orifice is accelerated up to 10^5g [60] , resulting in the falling small amount of ink fluid in an initial velocity as shown in Figure I. 16d. Afterwards, the falling drops morphology evolves in a much complex mechanism which will be discussed later on.

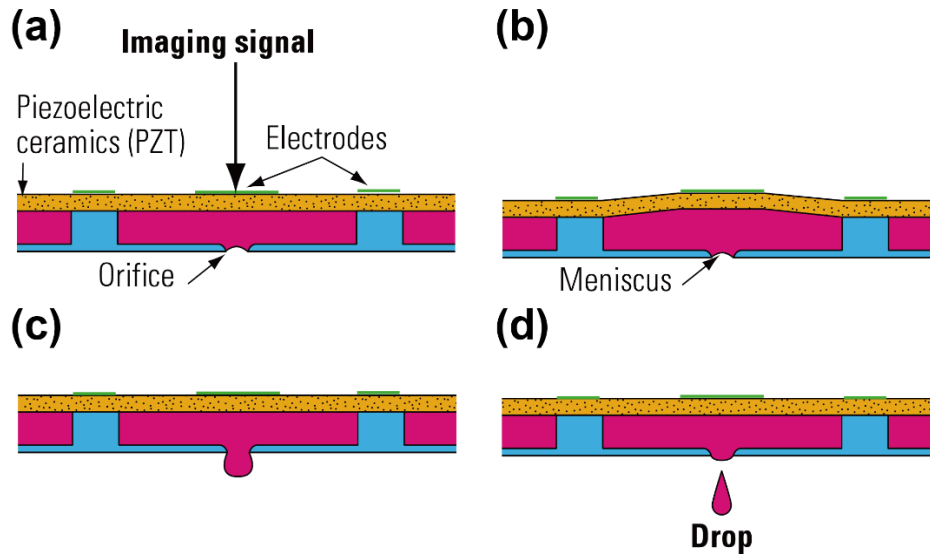


Figure I. 16 Schematic diagrams of the piezoelectric printhead, (a) the ink-filled reservoir chamber and piezoelectric element prior to the imaging signal applied; (b) piezoelectric buckling induced by electric information; (c) high fluid pressure in the chamber as the displacement piezoelectric element recovered; (d) droplet left the nozzle orifice. Adapted from illustration provided by Khan [60].

It should also be noted that before the next cycle, the ejection pause, so-called echo time t_{decho} was inserted between the piezoelectric element two actuating processes. The ink ejection is in equilibrium due to the overwhelming the surface energy of the inks meniscus against the

amount of transferred kinetic energy [69]. In practical printing system, the moderate voltage is frequently applied to the piezoelectric element and give rise to a contraction mode to avoid residual unwanted and excessive inks fluid ejection whereby the negative pressure (10~12 mbar) propagates through to the capillary to overcome the transferred kinetic energy of the ink fluid in the orifice [70]. The period of printing cycle relies on the frequency of applied information signal to the piezoelectric element up to decimal kilohertz (~10 kHz).

In fact, both geometric numbers of nozzle and voltage pulse contribute to the drop formation, as well as the droplet velocity, volume, etc. Mostly used applied voltage are unipolar or bipolar rectangular waves, which characterizes the pulse amplitude and width, highly accessible by using the computer-controlled modulator. The larger voltage pulse amplitude and longer width, the more the droplet volume [71, 72]. To sum up, the printable droplet formation is the fruit in combination of the printer system and physico-chemical properties of ink solution as well as rheological behaviors.

IV. 2 Ink Jettability

It is rather crucial to build the roadmap of parameter-to-morphology relationship for the drop formation during the inkjet printing, first and foremost. And extensive research has always been focused on this issue from physics and fluid mechanics point of view [73-75]. Generation of printable drop formation is a quite complex process, although the inertial, viscous and surface tension forces are identified as the key essential parameters seamlessly linking to the drop formation. The behavior of drops can be described by the Navier-Stokes equations and this can be simplified by evaluation of several dimensionless numbers grouping, some of which are Reynolds (Re), Weber (We), Capillary (Ca), Ohnesorge (Oh) numbers involvement. These dimensionless constant numbers, derived from ink density ρ (g ml^{-3}), surface tension σ (mN m^{-1}) of the droplet, velocity v (m s^{-1}) and viscosity η (mPa s) of the high shear rate fluid at outlet of the orifice with diameter equivalent to d (m), are expressed by Fromm's numerical stimulation with the following constitutive equations [75, 76]:

$$Re = \frac{\text{inertial force}}{\text{viscous force}} = \frac{\rho v d}{\eta} \quad \text{I. 5}$$

$$We = \frac{\text{inertial force}}{\text{surface tension}} = \frac{\rho v^2 d}{\sigma} \quad \text{I. 6}$$

$$Ca = \frac{\text{viscous force}}{\text{surface tension}} = \frac{\eta v}{\sigma} \quad \text{I. 7}$$

$$Oh = \frac{\eta}{\sqrt{\sigma \rho d}} \quad \text{I. 8}$$

Specific physical criterions necessitate to meet the requirement. *Re* number defines the inertial force overwhelming the viscous force of the ink solutions, highly depending on the velocity and rheological behaviors of ink fluids. Interfacial behavior of ink fluid at nozzle meniscus or interaction with the surroundings during the falling are also carefully considered. Besides, inertial force should outnumber the capillary force value to enable the realization of the drop falling. For this reason, the surface tension σ of the inks, strongly associated with solvent physics is taken into account. To overcome the ink liquid/air surface tension barrier at the nozzle, a considerably initial velocity of the drop expelled from the nozzle, is conferred to the drops. The minimal velocity needed for the drop ejection is described as equation I.9 [77]:

$$v_{min} = \sqrt{4\sigma/\rho d} \quad \text{I. 9}$$

Once the ink drop leaves the orifice, it flies freely upwards, during which the drop formation evolves upon the time elapses. The morphological behaviors of the droplets are monitored by a stroboscopic vision system mounted on the inkjet printer which should be synchronized with voltage waveform.

Fromm [77] also proposed that the physic mechanism involved in the stable and printable drop morphology can be explained by one single fluid mechanics parameter *Z*;

$$Z = \frac{\sqrt{\sigma \rho d}}{\eta} = \frac{1}{Oh} = \frac{Re}{\sqrt{We}} \quad \text{I. 10}$$

This gauge value is independent of ink fluid velocity and the empirical value $Z > 2$ was suggested for the limits of printable and stable drop generation by numerical simulation. Derby extended the limits of the printable benchmarks to a broader range of $10 > Z > 1$. The lower the value, the harder the generation of stable droplet and the higher, the more incident of the ink satellites. Feasible *Z* value should land between the *Z* number scales. Up to days, some authors have attempted to define the jettable range using *Z* number as $4 < Z < 14$ [78] and $0.67 < Z < 50$ [79]. Recently, Subramanian et al extended the wider *Z* number range of $1 < Z < 60$ based on gold nanoparticle hydrophobic ink solutions [80]. These inconsistencies are highly ink dependent and suggested that *Z* number alone cannot define the jettability of inks. Solely considering the drop morphology, Kim proposed to define a qualitative printability windows based on the two ink fluid mechanic parameters *Ca* and *We* which are plotted in a two-dimensional coordinate system [81].

Systematic design and exploration of jettable inks were conducted by Subramanian group taking nanoparticle based inks as an example. The two relevant dimensionless constant *We* and

Ca number pertinent to the drop formation were plotted by engineering the inks rheology, acoustic, jettability, etc with various hydrophobic solvents in Figure I. 17a. In the low We number region I and II, the ejection pillar was subjected to not enough inertial force to form the stable droplets. So there is only a small perturbation in the meniscus. In high Ca number region III, long filament attached to the nozzle occurs prior to the ligament pinch-off, resulting in

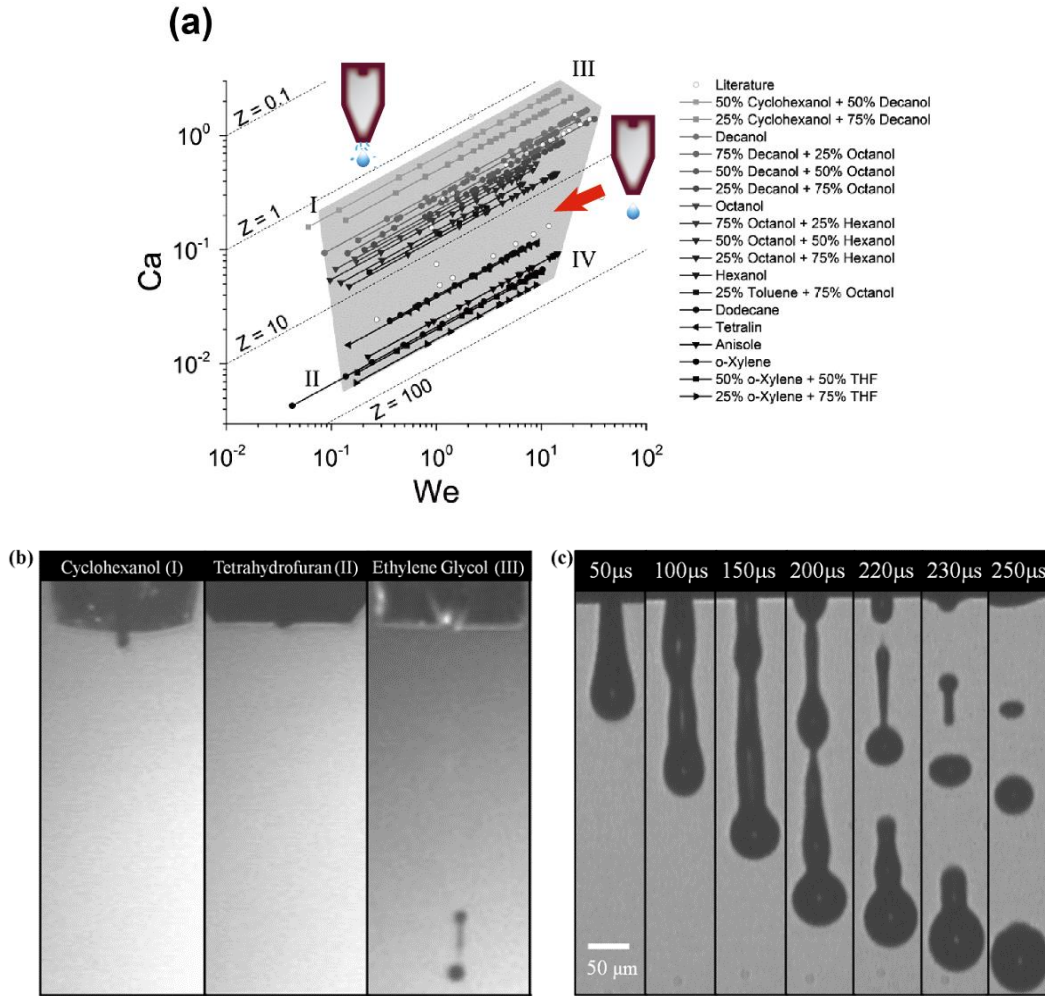


Figure 1. 17 (a) Capillary number (Ca)-Weber number two dimension coordinated space of the printability hydrophobic solvents based nanoparticle ink solutions. The hatched area defines the jettable bounds and within the polygon each data point represents jettable inks. Schemes inside the hatched area demonstrate the tailored drop morphology whereas outside the hatched area the drop ejection cannot give printable drop formation. (b) Inappropriate jetting condition causes the inks only a small perturbation in the meniscus. (c) Relatively inviscid fluid presenting wavelike instability of ink pillar, giving rising to satellites droplets. [80]

instability of droplet formation. Due to the large viscous force of inks, large inertial force driven drop ejection undergoes wavelike instability in the liquid thread at pinch-off, leading to multiple breakups and spraying behavior in Ca - We region IV.

IV.3 Drop Impact

Once generation of the printable droplets, there followed the falling and impact on the beneath substrate as an elapsed time. Along with three important mentioned dimensionless grouping numbers, gravitational force would be firstly considered. Note, however, universally printable droplet characteristics of low density and surface tension, high speed and small diameter size, gravity effects are typically not important. Thus, inertial and viscous forces continue to be the predominated elements. As the droplets start to collide with the substrate, it undergoes a sequence of five successive impact-driven phases, namely, kinematic, spreading, relaxation, wetting and equilibrium, accompanying with variations of the fluid shapes, maximum spreading diameter ratio to be a the representative β^* ($\beta^*=D^*/D_0$, D_0 and D^* are droplet diameter before impact and real-time diameter of wetting contact line), as time elapsed as shown in Figure I. 18a. During the five successive phase, two main regime forces were proposed, impact force and capillary force. This has been largely predicted by the experimental observation and numerical simulation in the literatures [82-84]. One of well-known model developed by Pasandideh-Fard et al. [85, 86] described that the spreading factor β^* has closely relationship with the three main forces, by using the advancing contact angle mode to calculate capillary effect, namely surface tension:

$$\beta^* = \left(\frac{We+12}{3(1-\cos\theta)+4We/\sqrt{Re}} \right)^{1/2} \quad \text{I.11}$$

here θ is advancing contact angle during the ink-substrate collision incidence.

But this is not the case in some conditions. For instance, Sungjune Jung et al [82] proposed an experimental measurements to investigate the dynamic behavior of liquid drops of diethyl phthalate and glycerol-water mixture using the DoD inkjet printing technique on the smooth ITO-coated glass surface. The spreading diameter during the kinematic phase, followed very simply in timescale mode (Figure I. 18b), regardless the ink velocity and surface properties of the support. Instead, the ink velocity and the dimensionless numbers of the inks play a crucial role in the wetting phases. So is the surface wettability which has a significant influence to the β^* value during the wetting phase where capillary force mainly functions.

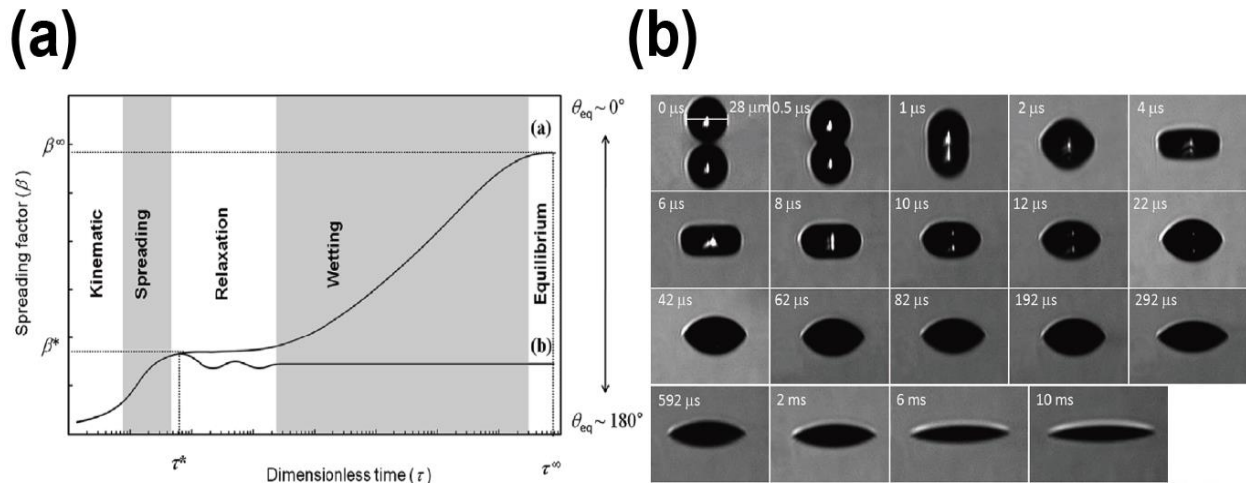


Figure I. 18 (a) Diagram illustration of the maximum spreading factor β versus time evolution τ . The increasing trend plot over the whole window corresponds to the drop impact scenario on the wettable substrate ($\beta^* < \beta^\infty$) while the remaining one represents the spreading factor changes with time elapsed in case of non-wettable substrate. The predominated phenomena for the spreading angle occur with time proceeding after the drop collision with substrate. (b) photographics in initial stage (0~10 ms) of the drop impacting on the ITO-coated glass substrate as time proceeds. Adapted from the illustration reported by Jung et al. [82].

IV.4 Flexible Substrate and Surface Treatment

It is well-known that liquid materials can be deposited onto versatile substrates, including silicon wafer [87], glass plates [88, 89], metallic layers [90] and plastic supports [36], either in planar or 3D mode etc. Emerging interests have been given to the flexible substrate, providing supports for the large area manufacturing technologies. To meet the requirements of printed electronic device, dimensional stability, thermal and chemical resistance, low coefficient of thermal expansion (CTE), good barrier properties for moisture and gase necessitate for the

Table I. 2 Comparison of the flexible polymer foil substrate. Adapted from review by Khan [55].

Properties	PET	PAcryl.	PEN	PC	PS	PI
T_g (°C)	70	105	120	145	203	270
T_m (°C)	115	175	268	115-160	180-220	250-320
CTE (ppm/(°C))	33	79	20	75	54	8-20
Transparency %	90	>90	88	92	89	35-60
Water Ab. %	0.6	0.2	0.4	0.25	1.4	2-3
Tensile Stren. GPa	2-2.7	2.4-3.4	0.1-0.5	2.6	nul	2.5
Solvent Resist.	good	good	good	poor	poor	good
Surface Roug.	poor	fair	poor	good	good	good
Geometry Stab.	good	good	good	fair	fair	fair

flexible support candidates. Among these flexible substrates, plastic foils have been widely employed as a passive, bendable, transparent and lost-cost support for large area printed electronic devices. Here summarized the most used plastic foil for printed electronics in Table I. 2.

Excellent wettable substrate facilitates the inks droplet spreading on the flexible substrate and then uniformity and adhesion of the inks residual. Otherwise the delamination between printed electronic elements and flexible occurs when printed systems are bended, leading to the short life cycle and even dysfunction. A quantitative parameter contact angle θ was introduced to describe the surface wettability of the supports. When the droplet impacts on the support, wetting process occurs depending on its surface properties, such as surface tension, roughness, homogeneity, porosity, etc. The equilibrium can be schemed in Figure I. 19. The relationship of driven forces, namely surface tension, between each interface of gas vapor, solid support and ink liquid can be describe by:

$$\gamma_{gs} = \gamma_{sl} + \gamma_{gl} \cos \theta \quad \text{I. 12}$$

Surface tension of ink liquid or support are often measured by Owens-Wendt-Kaelble (OWK) method according to the contact angle (principle and measurement shown in Appendix: Surface Energy Measurement). A good wettability goes to the fact that the liquid drop contact angle on the substrate is necessarily far less than 90° and substrate's surface tension must exceed the liquid ink's surface tension by 2-10 mN/m.

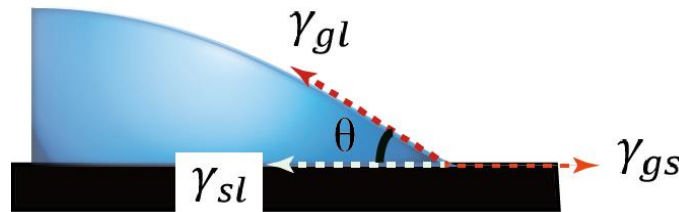


Figure I. 19 Scheme illustration of droplet wetted on the support in equilibrium state. Contact angle θ describes thermodynamic equilibrium between the three phases: the liquid phase (l), the solid phase (s), and the gas or vapor phase (g).

Many have reported the feasibility of the methods mainly from ink solution and substrate treatment aspects. A main strategic approach to enhance the surface wettability of the ink droplet with the flexible support is to improve the surface tension of the substrate by surface engineering. Corona discharge and plasma treatment are frequently used to make surface ionized temporarily, which is adequate to improve the surface energy for printability. However, challenges are risen that these usually cause the physical damage to the support being treated, for example, layer breakdown and thus dysfunction of printed electronic devices. A nondestructive, robust and compatible UV-ozone treatment was adapted for the brittle and fragile supports [91, 92]. The

basic mechanism is a photochemical oxidation process, introducing the hydrophilic hydroxyl group (-OH) onto the treated surface. In parallel, chemical treatment is also employed for surface clean and modification according to chemical functionalization. Simaite et al. [93] reported a surface engeering approach to an ionic liquid actuator, using argon-plasma-induced surface polymerization of poly-(ethylene glycol) monomethyl ether methacrylate (PEGMA) in order to improve the wetting properties of hydrophobic PVDF membrane. After treatment, good wettability and adhesion of water-based PEDOT:PSS electrodes to the PVDF was achieved. Further work has been focus on the inkjet printable conducting polymer artificial muscles using the similar strategy as presented in Figure I. 20.

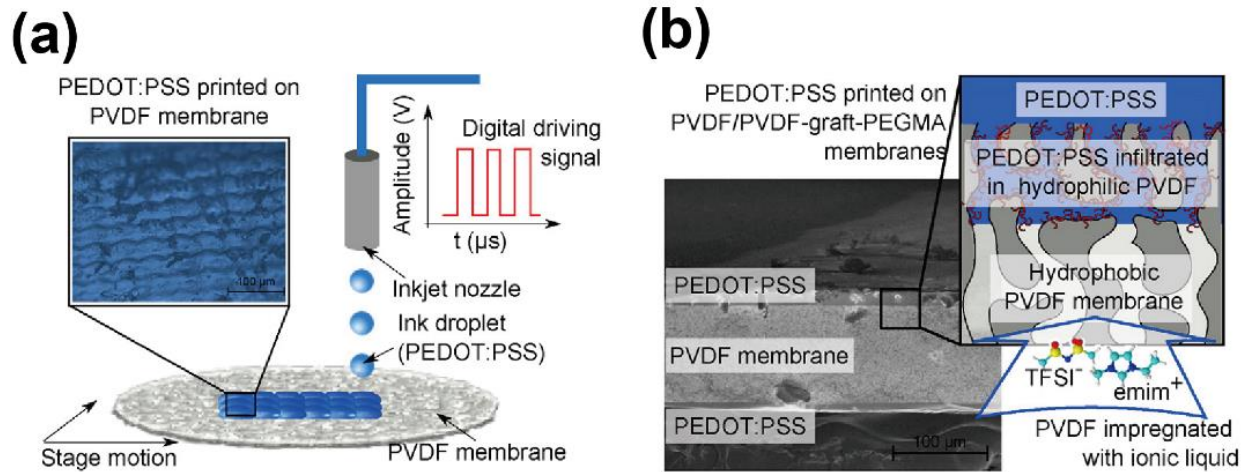


Figure I. 20 Schematic illustration of the DoD inkjet printing water-based PEDOT:PSS solution on PVDF-graft-PEG membrane (a). SEM image of the cross-section of the inkjet printed actuator based on the surface grafting polymerization treatment (b). Adapted from the illustration provided in the literature [94].

IV. 5 Dropped Ink Drying

Once deposited onto the substrate, the inkjet droplets start to dry, namely the occurrence of the solvent evaporation. During this process, the ink concentration gradually increases and eventually the ink material patterns remain on the substrate. It has been shown that pattern morphologies and distribution are strongly depending on the drying process [95, 96]. Therefore, controlling drying process is an essence in producing the wanted inkjet patterns, otherwise undesirable, incomplete and unwanted location of material deposition. And the performance and the lifetime of electronic devices critically rely on the morphology of printed patterns.

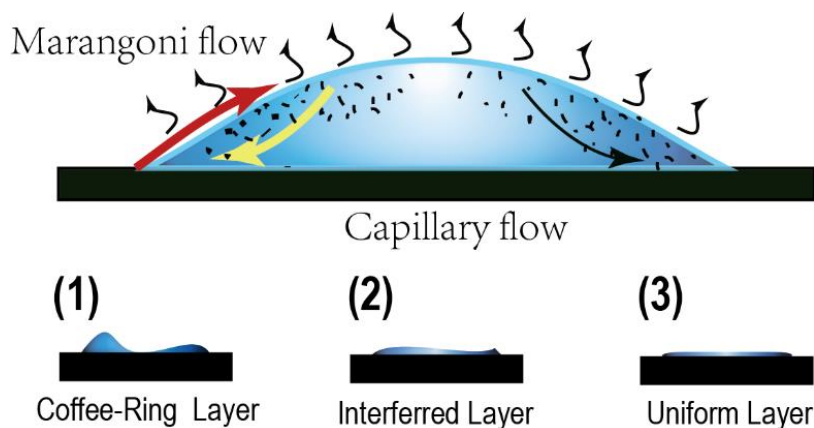


Figure I. 21 Schematics of the contact line and two driving flows along with most ubiquitous obtained patterns morphologies including coffee-ring. Yellow curvature arrow represents the outward capillary flow while the red one is the inward Marangoni flow.

Most common pattern morphology obtained is the coffee-ring like stain if the evaporation of solvent of ink solutions naturely takes place. Here we ascribe this specific stain to the several physics phenomena. Due to the lose of solvent volume in the initial stage of evaporation, the contact angle decreases and the contact line is pined on the substrate instead of contact radius receding according to the experimentation on evaporation beavior of many kinds ink droplets. Deegan [97, 98] proposed a unexplored force driven by outward capillary flow which is mainly responsible for the ring-like pattern as presented in Figure I. 21. This convective flow is caused by thermal gradients between the edge and the interior of the drying drop. The inks losing at edge was replenished by liquid from the interior, resulting in an outward flow carrying the dispersed materials to the edge. But his ourward flow can be conteracted by an inward marangoni flow which is driven by the surface tension contrasts between the edge and the center.

In order to obtain uniform film patterns. Measures have been taken to overcome the capillary flow through enigeering the evaporating conditions and ink physics aspects. For example, a fast initial evaporation rate could allow the dispersed materials to diffuse way from the phase surface and causes the accumulation of the suspended particles near the liquid-air interface, whereas a lower rate could probaly induce the coffee-ring stain [99] although Subramanian [100] reported water-based ink solution does not follow this rule, where outward marangoni flow is not that importantly considered. On top of that, cosolvent systems with addition of a minor solvent with high boiling point into the dominant solvent was also proposed to solve the problematic coffee-ring like stain. The convective flow was counterbalanced or enhanced by the Marangoni flow depending on the cosolvent physics, in particular surface tension. The water dominated cosolvent system for colloidal inks was reported by Jungho Park et al. [87]. Uniformity and well distribution of silica microspheres pattern was achieved by enigeering the amount of the drying control agents in terms of boiling point and surface tension. H. Minemawari [101] also showed

that organic single crystal film for thin-film transistor application was successfully inkjet printed on silicon-wafer using antisolvent crystallization based on cosolvent system.

V Fluorinated Electrostrictive Polymers

Electroactive materials (EAs), that perform electromechanical coupling effect, capable of responding with a geometric change upon the external electric excitation[102, 103], are promising and could be potentially employed in plenty of application fields, such as smart materials for artificial muscles[104], electromechanical sensors and actuators[105], medical imaging, acoustic transducer, specific polymers with high electric energy density for hybrid vehicles and high energy weapon systems[106]. Compared with the conventional piezoelectric ceramics, withstanding a rigid and high mechanical strength low field-induced strain, brittleness, heavy weight, the electroactive polymer has attracted a great deal of interests whatever in academia and industrial areas, thanks to its polymer nature of their flexibility, light weight, relatively low mechanical strength, processability, ease of processing into large-area films, and the possibility to be molded into a desirable dimension[107, 108]. Recently, emerging researches have been carried on the fluorinated polymer since ferroelectricity origin of PVDF polymer was explained firstly by Lovinger [109] in terms of structures and different levels from the molecular chains and chains conformations. PVDF is a semi-crystalline polymer with its crystal phase limited to 50-60% where the ferroelectric behavior originated from. Generally, the mostly common molecular conformation consisted of four main crystal forms, α , δ , γ , and β , depending on the dipole orientation which in detail are depicted in Figure I. 22 where the unite cell of crystal lattice were also presented. The PVDF films with different crystal form strongly depended on the polymer processing methodologies. For instance, the α form can be obtained by cooling from the polymer melt while γ has a $TTTG^+TTTG^-$ chain conformation and often obtained by solution-casting from polar solvents at temperature below 100 °C or annealing at high temperature. The dipole moments cancel out in the α form, then as nonpolar form while δ , γ , and β forms are ferroelectric. In order to obtain preferential ferroelectric β form with piezoelectricity, PVDF films must be mechanically stretched for circular times and poled under high electric field at high temperature. Thus the complexity of processing makes PVDF less potentially used in the practical implementation, let alone its low field-induced strain and weak electromechanical coupling behavior.

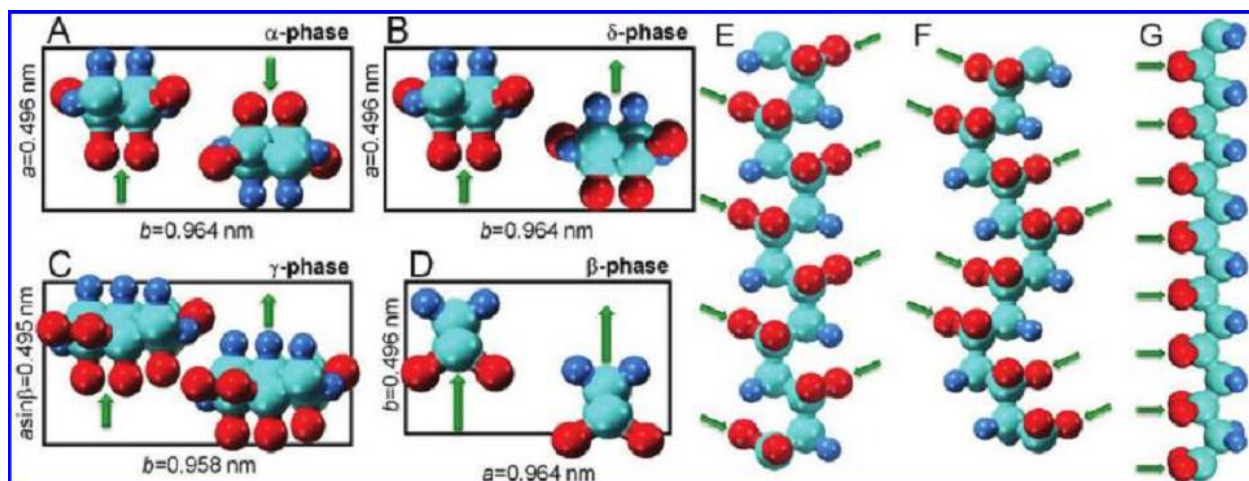


Figure I. 22 Unit cell of (A) α , (B) δ , (C) γ , and (D) β forms of PVDF crystals viewed along the c-axes and schematic chain conformations for (E) $TGTG'$ (α/δ), (F) $TTTGTTTG'$ (γ), and (G) all-trans (β) rotational sequences. Red, cyan, and blue spheres represent F (fluorine), C (Carbon), and H (Hydrogen) atoms. The projections of dipole directions are indicated by green arrows. Graphics adapted from the illustration in the literature [110].

The embarrassed issues presented for PVDF can be improved by a P(VDF-TrFE) copolymer strategy. The copolymer underwent the ferro-paraelectric transition, involving all *Trans* phase transition to nonpolar substitution of *Trans* and *Gauche* conformation at high temperature [111], during which a large lattice constant along the molecular chain but a small unit cell dimension of all *Trans* conformation switched to a significant shortened lattice constant with an expansion of unit cell dimension. The differences in crystal unit cell aroused the macroscopic strain when there is a ferro-paraelectric phase transition. This phase transition are reversible under at a relatively low poling electric field (<70 MV m⁻¹) [112]. P(VDF-TrFE) copolymer benefited a jump dielectric permittivity and piezoelectricity due to the enhanced ferroelectricity in the crystal phase. Furthermore, large polarizability should also depend on the orientation of dipole moments because the orientational polarization is more important than electronic and atomic polarizations in the crystals [113]. When the c-axis of the crystal form is parallel to the external electric field, all the dipole moments will distribute in a plane perpendicular to the electric field, reaching a maximal dipolar polarization, and thus high ferroelectric behavior. The favored crystal orientation also strongly depended on the processing condition [113, 114], which in turns affected the dielectric constant and a large strain. However, the large strain induced by such a transition is always accompanied with a relative large hysteresis due to the large energy barrier during the dipole orientations. Such scenario certainly undermined the development of out-performed electromechanical devices.

Recently, e-beam irradiated P(VDF-TrFE) copolymer unimorph demonstrated rather high tip displacement, providing novel concepts of designing materials with high electromechanical

response [115, 116]. Inspiring from this method, chemical defects were introduced into molecular backbone by copolymerization of bulk-like ternary CTFE monomer and as a consequence, sub-micro crystal size broke into sporadic nano-sized crystallites [117, 118]. Due to presence of CTFE, β -form ferroelectric domains with all-Trans (T_m , $m>3$) conformation in copolymers transformed into non-polar α -form paraelectric crystallites and less-ordered γ ($T_3G^+T_3G^-$) ferroelectric phase. Hence interactions between neighboring crystallites were weakened. And spontaneous polarizations of the sporadic nano-sized crystallites in terpolymer were relatively independent and the dipole moment of each nano-sized crystallites were randomly distributed. The dipolar polarization and diagram of microstructure was compared in Figure I. 23. Terpolymer exhibited diffusion phase transition frequently when subjected to the external stimulus. Such phase transition in chain conformation was responsible for high electrostrictive behavior. One of the obvious

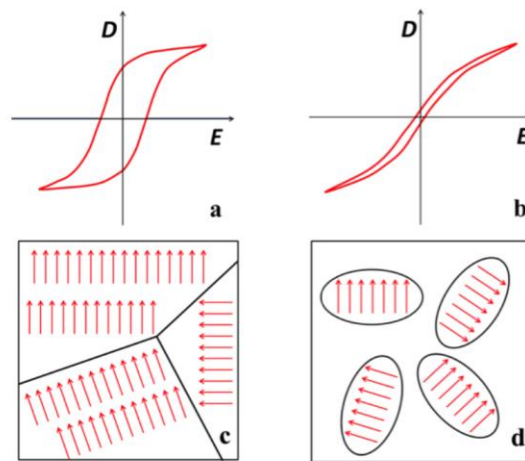


Figure I. 23 Schematic diagrams of the comparison of hysteresis loops and microscopic crystalline structures for ferroelectric polymer (a and c) and relaxor ferroelectric terpolymers (b and d)

drawbacks for fluorinated polymer is that relatively high electric field should be applied to generate high strain or mechanical deformation, although applied electric field is order of magnitude decreasing comparable with the non-fluorinated polymers which presented an equivalent electrostrictive deformation under very high electric field supply. It is well recognized that electrostrictive strain s is quadratic correlation with induced electric field E , being positively proportional to dielectric constant ϵ' [119, 120]. Extensive studies aiming at increase of dielectric constant were carried out for decades. Conductive metal-ligand [121] or nano-sized carbon homologous particles like carbon black [122], carbon nanotube [123, 124] and graphene nanosheets [125] were embedded into the terpolymer matrix in an attempt to enhance dielectric property. But the most embarrassed fact is that filler volume fraction should not reach the percolation threshold. Nanocomposite concept turns out to be an efficient way to augment

dielectric behavior but unfortunately at the expense of reinforced elastic mechanical properties. Such high Young's modulus was an adverse effect contribution to electromechanical behavior. In order to at least maintain mechanical properties, organic additive macromolecules like conductive polyaniline were doped and resulted in a large electrostrictive behavior at lower electric field due to significantly enhanced dielectric permittivity ϵ' . Recently, our study found that plasticized terpolymer exhibited thousand-fold increase of dielectric permittivity and thus 28-fold increase of the electrostrictive strain [126]. This plasticizer doped terpolymer was utilized to fabricate micro-pump device [127], showing a rather good candidate for MEMS system application.

VI Objective of This Work

Force sensors are playing an important role in industrial fields where sensing, detection, signal processing and reactive feedback necessitate in real world. Over the time, numbers of force sensors have been designed and fabricated to fulfill the requirements of the fast response, wide gauge range, accuracy, reliability, sensitivity and resolution, even environmental-friendly merits. Herein, we introduced the fundamental issues and working principles of force sensor system and then summarized state-of-the-art of the emerging nano- and microNewton force sensors for high precise measurement in imaging, medical and biological applications. Among these commonly employed transduction methods, special attention has been emphasized on the piezoelectric effect of polymer materials, which presents high sensitivity, wide scope of polymer candidate and free power consumption whenby making passive force sensor possible upon the requirements.

Studies have shown that the electronic devices involving force sensor, solar cell, OFET, eluminescent-LED and packaging objective, have been successfully printed by conventional technologies reviewed in the latter part of this chapter. We particularly described the revival inkjet printing technology, as a non-contact inks deposition technique to easily fabricate the dynamic force sensor. The jettability condition was firstly explored by engineering the printer system and inks system and it was found that the three dimensionless grouping numbers strictly determined the printable window and were based on the intrinsic physical forces, namely inertial force, capillary force and viscous force. And phases undergone during the impact and wetting process of droplet were analyzed and surface property of the support was declared as the critical essence for wettability. In this regard, the flexible substrate and surface treatment strategies were collected. Drop drying process on the support was focused finally. And we also proposed the measures taken to engineer the flows inside the drying drop so as to yield uniform and even distribution film layers.

The electromechanical behavior is closely related to several physical and electric parameters such as dielectric permittivity and mechanical properties, all of which heavily rely on the polymer microstructure. This thesis aims to systematically determine how these variables influence the

electromechanical behavior of the as-cast terpolymers by means of temperature annealing recrystallization and plasticization approaches. Additionally, inkjet printed sensors and electronic devices over large area flexible substrates are of significant interest due to its less production complexity, high throughput and cost-effectiveness. During this work, inkjet printing technology was considered to be employed for manufacturing flexible large-area sensor networks. The feasibility and maneuverability of the P(VDF-TrFE) copolymer and terpolymer were carefully carried out for a piezoelectric force sensor implementation.

References

1. Fraden, J., *Handbook of modern sensors: physics, designs, and applications*. 2004: Springer Science & Business Media.
2. Tichy, J., J. Erhart, and E. Kittinger, *Fundamentals of piezoelectric sensorics*. 2010: Springer.
3. Siciliano, B. and O. Khatib, *Springer handbook of robotics*. 2008: Springer Science & Business Media.
4. Lee, D.-H., et al., *A Capacitive-Type Novel Six-Axis Force/Torque Sensor for Robotic Applications*. IEEE Sensors Journal, 2016. **16**(8): p. 2290-2299.
5. Stoppa, M. and A. Chiolerio, *Wearable electronics and smart textiles: a critical review*. Sensors, 2014. **14**(7): p. 11957-11992.
6. Rothmaier, M., M.P. Luong, and F. Clemens, *Textile pressure sensor made of flexible plastic optical fibers*. Sensors, 2008. **8**(7): p. 4318-4329.
7. Hoffmann, T., B. Eilebrecht, and S. Leonhardt, *Respiratory monitoring system on the basis of capacitive textile force sensors*. IEEE Sensors Journal, 2011. **11**(5): p. 1112-1119.
8. Peirs, J., et al., *A micro optical force sensor for force feedback during minimally invasive robotic surgery*. Sensors and Actuators A: Physical, 2004. **115**(2): p. 447-455.
9. Berkelman, P.J., et al., *A miniature microsurgical instrument tip force sensor for enhanced force feedback during robot-assisted manipulation*. IEEE Transactions on Robotics and Automation, 2003. **19**(5): p. 917-921.
10. Weller, H., D. Setiadi, and T. Binnie, *Low-noise charge sensitive readout for pyroelectric sensor arrays using PVDF thin film*. Sensors and Actuators A: Physical, 2000. **85**(1): p. 267-274.
11. Eggins, B.R., *Chemical sensors and biosensors*. Vol. 28. 2008: John Wiley & Sons.
12. Yang, Q., et al., *Enhancing light emission of ZnO microwire-based diodes by piezo-phototronic effect*. Nano letters, 2011. **11**(9): p. 4012-4017.
13. Schwizer, J., M. Mayer, and O. Brand, *Force sensors for microelectronic packaging applications*. 2006: Springer Science & Business Media.
14. Ganet, F., et al., *Haptic feedback using an all-organic electroactive polymer composite*. Sensors and Actuators B: Chemical, 2015. **220**: p. 1120-1130.
15. Gautschi, D.-I.E.G., *Piezoelectric sensors*, in *Piezoelectric Sensorics*. 2002, Springer. p. 73-91.
16. Bonomo, C., et al., *A resonant force sensor based on ionic polymer metal composites*. Smart Materials and Structures, 2007. **17**(1): p. 015014.
17. Chen, L.-T., C.-Y. Lee, and W.-H. Cheng, *MEMS-based humidity sensor with integrated temperature compensation mechanism*. Sensors and Actuators A: Physical, 2008. **147**(2): p. 522-528.

18. Petersen, W., et al., *Importance of femoral tunnel placement in double-bundle posterior cruciate ligament reconstruction biomechanical analysis using a robotic/universal force-moment sensor testing system*. The American journal of sports medicine, 2006. **34**(3): p. 456-463.
19. Beccai, L., et al., *Design and fabrication of a hybrid silicon three-axial force sensor for biomechanical applications*. Sensors and Actuators A: Physical, 2005. **120**(2): p. 370-382.
20. Yokoyama, K., et al., *Novel contact force sensor incorporated in irrigated radiofrequency ablation catheter predicts lesion size and incidence of steam pop and thrombus*. Circulation: Arrhythmia and Electrophysiology, 2008. **1**(5): p. 354-362.
21. Dahiya, R.S. and M. Valle, *Robotic tactile sensing: technologies and system*. 2012: Springer Science & Business Media.
22. Littrell, R. and K. Grosh, *Modeling and characterization of cantilever-based MEMS piezoelectric sensors and actuators*. Journal of Microelectromechanical Systems, 2012. **21**(2): p. 406-413.
23. Schellin, R. and G. Hess, *A silicon subminiature microphone based on piezoresistive polysilicon strain gauges*. Sensors and Actuators A: Physical, 1992. **32**(1-3): p. 555-559.
24. Smith, C.S., *Piezoresistance effect in germanium and silicon*. Physical review, 1954. **94**(1): p. 42.
25. Barlian, A.A., et al., *Review: Semiconductor piezoresistance for microsystems*. Proceedings of the IEEE, 2009. **97**(3): p. 513-552.
26. Thaysen, J., et al., *Atomic force microscopy probe with piezoresistive read-out and a highly symmetrical Wheatstone bridge arrangement*. Sensors and actuators A: Physical, 2000. **83**(1): p. 47-53.
27. Zhu, S.-E., et al., *Graphene based piezoresistive pressure sensor*. Applied Physics Letters, 2013. **102**(16): p. 161904.
28. Birol, H., et al., *Fabrication of a millinewton force sensor using low temperature co-fired ceramic (LTCC) technology*. Sensors and Actuators A: Physical, 2007. **134**(2): p. 334-338.
29. Lakhmi, R., et al., *Force sensors based on screen-printed cantilevers*. IEEE Sensors Journal, 2010. **10**(6): p. 1133-1137.
30. Liu, X., et al., *Paper-based piezoresistive MEMS sensors*. Lab on a Chip, 2011. **11**(13): p. 2189-2196.
31. Gel, M. and I. Shimoyama, *Force sensing submicrometer thick cantilevers with ultra-thin piezoresistors by rapid thermal diffusion*. Journal of micromechanics and microengineering, 2003. **14**(3): p. 423.
32. Mukhopadhyay, R., et al., *Nanomechanical sensing of DNA sequences using piezoresistive cantilevers*. Langmuir, 2005. **21**(18): p. 8400-8408.
33. Kristiansen, K., et al., *3D force and displacement sensor for SFA and AFM measurements*. Langmuir, 2008. **24**(4): p. 1541-1549.

34. Guan, L., et al., *Stretchable - Fiber - Confined Wetting Conductive Liquids as Wearable Human Health Monitors*. Advanced Functional Materials, 2016.
35. Shimojo, M., et al., *A tactile sensor sheet using pressure conductive rubber with electrical-wires stitched method*. IEEE Sensors journal, 2004. **4**(5): p. 589-596.
36. Molina-Lopez, F., D. Briand, and N. De Rooij, *All additive inkjet printed humidity sensors on plastic substrate*. Sensors and Actuators B: Chemical, 2012. **166**: p. 212-222.
37. Liang, Q., et al., *Multi-dimensional MEMS/micro sensor for force and moment sensing: A review*. IEEE Sensors Journal, 2014. **14**(8): p. 2643-2657.
38. Viry, L., et al., *Flexible three - axial force sensor for soft and highly sensitive artificial touch*. Advanced Materials, 2014. **26**(17): p. 2659-2664.
39. Bekhti, R., V. Duchaine, and P. Cardou. *Miniature capacitive three-axis force sensor*. in *2014 IEEE/RSJ International Conference on Intelligent Robots and Systems*. 2014. IEEE.
40. Kim, K., et al., *Nanonewton force-controlled manipulation of biological cells using a monolithic MEMS microgripper with two-axis force feedback*. Journal of Micromechanics and Microengineering, 2008. **18**(5): p. 055013.
41. Xu, Q., *Design, fabrication, and testing of an MEMS microgripper with dual-axis force sensor*. IEEE Sensors Journal, 2015. **15**(10): p. 6017-6026.
42. Yin, X., et al., *Mechanical energy harvesting via a plasticizer-modified electrostrictive polymer*. Applied Physics Letters, 2016. **108**(4): p. 042901.
43. Giessibl, F.J., *Atomic resolution on Si (111)-(7× 7) by noncontact atomic force microscopy with a force sensor based on a quartz tuning fork*. Applied Physics Letters, 2000. **76**(11): p. 1470-1472.
44. Wang, Z., et al., *Enhancing sensitivity of force sensor based on a ZnO tetrapod by piezo-phototronic effect*. Applied Physics Letters, 2013. **103**(14): p. 143125.
45. Zhou, Y.S., et al., *Nano - Newton Transverse Force Sensor Using a Vertical GaN Nanowire based on the Piezotronic Effect*. Advanced Materials, 2013. **25**(6): p. 883-888.
46. Subannajui, K., et al., *Large - Scale Nano Piezo Force Position Arrays as Ultrahigh - Resolution Micro - and Nanoparticle Tracker*. Advanced Functional Materials, 2013. **23**(2): p. 191-197.
47. Dagdeviren, C., et al., *Conformable amplified lead zirconate titanate sensors with enhanced piezoelectric response for cutaneous pressure monitoring*. Nature communications, 2014. **5**.
48. Dagdeviren, C., et al., *Conformal piezoelectric systems for clinical and experimental characterization of soft tissue biomechanics*. Nature materials, 2015. **14**(7): p. 728-736.
49. Kim, D.-H., et al., *A superelastic alloy microgripper with embedded electromagnetic actuators and piezoelectric force sensors: a numerical and experimental study*. Smart materials and structures, 2005. **14**(6): p. 1265.

50. Dahiya, R.S., et al., *Piezoelectric oxide semiconductor field effect transistor touch sensing devices*. Applied Physics Letters, 2009. **95**(3): p. 034105.
51. Søndergaard, R., et al., *Roll-to-roll fabrication of polymer solar cells*. Materials today, 2012. **15**(1): p. 36-49.
52. Sankaran, S., et al., *Fabrication of polymer solar cells from organic nanoparticle dispersions by doctor blading or ink-jet printing*. Organic Electronics, 2016. **28**: p. 118-122.
53. Zirkl, M., et al., *Low - voltage organic thin - Film transistors with high - k nanocomposite gate dielectrics for flexible electronics and optothermal sensors*. Advanced Materials, 2007. **19**(17): p. 2241-2245.
54. Kang, B., W.H. Lee, and K. Cho, *Recent advances in organic transistor printing processes*. ACS applied materials & interfaces, 2013. **5**(7): p. 2302-2315.
55. Khan, S., L. Lorenzelli, and R.S. Dahiya, *Technologies for printing sensors and electronics over large flexible substrates: a review*. IEEE Sensors Journal, 2015. **15**(6): p. 3164-3185.
56. Dua, V., et al., *All - organic vapor sensor using inkjet - printed reduced graphene oxide*. Angewandte Chemie, 2010. **122**(12): p. 2200-2203.
57. Sandström, A., et al., *Ambient fabrication of flexible and large-area organic light-emitting devices using slot-die coating*. Nature communications, 2012. **3**: p. 1002.
58. Yang, L., et al., *RFID tag and RF structures on a paper substrate using inkjet-printing technology*. IEEE Transactions on Microwave Theory and Techniques, 2007. **55**(12): p. 2894-2901.
59. Yang, L., et al., *A novel conformal RFID-enabled module utilizing inkjet-printed antennas and carbon nanotubes for gas-detection applications*. IEEE Antennas and Wireless Propagation Letters, 2009. **8**: p. 653-656.
60. Kipphan, H., *Handbook of print media: technologies and production methods*. 2001: Springer Science & Business Media.
61. Mattana, G. and D. Briand, *Recent advances in printed sensors on foil*. Materials Today, 2016. **19**(2): p. 88-99.
62. Yang, J., et al., *Organic photovoltaic modules fabricated by an industrial gravure printing proofer*. Solar Energy Materials and Solar Cells, 2013. **109**: p. 47-55.
63. Clemens, W., et al., *From polymer transistors toward printed electronics*. Journal of Materials Research, 2004. **19**(07): p. 1963-1973.
64. Pease, R.F. and S.Y. Chou, *Lithography and other patterning techniques for future electronics*. Proceedings of the IEEE, 2008. **96**(2): p. 248-270.
65. Radha, B., et al., *Metal hierarchical patterning by direct nanoimprint lithography*. Scientific reports, 2013. **3**.
66. Meitl, M.A., et al., *Transfer printing by kinetic control of adhesion to an elastomeric stamp*. Nature materials, 2006. **5**(1): p. 33-38.

67. Migler, K.B., *String formation in sheared polymer blends: Coalescence, breakup, and finite size effects*. Physical review letters, 2001. **86**(6): p. 1023.
68. Derby, B., *Inkjet printing of functional and structural materials: fluid property requirements, feature stability, and resolution*. Annual Review of Materials Research, 2010. **40**: p. 395-414.
69. Tekin, E., P.J. Smith, and U.S. Schubert, *Inkjet printing as a deposition and patterning tool for polymers and inorganic particles*. Soft Matter, 2008. **4**(4): p. 703-713.
70. De Gans, B.-J. and U.S. Schubert, *Inkjet printing of well-defined polymer dots and arrays*. Langmuir, 2004. **20**(18): p. 7789-7793.
71. Reis, N., C. Ainsley, and B. Derby, *Ink-jet delivery of particle suspensions by piezoelectric droplet ejectors*. Journal of Applied Physics, 2005. **97**(9): p. 094903.
72. Reis, N. and B. Derby. *Ink jet deposition of ceramic suspensions: Modeling and experiments of droplet formation*. in *MRS proceedings*. 2000. Cambridge Univ Press.
73. McIlroy, C., O. Harlen, and N. Morrison, *Modelling the jetting of dilute polymer solutions in drop-on-demand inkjet printing*. Journal of Non-Newtonian Fluid Mechanics, 2013. **201**: p. 17-28.
74. Bhat, P.P., et al., *Formation of beads-on-a-string structures during break-up of viscoelastic filaments*. Nature Physics, 2010. **6**(8): p. 625-631.
75. Dong, H., W.W. Carr, and J.F. Morris, *An experimental study of drop-on-demand drop formation*. Physics of Fluids (1994-present), 2006. **18**(7): p. 072102.
76. Fromm, J., *Numerical calculation of the fluid dynamics of drop-on-demand jets*. IBM Journal of Research and Development, 1984. **28**(3): p. 322-333.
77. Duineveld, P.C., et al. *Ink-jet printing of polymer light-emitting devices*. in *International Symposium on Optical Science and Technology*. 2002. International Society for Optics and Photonics.
78. Jang, D., D. Kim, and J. Moon, *Influence of fluid physical properties on ink-jet printability*. Langmuir, 2009. **25**(5): p. 2629-2635.
79. Tai, J., et al. *Control of droplet formation in inkjet printing using Ohnesorge number category: materials and processes*. in *Electronics Packaging Technology Conference, 2008. EPTC 2008. 10th*. 2008. IEEE.
80. Nallan, H.C., et al., *Systematic Design of Jettable Nanoparticle-Based Inkjet Inks: Rheology, Acoustics, and Jetability*. Langmuir, 2014. **30**(44): p. 13470-13477.
81. Derby, B., *Inkjet printing ceramics: From drops to solid*. Journal of the European Ceramic Society, 2011. **31**(14): p. 2543-2550.
82. Jung, S. and I.M. Hutchings, *The impact and spreading of a small liquid drop on a non-porous substrate over an extended time scale*. Soft Matter, 2012. **8**(9): p. 2686-2696.
83. Antonini, C., et al., *Drop rebound after impact: The role of the receding contact angle*. Langmuir, 2013. **29**(52): p. 16045-16050.

84. Visser, C.W., et al., *Dynamics of high-speed micro-drop impact: numerical simulations and experiments at frame-to-frame times below 100 ns*. Soft matter, 2015. **11**(9): p. 1708-1722.
85. Pasandideh - Fard, M., et al., *Capillary effects during droplet impact on a solid surface*. Physics of Fluids (1994-present), 1996. **8**(3): p. 650-659.
86. Park, H., et al., *Single drop impaction on a solid surface*. AIChE journal, 2003. **49**(10): p. 2461-2471.
87. Park, J. and J. Moon, *Control of colloidal particle deposit patterns within picoliter droplets ejected by ink-jet printing*. Langmuir, 2006. **22**(8): p. 3506-3513.
88. Tekin, E., et al., *Inkjet printing of luminescent CdTe nanocrystal-polymer composites*. Advanced Functional Materials, 2007. **17**(1): p. 23-28.
89. Sirringhaus, H., et al., *High-resolution inkjet printing of all-polymer transistor circuits*. Science, 2000. **290**(5499): p. 2123-2126.
90. Pabst, O., et al., *All inkjet-printed piezoelectric polymer actuators: Characterization and applications for micropumps in lab-on-a-chip systems*. Organic Electronics, 2013. **14**(12): p. 3423-3429.
91. Fu, Y.-J., et al., *Effect of UV-ozone treatment on poly (dimethylsiloxane) membranes: surface characterization and gas separation performance*. Langmuir, 2009. **26**(6): p. 4392-4399.
92. Baunack, S. and A. Zehe, *A study of UV/ozone cleaning procedure for silicon surfaces*. physica status solidi (a), 1989. **115**(1): p. 223-227.
93. Simaite, A., et al., *Hybrid PVDF/PVDF-graft-PEGMA membranes for improved interface strength and lifetime of PEDOT: PSS/PVDF/ionic liquid actuators*. ACS applied materials & interfaces, 2015. **7**(36): p. 19966-19977.
94. Simaite, A., et al., *Towards inkjet printable conducting polymer artificial muscles*. Sensors and Actuators B: Chemical, 2016. **229**: p. 425-433.
95. Shen, X., C.-M. Ho, and T.-S. Wong, *Minimal size of coffee ring structure*. The Journal of Physical Chemistry B, 2010. **114**(16): p. 5269-5274.
96. Sun, J., et al., *Recent Advances in Controlling the Depositing Morphologies of Inkjet Droplets*. ACS applied materials & interfaces, 2015. **7**(51): p. 28086-28099.
97. Deegan, R.D., et al., *Capillary flow as the cause of ring stains from dried liquid drops*. Nature, 1997. **389**(6653): p. 827-829.
98. Deegan, R.D., et al., *Contact line deposits in an evaporating drop*. Physical review E, 2000. **62**(1): p. 756.
99. Narayanan, S., J. Wang, and X.-M. Lin, *Dynamical self-assembly of nanocrystal superlattices during colloidal droplet evaporation by in situ small angle X-ray scattering*. Physical review letters, 2004. **93**(13): p. 135503.
100. Soltman, D. and V. Subramanian, *Inkjet-printed line morphologies and temperature control of the coffee ring effect*. Langmuir, 2008. **24**(5): p. 2224-2231.

101. Minemawari, H., et al., *Inkjet printing of single-crystal films*. Nature, 2011. **475**(7356): p. 364-367.
102. Bar-Cohen, Y. *Electroactive polymers: current capabilities and challenges*. in *SPIE's 9th Annual International Symposium on Smart Structures and Materials*. 2002. International Society for Optics and Photonics.
103. Jaffe, B., *Piezoelectric ceramics*. Vol. 3. 2012: Elsevier.
104. Talbot, H., et al., *Towards an interactive electromechanical model of the heart*. Interface focus, 2013. **3**(2): p. 20120091.
105. Eom, C.-B. and S. Trolier-McKinstry, *Thin-film piezoelectric MEMS*. MRS Bulletin, 2012. **37**(11): p. 1007-1017.
106. Chen, Q., et al., *Polymer-Based Dielectrics with High Energy Storage Density*. Annual Review of Materials Research, 2015. **45**: p. 433-458.
107. Bauer, F., *Relaxor fluorinated polymers: novel applications and recent developments*. IEEE Transactions on Dielectrics and Electrical Insulation, 2010. **17**(4): p. 1106-1112.
108. Ramadan, K.S., D. Sameoto, and S. Evoy, *A review of piezoelectric polymers as functional materials for electromechanical transducers*. Smart Materials and Structures, 2014. **23**(3): p. 033001.
109. Lovinger, A.J., *Ferroelectric polymers*. Science, 1983. **220**(4602): p. 1115-1121.
110. Zhu, L. and Q. Wang, *Novel ferroelectric polymers for high energy density and low loss dielectrics*. Macromolecules, 2012. **45**(7): p. 2937-2954.
111. Barique, M. and H. Ohgashi, *Annealing effects on the Curie transition temperature and melting temperature of poly (vinylidene fluoride/trifluoroethylene) single crystalline films*. Polymer, 2001. **42**(11): p. 4981-4987.
112. Khan, S., et al., *Flexible tactile sensors using screen-printed P (VDF-TrFE) and MWCNT/PDMS composites*. IEEE Sensors Journal, 2015. **15**(6): p. 3146-3155.
113. Guan, F., et al., *Crystal orientation effect on electric energy storage in poly (vinylidene fluoride-co-hexafluoropropylene) copolymers*. Macromolecules, 2009. **43**(1): p. 384-392.
114. Guan, F., et al., *Effects of polymorphism and crystallite size on dipole reorientation in poly (vinylidene fluoride) and its random copolymers*. Macromolecules, 2010. **43**(16): p. 6739-6748.
115. Frecker, M.I. and W.M. Aguilera, *Analytical modeling of a segmented unimorph actuator using electrostrictive P (VDF-TrFE) copolymer* Presented in part at the ASME Design Engineering Technical Conferences, Symposium on Mechanisms and Devices for Medical Applications, Pittsburgh, PA, September, 2001 and at the SPIE 8th International Symposium on Smart Structures and Materials, Newport Beach, CA, March, 2001. Smart materials and structures, 2003. **13**(1): p. 82.
116. Li, Z.-M., M.D. Arbatti, and Z.-Y. Cheng, *Recrystallization study of high-energy electron-irradiated P (VDF-TrFE) 65/35 copolymer*. Macromolecules, 2004. **37**(1): p. 79-85.

117. Ang, C. and Z. Yu, *"Dielectric relaxor" behavior of electroactive fluorinated polymers*. Applied Physics Letters, 2005. **86**(26): p. 262903.
118. Ang, C. and Z. Yu, *Ferroelectric, Electroactive, and Dielectric - Relaxation Behavior of Fluoropolymers*. Advanced Materials, 2004. **16**(12): p. 979-982.
119. Carpi, F., et al., *Dielectric elastomers as electromechanical transducers: Fundamentals, materials, devices, models and applications of an emerging electroactive polymer technology*. 2011: Elsevier.
120. Liu, S., et al., *High Electromechanical Response of Ionic Polymer Actuators with Controlled - Morphology Aligned Carbon Nanotube/Nafion Nanocomposite Electrodes*. Advanced functional materials, 2010. **20**(19): p. 3266-3271.
121. Zhang, Q., et al., *An all-organic composite actuator material with a high dielectric constant*. Nature, 2002. **419**(6904): p. 284-287.
122. Yin, X., J.-F. Capsal, and D. Guyomar, *A comprehensive investigation of poly (vinylidene fluoride-trifluoroethylene-chlorofluoroethylene) terpolymer nanocomposites with carbon black for electrostrictive applications*. Applied Physics Letters, 2014. **104**(5): p. 052913.
123. Wang, H., et al., *Highly Stable Carbon Nanotube Top - Gate Transistors with Tunable Threshold Voltage*. Advanced Materials, 2014. **26**(26): p. 4588-4593.
124. Zhang, S., et al., *Microstructure and electromechanical properties of carbon nanotube/poly (vinylidene fluoride—trifluoroethylene—chlorofluoroethylene) composites*. Advanced Materials, 2005. **17**(15): p. 1897-1901.
125. Bae, S.-H., et al., *Graphene-P (VDF-TrFE) multilayer film for flexible applications*. ACS nano, 2013. **7**(4): p. 3130-3138.
126. Capsal, J.-F., et al., *Plasticized relaxor ferroelectric terpolymer: Toward giant electrostriction, high mechanical energy and low electric field actuators*. Sensors and Actuators A: Physical, 2014. **207**: p. 25-31.
127. Le, M.Q., et al., *All-organic electrostrictive polymer composites with low driving electrical voltages for micro-fluidic pump applications*. Scientific reports, 2015. **5**.

Chapter II

Control of Recrystallization and its Effect on Electromechanical Performances of Electrostrictive P(VDF-TrFE-CTFE) Terpolymer

I Introduction

Electromechanical coupling effect has been paid the increasing attention due to ability to realize conversion between electrical excitation and mechanical response, and vice versa. Electrostrictive mechanism in combination with electrostatic force was responsible for such coupling effect [1-3]. Thanks to its ease of processibility, flexibility, relatively large-induced strain and fast response to external stimulus, it is of great probability to employ electroactive polymers as rather good candidate for actuator like biomimetic assemblies and microelectromechanical system (MEMS) in large throughput implementation. In practical point of view, pure polymer like polyamide, polyimide [4], polyurethane elastomer [5, 6] exhibited weak electrostrictive response. To overcome the drawbacks, novel fluorinated ferroelectrics copolymer were developed and possessed out-performed in-plane electrostrictive properties at relatively low induced electric field [7-9]. Recently, e-beam irradiated poly(vinylidene fluoride-trifluoroethylene) (P(VDF-TrFE)) copolymer unimorph demonstrated rather high tip displacement, providing novel concepts of designing materials with high electromechanical response [10, 11]. Inspiring from this method, chemical defects were introduced into molecular backbone by copolymerization of bulk-like ternary CTFE monomer and as a consequence, sub-micro crystal size broke into sporadic nano-sized crystallites [12, 13]. Due to presence of CTFE, β -form ferroelectric domains with all-Trans (T_m , $m>3$) conformation in copolymers transformed into non-polar α -form paraelectric crystallites and less-ordered γ ($T_3G^+T_3G^-$) ferroelectric phase. Hence interaction between neighboring crystallites was weakened. And spontaneous polarization of the sporadic nano-sized crystallites in terpolymer was relatively independent and the dipole moment of each nano-sized crystallite was randomly distributed. Terpolymer exhibited diffusion phase transition frequently when subjected to the external stimulus. Such diffusion phase transitions in chain conformation were responsible for high electrostrictive behavior.

One of the obvious drawbacks for fluorinated polymer is that relatively high electric field should be applied to generate high strain or mechanical deformation, although applied electric field is order of magnitude decreasing comparable with the non-fluorinated electrostrictive polymers which presented an equivalent electrostrictive deformation under very high electric field supply. It is well recognized that electrostrictive strain s is quadratic correlation with induced electric field E , being positively proportional to dielectric constant ϵ' [14, 15]. Extensive studies aiming at increase of dielectric constant were carried out for decades. Conductive metal-ligand [16] or nano-sized carbon homologous particles like carbon black [17], carbon nanotube [18, 19] and graphene nanosheets [20] were embedded into the terpolymer matrix in an attempt to enhance dielectric property. But the most embarrassed fact is that filler volume fraction should not reach the percolation threshold. Nanocomposite concept turns out to be an efficient way to augment dielectric behavior but unfortunately at the expense of reinforced elastic mechanical

properties. Such high Young's modulus was an adverse effect contribution to electromechanical behavior. In order to at least maintain mechanical properties, organic additive macromolecules like conductive polyaniline were doped and resulted in a large electrostrictive behavior at lower electric field due to significantly enhanced dielectric permittivity ϵ' [21, 22]. Recently, our study found that plasticized terpolymer exhibited thousand-fold increase of dielectric permittivity and thus 28-fold increase of the electrostrictive strain [23]. This chemically doped terpolymer was utilized to fabricate micro-pump device [24], showing a rather good candidate for MEMS system application.

In addition to chemical modification of fluorinated polymers, crystallographic parameters should not be neglected when considering the intrinsic origins. In fact, electromechanical properties were significantly dependent upon the crystal size, degree of crystallinity and its morphology. Such parameters were highly determined by processing condition. Various film processes like conventional casting, hot-press and spin-coating were employed to control the crystallographic parameters [25-27]. Moreover, for a typical solution casting process, free-standing macromolecules in dilute polar solution underwent crystallization process when volatile solvent evaporated slowly. Its molecular chain folded back and forth into crystal lamellae by thermodynamic driving force. Due to bulk defects existing in P(VDF-TrFE-CTFE) backbone, much less fraction of crystallinity was obtained. And as temperature approaching to super-cooled liquid region (SLR) above sub-vitreous state, crystallization takes place in amorphous matrix. Therefore, isothermal crystallization process was subjected to freshly-prepared pristine films in order to enhance crystallinity fraction. In addition, flat-on orientation crystal lamellae accounted for most fraction of crystal lamellae in pristine bulk films, with its *c*-axis parallel to the external electric field. Terpolymer films show the minimal dipole polarization rather the edge-on orientation lamellae [25, 28] and thus low dielectric permittivity were obtained. On this point, one could deduce that both of crystallinity form and crystal orientation determine the dielectric properties of as-casted terpolymers.

As-stated, large electrostrictive strain was highly dependent on the relaxor ferroelectric behavior. What concerns us most is to picture the relationship between terpolymer microstructure and electrostrictive behavior. By controlling the terpolymer morphology, that is, microstructure, there is a possibility to fully understand the electrostrictive response. In present contribution, P(VDF-TrFE-CTFE) terpolymer with composition of 61.7/30.4/7.9 (mole ratio) was employed as representative to investigate the relaxor behavior and electrostrictive properties. Terpolymer samples with different morphology and crystallinity fraction were prepared by isothermal crystallization at given temperature. Their thermal properties and films morphology were monitored by Differential Scanning Calorimetry (DSC) and Atomic Force Microscopy (AFM) pattern. In addition, evolution of crystallization impact to dielectric constant and relaxor

ferroelectric behavior were addressed. Electrostrictive behavior was characterized by out-of-plane transverse strain in unimorph cantilever beam mode.

II Experimental Section

II. 1 Materials and Sample Elaboration

P(VDF-TrFE-CTFE) terpolymers studied in this current work with chemical composition of VDF/TrFE/CTFE=61.7/30.4/7.9 (mole ratio) was by courtesy of Piezotech S.A.S (Arkema, France) which was synthesized by a suspension polymerization. All the solvents as-stated were purchased from Sigma-Aldrich and used as received. The 14% (wt) terpolymer solution were prepared by dispersing 7.0 g P(VDF-TrFE-CTFE) terpolymer grains in 80 °C Meth Ethyl Ketone (MEK) and stirred vigorously. The color-less transparent solution was then cooled down to the room temperature and stocked in refrigerator at -4 °C to be harnessed. Prior to deposition of the terpolymer solution, glass plate was successively rinsed by ethanol and acetone. The fresh glass plate was then coated with a thin layer of lecithin molecules, on which the polymer solution was applied by slow solution casting of 14 wt% homogeneous terpolymer solution via an Elcometer 3700 doctor blade film applicator. As the films to be of solid during the solvent evaporation, fresh polymer deposit with plate was moved to a vacuum chamber for 2 hours at room temperature

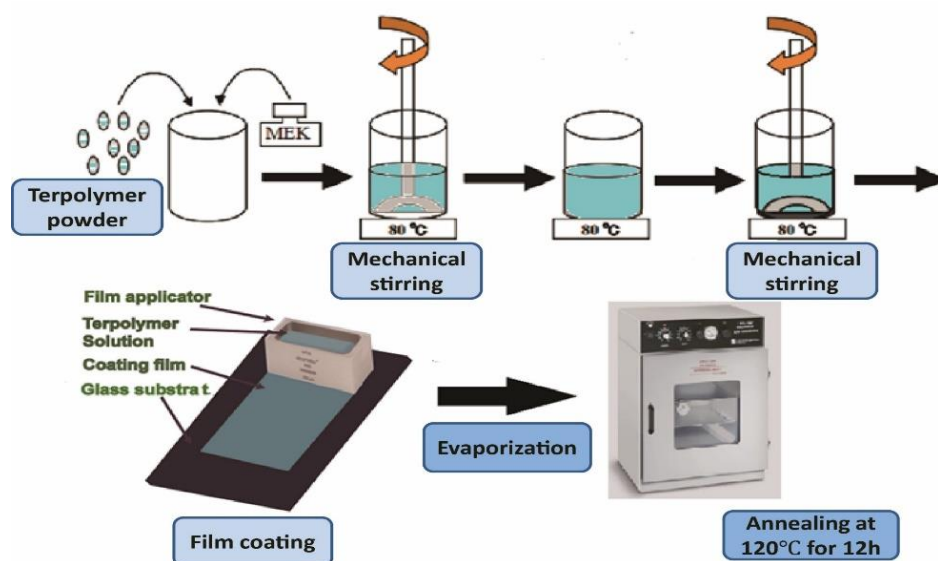


Figure II. 1 Processing flow schematics of preparation of terpolymer solution, film coating application and isothermal crystallization process

(R.T) which was named Film A. Recrystallization process was performed to elaborate the tailor-made crystal fraction and microstructure. Firstly post annealed specimens were obtained by Film A annealing in 60 °C oven for 12 hours and designated as Film B, 70 °C for 12 hours nominated as Film C, respectively. Film D were engineered via temperature annealing at 80 °C for 2 hours.

Film E and Film F were obtained under thermal treatment of Film A in 90 °C oven for 1 hour and 2 hours respectively. Median-crystallized Film G was elaborated from Film A in a programming control treatment at 110 °C for 2 hours. Crystallized Film H was finalized by temperature annealing Film A for 2 hours at 120 °C. In addition, a melt-recrystallized sample Film I, heated up to 140 °C and held the temperature for 2 hours, then quenched in the air, was also compared for surface microstructure investigation. Fully temperature annealed Film I were finalized by deeply annealing Film A 120 °C overnight (12h).

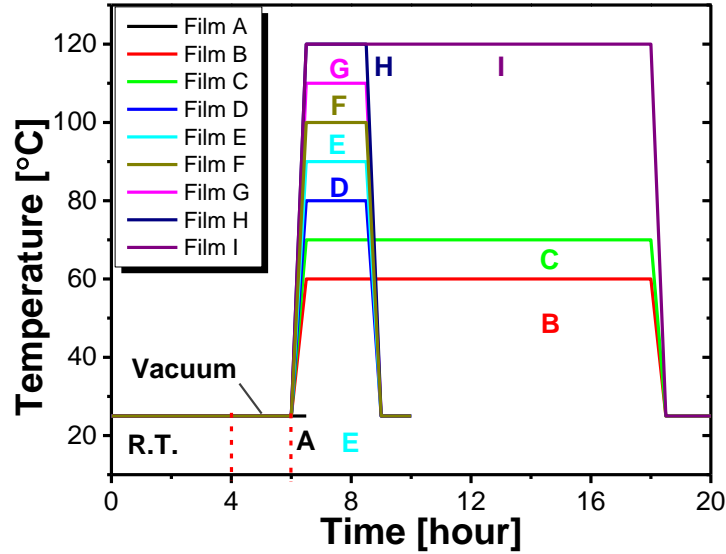


Figure II. 2 Schematic diagram of temperature annealing process program profiles

A schematic diagram of temperature annealing recrystallization process profiles were supplementarily depicted in Figure II. 2. Terpolymer films thickness in each case was normalized set to ca.60 μm in order to eliminate the disparities of electric field distribution in thickness mode. All as-cast resulting films were apparently homogeneous and slightly translucent for crystallized films.

The annealing time dependence of isothermal crystallization was also conducted in order to investigate the complementary crystallizing kinetics. In addition to the previous annealing process at 90 °C for 2 h, freshly renamed **Film K**, the 1, 4 and 10 h isothermal treatment were performed and denoted as **Film J**, **Film L** and **Film M**.

II. 2 Device Fabrication and Characterization Techniques

II.2.1 Differential Scanning Calorimetry (DSC)

Thermal behaviors of as-treated dielectric terpolymer films were monitored with DSC 131 Setaram Evo equipped with liquid nitrogen cooling accessory. Prior to thermal record, temperature was calibrated with alumina standard specimen and the baseline was carried out in

the temperature range from 203K to 473K, running with the empty cell. Each specimen with normalized mass heating upon the identical phase program was heated in the rate of $10\text{ }^{\circ}\text{C min}^{-1}$ under nitrogen flow rate of 1.5 bars. Each thermogram trace was analyzed by Calisto software package. Parameterized glass transition region (T_g) was designated by the midpoint of the transition region, Curie transition temperature (T_C) and bulk polymers melting region were also summarized in Table II. 1.

II.2.2 Atomic Force Microscopy (AFM)

The morphological characteristics of the as-casted thin films were characterized by atomic force microscopy. Prior to AFM pattern acquisition, $1\text{mm}\times 1\text{mm}$ rectangular shaped thin films were bonded to the silicon wafer surface via conductive glue. AFM images were acquired in air at room temperature on a Nanoscope IIIa Multimode (Digital Instruments/VEECO, CA). Tapping mode was performed in a scan rate of 1 Hz.

II.2.3 Mechanical Strength Properties

Mechanical Properties (Young's Modulus) were obtained by a non-conventional uniaxial strength tensile measurement described elsewhere [24]. The deformation and strain rate of sample was driven and recorded by a function generator through controlled Newport ultra-precision linear motor platform (Gain: $1\text{mm}/100\text{ mV}$). As shown in Figure II. 3, The x-axis tensile force was recorded by an explicit Microfused™ force sensor. 60 mm (L) \times 10 mm (W) rectangular film

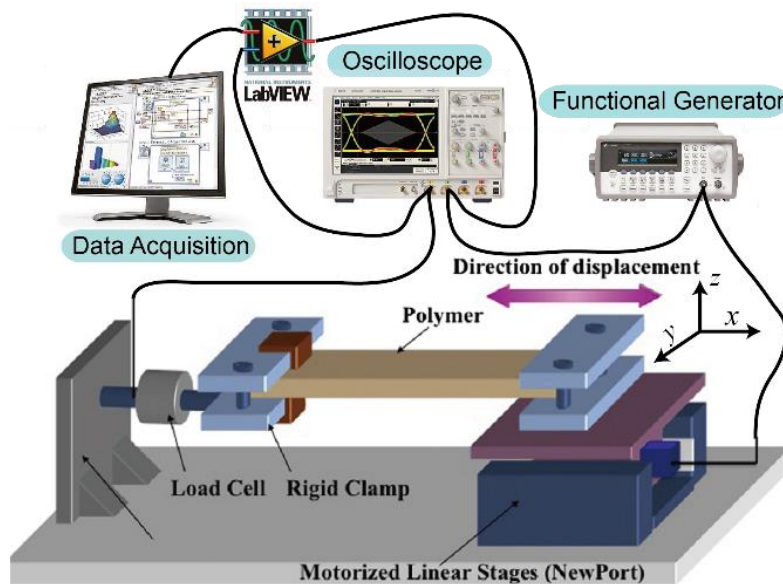


Figure II. 3 A schematic representation of measurement setups for mechanical strength properties specimens were mounted on one side to fixed clamp bar furnished on the Newport platform. 40mm normalized length of films was considered into data acquisition. A frequency of 100 mHz sinusoidal signal was applied to the precisely controlled Y-axis motor and 1% maximal sinusoidal

strain was set while the loading-unloading cycles, by which average Young's modulus of films were determined via slope of stress versus strain curves.

II.2.4 Dielectric Properties

Dielectric spectroscopy measurements were carried out with Solartron 1260 (UK) impedance-analyzer equipped with Model 129610A LHe LN2 Cryostat System. As-casted dielectric terpolymers circular film plates in diameter of 20 mm were metalized by sputtering gold on both surfaces through a shadow mask. The metal/polymer/metal parallel plate capacitor was clamped between electrodes sample holder. Dielectric spectra data acquisition were conducted in probe frequency range from 10^{-1} to 10^6 Hz at AC 1 bias Voltage under ambient temperature. Real and imaginary parts of complex permittivity for each as-deposited films were obtained.

II.2.5 Electric Breakdown Strength

Electrical breakdown strength was performed by home-made equipment. Circular capacitor samples with 10 mm diameter gold sputtered on both sides were clamped with a needle-like copper electrode. A DC voltage was applied in a ramp rate of 500 V/s via voltage amplifier governed by a functional generator. The voltage were recorded where capacitors were deliberately mechanical damaged induced by electrical current. In order to avoid air discharging and ionization, specimens and needle-like electrodes were immersed into silicon oil during the

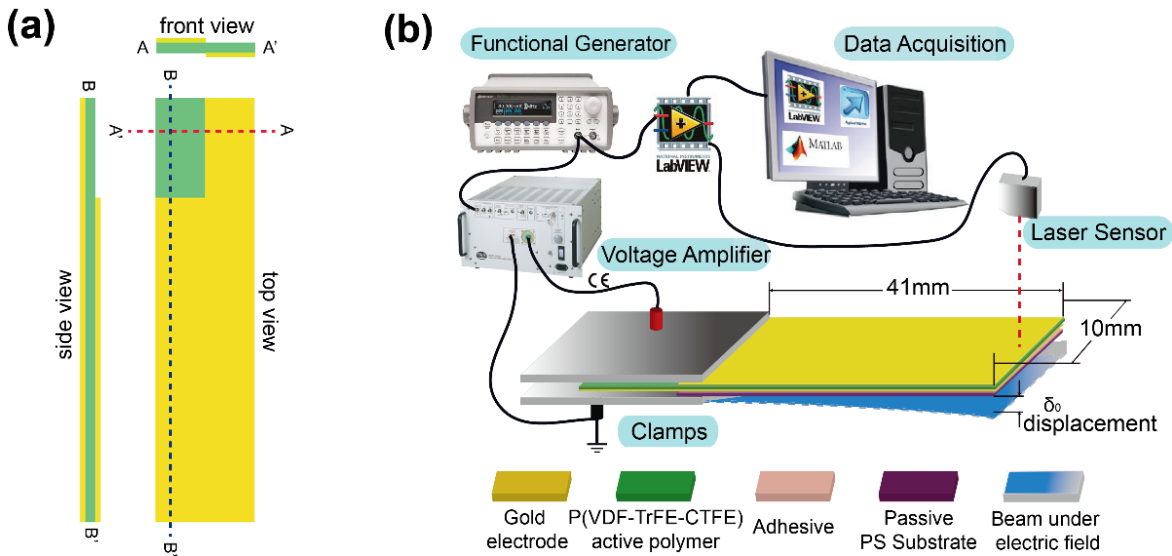


Figure II. 4 (a) Schematic representations of cantilever beam precursor multi-view for bending measurement, (b) configuration of cantilever beam and bending measurement setups

failure experiments. At least 20 duplicate breakdown tests in each case of sample were performed on each as-prepared film fulfilling the cumulative two-parameter Weibull failure probability statistics which will be discussed in later section.

II.2.6 Field-induced Electrostrictive Strain

Transverse strain of as-prepared films were carried out in a protocol with experiment set-up via bending test based on unimorph cantilever beam theory described elsewhere [9]. First of all, sample precursor for electromechanical evaluation was fabricated by sputtering Au electrode via designed shadow mask as shown in Figure II. 4. For cantilever beam assembly, sample precursor was bonded to 100 μm -thick passive polystyrene (PS) substrate film (Young's modulus, 4.5 GPa) via 25 μm -thick self-adhesive layer (3M Scotch ATG 924). In an attempt to optimization of bonding, multilayer was laminated by D&K 4468H laminator for 20min at room temperature.

The well-prepared samples were clipped on the aluminum scaffold. Laser sensor were then subjected to monitor unimorph tip displacement induced by external electric field perpendicular to the longitudinal direction as shown in Figure II. 5. Combining mechanical strength behavior, tip displacement (δ) reads,

$$\delta = \frac{3L^2}{2t} \frac{2\lambda\xi(1+\xi)^2}{\lambda^2\xi^4 + 2\lambda\xi(2+3\xi+2\xi^2)+1} S_{31} \quad \text{II. 1}$$

where L , t is unimorph length and thickness related to its dimension, λ represents the Young's modulus ratio of electric active polymers to elastic PS substrate (100 μm -thickness); ξ symbolizes the aspect ratio of thickness of dissipative substrate to the electric active layer, respectively, S_{31} donates terpolymer transverse train.

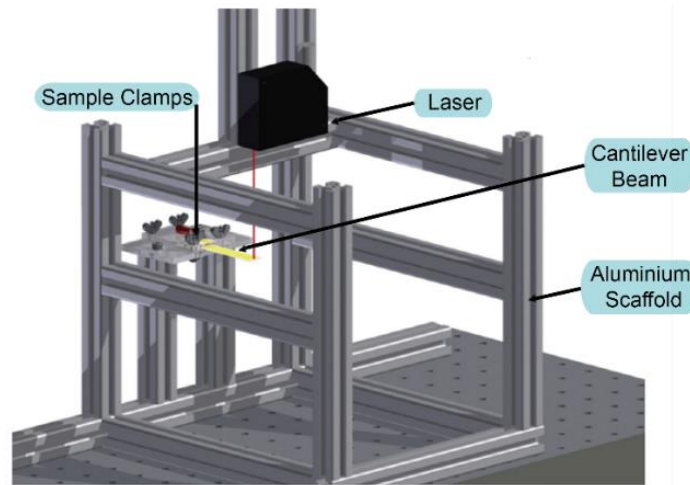


Figure II. 5 Schematic illustration of aluminum scaffold attached with cantilever beam sample holder

III Results and Discussions

III.1 Thermal Data Analysis and Crystalline Properties

III.1.1 Temperature Dependence of Isothermal Crystallization

Figure II. 6 illustrated the endothermal heat flow traces as a function of temperature for the respective P(VDF-TrFE-CTFE) terpolymer isothermally crystallized at various temperatures with 10°C interval between range from 60 °C to 120 °C for normalized 2h process duration. Before thermal behavior investigation, pre-heat running ramps for terpolymers annealed for 2h at 60 °C and 70 °C were performed and was observed that no distinct change over the original pristine **Film A** of the two endothermal anomalies. For the sake of better comparison regarding the annealing temperature (T_a) reason, annealing time duration were increased up to 12h period for sample annealed at 60 °C. Briefly, two endo-peaks were observed over the whole DSC curves where weak regime at lower temperature could be attributed to ferro-paraelectric transition, namely Curie transition while the remarkably strong peaks at high temperature were due to the fusion of the crystalline phase present in the annealed samples. For the pristine film A, a broader and less intense peak appeared at 47.4 °C, the highest Curie temperature T_c amongst the samples. Intriguingly, as annealing temperature increased, Curie transition region exhibited obvious diffusion towards the lower temperature as shown in Figure II. 7c. It should be also noted that T_c for various sample demonstrated two stepwise diminution. When the samples were annealed at temperature below 80 °C, T_c underwent strikingly decrease from 47.4 °C for the pristine to 33.9 °C for sample annealed at 80 °C, showing strong temperature dependent, followed by a quite moderate diffusion to 31.6 °C for 110 °C annealing protocol. Intriguingly, film annealed at 120 °C had an exceptional increase to 33.3 °C, suggesting these existed crystal phase transition process, e.g. melting-crystallization process. Further, Film I, annealed for a longer time duration showed considerable elevation of T_c to 34.0 °C except the enthalpy of Curie transition. Such result was in rather good agreement with the T_c values that were found for the hot-pressed terpolymer films (not shown here). It is mostly possible that the unusual increase in T_c here was attributable to the melt-crystallization process. A predominant α crystal phase yielded during the recrystallization from melting state [29]. And the reorganization and phase transition of unstable molecular chain conformation occurred to large extent, for instance, loosely packaging density, ferroelectric defects and head-to head/tail-to-tail (HHTT) linkage etc [25, 29]. Finally, higher energy excitation was needed to surmount the Curie phase transition.

In general, Curie transition was associated with phase transition, closely referring to the change in molecular chain conformation in crystal phase. So, decrease of T_c with increasing T_a was most probably due to the collapse of ferroelectric domain in crystal phase. Ferro-paraelectric transition barriers have been greatly reduced because of defect (ternary CTFE) incorporation to

that of copolymer. Consequently, γ crystal form with α anti-ferroelectric were predominated in the crystal lamellae. γ phase has the same unite cell as the α phase, but its joint dipoles rotated 180° to the c -axis. We hypothesize that Film A possessed the largest T_c value which is ascribed to the more γ crystal phase density formed during the solvent loss. The solvent evaporating and annealing at room temperature facilitate the amorphous phase to crystallize into γ crystal phase and remove the hexagonal phase defects driven by molecular chain thermodynamic force just below the T_c temperature. This assumption could be manifested by the largest enthalpy of Curie transition ΔH_C value detected for Film A as 4.4 J g^{-1} . However, the samples annealed at temperature far from T_c showed a sharp decrease in ΔH_C values in two stepwise, suggesting a diminished δ crystal phase content in the samples. During the annealing at temperature higher than T_c , the ferroelectric γ phase with $T_m G^+ T_m G^-$ ($m > 3$) chain conformation generated in solvent evaporation tended to become anti-ferroelectric, that is, amid the adjacent *Trans* dipoles switched 180° in order to accommodate the large chlorine atom substitution and relieve the steric congestion [30]. This would lead to a less net dipole moment. Therefore the enthalpy of Curie transition were greatly decreased from 4.4 J g^{-1} to ca. 3.6 J g^{-1} (70% of original pristine Film A) for terpolymer films, carried out annealing treatment at 80°C for 2h, in accordance with the cross point of Curie transition temperature in Figure II. 7c. Besides, their transition enthalpy followed

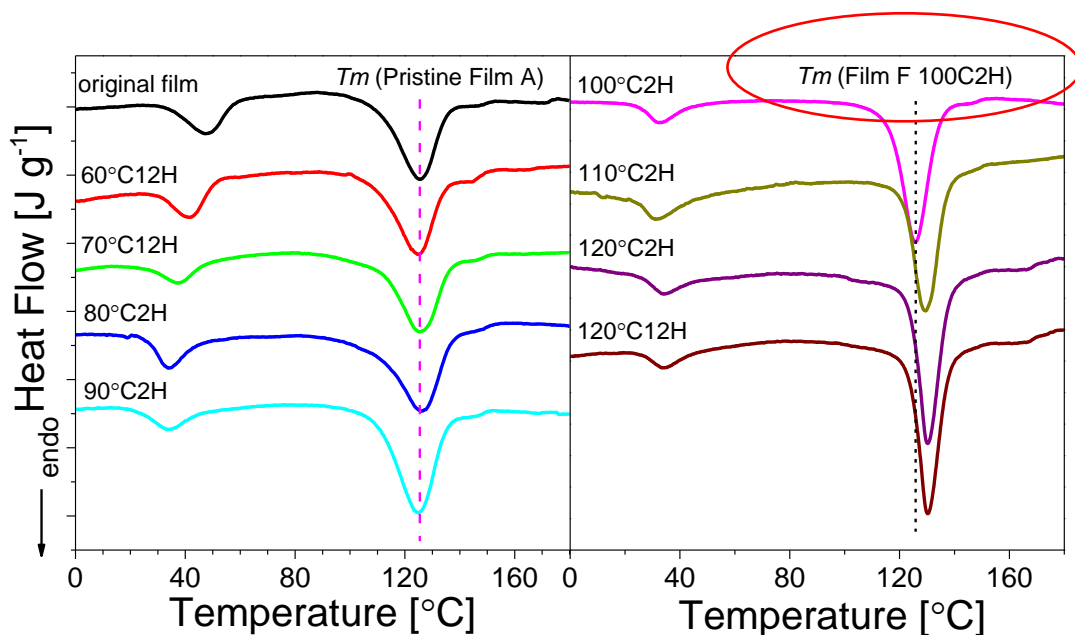


Figure II. 6 DSC thermogram traces of respective as-casted terpolymer films at various isothermal annealing temperature: pristine as-casted film (R.T.) (Film A), 60°C for 12h (Film B), 70°C for 12h (Film C), 80°C for 2h (Film D), 90°C for 2h (Film E), 100°C for 2h (Film F), 110°C for 2h (Film G), 120°C for 2H (Film H). Fully crystallized terpolymer Film I, with annealed at 120°C for 12h was also shown in the Figure. Vertical dash line in figure left marks the melting

peak of the pristine Film A and dots line in figure right denotes melting peak of Film F (100°C2H).

the similar compressing trend in a moderate rate. It was thus expected that a relatively low ΔH_c was obtained for the terpolymer Film I annealed at 110 °C with 3.3 J g⁻¹. This suggested that the *Trans* conformation in the single sequence slowly rotated to the *gauch* sequence during the annealing process at temperature below 110 °C. It should be noted that the single curie transition peak was observed in the DSC curve and this implied the terpolymers had the same thermally-induced paraelectric phase. However, terpolymer films which underwent melt-recrystallization process, possessed the lowest ΔH_c value amongst especially for Film I, having a 2.8 J g⁻¹ Curie transition enthalpy. This might be due to the dominant paraelectric phase resulting in films carried by the melt-recrystallization process. Nonetheless, melting regions exhibited quite disparities. As listed in Table II. 1, the heat of fusion values were gradually increasing as a function of annealing temperature T_a . This indicated the higher T_a favored the out-performed crystallization kinetics, that is, acceleration of molecular chain folding back and forth into the crystal lattice. For the better comparison, the crystallinity degree χ_c induced by isothermal annealing could be deduced from the DSC thermograms by $\chi_c = \Delta H_f / \Delta H_f^0 \times 100\%$, where H_f is fusion of enthalpy for annealed terpolymers. ΔH_f^0 is the melting enthalpy of 100% perfect crystal terpolymer films and for terpolymer studied currently, ΔH_f^0 value of full crystal films was reported as ca. 42 J g⁻¹ [27]. The degree of crystallinity were then calculated in Table II. 1. The crystallinity value as found for pristine Film H was greatly augmented from 30.8% to 43.2% for terpolymer annealed at 120 °C, reaching to 95.4% of fully crystallized Film I. When the process time duration was expanded to 12h, hardly distinct increase was observed in degree of crystallinity for Film I, only by 2.1% comparable with Film H. Enhancement of crystalline fraction by isothermal annealing process would trigger the crystal lamellae thickening process. As shown in Figure II. 6 endothermic curves, melting temperature T_m exhibited quite diffuse characteristic when annealing temperature was higher than 100 °C. Figure II. 7e plotted the T_m as a function of annealing temperature and saw a two stepwise increase in T_m between R.T and 120 °C. No distinct increase was observed between pristine film A and Film D annealed at 80 °C at which less than 1°C increment was obtained. This indicated that low temperature annealing process ($T_a \leq 80^\circ\text{C}$) seems not to trigger the crystal lamellae thickening process, but reorganize the molecular chain conformation and reduce the crystalline packaging defects. However, annealing at temperature larger than 80°C tended to make the T_m shift towards the higher temperature. This can be associated with the high crystallinity and crystalline size induced by molecular chain rearrangement thermodynamically. In order to analyze the crystal size distribution, full width at half maximal temperature (FWHM) values of melting peak regions

were introduced. FWHM values as a function of annealing temperature was plotted in Figure II. 7f, showing a clear two stepwise diminution. Below 80°C annealing, FWHM values showed

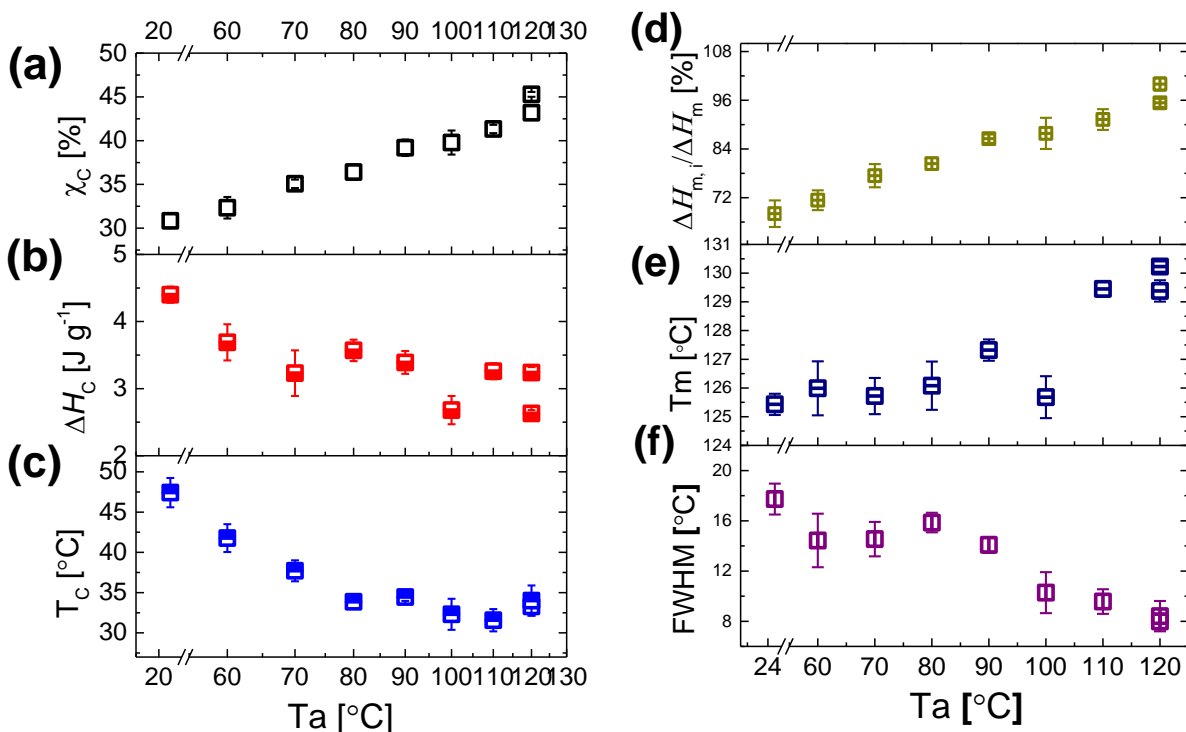


Figure II. 7 Plots of the degree of crystallinity (a), ΔH_c enthalpy of Curie transition (b), Curie transition temperature (c) and plots of ratio of heat of fusion $\Delta H_{m,i}$ for respective annealed terpolymer to the fusion of enthalpy ΔH_m of fully crystallized Film I (d), temperature values of melting peaks (T_m) (e) and full width at high maximal values (FWHM) of melting peak regions (f) on DSC heating curves over the temperature ramp.

a less dependence, decreasing only from 17.7 °C for pristine Film A to 15.9 °C for Film D, respectively. Large FWHM values indicated the large distribution of crystal size, implying the terpolymer films were strongly heterogeneous in crystalline phase. It is interesting that higher temperature intended to obtain a less heterogeneous terpolymer according to a sharp decrease in the FWHM values from 14.1 °C to 7.99 °C as annealing temperature rise to 120°C. This reflects much more homogeneous crystal size distributed in the amorphous region. In addition, the coherent lengths (l) of crystal nanodomains, being inversely proportional to the FWHM values [31], were increasing, also a sign of enlargement of crystal size for terpolymer annealed at higher temperature.

The results as stated showed that Curie transition and melting transition were strongly driven by thermodynamics behavior of each phase in polymer annealing process. For better

understanding the correlation between annealing temperature and Curie and melting transition properties was introduced. This relations were perfectly presented by several ferroelectric polymers, such as P(VDF-TrFE) [26, 31].

Annealing effects on the phase transition behaviors of the as-cast terpolymer are readily understood by the Gibbs free energy diagram [32, 33]. The free energy G_i at pressure P and temperature T can be satisfactorily described by $G_i = U_i + V_iP - S_iT$. Schematic diagrams of temperature dependence of Gibbs free energy of each phase G_i , simplified as an oblique line for P(VDF-TrFE-CTFE) terpolymer were depicted in Figure II. 8. The Annealing at temperature below Curie temperature T_C reduced the Gibbs free energy G_f of ferroelectric phase where free energy in paraelectric phase G_p was not changed. This resulted in an increasing of T_C . In our case, two distinct steps should be noted. At first step, even though T_a was set to 90°C, melting

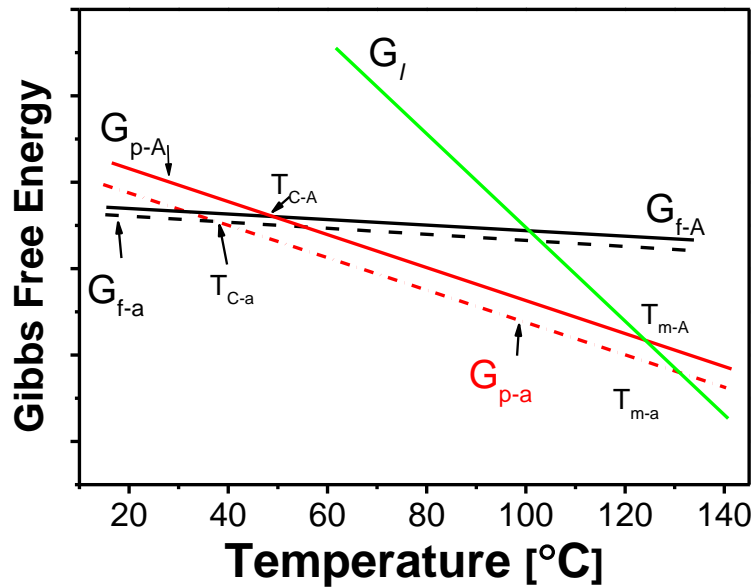


Figure II. 8 The solution casting films annealed in the hexagonal phase. T_{C-A} and T_{m-A} are the phase transition temperature and the melting temperature, respectively, of the original SC film.

T_m were likely to be constant. This indicated the free energy of G_{p-a} would not shift downward referring to the unchanged T_m . Only a decreasing trend of Curie transition T_C was observed. According to the Gibbs free energy scheme in Figure II. 8, the downward drift of G_f and G_p were both supposed to occur, resulting in an decrement of T_{C-A} . And free energy of paraelectric phase G_{p-A} of pristine Film A was compressed to G_{p-a} for annealed terpolymer as annealing temperature T_a large than 90 °C, definitely being $T_a > T_C$. This gave rise to an increasing melting temperature from T_{m-A} to T_{m-a} for pristine and annealed terpolymer respectively. Reduced Curie transition point to T_{C-a} was due to the combination of both downward shift of ferroelectric free

Table II. 1 Thermal parameters of Curie transition region and melting peak region for isothermally annealed terpolymer at various temperature for fixed 2h annealing time duration (from room temperature to 120 °C)

Acronym	T _g	ΔC _p	T _C	ΔH _C	ΔH _m	Crystallinity	Melting region (°C)	
	°C	(mW)	°C	(J g ⁻¹)	(J g ⁻¹)	χ _C	T _m	FWHM
Pristine Film A	-26.98	0.14	47.4	4.4	12.9	30.8	125.4	17.7
60C12H Film B	--	--	41.8	3.7	13.6	32.3	126.0	14.4
70C12H Film C	--	--	37.7	3.2	14.7	35.1	125.7	14.5
80C2H Film D	-22.96	0.23	33.9	3.6	15.3	36.4	126.1	15.9
90C2H Film E	-21.70	0.06	34.4	3.4	16.5	39.3	126.8	14.1
100C2H Film F	--	--	32.3	2.7	16.7	39.8	125.7	10.3
110C2H Film G	-24.39	0.18	31.6	3.3	17.4	41.3	129.4	9.57
120C2H Film H	--	--	33.3	3.2	18.1	43.2	129.4	8.41
120C12H Film I	-23.79	0.07	34.0	2.8	19.0	45.3	130.2	7.99

III.1.2 Temperature Dependence of Isothermal Crystallization

Annealing process results in previous section showed the annealing temperature at 90 °C was a cross point below which the annealing process only affected the Curie phase transition behavior and crystallinity instead of heterogeneity (recall Figure II. 6). Herein, 90 °C was chosen to study the isothermal annealing influences on Curie transition and melting peaks as function of time period. The DSC thermogram curves of the terpolymer annealed at 90 °C for various time duration were presented in Figure II. 9. Large diffusion was observed on Curie transition rather than melting peaks regions which saw a slight shift to the higher temperature as shown in inset Figure. Their degree of crystallinity χ_c , Curie transition enthalpy ΔH_C and Curie point T_C were plotted as function annealing time duration at given 90 °C as Figure II. 10. Time dependence of the evolution of crystallinity showed the expected sigmoidal shape. This behavior has been reported for many semi-crystalline polymers when undergoing the cold-crystallization [34-36]. The multiple stepwise characteristics of the crystallization were proposed during the cold-crystallization. In Figure II. 8, the initial stage saw a mild crystallization rate previous to the nucleation, during which only densification of the crystal domains by the parallel arrangement of the molecular chain. And the nucleation then occurs, leading to an acceleration of crystallization rate ν . As presented in Figure II. 10a, the crystallinity fraction underwent a remarkable high ν . The entangled molecular chain folded into crystal lamella rather quickly as the partial reason of a loose crystal lamellae packaging. As time duration increasing larger than 2h, ν decreased orders of magnitude.

The final degree of crystallinity with χ_c value of 44.5% for the 10h annealing was slightly higher than that of the terpolymer annealed for 4h, reaching a constant value. As expected, Curie transition enthalpy was decayed in an exponential rate as a function of the annealing time from

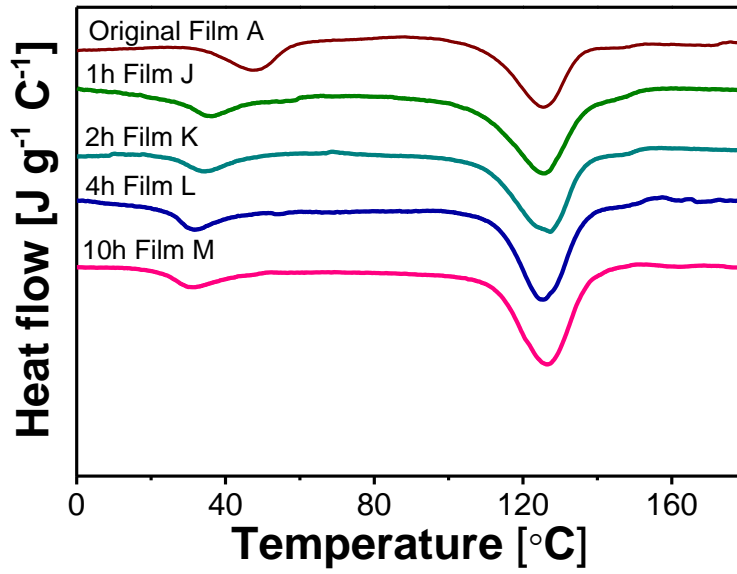


Figure II. 9 The DSC thermogram curves of the terpolymer annealed at 90 $^{\circ}\text{C}$ for various time duration for neat and 10h processing terpolymer.

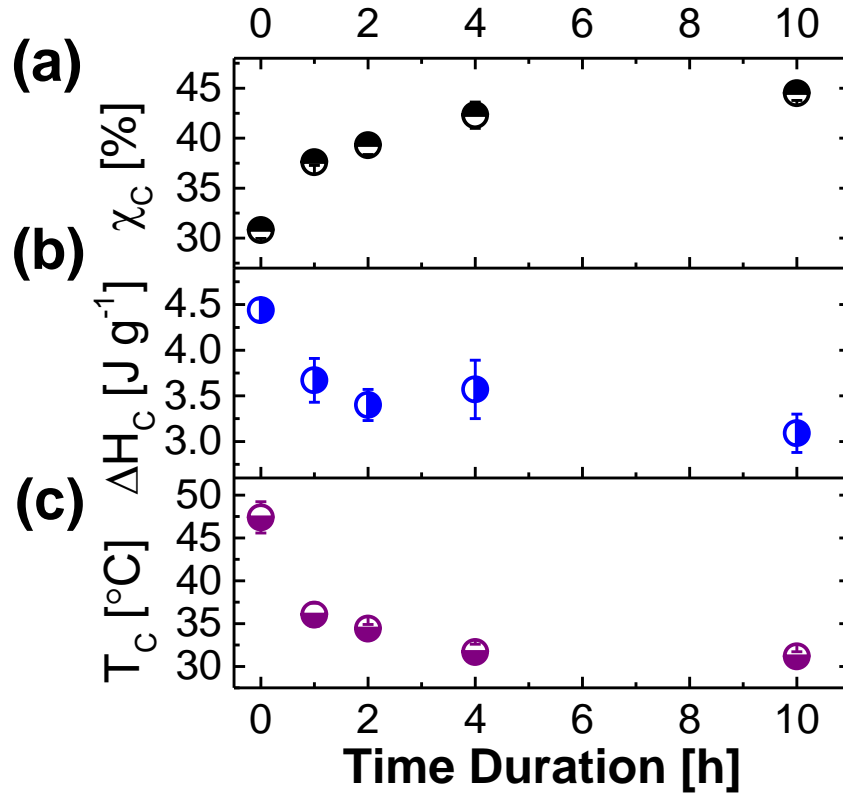


Figure II. 10 DSC thermogram curves of isochronal annealed terpolymer films, the vertical dash line designated as melting temperature of original Film A and inset figure showed normalized melting peak regions, which saw a distinct disparity. Dot plots of degree of crystallinity χ_c (a), Curie transition enthalpy ΔH_c (b) and Curie transition temperature T_c (c) as a function of annealing time period at 90 $^{\circ}\text{C}$.

4.4 J g⁻¹ to 3.09 J g⁻¹ for pristine Film A and Film M, respectively. On top of that, Curie transition temperature T_C shared the similar trend with Curie transition enthalpy, seen a markedly slump at the initial stage. The T_C stabilized after a 4h annealing process and reached to 31.17 °C eventually. This suggested there existed a thermodynamic equilibrium as the annealing time elapsing. Concerning the melting peak region, FWHM values decreased by only 3.3 °C comparable between the pristine Film A and Film M. The heterogeneity of the crystal phase was not altered by the longer time annealing time duration. Note that the crystallinity fraction of Film M was quite close to the fully crystallized Film I and we could assume that annealing at 90 °C could only improve the degree of crystallinity, irrespective of the time duration. The crystal size narrowing and loose lamellae thickening would not tend to occur. Both processes only took place when the annealing temperature was higher than 90 °C. This results was in rather good agreement with findings in the isochronal annealing process.

Table II. 2 Thermal data collection of Curie transition region and melting peak region of terpolymer annealed at fixed temperature for various time period at given temperature of 90 °C.

Acronym	T _g °C	ΔC _p (mW)	T _C °C	ΔH _c (J g ⁻¹)	ΔH _m (J g ⁻¹)	Crystallinity χ _c (%)	Melting region(°C)	
							T _m	FWHM
90C1H Film J	-22.37	0.12	36.05	3.67	15.81	37.6	125.8	17.4
90C2H Film K	-21.70	0.06	34.42	3.41	16.5	39.3	126.8	14.2
90C4H Film L	~	~	31.67	3.57	17.75	42.3	125.3	13.9
90C10H Film M	~	~	31.17	3.09	18.68	44.5	126.5	14.4

III. 2 Surface Topography

The physico-chemical properties involving the thermal transition behavior are correlated with the polymer microstructure closely, which should be necessarily and fully understood. The surface morphology and microstructure were revealed by AFM technique in a tapping mode. Figure II. 11 demonstrated the AFM tapping mode patterns of the pristine Film A (Figure II. 11A), intermediate annealed Film E (Figure II. 11B) and fully crystallized Film I, respectively. The worm-like crystal nanodomains were well stacked as presented in each AFM pattern, where also showed quite disparities. The pristine Film A, without performing isothermal crystallization process, had coarse and loose bumpy-like topographic morphology, where the amorphous phase and crystal phase interaction were indiscernible. Instead, intermediate crystallized Film E showed the pronounced needle-like crystal domains with less than approximately 100 nm length and 20 nm width. The crystal size of P(VDF-TrFE-CTFE) was largely reduced in comparable to its ferroelectric counterpart P(VDF-TrFE) [12, 37, 38]. Besides, the edge of the phase interaction was clarified and a densification of the crystalline phase was also revealed by AFM profiles. These phenomena suggested the somewhat different microstructure between the pristine Film A and the annealed Film E. In contrast to the pristine Film A, the size of crystal nanodomains in

median crystallized Film E was evenly distributed. The Film E pattern presented the similar surface morphology as the pristine Film A. Its surface topography was relatively smooth without any delicate crystal microstructure and the interfacial domains between the crystalline and amorphous phase blurred. Considering that Film I was annealed at 120 °C, rather close to the melting point, melt-recrystallization to some extent occurred during the annealing process.

According to Park's studies [25, 39], the crystal lamellae underwent the change of crystal orientation during the recrystallization process of P(VDF-TrFE) copolymer. For a typical solution casting process, the crystal lamellae has two main crystalline orientation, flat-on and edge-on depicted in Figure II. 11D. The distinct surface morphology of the annealed terpolymer was

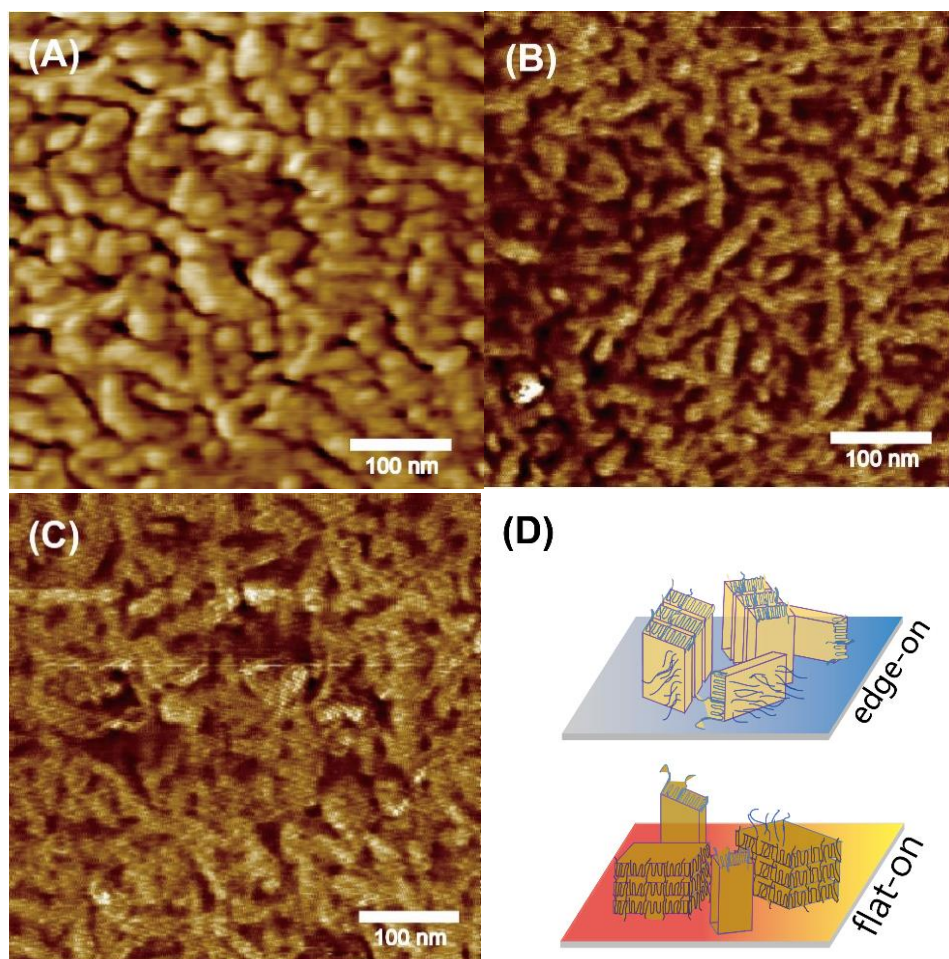


Figure II. 11 Surface topography (phase mode) of the AFM patterns for the isothermal crystallized P(VDF-TrFE-CTFE) terpolymer representatives of the pristine P(VDF-TrFE-CTFE) Film A (A), intermediate annealed Film E (B), fully crystallized Film I (C) and a schematic representation of flat-on and edge-on crystal lamellae orientation to the substrate (D).

attributed to the predominant edge-on crystal orientation in which molecular chain axis, namely *c*-axis, were preferentially in parallel to the supports. During the melt-recrystallization, the partial edge-on crystal orientation switched to the flat-on crystal lamellae. The less discernible surface

microstructure in Figure 11C suggested an amount of flat-on orientation crystal lamellae coexisted but not as dominant crystal lamellae, owing to the factor that the crystal grain could be still detected. At this point, more coarse and disordered surface microstructure observed in Figure II. 11A also implied that the pristine Film A consisted of both the flat-on and edge-on orientation crystal lamellae.

III. 3 Dielectric Permittivity and Breakdown Strength

III.3.1 Dielectric Behavior under a Low Electric Field

It is well documented that the crystal morphology and microstructure strongly depend upon its dielectric properties. The terpolymers with various annealing protocol were selected for dielectric property characterization regarding to the fraction of crystallinity. The dielectric properties of P(VDF-TrFE-CTFE) terpolymers under various annealed condition were investigated by using broadband dielectric spectroscopy (BDS). An overview of real part (ϵ') and dielectric loss $\tan \delta$ of complex permittivity temperature dependent for the representative Film G with 41.3 % degree of crystallinity were plotted in Figure II. 12a and b. The real permittivity spectra saw two distinct anomalies over the temperature range window which is in good accordance with our previous study [40]. And the values underwent slightly increase from ca. 5 at -70 °C to less than 10 at -30 °C and 0.1Hz. Then a weak anomaly appeared as the temperature proceeded. This less intense and diffuse behavior below 0 °C marked by black rectangle should be attributable to the glass transition. The structural (α) relaxation mode associated with glass transition temperature (T_g) of the representative Film G was unambiguously presented by the dielectric loss $\tan \delta$ spectra. The structural relaxation was identified as the relaxation peak at -25.7 °C and 0.1 Hz and showed a normal and rapid drift towards the high temperature with increasing frequency. This relaxation shift was also reflected upon the real part of permittivity as shown in Figure II. 12a. Recently, Yang [41] reported that the significant increase of real permittivity were observed when the temperature was above the glass transition temperature T_{g-PVDF} of BOPVDF films (-39 °C at 1 Hz). A remarkable increase of ϵ' near T_{g-PVDF} was ascribed to the polarization of the dipoles in amorphous phase, rather than in rigid crystal phase. As a result, the contribution of dipole polarization in crystal phase to the sum of polarization can be neglected. In fact, more than 55% amorphous interphase was found in order to further explain this phenomenon. The interphase with its molecular chain stemming from the crystal lamellae were composed of the head-to-head and tail-to-tail (HHTT) molecular stacks, forming more or less oriented crystallites. In this case, dipole polarization were enhanced when the amorphous phase was in super-cooled liquid region.

However these results were confined under the strict condition of a low electric field (0.0167V/ μ m). With the same measurement condition, considerable increment of ϵ' were

observed. For instance, ε' was found as ca. 5 at 0.1 Hz and -70°C far below the T_g whereas the value reached to ca. 26.6 at 15°C . The rest spectra for the selected frequency featured similarly, suggesting that comparative contribution originated from the amorphous phase in sum of the dipole polarization. As the temperature was elevated to around 30°C , ε' significantly surged at frequency below 100 kHz rather than in a moderate rate increase of ε' at 1 MHz frequency. For example, ε' was changed from 22.1 at 15°C to 52.2 at 43°C and 100 Hz. This several folds augmentation could be assigned to the dipole polarization in the crystal lamellae phase. Dipoles

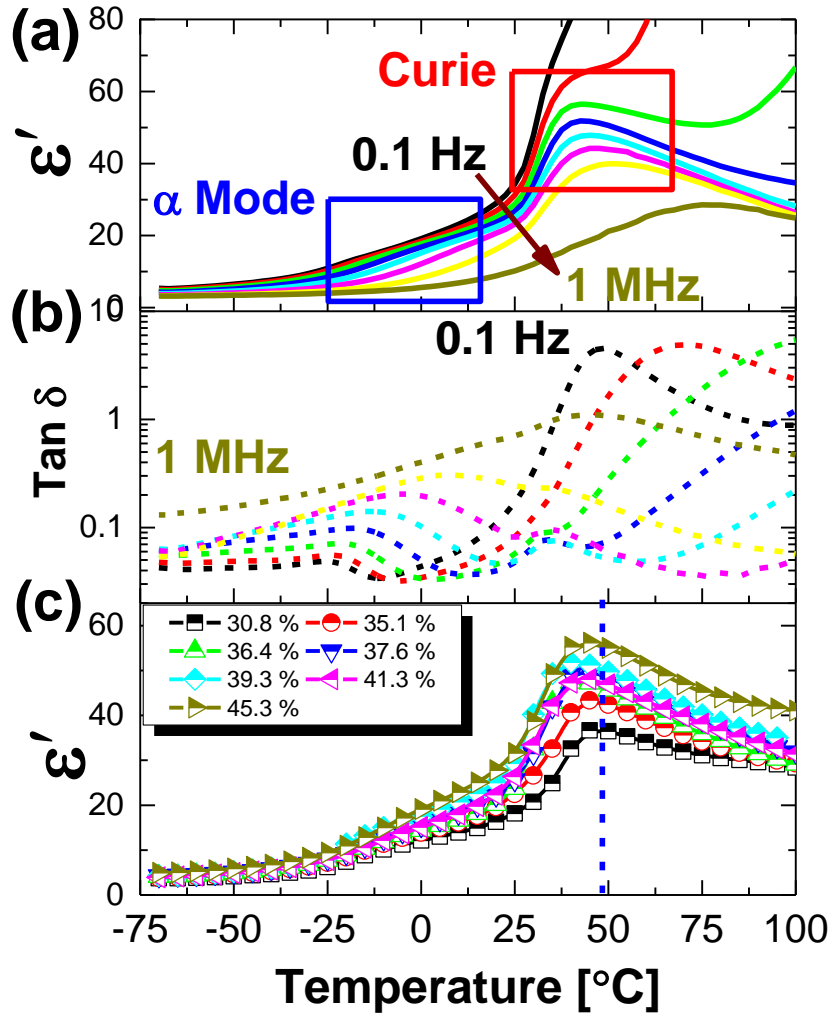


Figure II. 12 Isochronal real part (a) of permittivity (ε') and dielectric loss $\tan \delta$ (b) spectra at different temperature for the representative terpolymer with 41.3% crystal fraction. Temperature dependence of real permittivity ε' of annealed terpolymer containing various crystallinity fraction at given frequency of 100 Hz were also plotted (c). The rectangles in figure a marked the two phase transitions over temperature at various frequency, blue for glass transition and red for Curie transition.

switch in γ crystal form ($T_3G^+T_3G^-$) were activated owing to the elevated temperature, giving rise to the strong dipole polarization. The ferro-paraelectric peaks upon the temperature were highly frequency dependent, indicating a characteristic relaxor ferroelectric behavior. And the temperature dependence of ϵ' spectra for 0.1 Hz, 1 Hz and 10 Hz frequency showed the abnormal increase, comparable with ϵ' at frequency ≥ 100 Hz. Such result was most probably attributable to the DC conduction effects. Further evidence could be found by dielectric loss $\tan \delta$ spectra. The ferro-paraelectric transition peaks overlapped with DC conduction behavior for 0.1 Hz, 1 Hz and 10 Hz as temperature above 45 °C, showing a remarkable diffusion to the higher temperature. These transition peaks appeared at 34.4 °C at 100 Hz and 41.5 °C at 1 MHz. The two featured stepwise increase in dielectric permittivity behaviors implied that dipoles in crystalline and amorphous were both the contributing factors to the dipole polarization.

Figure II. 12c plotted the isochronal broadband dielectric permittivity ϵ' at 100 Hz against the selected films regarding the overall degree of crystallinity χ_c . At first glance, the ϵ' spectra featured the common trend as the representative Film G. At temperature far below the glass transition, ϵ' illustrated the identical values, whereas an enhanced intensity at higher temperature. It is interesting to note that an increasing peak amplitude against the fraction of crystallinity was observed over the whole dielectric spectroscopy, in particular in the glass transition region. Normally pending a typical crystallization process, crystal lamellae formed, accompanying with consumption of amorphous phase. This will lead to a fewer dipoles in amorphous phase, showing a decreasing dipole polarization. In our present case, the relatively high dielectric permittivity ϵ' near the glass transition region were found for the terpolymers containing the higher degree of crystallinity. In fact, the previous studies [45] reported dielectric strength $\Delta\epsilon$ demonstrated exceptionally enhanced behavior with increase of crystallinity fraction compared to the typical semi-crystalline polymers, such as poly(pentamethylene terephthalate) (PPT) [35], poly(L-lactic acid) (PLLA) [46, 47], and poly(ethylene terephthalate) (PET) [48, 49]. This is most possibly due to the enhanced interphase. The so-called interphase was amorphous in structure, although its molecular chain more or less orientated and constrained regarding the molecular mobility. Last but not least, AFM patterns in Figure II. 11 revealed that an edge-on crystal lamellae orientation was dominated for annealed terpolymer, which favored to the c-axis of oriented interphase perpendicular to the film normal direction. Taking this into account, more dipoles aligned to the applied external electric bias and the dipole polarization of the amorphous interphase were consequently enhanced.

High temperature also saw a distinct difference against the degree of crystallinity. The dielectric spectra in each case, linked to the Curie transition in crystal phase, peaked at around 46 °C for 100 Hz, then underwent a gradual decrease as temperature increasing. This was an ubiquitous behavior for the ferroelectric polymers because the molecular chain conformation

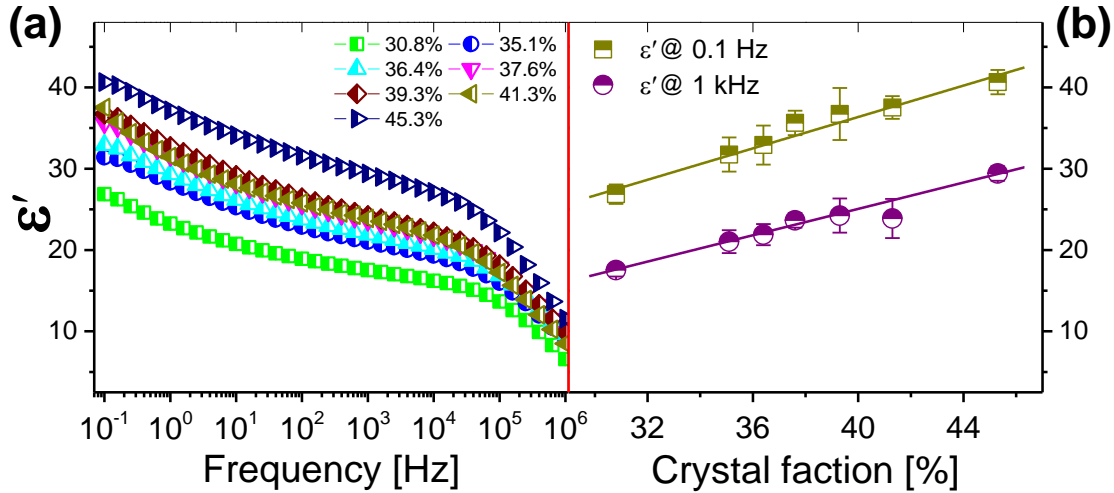


Figure II. 2 Dielectric permittivity of P(VDF-TrFE-CTFE) terpolymers under various annealing condition as function of logarithmic frequency (a) and real permittivity at selected frequency (0.1Hz and 1k Hz) against degree of crystallinity χ_c (b).

in ferroelectric crystal phase switched to the paraelectric phase, in accordance with the endothermic peaks of the DSC curves. The thermal induced paraelectric crystal phase showed the relatively lower dipole moment. Additionally, an increasing intensity of the dielectric peaks was enhanced with an increase in crystallinity fraction, suggesting the enhanced dipole orientation. The ϵ' peak value significantly increased from 36.7 to 56.7 for the pristine Film A and fully crystallized Film I, respectively. In previous section, AFM profiles illustrated the two typical crystal orientation, flat-on and edge-on crystal in annealed terpolymers. It has also been established the crystal orientation has an anisotropic influence on the dielectric behavior for the PVDF-based polymers [28]. For the sake of better investigation concerning crystal orientation, broadband dielectric permittivity against frequency at room temperature (25°C) was plotted in Figure II. 13a, showing typical frequency dependent. The ϵ' values gradually decreased until at 10^5 Hz, followed by an abrupt decline. This relaxation could be attributed to the glass transition region. Dielectric permittivity values at 0.1 Hz and 1 kHz for the annealed terpolymers were plotted against the fraction of crystallinity in Figure II. 13b. The ϵ' values increased in a quasi-linear relationship with increase in the overall crystallinity. It is also worth noticing that ϵ' values varied at 1 kHz mainly due to the dipole polarization, which was closely associated with crystal lamellae orientation in the annealed terpolymers. During the isothermal crystallization at higher temperature, the fraction of the edge-on orientation crystal lamellae was enhanced where the dipole moments were in parallel to the electric field, instead of the pristine Film A where the flat-on orientation crystal lamellae were dominant. Therefore, large dielectric permittivity ϵ' were obtained for the higher degree of crystal content in annealed terpolymer.

III.3.2 Breakdown Strength under High Electric Field

High dielectric polymeric material with high electric breakdown strength E_b was desired in application areas where a high electric field was applied, for instance, electric vehicle, medical device and high energy weapon system. In order to investigate the influence of annealing process on E_b values, the electric breakdown failure was performed at very high electric field. The 60 μm thickness of the specimens were normalized in order to eliminate the discrepancy of electric field distribution in the polymers. The 20 replicate breakdown manipulations ensured to fulfill the failure statistics, which could be described by a two-parameter exponential Weibull function as follows:

$$P(E) = 1 - \exp[-(E/\lambda)^k] \quad \text{II. 2}$$

Where $P(E)$ reads the breakdown probability of the P(VDF-TrFE-CTFE) as-cast films at DC electric breakdown strength E . λ is the scale parameter reflecting the electric breakdown strength E_b where 63.2% probability of the electric failure occurred; k is the slope parameter that evaluates the data scattering.

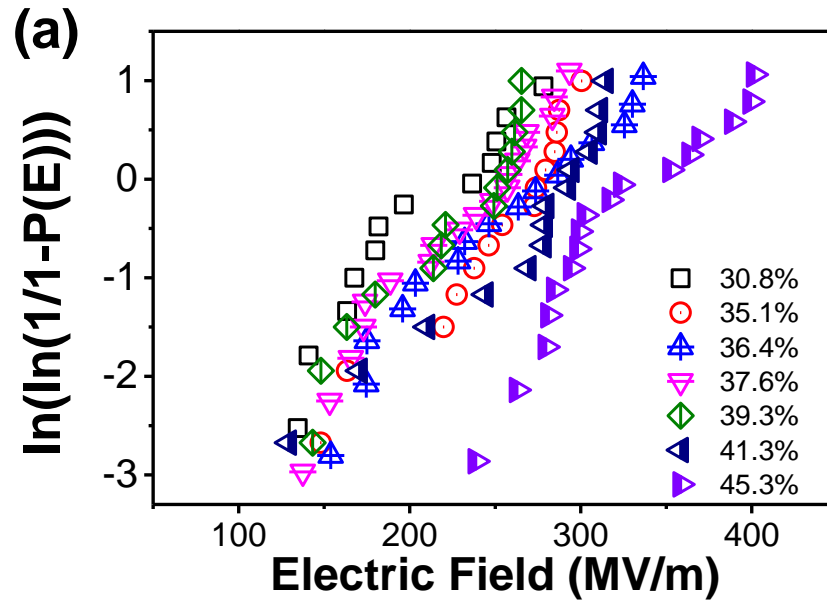
Weibull probability fitting for each annealed terpolymer films electric breakdown strength values were presented in Figure II. 14a. The E_b values for each terpolymer film at 63.2% probability breakdown and fitting parameters with estimated errors were summarized in Table II. 3. Obviously, E_b values significantly depended upon the degree of crystallinity for the terpolymer films. And the electric breakdown strength versus the fraction of crystallinity was depicted with the bar chart in Figure II. 14b. The E_b value was greatly elevated from 223.9 ± 17 MV/m for the pristine terpolymer to 340.4 ± 38 MV/m for fully crystallized Film I, indicating that polymer morphology and microstructure were the contributing factors. It has also been well recognized that the electric resistivity between the polymer chain was much larger than along them [50]. Thus processed terpolymers, consisting of the more well-ordered molecular chain stacks, favored the higher values of breakdown strength. Inversely, a terpolymer with more amorphous phase possessed the lower electric resistivity, resulting in a lower breakdown strength value. In addition, previous section revealed that the terpolymer constituted of the sandwich-like multiple phases, that is to say, the crystal, interphase and amorphous phase. Because of a large interfacial domain, one should not neglect the interfacial scattering effects to the accumulative charge carrier ions near the interphase. The charge carrier ions, introduced during the polymer synthesis strongly enhanced the conductivity of the annealed terpolymers [45]. However, the more or less oriented

interphase fraction increased during the crystallization process as revealed. And it is likely that the enhanced interphase retarded the ions transportation through the interphase and reduced the ions conduction in the annealed terpolymers.

Table II. 3 Electric breakdown values E_b , Weibull fitting parameters (k) and the average thickness of the measured films with estimate errors for the isothermally annealed terpolymers

Acronyms	Film A	Film C	Film D	Film J	Film F	Film G	Film I
Crystallinity (χ_c)	30.8	35.1	36.4	37.6	39.3	41.3	45.3
Thickness(μm)	66 ± 5^a	57 ± 4	59 ± 3	66 ± 4	65 ± 3	61 ± 3	58 ± 5
E_b (MV/m)	223.9 ± 17	271.1 ± 26	273.4 ± 23	249.7 ± 30	244.4 ± 21	291.3 ± 32	340.4 ± 18
Weibull (k)	3.6 ± 0.2^b	7.5 ± 0.5	4.2 ± 0.4	4.7 ± 0.2	6.5 ± 0.3	9.2 ± 0.4	5.8 ± 0.3

Note: a, the error bars were related to the standard deviation of the average values. b the propagation of error extrapolated from the Weibull fitting was used to determine the uncertainty of shape parameter k .



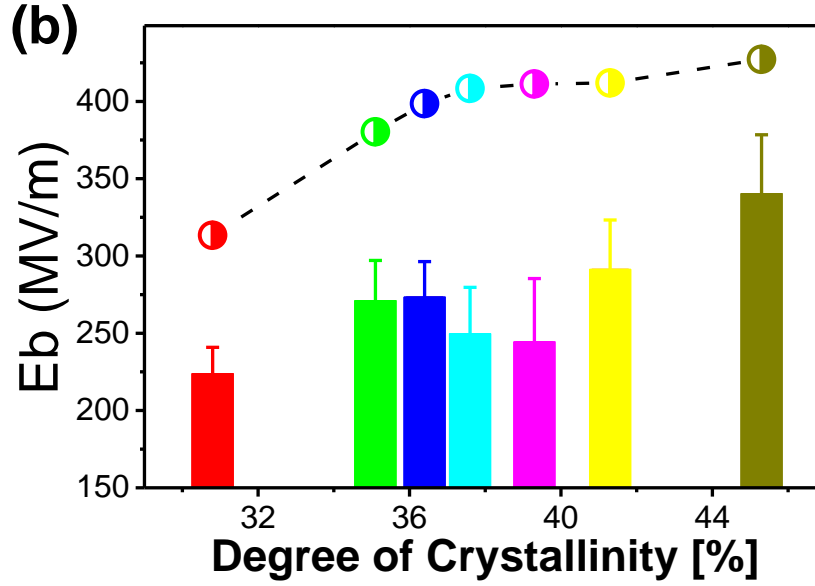


Figure II. 3 (a) Weibull distribution probability of the breakdown strength E_b for each annealed terpolymer film; (b) experimentally measured E_b as a function of degree of crystallinity in bar chart; half right circles were estimated electric breakdown strength values as a function of the degree of crystallinity.

In addition, it is reported that the fluorinated polymer was a non-linear dielectric polymer of which the electric displacement at high electric field changed irreversibly with the electric field rather than the linear dielectric polymer with its dielectric permittivity ϵ_r proportional to the electric displacement D upon electric field E which reads $\epsilon'_r = \frac{\partial D}{\epsilon_0 \partial E}$. The non-linear P(VDF-TrFE-CTFE) terpolymer, similar to the PVDF, showed a peak mode in its relative permittivity. For the insulating PVDF-based terpolymers, the Stark-Garton model has been employed to compensate the electromechanical breakdown strength which consists in the Young's modulus Y and dielectric permittivity ϵ'_r . When a sample subjected to the applied voltage V perpendicular to the terpolymer normal, its thickness d thins down, and the electric field increases. The relationship between electromechanical breakdown field and Young's modulus during deformation was expressed by $\frac{1}{2} \epsilon'_r \epsilon_0 \left(\frac{V}{d}\right)^2 = Y \ln \frac{d_0}{d}$, where ϵ_0 is the permittivity in vacuum, Y is Young's modulus, d is the real-time thickness during the manipulation and d_0 is the initial thickness of terpolymer sheet [51]. For simplicity, Stark-Garton electromechanical model could be written as follows:

$$E_b = 0.6 \left(\frac{Y}{\epsilon_0 \epsilon'_r} \right)^{\frac{1}{2}} \quad \text{II. 3}$$

where ϵ'_r is the dielectric permittivity of the polymers at the breakdown electric field [52]. The estimation of electric breakdown strength against degree of crystallinity were also plotted in

Figure II. 14b (ϵ'_r , Y values see Table II. 3). It should be noted that the Stark–Garton model overestimated the electric breakdown strength. This was commonly observed for PET [53], PP [54], PVDF-based polymers such as P(VDF-HFP) and polymer blends thereof [52, 55]. These higher modeling values were due to the assumption of the linear strain-stress behavior during field-induced dimensional change. Its plasticity was neglected near the occurrence of electric breakdown failure. Many polymeric materials would not follow the linear strain-stress correlation. Therefore, one should consider elastic-plastic deformation of the semi-crystalline polymer during the breakdown failure because of the physical viscoelasticity in nature. Taking consideration of the elastic-plastic behavior of the polymers, Zhou [55] developed a new model to estimate the breakdown strength, $E_b = \sqrt{\frac{2K}{\epsilon'_r \epsilon_0}} \left(\frac{N}{2}\right)^{\frac{N}{2}} \exp\left(-\frac{N}{2}\right)$. Here N is dimensionless within the range of 0.1 to 0.6, K parameter varies with yield strength where the values equals to Young's modulus as N coefficient is 1. Consequently, the estimated breakdown strength according to the new compensation law were in excellent consistent with the measured E_b values.

III. 4 Electromechanical Properties

III.4.1 Mechanical Behaviors

A large modulus of elasticity was associated with a high breakdown strength while a low Young's modulus would also determine the field-induced electrostrictive response. In our previous study [23, 56], a several-folds increase in field-induced electrostrictive behavior of the PVDF-based terpolymer was handled to obtain by adding the DEHP molecules into terpolymer matrix, owing to a significant decrease in the mechanical strength of the terpolymer blends. The strain-stress curves of various annealed terpolymer films were obtained by a non-conventional tensile strength equipment (see Figure II. 3 in experimental section). A maximal 1% elongation rate was subjected to the tensile strength test before reaching to the yield point. In order to have a good consistency with the evaluation of electrostrictive response during the forth-coming manipulation, 0.1 Hz sinusoidal stimulus signal was applied to the precisely controlled unidirectional motor. The representative mechanical strain-stress curves of the annealed terpolymers were plotted in Figure II. 15a. The Young's modulus values were extrapolated from the slope of the linear fit to the mechanical strain-stress curves. Figure II. 15b then plotted the Young's modulus as a function of degree of crystallinity. Before reaching the saturation of overall crystallinity, monotonic increase in Young's modulus (Y) against the degree of crystallinity (χ_c) were observed from 64.9 MPa for pristine to 182.5 MPa for fully crystallized one. The relationship between Y values and χ_c followed a sigmoidal growth compensation law which has also been reported for many polymers [57]. A decrease in Y values for the plasticizer doped terpolmer blends was explained by enhancement of molecular chain mobility. These results were caused by an expansion of molecular chain and free volume for molecular movement

[58]. Inversely in our case during the isothermal annealing process, the rigid crystal phase and interphase were enhanced, accompanying with a thermodynamic equilibrium due to the molecular chain relaxing. Meanwhile, molecular chain in amorphous phase was also densified. This caused a confined free volume in semicrystalline terpolymer [49, 59, 60]. Young's modulus dependent upon the sum of degree of crystal and interphase were eventually established.

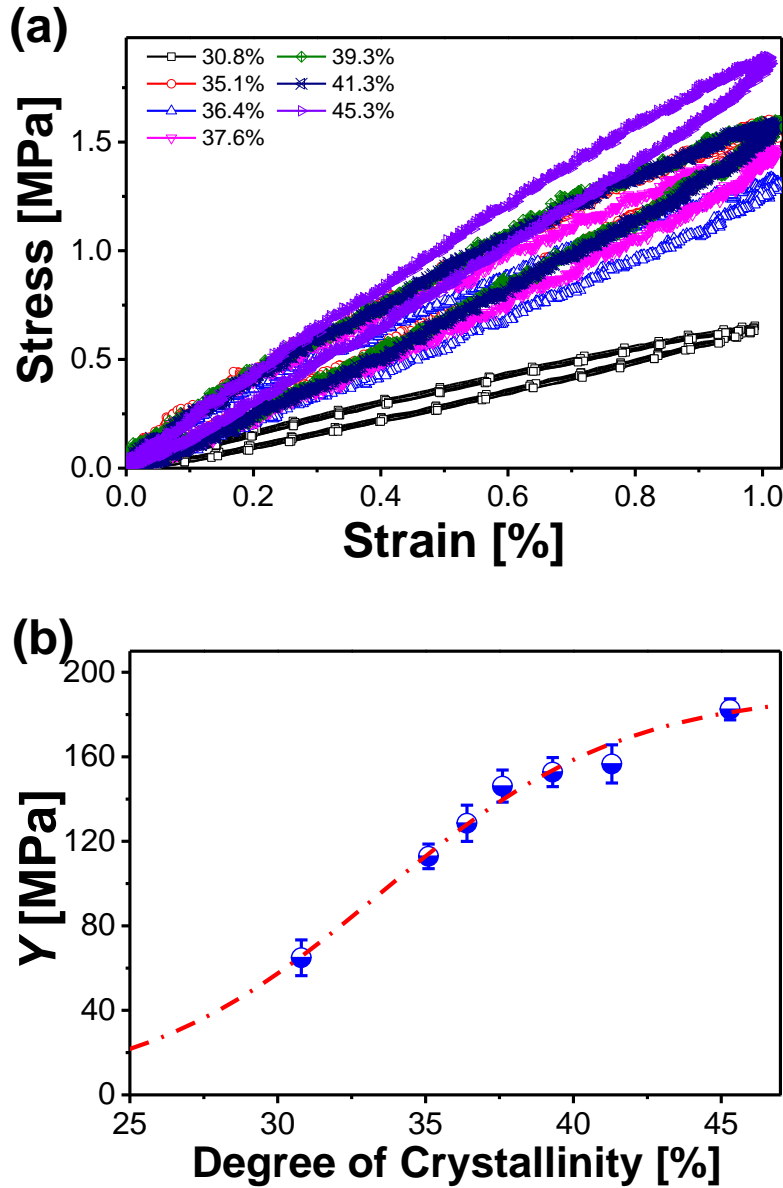


Figure II. 4 Mechanical behavior of annealed P(VDF-TrFE-CTFE) terpolymers: strain-stress curves in a sinusoidal functional mode (a), degree of crystallinity dependence of Young's modulus for the annealed films (b). The dash line was the sigmoidal growth fitting to the Y values.

III.4.2 Electromechanical Behaviors

Electromechanical properties for various annealed terpolymer were performed according to electrostrictive behavior. In order to realize a sufficient field-induced strain, the thickness of the

terpolymer membrane must be in the range of a few microns under high tension of voltage supply. Under a limited voltage supply, electrostrictive strain of the electroactive membranes were exaggerated via bending test based on a unimorph cantilever beam theory. The field-induced strain in in-plane mode propagates through the passive PET foil, resulting in a deflection response of the bilaminar beam. Normalized sample shape, dimension and assembling structure of unimorph beams were schemed in experimental section (recall Figure II. 3). Then beam samples were clamped and mounted to an aluminum sample holder. Afterwards, a full cycle electric field of sinusoidal signal up to maximal 25 MV/m was applied to the cantilever bilaminar beam in a frequency of 0.1 Hz. The vertical displacement δ of the sample tip (beam curvature was negligible because the displacement was limited within 3 mm) were collected by a laser via Labview data acquisition software package. Then the transverse strain S_{31} along the beam direction were extrapolated via Eq. (2). Both values were quadratic function of increase in electric field as plotted in Figure II. 16. It is interesting to investigate the origins since each response curve against electric field quite well following the quadratic relationship. The δ and transverse strain at given electric field 20 MV m⁻¹ as a function of crystal content were schemed in the bar chart Figure II. 17. The tip displacement values exhibited a distinct saddle shape, maximized at 2.89 mm for the mediate Film E with crystal content of 37.6%. In a molecular level, the external high electric filed (e.g. 10 MV/m) induced a reversible molecular chain conformation from TG^+TG^- and $T_3G^+T_3G^-$ (less-ordered ferroelectric phase) to the all-*Trans* (well-ordered ferroelectric phase) chain conformation, resulting in the electrostrictive deformation macroscopically [60]. This rationalized that the electrostrictive capability was reliably contingent upon the dielectric behaviors of the annealed terpolymers.

Previous reports described that for a dielectric polymeric material, the intrinsic electrostrictive effect dominated the electrostriction effects, which can be simplified as Eq. (5) [61, 62]:

$$S_{3i} = S_E + S_M \approx Q \cdot \varepsilon_0^2 \cdot (\varepsilon' - 1)^2 \cdot E^2 = M_{3i} \cdot E^2 \quad (5)$$

where S_M is the mechanical strain due to the electrostatic strain also known as Maxwell effect; S_E is the intrinsic electrostriction originating from the dipolar interaction; Q and M_{3i} are the intrinsic and global electrostrictive coefficient, respectively. Q was caused by the electrical field-induced polarization in the material matrix, of which the value is proportional to $\frac{1}{\varepsilon_0 \varepsilon'} \frac{1}{Y}$. Thus, M_{3i} can be rewritten as $M_{3i} = k \frac{\varepsilon_0 \cdot (\varepsilon' - 1)^2}{\varepsilon' \cdot Y}$, where k is a constant. Following the equation 5, the figure of merits of the global electrostrictive coefficient were dielectric constant ε' and Young' modulus. For the dielectric terpolymer with its $\varepsilon' \gg 1$, the transverse strain S_{3i} was qualitatively

simplified to be proportional to the ε'/Y . The predicted values of ε'/Y as a function of degree of crystallinity were plotted in Figure II. 18 and followed an exponentially decayed fitting trend.

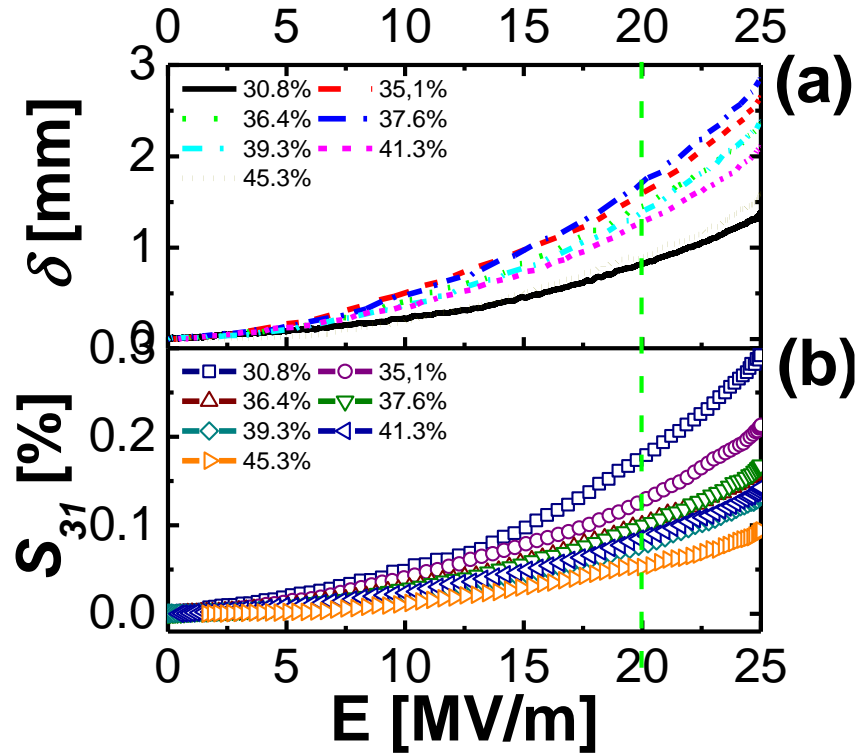


Figure II. 5 Tip displacement (a) and transverse stain (b) curves versus electric field for selected temperature annealing terpolymers; vertical (dash) line marks the electric field of 20 MV/m.

The measured transverse strain values against crystal content was highly agreeing with the estimated decreasing trend as presented in Figure II. 17b. Intriguingly, pristine film featured the largest electrostrictive strain amongst, more than 4 folds larger over the fully crystallized Film I performing the lowest electrostrictive strain of 0.059% at given 20 MV/m electric field. It should be noted that the Young's modulus value for Film I was remarkably increased by 3 times higher than that of pristine film whereas the contributing dielectric constant factor expanded by only 50% from 26.9 to 40.6. The bilaminar beams responded a much lower transverse strain as expected. The tip displacement values were reliably determined by the beam configuration, in current case of bilaminar structure according to the Eq (2). This is reflected by the maximal value behavior vs. crystal content in terpolymers undergoing the temperature annealing process in the Figure II. 17a, in which the tip displacement maximized for the terpolymer Film E with 37.6% crystal content. The Film E with transverse strain of 0.097% was twice higher than the deeply processed Film I due to a relatively lower Young's modulus. The $\frac{3L^2}{2t} \frac{2\lambda\xi(1+\xi)^2}{\lambda^2\xi^4+2\lambda\xi(2+3\xi+2\xi^2)+1}$ cluster term, reliably depends on the tunable Young's modulus ratio of electroactive polymer to the passive PET foil, being due to the terpolymer processing currently. A considerably remained tensile strain

induced by field for Film E intended to yield a large deflection of bilaminar beam in case of that the Young's modulus was satisfactorily high enough.

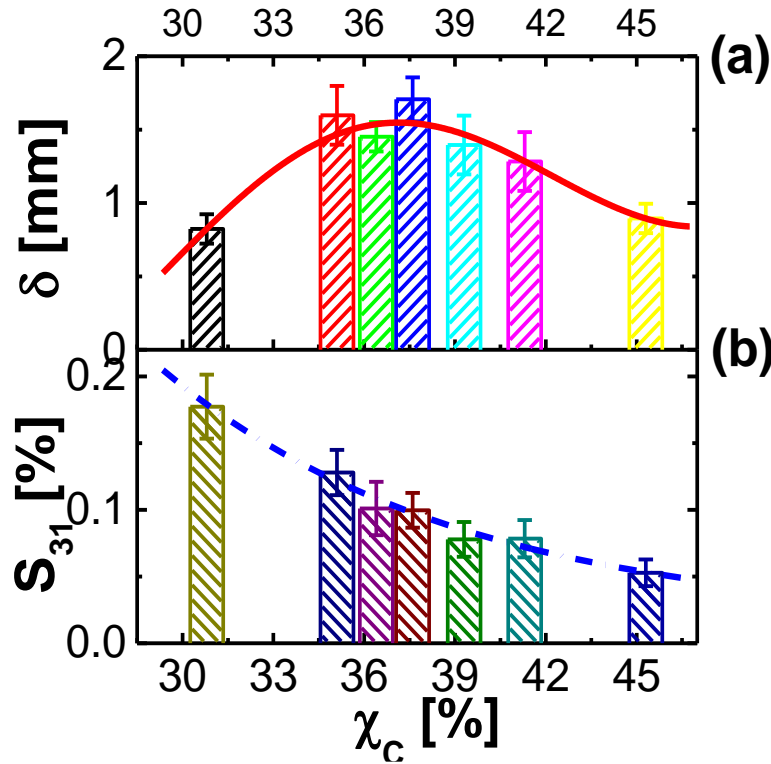


Figure II. 6 Electromechanical response obtained by cantilever beam unimorph, (a) tip displacement and (b) transverse strain bar charts upon the 20 MV/m electric field as a function of degree of crystallinity of each annealed polymer unimorph. Red solid line is the peak fit to the saddle shape distribution of the δ values and dash dot line is the exponential decay fit to the transverse strain values.

Given the reliability of dielectric permittivity and mechanical strength, it was convincing that terpolymer with a largest degree of crystallinity was not envisaged to the largest transverse deformation. The resulting transverse strain S_{31} was a trade-off between dielectric properties and mechanical tensile strength of the terpolymer upon the thermal processing. From an applicable point of view where tip displacement acted as an indicator, the performance of bilaminar cantilever beam, one of the applicable system structure, should be evaluated by seriously taking the passive support into account. Large transverse strain terpolymer membrane, possessing a very low tensile strength imparted a weak bending force to the bilaminar beam device, causing a small tip displacement. This resulting bending behavior was also shared by the deeply thermal treated terpolymer, it was although due to the insignificant electrostrictive elongation strain along the cantilever beams.

The decreasing apparent electrostrictive coefficient M_{31} values were displayed in Table II. 4 which expectedly followed the exponential decay decrease (not show here), rising from $M_{31} \sim \frac{\epsilon'}{Y}$. Thus in order to yield an outstanding electrostrictive behavior, relative dielectric constant ϵ' and elastic Young's modulus ratio should be seriously considered by properly engineering terpolymer. Previously, the conductive carbon materials were employed as fillers so as to enhance dielectric

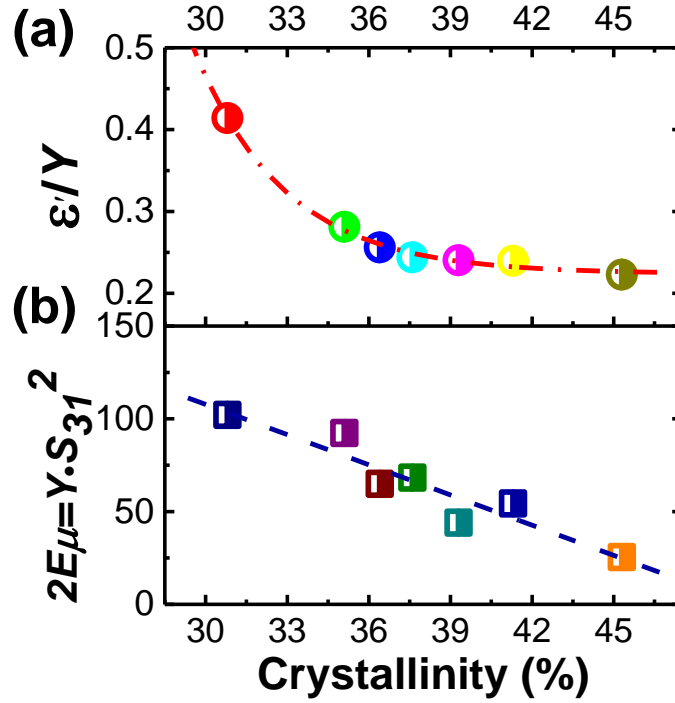


Figure II. 7 (a) ϵ'/Y , simplified electrostrictive coefficient parameter plotted against degree of crystallinity; (b) free elastic electric energy density over the degree of crystallinity.

properties on the expense of the enhanced mechanical strength simultaneously before reaching its percolation threshold [17]. To overcome the embarrassed case, plasticizer additive was helpful to tune the electromechanical behavior by greatly enhancing its dielectric constant and moderately decreasing the elastic Young's modulus [23], which is capable of leading us towards the high electromechanical response of a polymeric matrix. The transverse strain in response to the higher frequency of applied electric field compressed because of a decrease of the electrostrictive coefficient with increasing frequency (not shown), which mainly triggered by the slumping response in its dielectric constant ϵ' and rising Young's modulus, being in excellent agreement with our previous report [63].

Besides, in an attempt to fully picture the relation between the microstructure and electromechanical behavior, elastic free mechanical energy density E_μ were calculated in Table II. 4 according to $E_\mu = YS_{31}^2/2$ and also plotted against the crystal fraction in Figure II. 18b.

Surprisingly, it was found that the E_μ values over degree of crystallinity followed a quasi-linear decreasing correlation. The pristine terpolymer film exhibited the highest E_μ output of 102.1 J m^{-3} amongst due to its largest field-induced transverse strain. In contrary, the fully crystallized terpolymer with a high Young's modulus and dielectric constant afforded a lowest elastic mechanical energy density of 25.45 J m^{-3} . Thus, the high dielectric and mechanical behavior did not lead to the large mechanical energy output in case of current terpolymers tested. The E_μ results presented here consisted with high electrostrictive behavior, concerning the design concept of terpolymer actuators which were strongly determined by both two contributing factors---- ϵ' and Y . As-stated, electroactive polymers should be properly engineered to obtain the best application performance. Through analyzing the P(VDF-TrFE-CTFE) films electromachanical behavior and free mechanical energy upon the electric field via bilaminar cantilever bending beam, the mechanical energy density and bending displacement profiles were expected to allow a guide to the demanding sensor or actuator system realized via the terpolymer materials.

Table II. 4 Data collections of the transverse strain (S_{31}), Young's modulus (Y), free mechanical energy density (E_μ), fitted global electrostrictive coefficient (M_{31}) for each temperature treated terpolymer membrane.

Processed Polymers	χ_c (%)	δ (mm)	$S_{31}[\%]$ at 20 MV/m	Y (MPa)	E_μ J m^{-3}	$^a M_{31} \cdot E - 18$ ($\text{m}^2 \text{V}^{-2}$) ^a	ϵ' (0.1 Hz)
Film A SC NON	30.8	1.38	0.177	64.90	102.1	4.55	26.9
Film C 70C12H	35.1	2.68	0.128	112.9	92.34	3.36	31.7
Film D 80C2H	36.4	2.36	0.101	128.6	64.92	2.57	32.9
Film E 90C1H	37.6	2.89	0.097	146.1	68.32	2.53	35.6
Film F 90C2H	39.3	2.41	0.076	152.8	44.01	1.94	36.7
Film G 110C2H	41.3	2.12	0.083	156.6	54.35	1.98	37.5
Film I 120C12H	45.3	1.60	0.053	182.5	25.45	1.34	40.6

Note: vacuum permittivity, $\epsilon_0 = 8.854187 \times 10^{-12} \text{ F m}^{-1}$; a, apparent electrostrictive coefficient extrapolated from the quadratic fitting curves.

IV Conclusions

The purpose of the current study is to provide as much as information on the electromechanical properties of relaxor ferroelectric P(VDF-TrFE-CTFE) terpolymers. Its behaviors, strongly depending upon the morphological microstructure, were systematically investigated in terms of thermal behavior, dielectric property, electric breakdown strength and field-induced electrostrictive response. Firstly in DSC thermograms, two stepwise variation were observed in both Curie transition and melting regions for isochronally processed terpolymers against annealing temperature variable for 2h. Equivalently annealing temperature T_α below the Curie transition T_c , that is, pristine terpolymer, increased its T_c and thus ferroelectric crystal phase

while the decreases in T_c and Curie transition enthalpy were observed for the terpolymer annealed in hexagonal phase ($T_c < 80\text{ °C} \leq T_a$) This was strongly attributed to the reduced δ ferroelectric phase involved in crystal lamellae caused by the thermal treatment. No distinct variation were observed for the terpolymers annealed at temperature above 80°C due to the thermodynamic equilibrium. The crystallinity fraction increased monotonically upon the increase in annealing temperature. It is not the case for the melting temperature for corresponding terpolymers characterizing in an inverse fashion where saw a two stepwise decrease with the cross point at 90 °C. Annealing above 90 °C caused the loose crystal stacks thickening and reduction of the distribution of crystal size. This was reflected by a remarkably decreasing FWHM values from ca. 15 °C to around 8 °C. The coarse and loose bumpy-like topographic profile for the pristine also manifested the inhomogeneous microstructure and flat-on dominant crystal orientation. The regular needle-like nanocrystallites and distinct interfacial boundary suggested the existence of edge-on crystal orientation lamellae in intermediate and full terpolymers induced by isothermal crystallization.

Two dielectric anomalies as a function of temperature were strongly associated with two typical transitions where the peak at low temperature was ascribed to the glass transition in amorphous phase while the higher should be attributed to the Curie transition in crystal lamellae. Both regimes gave the contribution to the dielectric behavior at room temperature. An increase intensity of dielectric peak located at glass transition region was strongly due to the enrichment of the amorphous interphase where the molecular chain conformation was more or less oriented. This assumed to be one of the reason that the electric breakdown strength E_b of terpolymer with high crystal fraction were enhanced.

The finding disclosed for the electromechanical behavior shows that terpolymer with a largest degree of crystallinity was not envisaged to the largest transverse deformation. Pristine terpolymer beam gave the largest field-induced strain output and elastic mechanical energy density whilst out-performed tip displacement maximized for terpolymer beam having median crystal fraction. From material engineering point of view, the prominent transverse strain was a trade-off between dielectric properties and mechanical tensile strength of the terpolymer. On the other hand from an implementation point of view, structure of actuator devices should be carefully considered, along with terpolymer microstructure.

References

1. Xia, F., et al., *High electromechanical responses in a poly (vinylidene fluoride–trifluoroethylene–chlorofluoroethylene) terpolymer*. *Advanced Materials*, 2002. **14**(21): p. 1574-1577.
2. Zhang, Q., V. Bharti, and X. Zhao, *Giant electrostriction and relaxor ferroelectric behavior in electron-irradiated poly (vinylidene fluoride-trifluoroethylene) copolymer*. *Science*, 1998. **280**(5372): p. 2101-2104.
3. Park, C., et al., *Actuating single wall carbon nanotube-polymer composites: intrinsic unimorphs*. *ADVANCED MATERIALS-DEERFIELD BEACH THEN WEINHEIM-*, 2008. **20**(11): p. 2074.
4. Hamciuc, E., et al., *Phthalonitrile - containing poly (amide imide) s with nanoactuation properties*. *Polymer Engineering & Science*, 2013. **53**(2): p. 334-342.
5. Kim, B., et al., *Electric actuation of nanostructured thermoplastic elastomer gels with ultralarge electrostriction coefficients*. *Advanced Functional Materials*, 2011. **21**(17): p. 3242-3249.
6. Jomaa, M., et al., *Modeling of segmented pure polyurethane electrostriction behaviors based on their nanostructural properties*. *Polymer*, 2015. **62**: p. 139-147.
7. Martins, P., A. Lopes, and S. Lanceros-Mendez, *Electroactive phases of poly (vinylidene fluoride): Determination, processing and applications*. *Progress in polymer science*, 2014. **39**(4): p. 683-706.
8. Song, Y., et al., *Enhanced dielectric and ferroelectric properties induced by dopamine-modified BaTiO₃ nanofibers in flexible poly (vinylidene fluoride-trifluoroethylene) nanocomposites*. *Journal of Materials Chemistry*, 2012. **22**(16): p. 8063-8068.
9. Cheng, Z.-Y., et al., *Electrostrictive poly (vinylidene fluoride-trifluoroethylene) copolymers*. *Sensors and Actuators A: Physical*, 2001. **90**(1): p. 138-147.
10. Frecker, M.I. and W.M. Aguilera, *Analytical modeling of a segmented unimorph actuator using electrostrictive P (VDF-TrFE) copolymer* Presented in part at the *ASME Design Engineering Technical Conferences, Symposium on Mechanisms and Devices for Medical Applications, Pittsburgh, PA, September, 2001 and at the SPIE 8th International Symposium on Smart Structures and Materials, Newport Beach, CA, March, 2001*. *Smart materials and structures*, 2003. **13**(1): p. 82.
11. Li, Z.-M., M.D. Arbatti, and Z.-Y. Cheng, *Recrystallization study of high-energy electron-irradiated P (VDF-TrFE) 65/35 copolymer*. *Macromolecules*, 2004. **37**(1): p. 79-85.
12. Ang, C. and Z. Yu, *“Dielectric relaxor” behavior of electroactive fluorinated polymers*. *Applied Physics Letters*, 2005. **86**(26): p. 262903.

13. Ang, C. and Z. Yu, *Ferroelectric, Electroactive, and Dielectric - Relaxation Behavior of Fluoropolymers*. Advanced Materials, 2004. **16**(12): p. 979-982.
14. Carpi, F., et al., *Dielectric elastomers as electromechanical transducers: Fundamentals, materials, devices, models and applications of an emerging electroactive polymer technology*. 2011: Elsevier.
15. Liu, S., et al., *High Electromechanical Response of Ionic Polymer Actuators with Controlled - Morphology Aligned Carbon Nanotube/Nafion Nanocomposite Electrodes*. Advanced functional materials, 2010. **20**(19): p. 3266-3271.
16. Zhang, Q., et al., *An all-organic composite actuator material with a high dielectric constant*. Nature, 2002. **419**(6904): p. 284-287.
17. Yin, X., J.-F. Capsal, and D. Guyomar, *A comprehensive investigation of poly (vinylidene fluoride-trifluoroethylene-chlorofluoroethylene) terpolymer nanocomposites with carbon black for electrostrictive applications*. Applied Physics Letters, 2014. **104**(5): p. 052913.
18. Wang, H., et al., *Highly Stable Carbon Nanotube Top - Gate Transistors with Tunable Threshold Voltage*. Advanced Materials, 2014. **26**(26): p. 4588-4593.
19. Zhang, S., et al., *Microstructure and electromechanical properties of carbon nanotube/poly (vinylidene fluoride—trifluoroethylene—chlorofluoroethylene) composites*. Advanced Materials, 2005. **17**(15): p. 1897-1901.
20. Bae, S.-H., et al., *Graphene-P (VDF-TrFE) multilayer film for flexible applications*. ACS nano, 2013. **7**(4): p. 3130-3138.
21. Huang, C. and Q. Zhang, *Enhanced Dielectric and Electromechanical Responses in High Dielectric Constant All - Polymer Percolative Composites*. Advanced Functional Materials, 2004. **14**(5): p. 501-506.
22. Li, J.Y., C. Huang, and Q. Zhang, *Enhanced electromechanical properties in all-polymer percolative composites*. Applied physics letters, 2004. **84**(16): p. 3124-3126.
23. Capsal, J.-F., et al., *Plasticized relaxor ferroelectric terpolymer: Toward giant electrostriction, high mechanical energy and low electric field actuators*. Sensors and Actuators A: Physical, 2014. **207**: p. 25-31.
24. Le, M.Q., et al., *All-organic electrostrictive polymer composites with low driving electrical voltages for micro-fluidic pump applications*. Scientific reports, 2015. **5**.
25. Park, Y.J., et al., *Irreversible extinction of ferroelectric polarization in P (VDF-TrFE) thin films upon melting and recrystallization*. Applied physics letters, 2006. **88**(24): p. 242908.
26. Oliveira, F., et al., *Process influences on the structure, piezoelectric, and gas - barrier properties of PVDF - TrFE copolymer*. Journal of Polymer Science Part B: Polymer Physics, 2014. **52**(7): p. 496-506.

27. Klein, R.J., J. Runt, and Q. Zhang, *Influence of Crystallization Conditions on the Microstructure and Electromechanical Properties of Poly (vinylidene fluoride-trifluoroethylene-chlorofluoroethylene) Terpolymers*. *Macromolecules*, 2003. **36**(19): p. 7220-7226.
28. Guan, F., et al., *Crystal orientation effect on electric energy storage in poly (vinylidene fluoride-co-hexafluoropropylene) copolymers*. *Macromolecules*, 2009. **43**(1): p. 384-392.
29. Zhu, L. and Q. Wang, *Novel ferroelectric polymers for high energy density and low loss dielectrics*. *Macromolecules*, 2012. **45**(7): p. 2937-2954.
30. Xu, H., et al., *Ferroelectric and electromechanical properties of poly (vinylidene-fluoride-trifluoroethylene-chlorotrifluoroethylene) terpolymer*. *Applied Physics Letters*, 2001. **78**(16): p. 2360-2362.
31. Kim, K.J., et al., *Curie transition, ferroelectric crystal structure, and ferroelectricity of a VDF/TrFE (75/25) copolymer 1. The effect of the consecutive annealing in the ferroelectric state on curie transition and ferroelectric crystal structure*. *Journal of Polymer Science Part B: Polymer Physics*, 1994. **32**(15): p. 2435-2444.
32. Barique, M. and H. Ohgashi, *Annealing effects on the Curie transition temperature and melting temperature of poly (vinylidene fluoride/trifluoroethylene) single crystalline films*. *Polymer*, 2001. **42**(11): p. 4981-4987.
33. Tanaka, R., K. Tashiro, and M. Kobayashi, *Annealing effect on the ferroelectric phase transition behavior and domain structure of vinylidene fluoride (VDF)-trifluoroethylene copolymers: a comparison between uniaxially oriented VDF 73 and 65% copolymers*. *Polymer*, 1999. **40**(13): p. 3855-3865.
34. Mano, J.F., et al., *Cold crystallization of PLLA studied by simultaneous SAXS and WAXS*. *Macromolecular Materials and Engineering*, 2004. **289**(10): p. 910-915.
35. Soccio, M., et al., *Relaxation dynamics and cold crystallization of poly (pentamethylene terephthalate) as revealed by dielectric spectroscopy*. *Polymer*, 2014. **55**(6): p. 1552-1559.
36. Sanz, A., et al., *Cold crystallization of poly (trimethylene terephthalate) as revealed by simultaneous WAXS, SAXS, and dielectric spectroscopy*. *Macromolecules*, 2009. **43**(2): p. 671-679.
37. Shin, Y.J., et al., *Chemically cross-linked thin poly (vinylidene fluoride-co-trifluoroethylene) films for nonvolatile ferroelectric polymer memory*. *ACS applied materials & interfaces*, 2011. **3**(2): p. 582-589.
38. Yang, L., et al., *Novel polymer ferroelectric behavior via crystal isomorphism and the nanoconfinement effect*. *Polymer*, 2013. **54**(7): p. 1709-1728.

39. Bae, I., et al., *Laser-Induced Nondestructive Patterning of a Thin Ferroelectric Polymer Film with Controlled Crystals using Ge₈Sb₂Te₁₁ Alloy Layer for Nonvolatile Memory*. ACS applied materials & interfaces, 2014. **6**(17): p. 15171-15178.
40. Capsal, J.-F., E. Dantras, and C. Lacabanne, *Molecular mobility interpretation of the dielectric relaxor behavior in fluorinated copolymers and terpolymers*. Journal of Non-Crystalline Solids, 2013. **363**: p. 20-25.
41. Yang, L., et al., *Semicrystalline Structure–Dielectric Property Relationship and Electrical Conduction in a Biaxially Oriented Poly (vinylidene fluoride) Film under High Electric Fields and High Temperatures*. ACS applied materials & interfaces, 2015. **7**(36): p. 19894-19905.
42. Urayama, K., M. Tsuji, and D. Neher, *Layer-thinning effects on ferroelectricity and the ferroelectric-to-paraelectric phase transition of vinylidene fluoride-trifluoroethylene copolymer layers*. Macromolecules, 2000. **33**(22): p. 8269-8279.
43. Ducharme, S., et al., *Critical point in ferroelectric Langmuir-Blodgett polymer films*. Physical Review B, 1998. **57**(1): p. 25.
44. Reece, T.J., et al., *Nonvolatile memory element based on a ferroelectric polymer Langmuir–Blodgett film*. Applied Physics Letters, 2003. **82**(1): p. 142-144.
45. LIU, Q., *Influence of Crystallization on Molecular Mobility and Ionic DC Conductivity Behaviors of Relaxor Ferroelectric P(VDF-TrFE-CTFE) Terpolymer*. Journal of Polymer Science Part B: Polymer Physics, 2016.
46. Bras, A., et al., *Influence of crystallinity in molecular motions of poly (L-lactic acid) investigated by dielectric relaxation spectroscopy*. Macromolecules, 2008. **41**(17): p. 6419-6430.
47. Brás, A.R., et al., *Crystallization of poly (L-lactic acid) probed with dielectric relaxation spectroscopy*. Macromolecules, 2006. **39**(19): p. 6513-6520.
48. Arnoult, M., E. Dargent, and J. Mano, *Mobile amorphous phase fragility in semi-crystalline polymers: Comparison of PET and PLLA*. Polymer, 2007. **48**(4): p. 1012-1019.
49. Álvarez, C., et al., *Structure-dynamics relationship in crystallizing poly (ethylene terephthalate) as revealed by time-resolved X-ray and dielectric methods*. Polymer, 2004. **45**(11): p. 3953-3959.
50. Chu, B., et al., *A dielectric polymer with high electric energy density and fast discharge speed*. Science, 2006. **313**(5785): p. 334-336.
51. Stark, K.H. and C.G. Garton, *Electric Strength of Irradiated Polythene*. Nature, 1955. **176**(4495): p. 1225-1226.

52. Rahimabady, M., et al., *Intermolecular interactions and high dielectric energy storage density in poly (vinylidene fluoride-hexafluoropropylene)/poly (vinylidene fluoride) blend thin films*. Applied Physics Letters, 2012. **100**(25): p. 252907.
53. Zebouchi, N. and D. Malec, *Combination of thermal and electromechanical breakdown mechanisms to analyze the dielectric breakdown in polyethylene terephthalate*. Journal of applied physics, 1998. **83**(11): p. 6190-6192.
54. Nash, J.L., *Biaxially oriented polypropylene film in power capacitors*. Polymer Engineering & Science, 1988. **28**(13): p. 862-870.
55. Zhou, X., et al., *Electrical breakdown and ultrahigh electrical energy density in poly (vinylidene fluoride-hexafluoropropylene) copolymer*. Applied physics letters, 2009. **94**(16): p. 162901.
56. Capsal, J.F., et al., *Enhanced electrostriction based on plasticized relaxor ferroelectric P (VDF - TrFE - CFE/CTFE) blends*. Journal of Polymer Science Part B: Polymer Physics, 2015. **53**(19): p. 1368-1379.
57. Humbert, S., et al., *A re-examination of the elastic modulus dependence on crystallinity in semi-crystalline polymers*. Polymer, 2011. **52**(21): p. 4899-4909.
58. Yin, X., et al., *Enhanced Electromechanical Performances in Plasticizer Modified Electrostrictive Polymers*. European Polymer Journal, 2016.
59. Dlubek, G., et al., *Glass transition and free volume in the mobile (MAF) and rigid (RAF) amorphous fractions of semicrystalline PTFE: a positron lifetime and PVT study*. Polymer, 2005. **46**(16): p. 6075-6089.
60. Fukao, K. and Y. Miyamoto, *Dynamical transition and crystallization of polymers*. Physical review letters, 1997. **79**(23): p. 4613.
61. Roland, C., et al., *Mechanical and electromechanical properties of vinylidene fluoride terpolymers*. Chemistry of materials, 2004. **16**(5): p. 857-861.
62. Jaaoh, D., C. Putson, and N. Muensit, *Deformation on segment-structure of electrostrictive polyurethane/polyaniline blends*. Polymer, 2015. **61**: p. 123-130.
63. Bennett, M.D., et al., *A model of charge transport and electromechanical transduction in ionic liquid-swollen Nafion membranes*. Polymer, 2006. **47**(19): p. 6782-6796.

Chapter III

Influence of the Crystallization on the Molecular Mobility and Ionic DC Conductivity Behaviors of Relaxor Ferroelectric $P(\text{VDF-TrFE-CTFE})$ Terpolymers

The dynamics of semi-crystalline poly(vinylidene fluoride-trifluoroethylene-chlorotrifluoroethylene) (P(VDF-TrFE-CTFE)) terpolymers were fully investigated as a function of temperature and frequency, by means of broadband dielectric spectroscopy. Four types of relaxation regimes were observed over the full dielectric spectroscopy, namely β (second) relaxation in the sub-glass state, α (segmental dynamics) in the rubbery state, the Curie transition and space charge carrier motion at high temperatures. Constrained segmental dynamics were observed in the terpolymer containing the highest crystallinity fraction for which a narrow relaxation time distribution was found. These results indicate a decreasing average size of the cooperative rearranging region over the crystalline fraction. A decrease of the strength index values also implied a more fragile behavior for terpolymers with a higher degree of crystallinity. An exceptional increase in dielectric strength $\Delta\epsilon_\alpha$ was found as the crystallinity increased. This behavior could be explained by an enhanced interphase (rigid amorphous phase). The Curie transition showed an accelerating relaxation rate for a more fragile terpolymer. Moreover, a motion of the space charge carrier ions was observed in the higher temperature range. Finally, there was evidence that the segmental dynamics in the amorphous phase was responsible for the motion of the space charge carrier ions.

I Introduction

Ferroelectric materials have been paid increasing attention due to their capability of converting external electric stimulus into other mainly available energy forms such as mechanical force [1, 2], heat (electrocaloric effect) [3-5], and magnetoelectric fields [6, 7] and vice versa. Recently, ferroelectric polymers have attracted great interest thanks to their flexibility, light weight, relatively low mechanical strength, ease of processability into large-area films, and the ability to be molded into a desirable dimension. However, compared with polyamide (PA) and polyimide (PI) ferroelectric polymers [8, 9], PVDF and fluorinated copolymers exhibit a high dielectric constant, a low dissipation factor, as well as rapid and excellent electromechanical responses [10, 11].

With rapid development of demands for power electronics like portable devices, wireless sensors, medical equipment and nonvolatile memory, novel PVDF-based ferroelectric polymers have been designed and synthesized. In parallel, new chemical and physical methods were developed to enhance their dielectric behavior and storage energy density. And thus by adding an amine cross-linker or photo-initiator, films of thermal and photo-induced cross-linked poly(vinylidene fluoride-trifluoroethylene) P(VDF-TrFE) copolymers were obtained with a greatly enhanced storage energy density and reduced dielectric losses [12, 13], paving the way towards the high performance ferroelectric polymers. On the other hand, a variety of facile processes such as solution casting, hot-pressing, uniaxial or biaxial stretching and spin-coating

[14, 15] were employed to fabricate polymer films with tunable dielectric properties by the control of the crystal forms and the film morphology.

Intrinsically, for most semi-crystalline polymers such as PVDF-based polymers, their physico-chemical properties are significantly dependent upon the crystallographic behavior [16, 17]. Theoretically, when the temperature surpasses the glass transition temperature (T_g), crystallization occurs, during which the molecular chain in the amorphous phase folds back and forth to form crystal lamellae. Furthermore, in PVDF-based polymers, the crystal forms are categorized into different crystal phases with regard to the Trans (T) or Gauche (G) chain conformation. The crystallization process determines which crystal form is favored during molecular chain rearrangement [18, 19]. For a solution-cast film [20], the c-axis of the crystal lamellae (flat-on) is normal to the film plane, with its dipole moments perpendicular to the external applied electric field. This crystal form shows weak polarization in bulk-like films. However, in the case of nanometer-thick films with a nano-confinement effect [21], edge-on crystal lamellae (with the c-axis parallel to the film plane) were forced to be predominant and thus their dielectric polarization response was maximized. Diffractogram profiles provide us with a massive amount of information on crystallography such as the overall crystallinity, the crystal size and lattice parameters. In parallel, the molecular mobility and crystallization behavior remain key research interests upon the crystallization process.

Generally, the dynamic mechanical analysis (DMA) technique is employed to track changes or fluctuations in molecular chain conformation regardless of the chemical composition. Nonetheless, dynamic mechanical spectra were confined within a small range of mechanical frequency due to the experimental manipulation limit. Thanks to the fact that most semi-crystalline polymers are isolating materials, polymers are better for dielectric measurements over a large scale of electric frequency and atmospheric temperature. In particular, polymeric materials containing functional groups or atoms such as fluorine and chlorine are rather sensitive to external electric fields, and changes in molecular chain conformation or long-term/short-term chain motion have been detected. This could lead to pronounced high-resolution broadband dielectric spectroscopy (BDS). By using the BDS technique, PVDF-based random copolymers were investigated and their segmental α -relaxation process within a super-cooled liquid region and β -relaxation process in the sub-glass state were fully understood.

Also, the ferroelectric-paraelectric phase transition point (Curie point) was located over the isochronal dielectric loss spectra and did not shift with the frequency, showing a typical ferroelectric behavior [22, 23]. Due to its high dielectric constant and low loss dissipation factor, the ferroelectric copolymer showed considerable shape deformation upon the application of an electric field. However, the high energy beam-irradiated copolymer P(VDF-TrFE) displayed a

slim hysteresis loop rather than a large displacement-electric (D - E) loop. Its Curie temperature was greatly reduced and was highly frequency-dependent, showing a relaxor ferroelectric behavior as revealed by the BDS technique. Inspired by the introduction of defects to PVDF-based copolymers according to the high energy beam, the CTFE monomer was copolymerized into the P(VDF-TrFE) backbone. Relatively large crystalline phases in the copolymer broke into ergodic nanoscale crystallites concomitant with an all-Trans β (T_m , $m > 3$) ferroelectric transforming into a nonpolar paraelectric crystalline α phase (TG^+TG^-) and metastable δ ($T_3G^+T_3G^-$) ferroelectric phase. The directions of their dipole moment were randomly orientated and separately distributed in the nonpolar amorphous phase. Therefore, interactions between crystallite nanodomains and the amorphous phase were greatly weakened accordingly. Such an evolution was responsible for a much higher electrostrictive response comparable to the ferroelectric copolymers according to our previous study [24].

On the basis of studies on poly(vinylidene fluoride-trifluoroethylene-chlorotrifluoroethylene) (P(VDF-TrFE-CTFE)) terpolymers, a rather high dielectric constant ($\epsilon' > 50$), a large electrostrictive strain and a high storage energy density, were demonstrated making it a rather good candidate for sensor and actuator implementation. Note that the crystallinity decreased a lot when incorporating bulk ternary monomer into P(VDF-CTFE) and thus its pristine film had a very low overall crystallinity, exhibiting less ferroelectricity. Consequently, (non)-isothermal crystallization at high temperature within a large scale range was subjected to the pristine terpolymer films. It has been reported that the microstructure and electromechanical properties of the P(VDF-TrFE-CTFE) terpolymer significantly depend upon the film-forming process and correlation between the process and properties have also been revealed [25]. Thus, it was interesting to understand the influence of the crystallinity on the molecular mobility, the Curie transition and the space charge carrier motion behavior within a full temperature range since these scenarios have a crucial impact on dielectric and electromechanical behaviors.

In this work, the BDS technique was employed to monitor molecular mobility based on the overall crystallinity, where four typical relaxation modes were detected: segmental dynamics, so-called α -relaxation appearing at temperatures within the super-cooled liquid region; a secondary relaxation concerning the local molecular motion, designated as β -relaxation in the sub-glass state. The Curie transition, assigned to the dipolar reorientation in the crystal lamella merged with segmental relaxation at higher temperature. Moreover, the relaxation behavior associated with parameters change in amorphous phase was also investigated. Finally, the relaxation of charge carrier ions at high temperature was analyzed by the imaginary part of complex electric modulus spectra.

II Experimental Section

II. 1 Materials and Isothermal Crystallization

The P(VDF-TrFE-CTFE) terpolymer studied in the current work had the following chemical composition: VDF/TrFE/CTFE=61.7/30.4/7.9 (mole ratio), and was graciously provided by Piezotech S.A.S (Arkema Group, France). It was synthesized by suspension polymerization engineering. The pristine film was denominated pristine **Film A** and was prepared by slow solution casting from 14 wt% terpolymer solution on a glass plate, without post annealing, giving an average thickness of ca. 60 μm . Post annealed specimens were intimately prepared by annealing the pristine film at 70 °C in an oven for 12h; these were designated as **Film B**. Those kept at 80 °C for 2H were called **Film C**, and the specimens denoted **Film D** and **Film E** were prepared by annealing pristine Film A at 90 °C in the oven for 1h and 2h, respectively. The intermediately crystallized **Film F** was obtained by isothermally annealing pristine Film A at 110 °C for 2h. Fully crystallized films were finalized by a deep annealing of pristine **Film A** at 120 °C overnight and were called **Film G**.

The overall degree of crystallinity of each crystallized film was obtained by the first DSC heating ramp (10 °C min⁻¹), as the integral of the melting region divided by the fusion of enthalpy for hypothetically 100% crystallinity in terpolymers ($\sim 42 \text{ J g}^{-1}$) [25]. The overall crystallinity fraction of the as-treated terpolymer films ranged between 30.83% (**Film A**) and 45.28% (**Film G**) (see Table III. 1). And each terpolymer film thickness was normalized to ca. 60 μm in order to ensure an even electric field distribution. All as-cast films were homogeneous and the crystallized films were slightly translucent.

II. 2 Device Fabrication and Characterization Techniques

II.2.1 Dielectric Data Acquisition.

Broadband dielectric relaxation spectroscopy was carried out on a Solartron 1260 impedance-analyzer equipped with Model 129610A LHe LN2 Cryostat temperature-controlled system. The as-deposited dielectric terpolymer circular films with a diameter of 20 mm were metalized by sputtering gold on both surfaces through a shadow mask. The metal/terpolymer/metal parallel capacitors were sandwiched between two polished copper electrodes mounted on the sample holders. The samples were then exposed to the evaporated nitrogen stream from the liquid nitrogen dewar by which temperature control was performed with a precision of $\pm 0.1\text{K}$. Dielectric data acquisition was conducted with frequency sweeping from 10^{-1} to 10^6 Hz at a low bias voltage (1 V). Isothermal broadband dielectric measurements were carried out within an extended temperature (T) range of 203 K (-70 °C) $\leq T \leq 373 \text{ K}$ (100 °C). The capacitor-like sample was cooled down to 203 K with a moderate cooling rate so as to eschew a

thermodynamical non-equilibrium of molecular chain entanglement during the cooling step. Then the dielectric measurements were triggered isothermally in 5K intervals. The real and imaginary parts of the permittivity frequency-dependent dielectric data were collected by the Solartron software package.

II.2.2 Dielectric Data Analysis

To picture the quantitative relaxation time distribution and dielectric strength ($\Delta\epsilon$), isothermal dielectric spectroscopy data were analyzed by the phenomenological Havriliak-Negami (HN) equation [26]. All the dielectric data were fitted with the Winfit software package (Novocontrol, Germany). For the sum of superimposed dielectric spectra, the HN equation reads:

$$\epsilon^* = \epsilon_\infty + \sum_j \frac{\Delta\epsilon_j}{[1+(i\omega\tau_{HNj})^{\alpha_{HN}}]^{\beta_{HN}}} - i \left(\frac{\sigma}{\epsilon_0\omega} \right)^S \quad \text{III. 1}$$

where ϵ_0 is the dielectric permittivity in vacuum; ϵ_∞ represents the dielectric constant at infinite frequency, much higher than the relaxation rate within the limited frequency scale; $\Delta\epsilon_j$ is the respective dielectric strength of relaxation at an index above which appears the dielectric relaxation process; τ_{HNj} denotes the average characteristic relaxation time of each process; α_{HN} , β_{HN} ($0 < \alpha_{HN} < 1$, $0 < \alpha_{HN}\beta_{HN} \leq 1$) are the shape parameters which describe respectively the symmetry, asymmetry and broadness of the corresponding spectra over the spectral window. The right hand expression cluster denotes the conductive effects on the dielectric measurements where σ is the sample conductivity mainly contributing to the imaginary spectra at high temperature and low frequency. S ($0 < s \leq 1$) is the conductive fitting parameter that describes the Ohmic effects of the direct current (DC) conductivity. Empirically, for $\beta_{HN} = 1$, the Havriliak–Negami equation deduce to the Debye relaxation model as a Cole-Cole equation. Fitting parameters characteristic of the relaxation time τ_{HN} , α_{HN} and β_{HN} are extrapolated and τ_{HN} is related to model-independent relaxation time $\tau_{max} = 1/2\pi f_{max}$ which corresponds to the peak position of the maximum dielectric loss calculated according to equation III.2.

$$\tau_{max} = \tau_{HN} \left[\sin \frac{\alpha_{HN}\beta_{HN}\pi}{2(\beta_{HN}+1)} \right]^{1/\alpha_{HN}} \left[\sin \frac{\alpha_{HN}\pi}{2(\beta_{HN}+1)} \right]^{-1/\alpha_{HN}} \quad \text{III. 2}$$

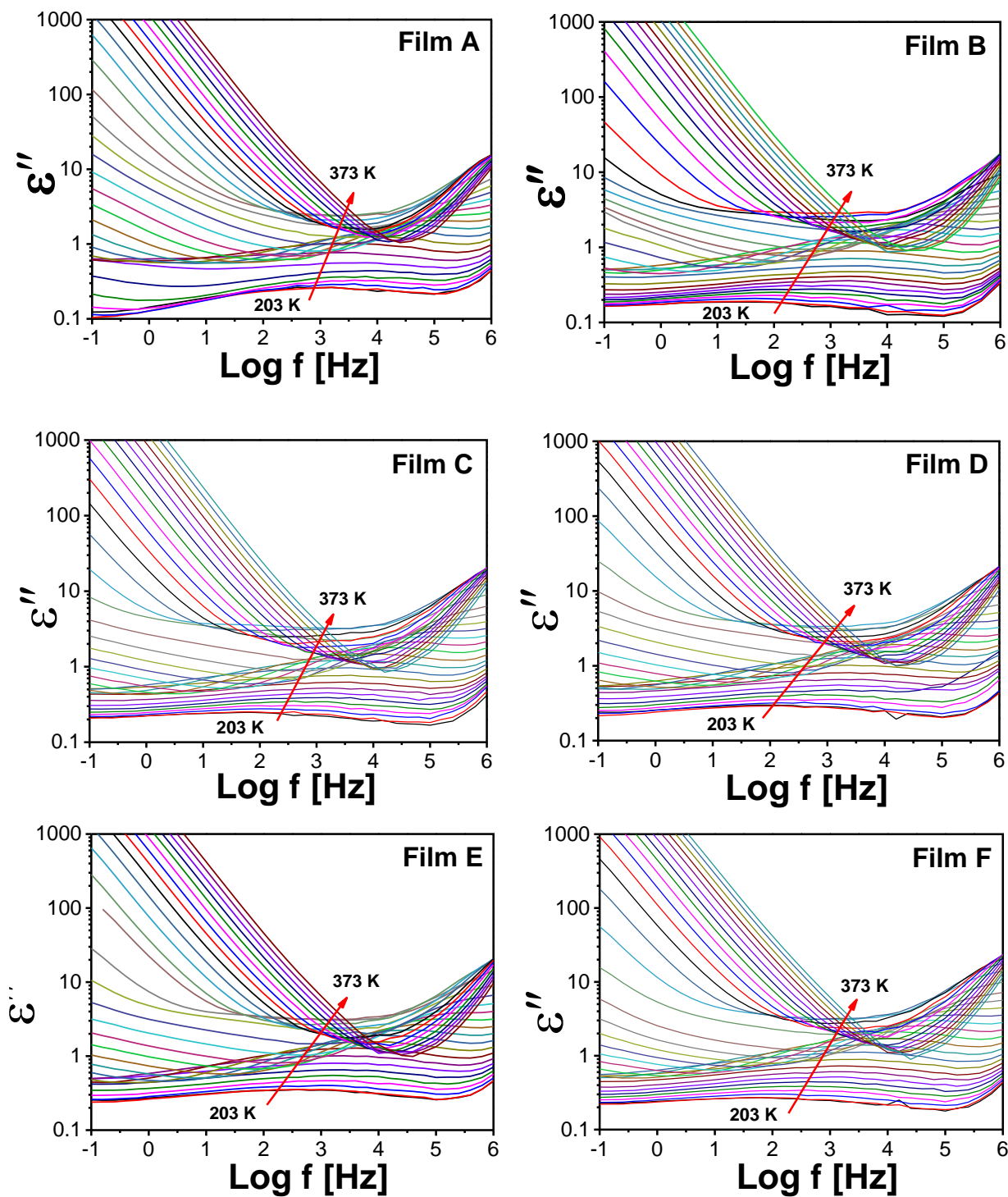
III Results and Discussions

III. 1 Broadband Dielectric loss spectra and Tan δ

III.1.1 Dielectric Loss Spectra

It is well-documented that dielectric spectroscopy originates from the amorphous phase of semi-crystalline structures rather than the rigid crystalline phase where the relaxation is shielded by the entangled crystal lamellae. These lamellae show no dielectric relaxation. However, molecular dynamics in semi-crystalline polymers are determined by the proportion of the crystalline vs. amorphous phase [27-29]. The dielectric loss spectra recorded in the available

frequency range at temperature from -70 °C to 100 °C were presented in a logarithmic plot in Figure III. 1. In all cases dielectric spectra shared the similar relaxation trend. At low temperature, the broad and less intense dielectric anomaly was visible, which is associated with



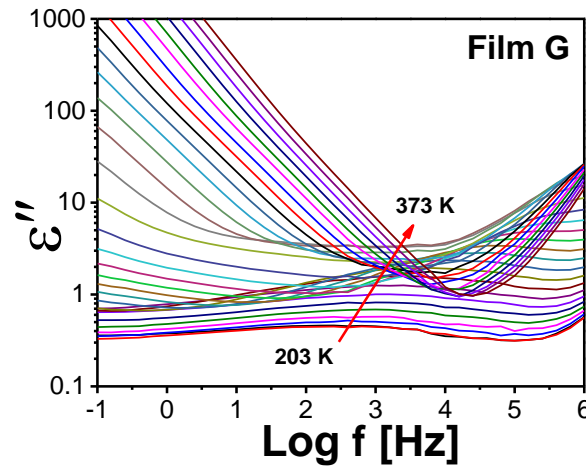


Figure III. 1 isothermal dielectric loss spectra for each as-casted polymer thin films in a temperature range from $-70\text{ }^{\circ}\text{C}$ to $100\text{ }^{\circ}\text{C}$ in step of $5\text{ }^{\circ}\text{C}$ interval. Lines are guides to the eyes.

relaxation in sub-glass state. The relaxation peak shifted towards the high frequency with its relaxation strength enhanced and shape altered. On top of that, the relaxation strength of the dielectric spectra at relatively low frequency was increased several orders of magnitude. This could be due to the occurrence of interfacial polarization and conductivity linked to the charge carrier ions. Besides, three dimensional relaxation spectra were also drawn, allowing us to distribute and identify the dielectric characteristics.

III.1.2 Dielectric Relaxation Behavior

Figure III. 2 shows an overview of the temperature and frequency dependence of the dielectric loss ϵ'' (a) and dielectric loss angle $\tan \delta$ (b) for the representative as-processed semicrystalline Film C with 36.40% crystallinity. The dielectric loss (ϵ'') showed three distinctive relaxation anomalies over the temperature range which was in agreement with our previous study [23] where, at low temperature, a broad and less intense β relaxation regime was associated with the local motion of fluorinated dipoles in a short molecular chain sequence. As the temperature increased, the β relaxation regimes superposed with the segmental α relaxation, showing considerable complexity for this scenario where multicomponent relaxation modes contributed to the sum of dielectric loss spectra covered by the glass transition region. This was followed by a modest increase in dielectric loss, identified as a strong α relaxation anomaly versus temperature [30, 31]. The relaxation, associated with the structural dynamics mode within the Super-cooled Liquid Region (SLR), accelerated its shift towards higher temperature and overlapped with the relaxation at higher frequency. The lower temperature dependence of the relaxation regime located at a temperature around 33°C was unambiguously attributed to the Curie transition in agreement with evidence established from DSC endothermic and dielectric spectra [23]. The DC conductivity that dominated at high temperature [32] overlapped with the Maxwell-Wagner-

Sillars (MWS) interfacial polarization at low frequency. The former relaxation regimes were visualized by the dielectric loss angle $\tan \delta$ spectra in Figure III. 2b which will be discussed later on.

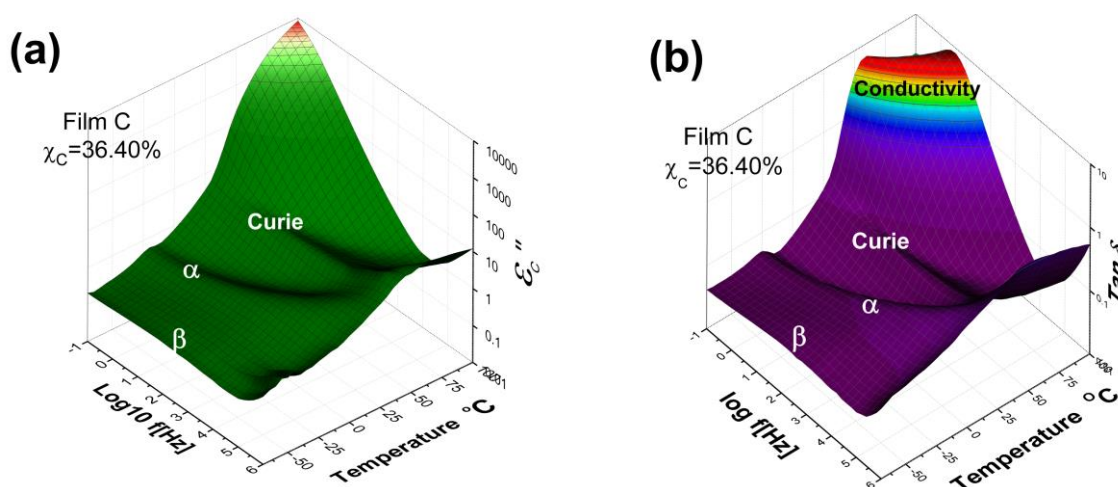


Figure III. 2 Frequency and temperature dependence of the dielectric loss (a) and dielectric loss angle $\tan \delta$ (b) for the representative as-processed Film C with a crystal fraction of 36.40 wt%.

Moreover, isochronal dielectric loss spectra at a given frequency of 2511 Hz obtained through isothermal dielectric spectroscopy are plotted in Figure III 3 for the as-processed films of varying crystallinity. A more intense relaxation associated with the Curie transition regimes shifted the spectra towards a lower temperature comparable with that of the pristine film with a T_C of 42.9 $^{\circ}\text{C}$. This frequency-dependent relaxation was assigned to the dipolar reorientation in the crystal lamella [33, 34].

The Curie transition is associated with the conversion of the ferroelectric phase, comprised of a predominant δ phase with $T_3G^+T_3G^-$ chain conformation which only exists below the Curie transition point, to the paraelectric α (TG^+TG^-) phase for as-casted PVDF-based copolymers and terpolymers. However, the terpolymers exhibited a suppressed Curie transition temperature within the range of 30-50 $^{\circ}\text{C}$ rather than very high Curie temperature for copolymers. In our case, the pristine film A underwent crystallization at ambient temperature below the Curie temperature during which the ferroelectric δ phase was maximized with an even lower overall crystallinity. As the annealing temperature (70-120 $^{\circ}\text{C}$) was raised far beyond the Curie point, the low amount of the ferroelectric phase would engage in the Curie transition whereas the overall crystallinity would increase a lot. Consequently, the Curie transition in the less ferroelectric phase of the crystal lamellae was ignited at lower temperature in accordance with KAP's study [35]. Such results rationalize a lower temperature shift trend regarding the ferroelectric-paraelectric conversion. Quantified parameters concerning the Curie transition will be presented in the section *Influence of segmental dynamics on the Curie transition behavior*.

Nevertheless, it was observed that the less intense α relaxation modes located on the left shoulder of the Curie mode showed an enhanced shift towards the higher temperature with an increased crystallinity. This implied an increasing restriction of the molecular mobility in the amorphous phase which was due to the evolution of a three-phase microstructure, i.e., an amorphous-interphase-crystal phase of the crystalline polymer. Details will be discussed in the section *Segmental dynamics of semicrystalline terpolymers*. Note that an enlarged intensity of the α relaxation peaks was observed as the degree of crystallinity increased, and these results were in accordance with recent studies of relaxor ferroelectric polymer films [36].

Generally, non-relaxor ferroelectric glassy polymers such as poly(ethylene terephthalate) (PET) [37], poly(pentamethylene terephthalate) (PPT) [38], poly(lactic acid) (PLA) [39] etc. have exhibited inversely compressed relaxation amplitudes. It is thus reasonable to assume that an enhanced α relaxation is closely correlated with the Curie transition. Additionally, a high temperature gave an abrupt increase of the relaxation peak which was attributed to the charge carrier ion motions through the interphase of the amorphous and crystal phases in the semicrystalline terpolymers. Details of each relaxation regime are given in the up-coming section.

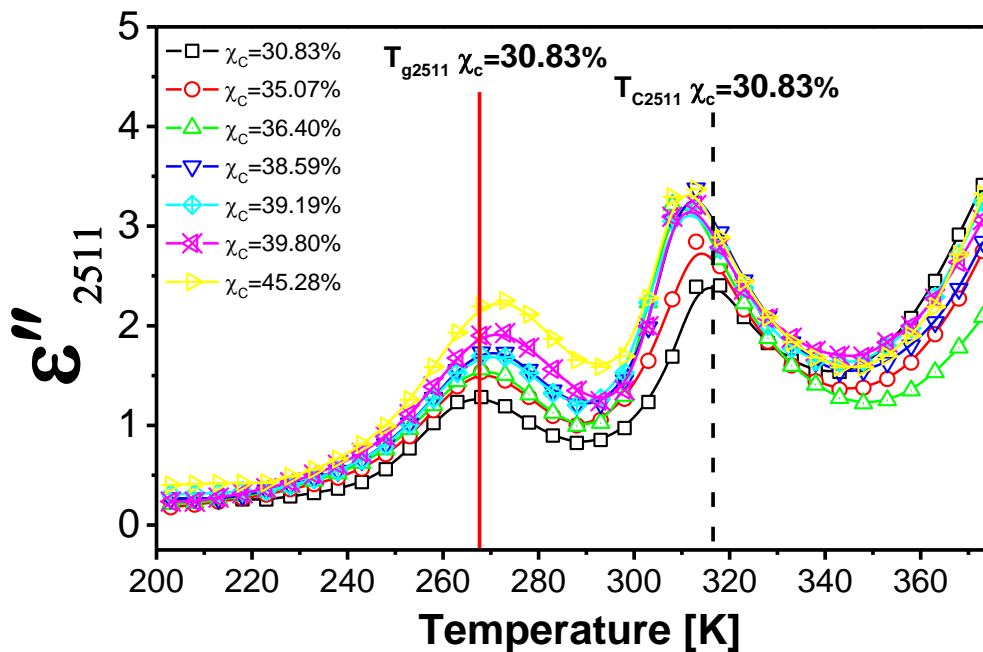


Figure III. 3 Isochronal dielectric loss spectra picked up from isothermal dielectric relaxation

III. 2 Segmental Dynamics of Semicrystalline Terpolymers

As stated in the previous section, multiple anomalies were distinctly observed when analyzing the molecular dynamics in a broad range of temperature and frequency. The α relaxation interacting with neighboring β relaxation and the Curie transition showed considerable

complexity. As presented in Figure III. 2a, the β relaxation located at much higher frequency and low temperature merged with the main α relaxation at higher frequency. In order to fully picture the segmental dynamics, dielectric losses at low temperature (above T_g) were compared. At this point, the relaxation at high frequency showed a much lower contribution to the main dielectric loss as can be seen in the representative spectroscopy results in Figure III. 2.

It is well-known that when amorphous polymers or metallic materials are put through a thermal annealing process above the glass transition, crystallization tends to take place and molecular chains fold back and forth into well-ordered crystal lamellae [40-42]. What concerns us most is the influence of the crystallization kinetics on the segmental dynamics. Respective isothermal dielectric losses (ϵ_D'') were plotted versus the broadband frequency (f) at a given temperature (248K) in Figure III. 4a. This graph shows significant disparity. A clear evolution of the peak intensity and position depended closely upon the degree of crystallinity revealed by DSC. Normally pending a typical crystallization process for non-ferroelectric bulk polymers, crystal lamella form concomitantly with the consumption of relaxing segments in the amorphous phase, showing the apparently dwarfed relaxation peaks. This was not the case for our present results which displayed abnormally enhanced peak intensities. Note that the relaxation position in Figure III. 4a shifted towards lower frequencies as the crystal phase increased. In fact, many authors have argued that the consumption of the amorphous phase led to the formation of the more constrained segmental relaxation phase. Their coherent length (CL), corresponding to the average size of crystal (polar) domains, was greatly increased with the enhancement of the crystalline fraction [35, 36].

More recently, Zhu's group [43] found, by a combination of calculation and computer simulation, that the enhanced dielectric property was due to the microstructure of the oriented amorphous interphases. At least a 55% interphase (rigid or constrained amorphous phase) in which the molecular chains directly stemmed from the crystalline basal planes, accounted for the whole amorphous phase in a film of biaxially oriented PVDF. The crystalline fraction densified due to high temperature annealing, accompanied by an increment of the interphase layer. It was likely that the large amount of interphase layers exerted a significant influence on the molecular mobility of the whole amorphous phase. In this case, the entire amorphous phase showed more constrained behaviors. Such that the constrained relaxation phases gave rise to a prolonged fluctuation in process time comparable with the mobile amorphous phase as the crystallization proceeded [44, 45].

Peak position shifts in Figure III. 4a correlated with the constraining amorphous phase, showing a slowing down of the relaxation rate which was consistent with the intensively studied polymers, i.e., PET, poly(butylene terephthalate) (PBT), poly(L-lactic acid) (PLLA), and

polycarbonate (PC) [37-39, 46]. Such results were in rather good agreement with a higher temperature shift trend of isochronal segmental relaxation as shown in Figure III. 4a. Moreover, Figure III. 4b displays dual normalized dielectric spectra and small variations were found for the relaxation peak shape as a function of the crystallinity fraction. Such results implied that the size of the amorphous phase or coherent length values became more homogeneous and smaller with an increased crystallinity. A narrower relaxation time distribution also provided evidence of a reduced average size of the Cooperative Rearranging Region (CRR) introduced by Adam and Gibbs [47]. This led to an increased interaction between the amorphous phase and the crystal lamellae in the terpolymer. E. Dargent [48, 49] has reported a similar finding: that a constrained size of the CRR near the glass transition temperature correlated with a decrease of the interspherulitic amorphous phase according to a DSC method developed by Donth [50, 51].

In an attempt to clarify the effect of isothermal crystallization on the segmental relaxation, dielectric loss ϵ'' spectra were fitted to the well-known phenomenological HN equation. Estimated breadth shape parameters α_{HN} increased with the temperature from 0.22 ± 0.03 (248K) to 0.56 ± 0.04 (288K) for a representative moderately crystallized terpolymer with a crystalline fraction of 36.40%. This similar trend was shared by PLLA polymers [45]. As shown in Figure III. 4b, α_{HN} increased upon the evolution of the crystallization range from 0.20 ± 0.02 ($\chi_c = 30.83\%$) to 0.31 ± 0.02 ($\chi_c = 45.28\%$). A decrease of the relaxation time distribution has already been observed in different polymeric systems [52] and has been related to the variation of the CRR values as mentioned above. Reduced CRR size values only occur if the number of neighboring repeating units (for polymeric systems) participating in the relaxation process near the glass transition temperature T_g decreases. Indeed, the PVDF-based terpolymers became more constrained as the crystallization evolved. Moreover, symmetric β_{HN} parameters have also been deduced and exhibited a relatively narrow distribution within the defined temperature range.

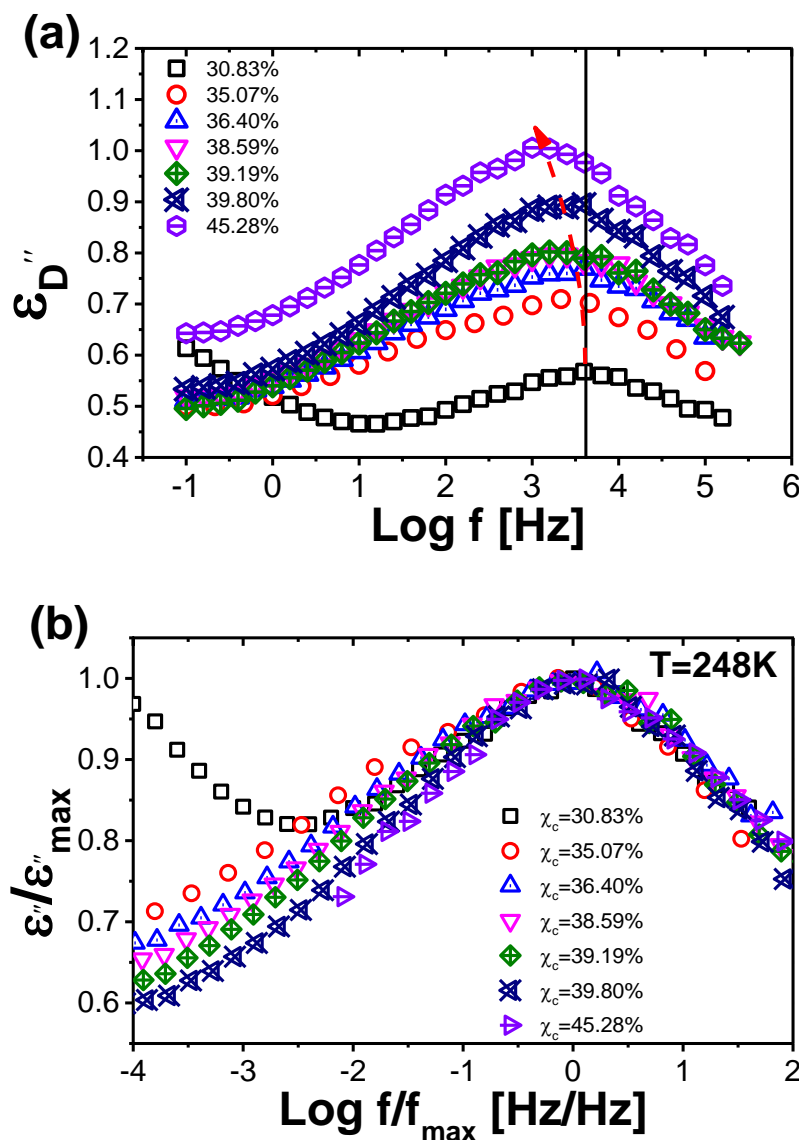


Figure III. 4 (a) The dielectric loss fraction as a function of frequency for isothermally crystallized films at 248 K. The vertical line denotes the relaxation peak position (frequency) for pristine terpolymer films and the dashed curve marks the shift trend of the relaxation position for each processed material; (b) normalized dielectric loss spectra as a function of frequency for isothermally crystallized terpolymers at 248 K.

During the crystallization process for semicrystalline polymers, the amplitude of the segmental relaxation peaks decays as the crystallization proceeds [53]. Nevertheless, as depicted in Figure III. 4a, the presence of a relatively high crystallinity tends to induce a larger relaxation strength, which is quite surprising. These results were somewhat contrary to the segmental dynamics of non-ferroelectric semicrystalline polymers which presented a decreasing trend of peak intensity with the evolution of the crystallization. However, the present findings are in rather

good accordance with results on a homological P(VDF-TrFE-CFE) relaxor ferroelectric terpolymer, showing a larger relaxation strength as the crystalline fraction increased [36].

Isothermal dielectric losses (recall Figure. III. 4) also showed an identical trend with regard to the α relaxation anomaly. The dielectric strength $\Delta\epsilon$, an indicator of the relaxation intensity, was introduced in order to quantify the extent of crystallinity effects. Generally, the dielectric strength can be predicted by the Onsager/Kirkwood/Fröhlich theory [54], expressed as follows:

$$\Delta\epsilon \sim F_{\text{Onsager}} g \mu^2 N_p / k_B T V \quad \text{III. 3}$$

where the Onsager factor $F_{\text{Onsager}} \approx 1$. Clearly, the dielectric strength is the number of contributing dipoles N_p or the angular extension of the dependent fluctuations, albeit proportional to the reciprocal temperature. The obtained fitting $\Delta\epsilon_\alpha$ values versus the degree of crystallinity at two given temperatures were plotted in Figure III. 5. For many non-relaxor ferroelectric polymers, the values of dielectric strength $\Delta\epsilon$ show the linearly decreasing trend with an increase in crystallinity fraction due to consumption of the amorphous phase. The extract $\Delta\epsilon_\alpha$ of the α relaxation was compared with the dielectric strength extrapolated from its polymer counterpart with a fully amorphous phase. The ratio $\Delta\epsilon_R = \Delta\epsilon_\alpha / \Delta\epsilon_{am,\alpha}$ versus crystallinity fraction showed a large deviation from the slope equal to 1. This means that not the whole amorphous fraction contributed to the segmental dynamics and the rigid amorphous phase (RAP) was revealed as a consequence [55-57].

Intriguingly, the increasing trend of the $\Delta\epsilon_\alpha$ values demonstrated a complexity, implying that not only the consumption of the amorphous fraction led to such results. This was mostly due to the large amount (more than 55%) of rigid amorphous phase in the PVDF-based polymers [43]. A schematic diagram of microstructure of semi-crystalline polymer was depicted in Figure III. 6. As presented, the constrained amorphous molecular chains stemmed directly from the non-relaxation crystal lamellae, forming a more or less oriented amorphous interphase. Thus, the dielectric relaxation response was enhanced as a consequence. A larger interphase layer associated with an increasing crystallinity fraction led to enhanced dielectric strength. Moreover, the Curie relaxation spectra overlapping with segmental relaxation combined with enhanced rigid amorphous phase might explain the abnormal scenario with regard to $\Delta\epsilon_\alpha$. $\Delta\epsilon_\alpha$ values in each treated terpolymer are plotted in Figure III. 5b as a function of temperature. In all cases, $\Delta\epsilon_\alpha$

showed a common increase, as a general behavior in accordance with a study on semi-crystalline polymers [45, 52] while completely amorphous polymers showed a decreasing behavior.

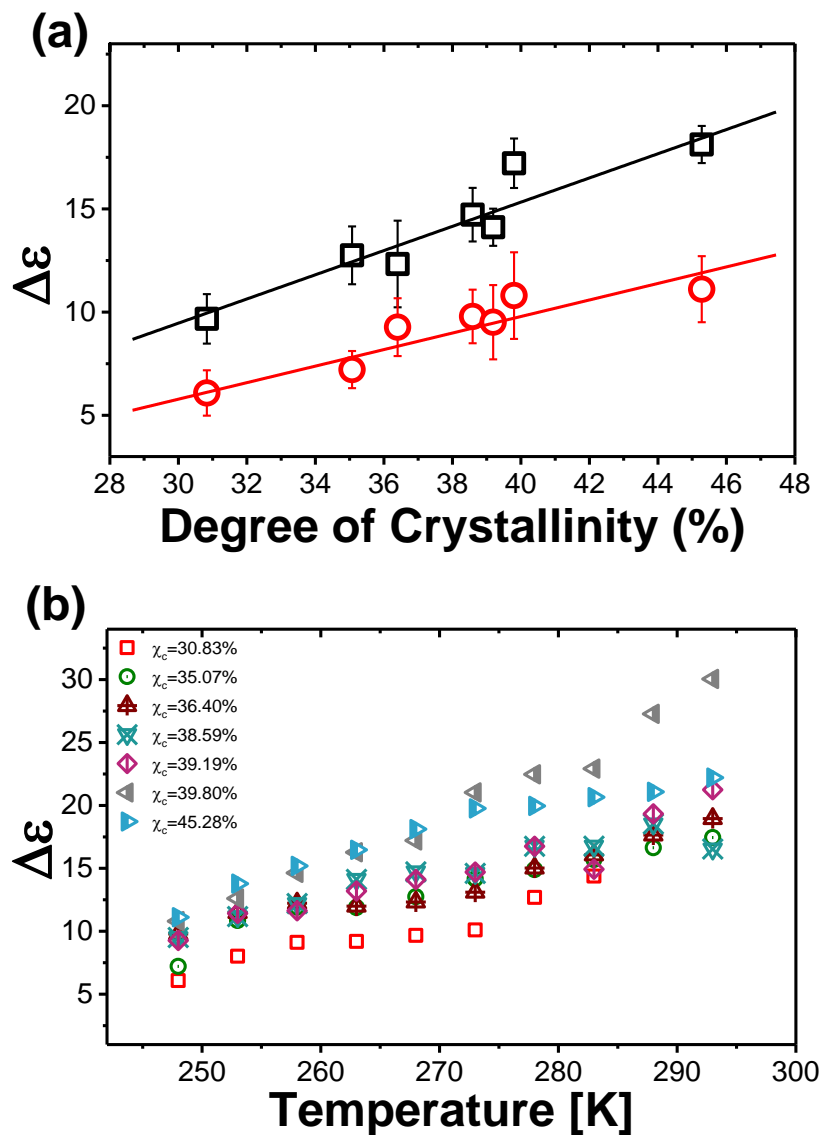


Figure III. 5 (a) Dielectric strength $\Delta\epsilon$ as a function of the degree of crystallinity for as-treated semi-crystalline terpolymers at 248K (open circles) and 268K (open squares); (b) the temperature dependence of the dielectric strength $\Delta\epsilon$ for as-prepared terpolymers. The solid lines are linearly fitted to the $\Delta\epsilon$ values at 248K and 268K, respectively.

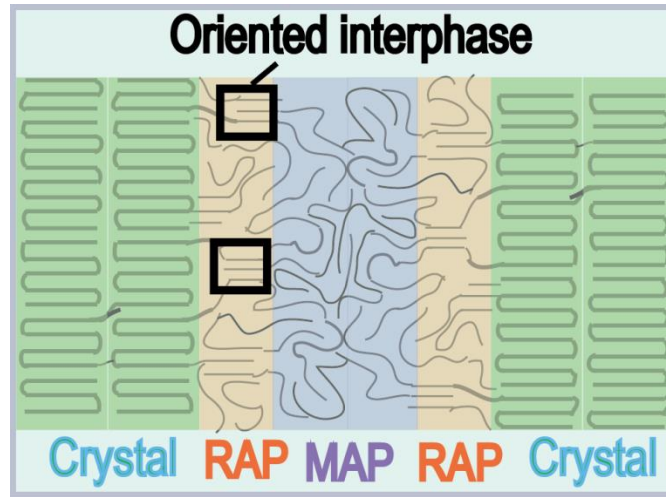


Figure III. 6 A schematic diagram of crystal-rigid-mobile amorphous phase mode for PVDF-based polymer. **Crystal**: molecular chain well-ordered crystal phase; **RAP**: Rigid amorphous phase being oriented; **MAP**: mobile amorphous phase region whose molecular chains were randomly oriented.

III. 3 Influence of segmental dynamics on the Curie transition behavior

In order to trace the two regimes, the characteristic HN relaxation times were extrapolated which allowed us to quantitatively picture the molecular mobility and influence of the isothermal crystallization annealing on the molecular dynamics. Then, the characteristic relaxation times τ_α were plotted against the reciprocal of the temperature in a logarithmic function in Figure III. 7. Plots of the α anomaly relaxation time τ_α as a function of $1/T$ exhibited the usual curvature of cooperative processes. Instead, α regime plots (relaxation ranging between 245K and 285K) were split as the temperature approached to the cross point with subglass regimes. This scenario was not seen at higher temperature. Terpolymers with higher crystallinity afforded long relaxation times as τ_α for $\chi_c=45.28\%$ was almost one decade larger than for terpolymers with minimal crystallinity. This is indicative of a significant slowing down of the relaxation rate. The temperature ($T > T_g$) dependence of the segmental relaxation times $\tau_\alpha(T)$ are well described over several decades by the Vogel-Fulcher-Tammann (VFT) equation, which reads [53, 58]:

$$\tau_\alpha(T) = \tau_\infty \exp\left(\frac{B}{T-T_0}\right) \quad \text{III. 4}$$

where τ_∞ is a pre-exponential factor, T_0 is the so-called Vogel temperature where the characteristic relaxation time is infinitely great and the molecular chain motion is frozen; B is related to the apparent activation energy of the α relaxation and can be rewritten as DT_0 . Here, D denotes the strength index parameter providing a way to classify glass formers according to the degree of deviation to the Arrhenius-type equation induced by varying the cooperative rearranging region [59]. Fragile glass formers show the largest deviations from the Arrhenius law

corresponding to small D values ($D \leq 10$) [60], while the glass formers show a quite strong behavior if the D value is very high (D_∞ or $T_0 = 0$) [61]. Extremely, the temperature dependence of the relaxation time τ_α closely obeys the Arrhenian relationship as $D \geq 100$. And the ratio of the dielectric glass transition temperature to the Vogel temperature $T_{g,die}/T_0$ has a linear relationship with the strength index D :

$$T_{g,die}/T_0 = 1 + D/(2.303 \log \frac{\tau_g}{\tau_0}) \quad \text{III. 5}$$

where $\log \tau_g/\tau_0$ is around 17. The VFT fitting parameters are summarized in Table III. 1.

Meanwhile, the pre-exponential factor τ_∞ - relaxation time at infinite temperature displayed a drastic shift of several orders of magnitude towards the higher values depending on the crystallinity. The values were in rather good agreement with reported findings [36] as presented for many other polymeric systems. And the estimated glass transition temperature $T_{g,die}$ at which τ_α is equal to 100s was replaced, which was consistent with the glass transition found by DMA and DSC in our previous study [23, 31]. It should be emphasized that these values were powerful indicators for evaluating the influence of the crystallinity on the molecular mobility.

As shown in Table III. 1, the Vogel temperature and the estimated $T_{g,die}$ both followed the similar increasing trend. As documented previously, a large number of semi-crystalline polymers present similar phenomena, e.g., poly(methyl methacrylate) (PMMA) [62], PVDF and blends thereof [63], network polymers [64], PC [65] and poly(bisphenol A carbonate) (PBAC) [66] etc. The enhanced T_0 and $T_{g,die}$ were equivalent to the constrained molecular mobility, and the results were in rather good agreement with the slowing down of the relaxation rate. Some reports have attributed this effect to the increasing rigid amorphous phase. The RAP is still amorphous but constrained with its molecular chain partially folded in the crystal lamella. As a consequence, the α relaxation in the whole amorphous phase became disturbed due to the number of molecular units participating in the relaxation. This led to a decrease of the average size of the cooperative rearranging region [48, 49, 67].

JF Mano proposed an increase of the RAP layer as the crystallinity fraction increased [45]. Note that more than 55% of the rigid amorphous phase accounted for the whole amorphous phase in the PVDF films [43], why it is understandable that a large amount of constrained amorphous material existed in the PVDF-based terpolymer. This might rationalize the slowing down of the relaxation rate depending on the degree of crystallization. Considering that the terpolymer has a

relative low crystallinity [25, 68], even in fully crystallized PVDF-based copolymers ($\chi_c > 60\%$) [21], the influence of the rigid interphase layer on the segmental relaxation is concomitant with the restriction on the conformational mobility of this phase. In addition, two amorphous phase modes would be verified by a plot of the normalized relaxation strength as a function of the crystalline fraction. However, in the case of our relaxor ferroelectric terpolymer, the extraction of the α relaxation part seemed inaccessible.

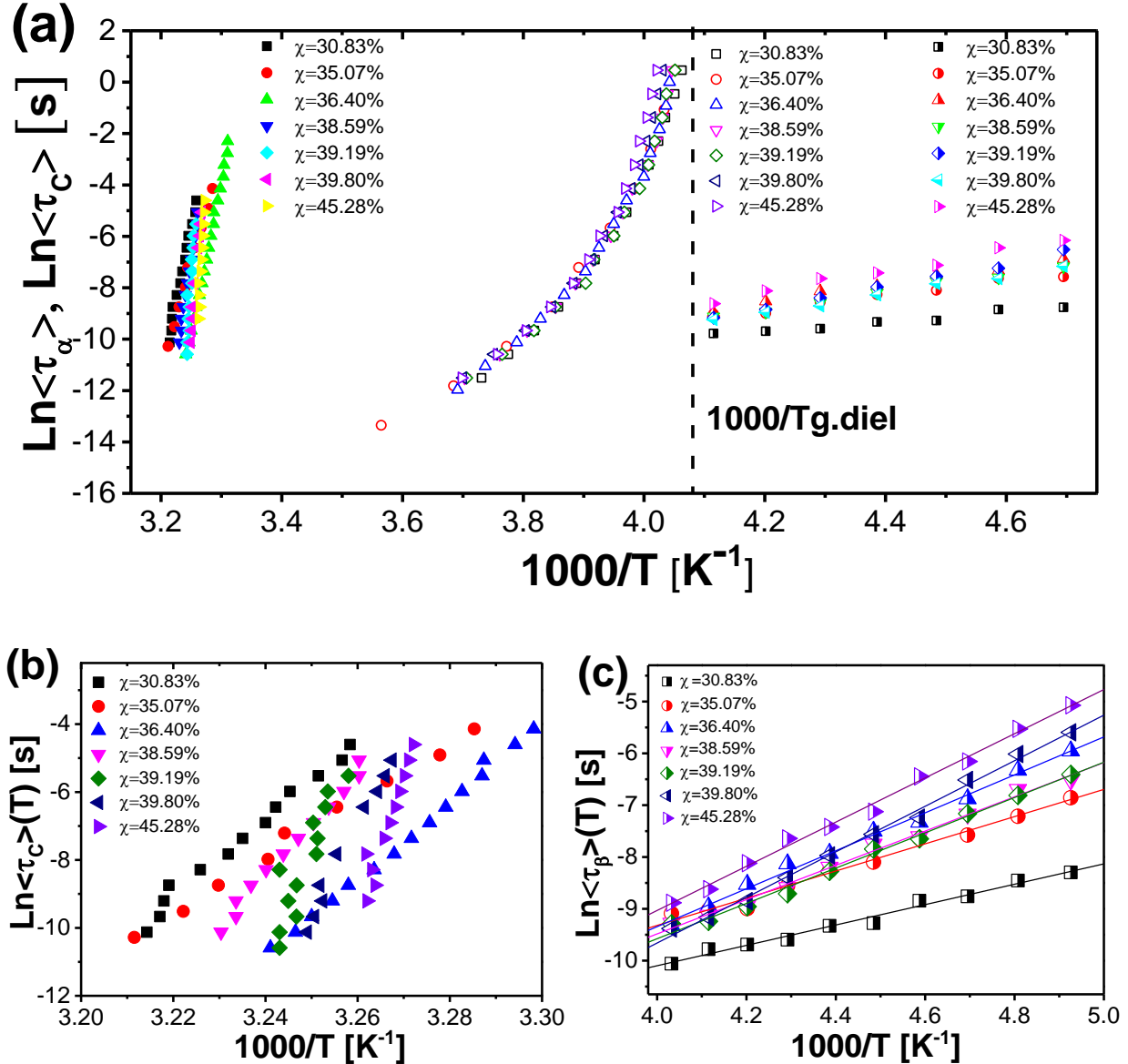


Figure III. 7 (a) Temperature dependence of all relaxation anomalies for as-treated semicrystalline terpolymers regarding the amount of crystallinity: filled symbols (for instance, ■, ●, ▲...) represent the Curie transition; open symbols (□, ○, △...) denote the α relaxation regimes; half-filled symbols (◐, ◑, ◒...) correspond to sub-glass relaxation processes. (b) Highlighted Curie relaxation time τ_c and (c) secondary relaxation times versus the reciprocal of temperature.

Otherwise, the Curie relaxation mode would show a diffusion phase transition upon the heating process. It is well-documented that the Curie transition is associated with dipolar reorientations in the crystal lamellae phase. The introduction of CTFE bulk monomers, acting as defects, disturbed the tight packing of molecular chains in the crystal phase, resulting in an expansion of inter-chain spacing and the termination of crystal growth. Submicron-sized P(VDF-TrFE) crystal grains consequently broke into ~ 10 nm sized crystal domains [69, 70]. As the crystal domain reduced in size, interactions between each crystal nanodomain became dwarfed. Its transition temperature at low frequency shifted towards the lower temperature (~ 310 K in the present work) to a large extent comparable with that of P(VDF-TrFE) copolymers (> 373 K [71, 72]), showing relaxor ferroelectric behavior.

Characteristic relaxation times of the Curie transition were extrapolated and plotted against the reciprocal of the temperature $1/T$ as presented in the inset of Figure III. 7b. In each case, τ_C versus the reciprocal of the temperature exhibited a quasi-linear correlation and followed an Arrhenius-type behavior. By the slope of the linear fitted curve, we could calculate the apparent activation energy of the Curie transition, listed in Table III. 1. The enthalpies of the Curie transition relaxation were an order of magnitude higher than those of the segmental relaxation. This was consistent with the fact that the ferroelectric-paraelectric transition occurred in a shielded crystal phase with a large activation energy barrier in accordance with previous investigations.

C. Ang reported that an increase of the amorphous content resulted in the suppression of the Curie relaxation mode [73]. Intriguingly, the Curie transition relaxation times were in our cases activated upon the increase of the crystalline content, in rather good agreement with the isochronal dielectric loss profile shifting towards lower temperatures depending on the crystallinity, cf. Figure III. 3. This means that a higher crystallinity favors an enhanced relaxation rate of the Curie transition regime.

In addition, one should note that the two concurrent relaxation modes merged at high frequency. On this point, segmental relaxation processes tended to affect the Curie transition mode at higher frequency. The merging temperature T_{me} of the two relaxation regimes is summarized in Table III. 1. The merging temperature at high frequency tended to decrease when increasing the crystallinity with a large distribution ($\Delta T \approx 8$ K). According to our previous investigation, the amorphous phase showed a reduced average size of CRR to a large extent, by the fact that the segmental dynamics in the amorphous phase could affect the Curie transition mode. This rationalized the lower temperature where the Curie transition modes were activated by segmental dynamics in mobile and constrained amorphous phases.

Table III. 1 Degree of crystallinity (χ_c), VTF fitting parameters, VFT temperature (T_0), glass transition temperature ($T_{g,diel}$) defined for a relaxation time τ_α of 100s, merging temperature T_{me} and the activation energy E_C of the Curie transition.

Films	χ_c (%)	τ_∞ (s)	Segmental Dynamics			Curie Transition Region	
			B(K)	T_0 (K)	$T_{g,diel}$ (K)	T_{me} (K)	E_C (kJ mol ⁻¹)
Film A	30.83	1.04×10^{-9}	360.5	229.0	243.5	316.4	948.38
Film B	35.07	2.98×10^{-9}	314.6	230.9	244.0	317.9	691.97
Film C	36.40	3.76×10^{-9}	291.4	232.1	244.1	312.5	977.47
Film D	38.59	9.91×10^{-9}	251.9	233.4	244.1	313.1	1270.71
Film E	39.19	1.75×10^{-8}	219.2	234.9	244.3	309.9	1908.15
Film F	39.80	2.75×10^{-8}	196.2	236.9	246.1	309.6	2196.39
Film G	45.28	4.02×10^{-8}	173.8	238.7	247.2	308.9	3295.92

Last but not least, in Table III. 1, B values (activation energy of the α relaxation) exhibited the usual decreasing trend as the crystallinity increased. In order to describe the change in fragile behavior, the strength index D was introduced. The strength index, $D = B/T_0$ is generally used as a quantitative evaluation of the fragile extent in glassy materials or super-cooled liquids and

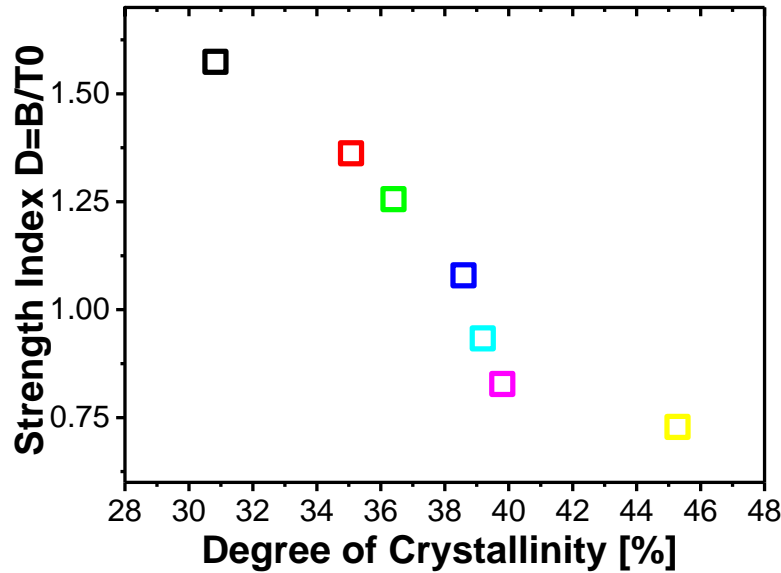


Figure III. 8 Strength index $D = B/T_0$ as a function of the degree of crystallinity for each processed terpolymer.

Figure III. 8 shows a plot of the index as a function of the degree of crystallinity. The strength indices D for the crystallized terpolymers followed a decreasing trend, indicating that their behavior went towards a more fragile character according to the Angell law [74, 75]. An increase in the fragile behavior reflects a more homogeneous amorphous phase in the terpolymer with a

higher degree of crystallinity which was in rather good agreement with the decrease of the average size of the CRR in the amorphous phase as mentioned in the section *Segmental Dynamics of Semicrystalline Terpolymers*. When it comes to the $T_{g,diel}/T_0$ values determined by VTF fitting parameters, as was the case of for the pristine terpolymer, $T_{g,diel}/T_0$ was estimated at ~ 1.089 and thus D was calculated as ~ 1.89 . This is slightly higher than the experimental value of 1.61 as extrapolated from B/T_0 . However, it was acceptable within the experimental uncertainty.

III. 4 Sub-glass β -relaxation mode

The β -relaxation regime has been identified as a broader and less intense typical relaxation mode at higher frequency or lower temperature. This phenomenological relaxation arose from localized dipole fluctuations. The β regime correlates with the twisting motion of the C-C backbone for terpolymer because no free and flexible side-groups on studied in the present work. This means that the effects originated from the local motion of rather short sequences comparable to the segmental dynamics [59, 76]. Multiple β relaxation components were decomposed when fitted to the HN equation. Given the non-instrumental role of the two shoulder components herein, current work would address the dominated relaxation component. By fitting to the HN equation, characteristic relaxation times τ_β were extrapolated and their values versus the reciprocal of the temperature ($1/T$) were plotted as shown in the full relaxation map of Figure III. 7c. The dependence of τ_β on the reciprocal of the temperature showed a quasi-linear correlation which is well described by an Arrhenius-type law, $\tau_\beta = \tau_\infty \exp(-E_A/RT)$, where τ_∞ is the pre-exponential factor; E_A denotes the apparent activation energy and R is the ideal gas constant. A lower E_A was observed for the pristine terpolymer at ca. 16.34 ± 1 kJ mol⁻¹, cf. Table III. 2. A considerable increase in E_β of 35.46 ± 3 kJ mol⁻¹ was obtained for the fully crystallized terpolymer as observed in several glass formers [45, 52, 77], suggesting the existence of a small energy barrier between the pristine terpolymer and its crystallized counterparts. Such results also imply that a local motion below T_g changes the relaxation dynamics, giving rise to the thermodynamic stability as the crystallization evolves. Hence, it is reasonable to assume that the evolution of β relaxation parameters is linked to the constrained molecular segmental dynamics in the amorphous phase. Moreover, the width of α_{HN} , independent of the temperature in the glass state, was around 0.20 ± 0.02 and showed a rather good symmetry ($\beta_{HN}=1.00$) as presented in Table III. 2.

Driven by the origins of two typical relaxation modes in P(VDF-TrFE-CTFE) terpolymers, a Johari-Goldstein (J-G)-like secondary relaxation, taken as the precursor of the α relaxation process, was transferred to the segmental structure relaxation as the temperature approached $T_{g,diel}$. Ngai reported on a separation of the α - and β -relaxations near the regulated T_g [78, 79]:

the logarithmic $\tau_\alpha(T_g)/\tau_\beta(T_g)$ had a linear dependence upon the magnitude of the β_{KWW} parameter derived from the KWW function which could be expressed as $\phi(t) = \tau(0)\exp[-(\tau/\tau_{KWW})^{\beta_{KWW}}]$ ($0 < \beta_{KWW} < 1$).

Table III. 2 Crystallinity dependence of the Havriliak-Negami fitting parameters and the apparent activation energy E_β for a terpolymer in the sub-glass state.

<i>Films</i>	χ_c (%)	α_{HN}	β_{HN}	τ_∞ (s)	E_β (kJ mol ⁻¹)
Film A	30.83	0.20±0.02	0.98±0.02	1.58±0.13 ×10 ⁻¹¹	16.34±0.9
Film B	35.07	0.21±0.02	0.98±0.02	2.46±0.21 ×10 ⁻¹²	21.83±1.2
Film C	36.40	0.21±0.03	1.00	3.81±0.08 ×10 ⁻¹⁴	30.44±2.3
Film D	38.59	0.19±0.02	0.99±0.01	1.36±0.17 ×10 ⁻¹³	27.50±4.8
Film E	39.19	0.20±0.01	0.97±0.03	8.39±0.23 ×10 ⁻¹⁴	28.32±3.4
Film F	39.80	0.19±0.02	1.00	1.46±0.18 ×10 ⁻¹⁵	36.56±4.3
Film G	45.28	0.21±0.03	0.98±0.02	4.67±0.27 ×10 ⁻¹⁶	35.46±3.9

III. 5 Mobility of Space Charges during High-Temperature processing

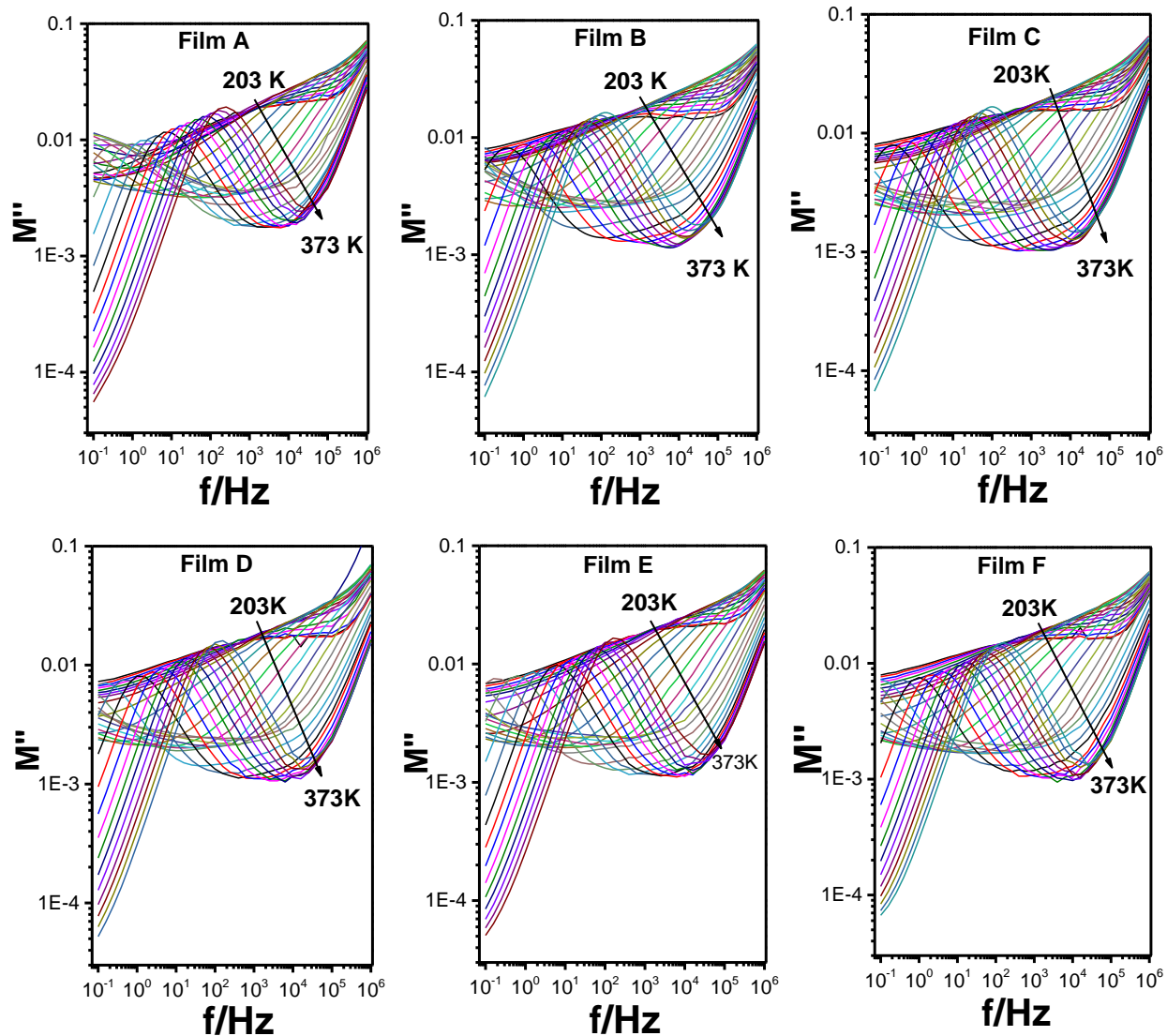
Ohmic conductivity effects at high temperature were several orders of magnitude higher than that in sub-glass state as shown in Figure III. 2. Values of real conductivity were calculated according to the complex conductivity ($\sigma^* = \sigma' + i\sigma''$) as a function of the frequency in Figure III. 10a. Two distinctive regions were observed as the temperature proceeded. At lower frequency and low temperature, the conductivity curves was less dependent upon the frequency increasing. This is reportedly ascribed to charge carrier transportation which leads to a main contribution in the dielectric loss spectra. The conductivity depended strongly upon the higher frequency which corresponded to a typical capacitive behavior. DC conductivity values for representative curve at 1Hz showed a VFT-type mode as a function of the reciprocal of the temperature as shown in inset of Figure III. 10a.

Generally, the charge carrier mobility has an influence on the conductivity relaxation modes in two typical mechanisms: one is termed as a proton-hopping theory and describes the charge motion trapped in the pendant H-bonds such as polymeric systems functionalized with hydroxyl, amide and amine groups [80, 81]. This mechanism functions without the pre-requisite of molecular mobility whereas another mode, the so-called Grotthuss mechanism, significantly depends upon the molecular diffusion process. Considering that there are no free protons in the P(VDF-TrFE-CTFE) terpolymer, the DC conductivity was ascribed to charge carrier motion in our case, i.e., ion transportation driven by the segmental dynamics in the amorphous phase [82]. Such ions were probably impurities which were introduced during the suspension polymerization process.

Due to conductivity of the amorphous phase in terpolymer films, free charge carrier ions, transferring through the conductive amorphous phase, piled up near the interfaces of the amorphous-crystal boundary, could give rise to interfacial polarization. The acquisition of DC conductivity relaxation times could not be extrapolated by dielectric loss spectra by fitting the HN equation at low frequency over high temperature. Instead, we introduced the electric modulus M^* in order to erase the main conductivity at low frequency. By using M^* , the influence of the dipolar polarization and electrode polarization at low frequency was minimized, while the motion of the charge carrier ions was emphasized at high temperature:

$$M^* = M' + iM'' = \frac{1}{\varepsilon^*} = \frac{i\varepsilon_0\omega}{\sigma^*} = \frac{\varepsilon'}{\varepsilon'^2 + \varepsilon''^2} + i \frac{\varepsilon''}{\varepsilon'^2 + \varepsilon''^2} \quad \text{III.6}$$

electric modulus loss spectra as a function of temperature for each case were depicted in Figure III. 9, sharing a very similar trend.



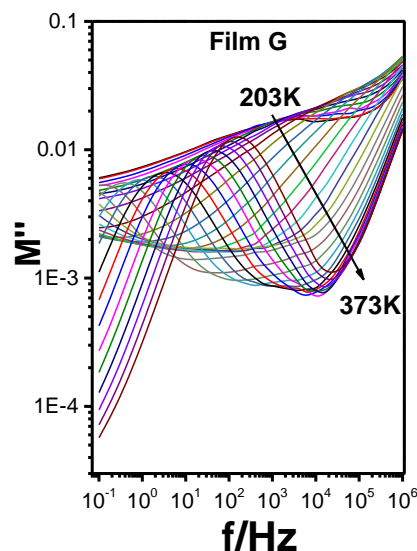
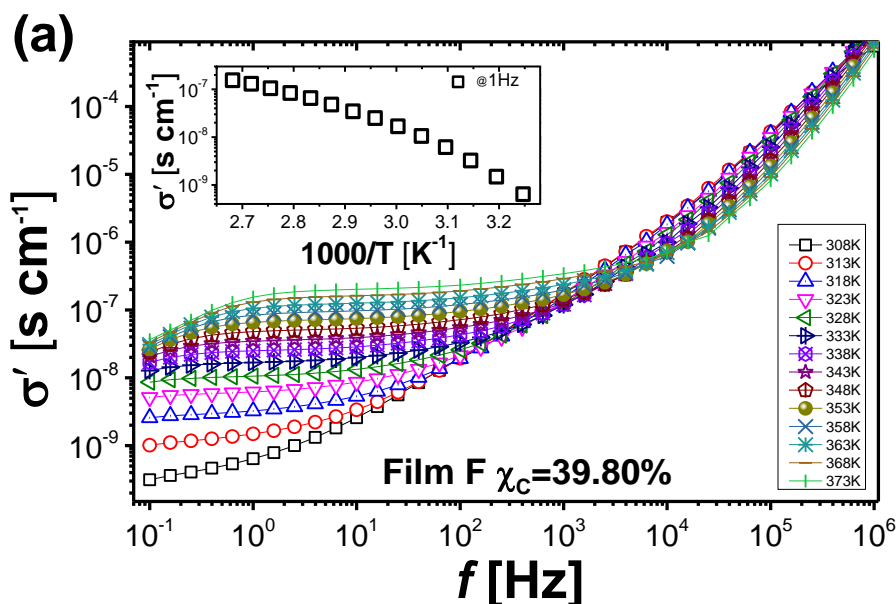


Figure III. 9 Imaginary part of dielectric modulus spectroscopies as function of frequency and temperature for each as-cast terpolymer film

By comparing the conductivity and the imaginary part of the electric modulus in Figure III. 10a and b, conductivity peaks were found to be highly temperature dependent for the representative Film F ($\chi_c=39.8\%$). It was also clearly observed that a characteristic plateau emerged expectedly as a function of frequency with an increase in temperature. Correspondingly, peaks of the fractional part of the imaginary electric modulus M'' moved to higher frequency as the temperature increased (no distinct peaks shown between 203 K and 303 K), indicating an enhanced motion of the charge carrier ions.



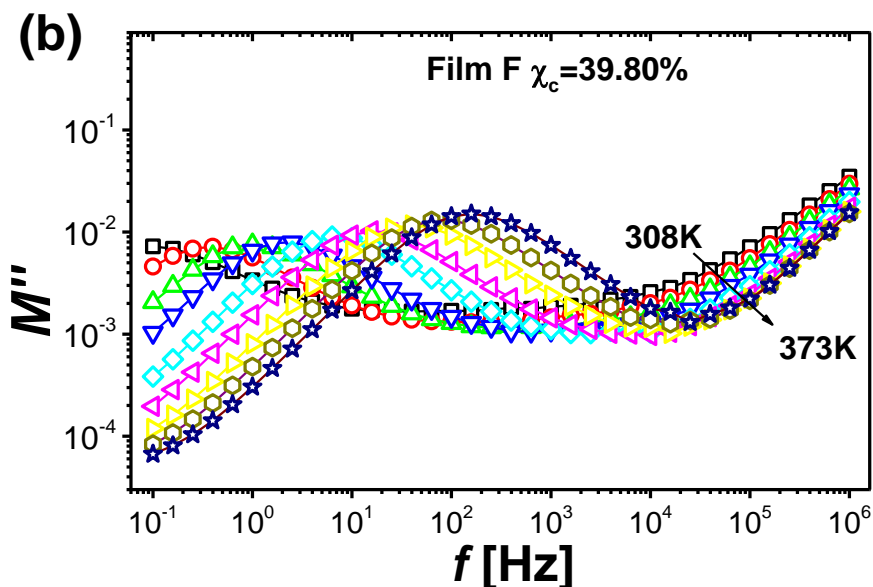


Figure III. 10 (a) The isothermal real part of the conductivity versus the full frequency scale for temperatures ranging from 203K to 373K for the as-treated terpolymer Film F; (b) the imaginary part of the electric modulus demonstrating a the shift towards higher frequency for the representative Film F. The lines are guides to the eye.

In order to characterize the main conductivity process due to the motion of the charge carrier ions, values of the DC conductivity relaxation time τ_{con} were extrapolated by localizing the peak frequency (f_{max}) of each isothermal electric modulus spectrum. As presented in Figure III. 11, the temperature dependence of τ_{con} , following a VTF-type behavior, was plotted. The Vogel temperature for pristine (T_{V-P}) and fully crystallized terpolymer (T_{V-F}) was found to be 223.5K and 228.2K, which is quite close to the Vogel temperature values found via VFT fitting to the segmental relaxation map (recall Table III. 2). As already stated, the terpolymer with the higher crystallinity had a significant interphase content, showed more fragile behavior and a constrained relaxation mobility. Fully crystallized terpolymers had a large Vogel temperature (T_V) which was in rather good agreement with the fact that the conductivity relaxation rate significantly depended upon the segmental molecular mobility in the amorphous phase [83]. When considering the constrained amorphous phase as the intermediate place for the diffusion of space charge carrier ions, it is reasonable to assume that with the evolution of the crystallization, transportation of the charge carrier ions was likely to be hindered in the interphase rather than continue towards the interface of the amorphous-crystal phase.

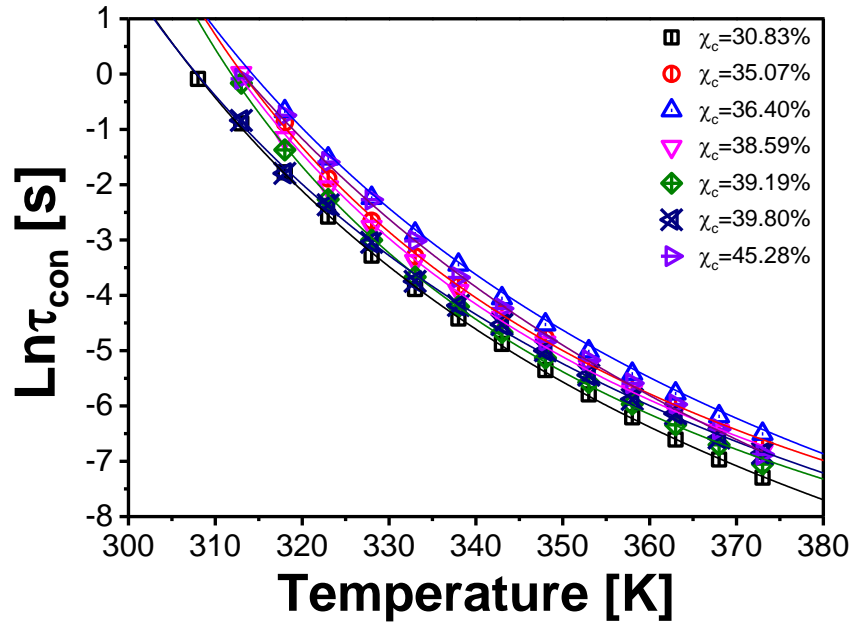


Figure III. 11 Temperature-dependence of the relaxation time upon crystallization evolution as obtained from M'' maxima. The lines correspond to VFT-type fitting curves.

IV Conclusions

The purpose of the current study was to provide as much information as possible on frequency and temperature dependence of the dielectric relaxation behavior of semi-crystalline P(VDF-TrFE-CTFE) terpolymers. In order to evaluate the relaxation map, terpolymers containing different fractions of crystallinity were prepared by an isothermal crystallization process. Firstly, a slowing down of the segmental relaxation rate was found in the terpolymer with the highest crystallinity. The size of the Cooperative Rearranging Region in the amorphous phase declined. The decrease of the strength index D indicated that the crystallized terpolymer had become more fragile with higher degree of crystallinity. However, a large interphase region led to an increase in dielectric strength as opposed to the non-ferroelectric polymer. Such a phenomenon was ascribed to the enhanced fraction of the interphase which was more or less orientated.

The Curie relaxation was accelerated by increasing the amounts of crystalline lamellae, which had a great influence on the segmental relaxation. Secondly, sub-glass β relaxation processes were also constrained and followed an Arrhenius-type mode. Considering the chemical composition of terpolymers, it is reasonable to assume that the β relaxation processes correlated with the segmental relaxation. Finally, the mobility of the space charge at high temperature was analyzed by an electric modulus method. A VFT-type mode revealed the DC conductivity vs. the relaxation at several temperatures, and suggested that segmental dynamics in the amorphous mode were responsible for the motion of the space charge carrier ions. A dielectric relaxation

map provided a full picture of the dielectric behavior based on frequency and temperature. The results gave us an idea of the implementation of a point of view for the electromechanical system. The correlation of these behaviors with electromechanical properties is currently being studied.

References

1. Zhang, Q., V. Bharti, and X. Zhao, *Giant electrostriction and relaxor ferroelectric behavior in electron-irradiated poly (vinylidene fluoride-trifluoroethylene) copolymer*. Science, 1998. **280**(5372): p. 2101-2104.
2. Capsal, J.-F., et al., *Plasticized relaxor ferroelectric terpolymer: Toward giant electrostriction, high mechanical energy and low electric field actuators*. Sensors and Actuators A: Physical, 2014. **207**: p. 25-31.
3. Neese, B., et al., *Large electrocaloric effect in ferroelectric polymers near room temperature*. Science, 2008. **321**(5890): p. 821-823.
4. Lu, S.G. and Q. Zhang, *Electrocaloric Materials for Solid - State Refrigeration*. Advanced Materials, 2009. **21**(19): p. 1983-1987.
5. Sebald, G., et al., *Differential scanning calorimeter and infrared imaging for electrocaloric characterization of poly (vinylidene fluoride-trifluoroethylene-chlorofluoroethylene) terpolymer*. Applied Physics Letters, 2012. **101**(2): p. 022907.
6. Jin, J., et al., *Multiferroic polymer composites with greatly enhanced magnetoelectric effect under a low magnetic bias*. Advanced Materials, 2011. **23**(33): p. 3853-3858.
7. Nguyen, T.H.L., et al., *Magnetoelectric properties of nickel nanowires-P (VDF-TrFE) composites*. Materials Chemistry and Physics, 2015. **153**: p. 195-201.
8. Capsal, J.-F., et al., *Dielectric relaxations and ferroelectric behaviour of even-odd polyamide PA 6*, 9. Polymer, 2010. **51**(20): p. 4606-4610.
9. Capsal, J.-F., et al., *Dynamic mechanical behaviour of polyamide 11/Barium titanate ferroelectric composites*. Polymer, 2010. **51**(22): p. 5207-5211.
10. Guo, S., et al., *Electron-irradiated electrostrictive P (VDF-TrFE) copolymer transducers*. Sensors and Actuators A: Physical, 2004. **112**(1): p. 134-141.
11. Koga, K. and H. Ohgashi, *Piezoelectricity and related properties of vinylidene fluoride and trifluoroethylene copolymers*. Journal of applied physics, 1986. **59**(6): p. 2142-2150.
12. Shin, Y.J., et al., *Chemically cross-linked thin poly (vinylidene fluoride-co-trifluoroethylene) films for nonvolatile ferroelectric polymer memory*. ACS applied materials & interfaces, 2011. **3**(2): p. 582-589.
13. Khanchaitit, P., et al., *Ferroelectric polymer networks with high energy density and improved discharged efficiency for dielectric energy storage*. Nature communications, 2013. **4**.
14. Guan, F., et al., *Crystal orientation effect on electric energy storage in poly (vinylidene fluoride-co-hexafluoropropylene) copolymers*. Macromolecules, 2009. **43**(1): p. 384-392.
15. Smith, O.N.L., et al., *Enhanced Permittivity and Energy Density in Neat Poly (vinylidene fluoride-trifluoroethylene-chlorotrifluoroethylene) Terpolymer Films through Control of Morphology*. ACS applied materials & interfaces, 2014. **6**(12): p. 9584-9589.

16. Fukao, K. and Y. Miyamoto, *Dynamical transition and crystallization of polymers*. Physical review letters, 1997. **79**(23): p. 4613.
17. Nogales, A., et al., *Influence of the crystalline structure in the segmental mobility of semicrystalline polymers: poly (ethylene naphthalene-2, 6-dicarboxylate)*. Macromolecules, 2000. **33**(25): p. 9367-9375.
18. Zhu, L. and Q. Wang, *Novel ferroelectric polymers for high energy density and low loss dielectrics*. Macromolecules, 2012. **45**(7): p. 2937-2954.
19. Martins, P., A. Lopes, and S. Lanceros-Mendez, *Electroactive phases of poly (vinylidene fluoride): Determination, processing and applications*. Progress in polymer science, 2014. **39**(4): p. 683-706.
20. Lin, Y., et al., *Casting solvent effects on molecular dynamics of weak dynamic asymmetry polymer blend films via broadband dielectric spectroscopy*. Journal of Membrane Science, 2013. **439**: p. 20-27.
21. Park, Y.J., et al., *Irreversible extinction of ferroelectric polarization in P (VDF-TrFE) thin films upon melting and recrystallization*. Applied physics letters, 2006. **88**(24): p. 242908.
22. Capsal, J.-F., et al., *Molecular mobility in piezoelectric hybrid nanocomposites with 0–3 connectivity: Volume fraction influence*. Journal of Non-Crystalline Solids, 2011. **357**(19): p. 3410-3415.
23. Capsal, J.-F., E. Dantras, and C. Lacabanne, *Molecular mobility interpretation of the dielectric relaxor behavior in fluorinated copolymers and terpolymers*. Journal of Non-Crystalline Solids, 2013. **363**: p. 20-25.
24. Capsal, J.F., et al., *Enhanced electrostriction based on plasticized relaxor ferroelectric P (VDF - TrFE - CFE/CTFE) blends*. Journal of Polymer Science Part B: Polymer Physics, 2015. **53**(19): p. 1368-1379.
25. Klein, R.J., J. Runt, and Q. Zhang, *Influence of Crystallization Conditions on the Microstructure and Electromechanical Properties of Poly (vinylidene fluoride-trifluoroethylene-chlorofluoroethylene) Terpolymers*. Macromolecules, 2003. **36**(19): p. 7220-7226.
26. Schönhals, A. and F. Kremer, *Theory of Dielectric Relaxation*, in *Broadband Dielectric Spectroscopy*, F. Kremer and A. Schönhals, Editors. 2003, Springer Berlin Heidelberg. p. 1-33.
27. Linares, A., et al., *Molecular dynamics in PVDF/PVA blends as revealed by dielectric loss spectroscopy*. Journal of Polymer Science Part B: Polymer Physics, 2007. **45**(13): p. 1653-1661.
28. Ezquerro, T., et al., *Double ferroelectric - to - paraelectric transition in 70/30 vinylidene fluoride - trifluoro ethylene copolymer as revealed by dielectric spectroscopy*. Journal of Polymer Science Part B: Polymer Physics, 1994. **32**(8): p. 1449-1455.
29. Fukao, K. and Y. Miyamoto, *Glass transitions and dynamics in thin polymer films: dielectric relaxation of thin films of polystyrene*. Physical Review E, 2000. **61**(2): p. 1743.

30. Li, J., et al., *Nanocomposites of ferroelectric polymers with TiO₂ nanoparticles exhibiting significantly enhanced electrical energy density*. Advanced Materials, 2009. **21**(2): p. 217-221.
31. Yin, X., J.-F. Capsal, and D. Guyomar, *A comprehensive investigation of poly (vinylidene fluoride-trifluoroethylene-chlorofluoroethylene) terpolymer nanocomposites with carbon black for electrostrictive applications*. Applied Physics Letters, 2014. **104**(5): p. 052913.
32. Castagna, A.M., et al., *The role of hard segment content on the molecular dynamics of poly (tetramethylene oxide)-based polyurethane copolymers*. Macromolecules, 2011. **44**(19): p. 7831-7836.
33. Lu, Y., et al., *Structural Dependence of Phase Transition and Dielectric Relaxation in Ferroelectric Poly (vinylidene fluoride– chlorotrifluoroethylene– trifluoroethylene) s*. The Journal of Physical Chemistry B, 2008. **112**(34): p. 10411-10416.
34. Xu, H., et al., *Ferroelectric and electromechanical properties of poly (vinylidene-fluoride–trifluoroethylene–chlorotrifluoroethylene) terpolymer*. Applied Physics Letters, 2001. **78**(16): p. 2360-2362.
35. Kim, K.J., et al., *Curie transition, ferroelectric crystal structure, and ferroelectricity of a VDF/TrFE (75/25) copolymer 1. The effect of the consecutive annealing in the ferroelectric state on curie transition and ferroelectric crystal structure*. Journal of Polymer Science Part B: Polymer Physics, 1994. **32**(15): p. 2435-2444.
36. Bao, H.M., et al., *Phase transitions and ferroelectric relaxor behavior in P(VDF-TrFE-CFE) terpolymers*. Macromolecules, 2007. **40**(7): p. 2371-2379.
37. Álvarez, C., et al., *Structure-dynamics relationship in crystallizing poly (ethylene terephthalate) as revealed by time-resolved X-ray and dielectric methods*. Polymer, 2004. **45**(11): p. 3953-3959.
38. Soccio, M., et al., *Relaxation dynamics and cold crystallization of poly (pentamethylene terephthalate) as revealed by dielectric spectroscopy*. Polymer, 2014. **55**(6): p. 1552-1559.
39. Brás, A.R., et al., *Crystallization of poly (L-lactic acid) probed with dielectric relaxation spectroscopy*. Macromolecules, 2006. **39**(19): p. 6513-6520.
40. Mano, J.F., et al., *Cold crystallization of PLLA studied by simultaneous SAXS and WAXS*. Macromolecular Materials and Engineering, 2004. **289**(10): p. 910-915.
41. Sperling, L.H., *Introduction to physical polymer science*. 2005: John Wiley & Sons.
42. Qiao, J., et al., *Characteristics of the structural and Johari–Goldstein relaxations in Pd-based metallic glass-forming liquids*. The Journal of Physical Chemistry B, 2014. **118**(13): p. 3720-3730.
43. Yang, L., et al., *Semicrystalline Structure–Dielectric Property Relationship and Electrical Conduction in a Biaxially Oriented Poly (vinylidene fluoride) Film under High Electric Fields and High Temperatures*. ACS applied materials & interfaces, 2015. **7**(36): p. 19894-19905.
44. Wang, Y., et al., *Morphological contributions to glass transition in poly (L-lactic acid)*. Macromolecules, 2005. **38**(11): p. 4712-4718.

45. Bras, A., et al., *Influence of crystallinity in molecular motions of poly (L-lactic acid) investigated by dielectric relaxation spectroscopy*. Macromolecules, 2008. **41**(17): p. 6419-6430.
46. Delbreilh, L., et al., *Study of poly (bisphenol A carbonate) relaxation kinetics at the glass transition temperature*. European polymer journal, 2007. **43**(1): p. 249-254.
47. Adam, G. and J.H. Gibbs, *On the temperature dependence of cooperative relaxation properties in glass - forming liquids*. The journal of chemical physics, 1965. **43**(1): p. 139-146.
48. Delpouve, N., et al., *Cooperative rearranging region size in semi-crystalline poly (l-lactic acid)*. Polymer, 2008. **49**(13): p. 3130-3135.
49. Delpouve, N., A. Saiter, and E. Dargent, *Cooperativity length evolution during crystallization of poly (lactic acid)*. European Polymer Journal, 2011. **47**(12): p. 2414-2423.
50. Donth, E., *Characteristic length of the glass transition*. Journal of Polymer Science Part B: Polymer Physics, 1996. **34**(17): p. 2881-2892.
51. Donth, E., *Phenomenological treatment of dynamic glass transition heterogeneity*. Acta polymerica, 1999. **50**(7): p. 240-251.
52. Martín-Fabiani, I., et al., *Dielectric relaxation of poly (trimethylene terephthalate) in a broad range of crystallinity*. Polymer, 2013. **54**(21): p. 5892-5898.
53. Schönhals, A., *Molecular dynamics in polymer model systems, in Broadband dielectric spectroscopy*. 2003, Springer. p. 225-293.
54. Onsager, L., *Electric moments of molecules in liquids*. Journal of the American Chemical Society, 1936. **58**(8): p. 1486-1493.
55. Wunderlich, B., *Reversible crystallization and the rigid–amorphous phase in semicrystalline macromolecules*. Progress in polymer science, 2003. **28**(3): p. 383-450.
56. Androsch, R. and B. Wunderlich, *The link between rigid amorphous fraction and crystal perfection in cold-crystallized poly (ethylene terephthalate)*. Polymer, 2005. **46**(26): p. 12556-12566.
57. Arnoult, M., E. Dargent, and J. Mano, *Mobile amorphous phase fragility in semi-crystalline polymers: Comparison of PET and PLLA*. Polymer, 2007. **48**(4): p. 1012-1019.
58. Rault, J., *Origin of the Vogel–Fulcher–Tammann law in glass-forming materials: the α – β bifurcation*. Journal of Non-Crystalline Solids, 2000. **271**(3): p. 177-217.
59. Leon, C., K. Ngai, and C. Roland, *Relationship between the primary and secondary dielectric relaxation processes in propylene glycol and its oligomers*. The Journal of chemical physics, 1999. **110**(23): p. 11585-11591.
60. Angell, C., *The old problems of glass and the glass transition, and the many new twists*. Proceedings of the National Academy of Sciences, 1995. **92**(15): p. 6675-6682.
61. Böhmer, R., et al., *Nonexponential relaxations in strong and fragile glass formers*. The Journal of chemical physics, 1993. **99**(5): p. 4201-4209.

62. Faria, L. and R. Moreira, *Dielectric behavior of P (VDF - TrFE)/PMMA blends*. Journal of Polymer Science Part B: Polymer Physics, 1999. **37**(21): p. 2996-3002.
63. Sharma, M., G. Madras, and S. Bose, *Cooperativity and structural relaxations in PVDF/PMMA blends in the presence of MWNTs: an assessment through SAXS and dielectric spectroscopy*. Macromolecules, 2014. **47**(4): p. 1392-1402.
64. Fitz, B.D. and J. Mijovic, *Segmental dynamics in poly (methylphenylsiloxane) networks by dielectric relaxation spectroscopy*. Macromolecules, 1999. **32**(10): p. 3518-3527.
65. Arabeche, K., et al., *Fragility and molecular mobility in micro- and nano-layered PC/PMMA films*. Polymer, 2014. **55**(6): p. 1546-1551.
66. Yin, H., S. Napolitano, and A. Schönhals, *Molecular mobility and glass transition of thin films of poly (bisphenol a carbonate)*. Macromolecules, 2012. **45**(3): p. 1652-1662.
67. Saiter, A., et al., *Cooperative rearranging region size determination by temperature modulated DSC in semi-crystalline poly (L-lactide acid)*. European Polymer Journal, 2007. **43**(11): p. 4675-4682.
68. Buckley, G., et al., *Electrostrictive Properties of Poly (vinylidene fluoride-trifluoroethylene-chlorotrifluoroethylene)*. Chemistry of materials, 2002. **14**(6): p. 2590-2593.
69. Ang, C. and Z. Yu, *"Dielectric relaxor" behavior of electroactive fluorinated polymers*. Applied Physics Letters, 2005. **86**(26): p. 262903.
70. Yang, L., et al., *Novel polymer ferroelectric behavior via crystal isomorphism and the nanoconfinement effect*. Polymer, 2013. **54**(7): p. 1709-1728.
71. Bobnar, V., et al., *Dielectric properties of relaxor-like vinylidene fluoride-trifluoroethylene-based electroactive polymers*. Macromolecules, 2003. **36**(12): p. 4436-4442.
72. Bobnar, V., et al., *Glassy dynamics in an electron-irradiated poly (vinylidene fluoride-trifluoroethylene) copolymer system*. Physical Review B, 2003. **67**(9): p. 094205.
73. Ang, C. and Z. Yu, *Ferroelectric, Electroactive, and Dielectric - Relaxation Behavior of Fluoropolymers*. Advanced Materials, 2004. **16**(12): p. 979-982.
74. Angell, C.A., *Formation of glasses from liquids and biopolymers*. Science, 1995. **267**(5206): p. 1924-1935.
75. Angell, C., *Relaxation in liquids, polymers and plastic crystals—strong/fragile patterns and problems*. Journal of Non-Crystalline Solids, 1991. **131**: p. 13-31.
76. Ngai, K., *Correlation between the secondary β -relaxation time at T_g with the Kohlrausch exponent of the primary α relaxation or the fragility of glass-forming materials*. Physical Review E, 1998. **57**(6): p. 7346.
77. Jomaa, M., et al., *Dielectric properties of segmented polyurethanes for electromechanical applications*. Polymer, 2015. **63**: p. 214-221.
78. Ngai, K. and C. Roland, *Chemical structure and intermolecular cooperativity: dielectric relaxation results*. Macromolecules, 1993. **26**(25): p. 6824-6830.

79. Ngai, K. and S. Capaccioli, *Relation between the activation energy of the Johari-Goldstein β relaxation and T_g of glass formers*. Physical Review E, 2004. **69**(3): p. 031501.
80. Adrjanowicz, K., et al., *Dynamic Glass Transition and Electrical Conductivity Behavior Dominated by Proton Hopping Mechanism Studied in the Family of Hyperbranched Bis-MPA Polyesters*. Macromolecules, 2014. **47**(16): p. 5798-5807.
81. Sangoro, J., et al., *Charge transport and dipolar relaxations in hyperbranched polyamide amines*. Macromolecules, 2009. **42**(5): p. 1648-1651.
82. Fragiadakis, D., et al., *Molecular mobility, ion mobility, and mobile ion concentration in poly (ethylene oxide)-based polyurethane ionomers*. Macromolecules, 2008. **41**(15): p. 5723-5728.
83. Sui, G., et al., *Dielectric properties and conductivity of carbon nanofiber/semi-crystalline polymer composites*. Acta Materialia, 2008. **56**(10): p. 2381-2388.

Chapter IV

Plasticization Effects on Relaxor Ferroelectric P(VDF-TrFE-CTFE) Terpolymers: Mechanical Behavior, Morphology and Molecular Mobility

I Introduction

Fluorinated polymer, a family of the electroactive polymer, which responds to the external electric excitation by a significantly dimensional change in its geometric shapes, attracts an increasing attention for many decades, due to the rapid development of the needs for a wide range of advanced electromechanical device applications, including wireless mobile devices, hybrid power vehicles, high energy weapon system and medical monitoring devices, etc. However, ferroelectric fluorinated polymers also suffered some strategic issues, for instance, limited shape change in defined direction, dwarf elastic energy density and thus low load capacity application, etc. And actions have already been carried out to tackle these challenges. In previous chapter, we reviewed the main strategies being employed to improve the electric field-induced strain S_{ij} , electric energy density $U = \int E dD$ and elastic mechanical energy density E_μ , which the latter can be read as $E_\mu = 1/2 Y S_{ij}^2$. Briefly, the E_μ value consists in the two contributing factors, Young's modulus Y and defined field-induced strain S_{ij} . For an electrostrictive polymer materials, the figure of merit of the electrostrictive strain S_{ij} can be reliably determined by the factor $k \frac{(\varepsilon' - 1)^2}{\varepsilon' \cdot Y}$, where ε' is the relative dielectric constant of the electrostrictive polymers. In case of electrostrictive P(VDF-TrFE-CTFE) or P(VDF-TrFE-CFE) terpolymers with their $\varepsilon' \gg 1$, the figure of merit of electrostrictive strain can be simplified as ε'/Y . And the electrical and mechanical energy can both benefit from the polymer materials with high dielectric permittivity. Based on this conception in mind, Lu et al [1] synthesized a family of PVDF-based terpolymers with high and tunable dielectric permittivity relying on a copolymerization reaction approach. They disclosed that the dielectric permittivity heavenly depends on the ternary CTFE composition. Zhang group [2, 3] has also reported an environmental friendly and controllable P(VDF-CTFE) hydrogenation en route to the synthesize P(VDF-CTFE-TrFE) via a transition-metal complex mediated radical chain transfer reaction. These chemical approaches are limited to revolutionarily improve the dielectric permittivity. Doping with the filler is an alternative fashion to achieve this destination. Generally, fillers employed for doping are the family of materials either with high energy density or enormous dielectric constant. Li et al [4] report high-energy-density polymer nanocomposites based on surface-functionalized TiO₂ nanocrystals as dopants in P(VDF-TrFE-CTFE) matrix. High dielectric performance in the nanocomposites is realized via the large enhancement in polarization response at high electric fields and changes in polymer microstructure induced by the nanofillers. Our group recently proposed a terpolymer nanocomposite with carbon black as a dopant and showed a several-fold increase of dielectric constant with low dielectric loss. Besides, the out-performance electric energy density material were also obtained by incorporation of ultra-thin boron nitride nanosheets into terpolymer matrix due to the remarkable improvements in electric breakdown strength based on the underlying mechanism $U = 1/2 \varepsilon_0 \varepsilon' E^2$. However, there always rises the compatible challenges involving

the affinity between inorganic fillers and terpolymer matrix and then an unwanted increase in mechanical strength, both of which attracted the extensive research attentions. The problems in inorganic organic hybrid composite could be addressed via an all-organic blend system. Zhang et al [5] firstly reported an ultra-high-dielectric-constant conductive polymer copperphthalocyanine (CuPc) doped terpolymer composite, the feasibility of the doping was successfully manifested by high strain and high elastic energy density under low applied electric fields. Wang et al [6] further developed Zhang's proposition and improved the incompatibility of CuPc in terpolymer matrix. Although the key issue of compatibility was solved, undesirable increase of mechanical strength and a percolative all-organic composite were yielded.

More recently, our research group [7, 8] proposed a facile and efficient approach via doping a small molecule plasticizer in the terpolymer matrix. The resulting composite blends characterized a several-fold surge of dielectric constant and elastic mechanical energy density as shown in Figure IV. 1. This also accompanied with a tremendous enhancement of the electromechanical coupling effect except a slight slump down trend of electric breakdown strength and mechanical strength Y .

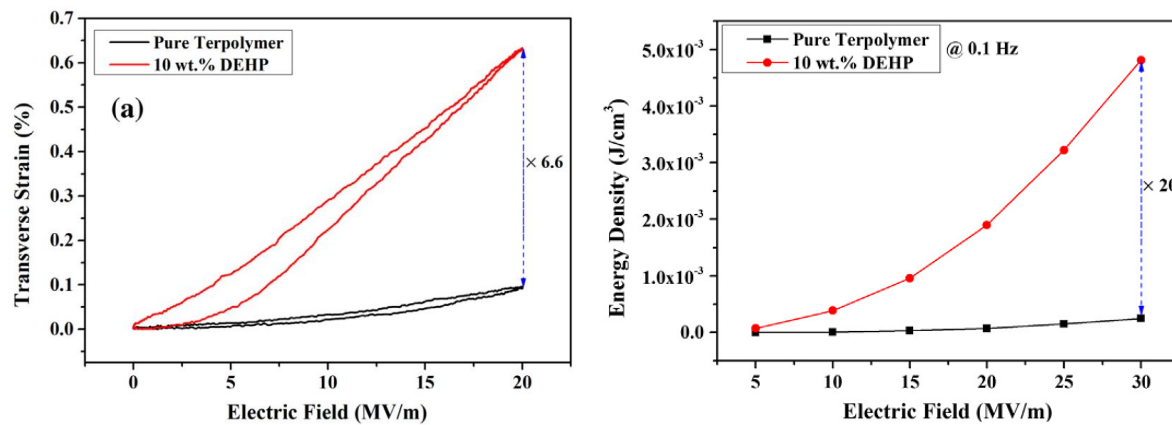


Figure IV. 1 (a) electric field-induced transverse strain for the pure and 10% DEHP modified terpolymers under 0.1 Hz sinusoidal signal controlled tensile mode; (b) elastic mechanical energy density for pure and 10% DEHP modified terpolymers as a function of external electric field. Adapted from the graphics from the literature[8].

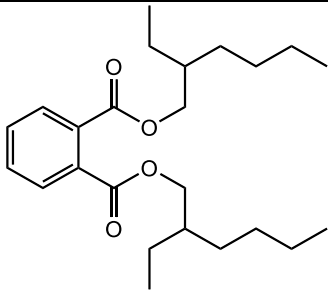
II Experimental Section

II. 1 Materials and Elaboration

P(VDF-TrFE-CTFE) terpolymer powder with molar composition ratio of VDF/TrFE/CTFE=61.7:30.4:7.9 were purchased from Piezotech S.A.S (Arkema Group, France) which was synthesized by a suspension polymerization with molecular weight of $\langle M_w \rangle = 22,600$ g mol⁻¹. Prior to use, no further purification was carried out. Commercial Di-2-ethylhexyl

phthalate (DEHP) and organic solvents were all purchased from Sigma-Aldrich and used as received. The physico-chemical characteristics of DEHP plasticizer were listed in Table IV. 1. The transparent terpolymer solution were prepared by solubilizing the terpolymer powder in Meth Ethyl Ketone (MEK) solvent in a concentration of 14% (mass fraction). Pristine Film A was prepared by solution-casting on a polished and acetone (reagent grade)-rinsed glass support from the well-prepared MEK transparent solution. The tailor-made film thickness was normalized by a doctor blade film applicator. Afterwards, the fresh terpolymer deposition then moved to a sealed chamber equipped with the ventilating system, allowing the airborne dust impurities

Table IV. 1 Summary of DEHP physico-chemical properties

Acronym	Properties and Formula
Chemical structure	
CAS number	117-81-7
Formula	$C_{24}H_{38}O_4$
Molecular Weight ($g \cdot mol^{-1}$)	390.56
Density ($g \cdot mL^{-1}$)	0.986
Melting point	-55 °C (218 K)
Boiling point	385 °C (658 K)
Glass transition temperature (K)	-76.3 °C (196.8 K) [9, 10]
Appearance	Transparent, Oily liquid

minimized. Freshly-made bulk terpolymer films were dried for 48h over vacuum at room temperature. Subsequently, bulk as-casted pristine films were followed by 2h annealing in a 80°C ($T_a = T_g + 105$ K, $T_{g,bulk} = ca. 248$ K) oven. Then the variety of series 5%, 10% and 15% (mass fraction) plasticizer to the terpolymer residual were dissolved in the neat terpolymer solution and mixed thoroughly. The modified terpolymer blends were obtained by film casting of the corresponding polymer solution. The average thickness of as-casted terpolymer films was approximately $50 \pm 5 \mu m$. For the dielectric spectroscopy measurement, the 10 nm-thick Au-electrode layer was sputtered on both sides of circular terpolymers film plates in a diameter of 20 mm with the aid of a plastic shadow mask. It should be noted that metal electrode layer would influence the dielectric behavior in terms of thickness, metal type and oxidized byproduct [11], etc, especially when investigating the ultrathin films [12]. Bulk polymer exploited in this current

contribution made this issue far less significance. The metal/terpolymer/metal parallel plate capacitors were prepared for broadband dielectric spectroscopy measurement.

II. 2 Methods and Techniques

II.2.1 Characterization Technique

Before characterization, terpolymer films were merged into absolute ethanol to rinse the free surface DEHP leaching from the terpolymer blends. After that, solvent-free terpolymer blends were obtained under ultrahigh vacuum for mechanical and dielectric characterization. Non-conventional assembly was established to evaluate the plasticizing effects on mechanical strength Young's modulus properties and part of this study has been reported in our previous contribution [8, 13]. The terpolymer film belts with the effective 50 mm in length, 10 mm in width were clamped and drawn through the controlled Newport platform by a functional generator. A triangular signal was input to the unidirectional motor and the samples were stretched at maximal 1% elongation at a tensile rate of 30 mm/min. The strain-stress data acquisition was recorded by LabVIEW software (National Instrument, Austin US) and the slopes of linear fit to the strain-stress curves were taken as Young's modulus for terpolymers pristine and blends. The surface morphology and microstructure profiles of the pristine and terpolymer blends were characterized by atomic force microscopy (AFM). Prior to AFM patterns acquisition, 10×10 mm² rectangular terpolymer samples were bonded to the freshly-cleaned silicon wafer via a conductive glue. AFM images were acquired in air at room temperature using a Nanoscope IIIa Multimode (Digital Instruments/VEECO, CA) with a tapping mode in a scan rate of 1 Hz. The thermal behaviors of neat and DEHP doped terpolymer blends were performed by Differential Scanning Calorimetry (DSC) technique with the help of DSC 131 Setaram Evo equipped with a liquid nitrogen cryostat accessory. A normalized 18 mg amount of each specimen were placed in an aluminum pan and was heated with a wide temperature range from 203K (-70 °C) to 473K (200 °C) in a ramp rate of 10 K/min under a nitrogen purge of 1.5 bars. Prior to DSC thermogram trace collection, the temperature and enthalpy were calibrated using an alumina standard. The baseline curve was also performed by running with the empty sample cell as blank. Each thermogram trace was analyzed by Calisto software package. The glass transition (T_g) was designated by the midpoint of the glass transition region. And Curie transition temperature (T_C) and melting regions of neat and terpolymers blends were also tabulated.

II.2.2 Device Fabrication and Characterization

Dielectric Data Acquisition. Broadband dielectric relaxation spectroscopy was carried out on a Solartron 1260 impedance-analyzer equipped with Model 129610A LHe LN2 Cryostat temperature-controlled system. The as-deposited dielectric terpolymer circular films with a diameter of 20 mm were metalized by sputtering gold on both surfaces through a shadow mask.

The metal/terpolymer/metal parallel capacitors were sandwiched between two polished copper electrodes mounted on the sample holders. The samples were then exposed to the evaporated nitrogen stream from the liquid nitrogen dewar by which temperature control was performed with a precision of $\pm 0.1\text{K}$. Dielectric data acquisition was conducted with frequency sweeping from 10^{-1} to 10^6 Hz at a low bias voltage (1 V). Isothermal broadband dielectric measurements were carried out within an extended temperature (T) range of $203\text{K} \leq T \leq 373\text{K}$. The capacitor-like sample was cooled down to 203K in a moderate cooling rate so as to eschew a thermodynamical non-equilibrium of molecular chain entanglement during the cooling step. Then the dielectric measurements were triggered isothermally in 5K intervals. The real and imaginary parts of the permittivity frequency-dependent dielectric data were collected by the Solartron software package.

Dielectric Data Analysis. To picture the quantitative relaxation time distribution and dielectric strength $\Delta\epsilon$, isothermal dielectric spectroscopy data were analyzed by the phenomenological Havriliak-Negami (HN) equation [14]. All the dielectric data were fitted with the Winfit32 software package (Novocontrol, Germany). For the sum of superimposed dielectric spectra, the HN equation reads:

$$\epsilon^* = \epsilon_{\infty} + \sum_j \frac{\Delta\epsilon_j}{[1 + (i\omega\tau_{HNj})^{\alpha_{HN}}]^{\beta_{HN}}} + i \left(\frac{\sigma}{\epsilon_0\omega} \right)^s \quad \text{IV. 1}$$

where ϵ_0 is the dielectric permittivity in vacuum; ϵ_{∞} represents the dielectric constant at infinite frequency, much higher than the relaxation rate within the limited frequency scale; $\Delta\epsilon_j$ is the respective dielectric strength of relaxation at an index above which appears the dielectric relaxation process; τ_{HNj} denotes the average characteristic relaxation time of each process; α_{HN} , β_{HN} ($0 < \alpha_{HN} < 1$, $0 < \alpha_{HN}\beta_{HN} \leq 1$) are the shape parameters which describe respectively the symmetry, asymmetry and broadness of the corresponding spectra over the spectral window. The right hand expression cluster denotes the conductive effects on the dielectric measurements where σ is the sample conductivity mainly contributing to the imaginary spectra at high temperature and low frequency. S ($0 < s \leq 1$) is the conductive fitting parameter that describes the Ohmic effects of the direct current (DC) conductivity. Empirically, for $\beta_{HN} = 1$, the Havriliak–Negami equation deduce to the Debye relaxation model as a Cole-Cole equation. Fitting parameters characteristic of the relaxation time τ_{HN} , α_{HN} and β_{HN} are extrapolated and τ_{HN} is related to model-independent relaxation time $\tau_{max} = 1/2\pi f_{max}$ which corresponds to the peak position of the maximum dielectric loss, calculated according to equation 4. 2.

$$\tau_{max} = \tau_{HN} \left[\sin \frac{\alpha_{HN} \beta_{HN} \pi}{2(\beta_{HN} + 1)} \right]^{1/\alpha_{HN}} \left[\sin \frac{\alpha_{HN} \pi}{2(\beta_{HN} + 1)} \right]^{-1/\alpha_{HN}} \quad \text{IV. 2}$$

III Results and Discussions

III. 1 Miscibility and Effects of plasticizer on thermal behaviors of terpolymers

The influence of the varying mass fraction of DEHP molecules on thermal transition behaviors of P(VDF-TrFE-CTFE) was examined by DSC traces. Firstly, the thermogram traces of pristine and DEHP modified terpolymer blends were demonstrated over a wide temperature range in Figure IV. 2. During the DSC heating ramps owing to its molecular chain nature comprising of double carbon bonds backbone with pendant free groups, the obscure changes of enthalpy appearing at approximately -22.9 °C can be attributed to the glass transition temperature for the plasticizer-free pristine film, in accordance with the value in our previous study. And it has widely been recognized that the glass transition temperature T_g anomaly is the most important criteria of the miscibility of the polymer blends [9, 15, 16]. This is also an indicative parameter of the plasticizing effects since the plasticizer in theory results in enhanced flexibility of macromolecular chain in terpolymers. Not surprisingly, the single glass transition values were revealed for each case of pristine and DEHP loaded terpolymer matrix. Otherwise, the multiphase transition would be observed referring to the macro-phase of the DEHP agglomeration. The plasticizing effects on the segmental relaxation of the molecules near glass transition were availably disclosed by other techniques latter on. And it should be also noted that no endothermic peaks appeared at around -50 °C, below which the solid DEHP was supposed to start melting. All these phenomena lead to a conclusion, that is, the excellent miscibility of each components between terpolymer host and DEHP molecules.

However, the broad and moderate thermal peaks at lower temperature and the strong enthalpy flow regimes at higher, the both two endothermic peaks saw the distinct characteristics. The intensive peaks located at higher temperature were unambiguously ascribed to the melting regions of the terpolymer matrices, showing a reduction of the peaks' temperature, assigned to the melting point T_m as increase in mass fraction of the DEHP load. As listed in Table IV. 2, the T_m values in case of plasticizer-free terpolymers appeared at 126.1 °C. With the addition of DEHP of a 10% mass fraction, melting peaks constantly shifted toward the lower temperature at 119.8 °C. The previous study revealed that the diffusion of T_m values was related to the change in crystal phase stacking and size growing, rather than the growth of crystalline fraction of the semicrystalline polymers [17-19]. In current case, the crystalline fraction was calculated by modified expression $\chi_c = \frac{1}{1-\lambda} \Delta H_f / \Delta H_f^0 \times 100\%$, where λ is the mass fraction of DEHP plasticizer load. H_f is the fusion of enthalpy for terpolymer samples; ΔH_f^0 is the enthalpy of hypothetically 100% crystal terpolymer film and for terpolymers studied currently, ΔH_f^0 value of

full crystal film was reported as ca. 42 J g^{-1} [20]. Within the measurement uncertainty, no distinct variation of crystalline fraction (maximal 1.3% gap) was observed for the pristine and DEHP modified blends. In this case, the origin of diffusion of T_m values due to the fraction of crystallites was ruled out. It is often assumed that the melting temperature is connected to the imperfect crystal and crystal size. For a typical solution-cast process, the crystallization of

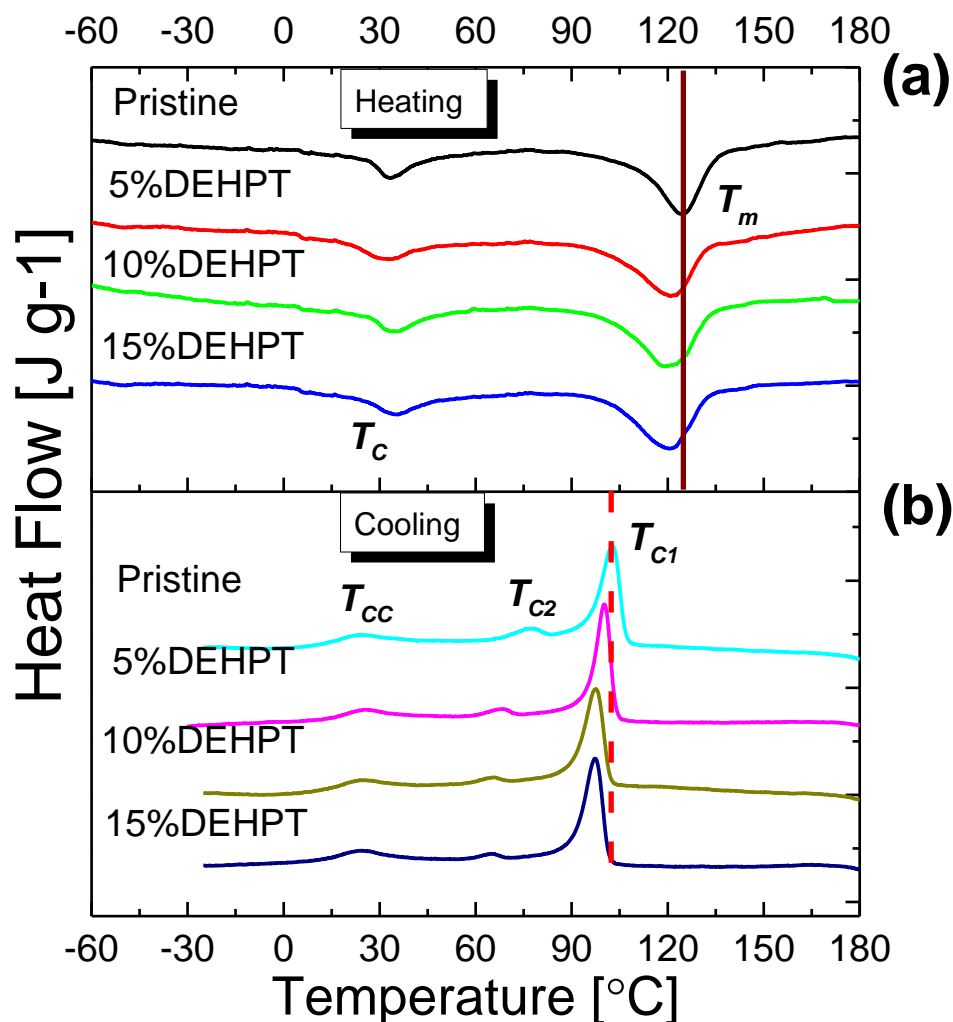


Figure IV. 2 DSC thermogram traces of heating (a) and cooling ramp (b) for the pristine and various DEHP doped terpolymer blends. Solid vertical line and dashed vertical line denote the melting and melt-recrystallization peak of the neat terpolymer, respectively.

polymer materials occurred with its molecular chain folding back and forth into the crystal lamellae during the losses of the volatile solvent. With presence of DEHP at initial stage of crystallization, small DEHP molecules were expelled from the crystal nucleation and eventually only resided in the amorphous phase. The growth of crystal nucleus was most probably retarded by the impurities and this led to a small crystal size and imperfection. It was conceivable that

DEHP was only and evenly distributed in the amorphous phase of PVC polymers [21]. In current study, the presence of DEHP molecules was not likely to reduce the fraction of crystallinity in terpolymer blends but to raise a diminution and broadening distribution of the crystallite size. The melting regions also demonstrated the broadening peaks with the addition of DEHP, which has intensively acknowledged that is strongly dependent upon the degree of heterogeneity of the crystal phase rose from DEHP molecules in terpolymer blends. The full width at high maximal (FWHM) values underwent a moderate increase from 15.2 °C for pristine to 19.7 °C for terpolymer with 10% DEHP loading as shown in Table IV 2. This provided the indicative information of inhomogeneous crystallites in blends. The 15% DEHP blends possessed the near T_m and remained FWHM values, since the mass fraction of DEHP load was excessive, of which characteristics of peak regimes were summarized in Table IV. 2.

The thermal data were collected in heating ramp of 10 ·min⁻¹ from -70 °C up to 200 °C, followed by a cooling down process where the melt-recrystallization occurred in a cooling rate of 10 °C ·min⁻¹. However, the weak endothermic peaks, which could be assigned to Curie transition appearing at lower temperature, moved slightly to the higher temperature against the addition of DEHP molecules with a limited expansion from 33.4 °C of neat terpolymer to 35.8 °C of saturated 15% DEHP load terpolymer. It should be noted that the weak peak was clearly associated with the ferro-paraelectric phase transition of the crystal phase in terpolymers. In Chapter III, we carefully observed a depression of Curie transition temperature in reverse contrast to the present results and inferred that this was certainly due to the compressed amorphous phase. The presence of DEHP molecules was likely to act as a lubricant between the molecular sheets uniquely for an amorphization blend. A progressive increase of Curie transition corroborated the hypothesis and consisted with the established observation. In this case, a slightly more *less-ordered* chain conformation was introduced into the orthorhombic phase, resulting in a higher content of ferroelectric phase. The elevated enthalpy of Curie transition experimentally provided the further evidence of this assumption and was also satisfactorily reflected by a continuous increase in Curie transition temperature T_C .

The influence of DEHP molecules on non-isothermal melt-recrystallization behaviors of terpolymers blends were revealed and illustrated in Figure IV. 2b. Two endothermic peaks were observed covering the melt-crystallization process. In order to identify the peaks attribution, several controversial interpretations were involved: (1) Crystallite size and chain packing. Two or

Table IV. 2 Temperature and enthalpy parameters concerning Curie transition regimes and melting region monitored by a DSC heating ramp

Acronym	T_g	ΔC_p	T_C	ΔH_C	ΔH_m	χ_C	Melting region(°C)		
	°C	(mW)	°C	(J/g)	(J/g)	%	T_m	T_{onset}	FWHM
Pristine Film A	-22.98	0.15	33.4	3.5	15.3	36.4	126.1	110.5	15.2
5%DEHP Film B	--	--	33.5	3.5	15.2	36.1	122.7	105.4	18.7
10%DEHP Film C	--	--	34.1	3.6	15.8	37.6	119.8	104.3	19.7
15%DEHP Film D	--	--	35.8	3.7	15.8	37.7	120.4	102.7	19.3

Table IV. 3 Corresponding temperature and enthalpy parameters collection in a cooling ramp of DSC measurement.

Acronym	T_{CC}	T_{onset}	ΔH_{CC}	ΔH_C	χ_{CC}	Crystallization		
	°C	°C	(J/g)	(J/g)	%	T_{c1}	T_{onset}	T_{c2}
Pristine Film A	24.7	34.7	-2.7	17.36	41.33	102.8	106.7	77.4
5%DEHP Film B	25.1	35.3	-2.6	16.75	39.88	100.2	103.7	68.3
10%DEHP Film C	24.9	37.7	-2.4	16.83	40.07	98.2	102.2	65.4
15%DEHP Film D	25.6	35.3	-2.2	15.97	38.02	97.1	101.6	65.0

more crystallite size were created as the temperature declining. This can be ruled out by running the second successive heating run of the DSC curve, seeing a single broad peak covering the range of melting temperature regions (not shown here). (2) Polymorphism. Multiple crystal phases of the different polymorphisms were presumably formed during the cooling process. However, ferroelectric crystal phase were erased at raised temperature (ca. 90 °C) since the indiscernible net dipole moment of the paraelectric crystal phase (TG^+TG^-) were predominant in terpolymer blends. The absence of polymorphic transitions at increasing temperature indeed contradicted with the multiplicity of the melting peaks. (3) Differences of CTFE defects fraction. The crystallization of loose crystal lamellae containing less CTFE bulk ternary was responsible for the intensive endothermic peak, located at higher temperature, while the massive CTFE ternary defects crystallized into the crystal sheets at lower temperature. And one can assume that a small variation of enthalpy was expected. The results led to a consistent conclusion that the two stepwise stages of melt-recrystallization took place during the non-isothermal cooling.

As illustrated in Figure IV 2b (cooling), the peak temperature (T_{c1}) of melt-recrystallization regimes appeared a clear dispersion by almost 10 °C towards the lower temperature as a function of mass fraction of DEHP load. Several observations could be employed to interpret these phenomena. It has been confirmed that addition of plasticizer could enhance the molecular mobility and favor its transportation to the crystallization sites in the polymer melt-

recrystallization [22]. During the initial stage of nucleation and growth of the crystallites, even though the formation of the crystalline nuclei aroused a strict molecules mobility, the presence of DEHP plasticizer might delay the immobilization of molecular chains transfer rising from nuclei and extended the crystallization induction period. In other words, the propagation of crystal stacks in the terpolymers amorphous phase were significantly reduced in case of DEHP terpolymer blends. Therefore, there appeared the detaining crystallization region, reflected as a peak shift in DSC curves upon cooling. The less intense peak satellites also had a large dispersion drift to the depressed temperature from ca. 77.4 °C to 65 °C for 15% DEHP load blend, showing a distinct plasticization. And we could also inferred that the enhancement of the molecules mobility with presence of DEHP was in favor of the CTFE ternary defects inserting into the crystal sheets effectively, even at low crystallization temperature. The influence of the plasticizer molecules on total crystalline fraction upon cooling were compared in Figure IV. 3. The crystallinity fraction values were picked up from the second heating ramp of DSC curves. Note that no distinct cold-crystallization peaks occurred for the pristine and terpolymers blends and the overall crystallinity

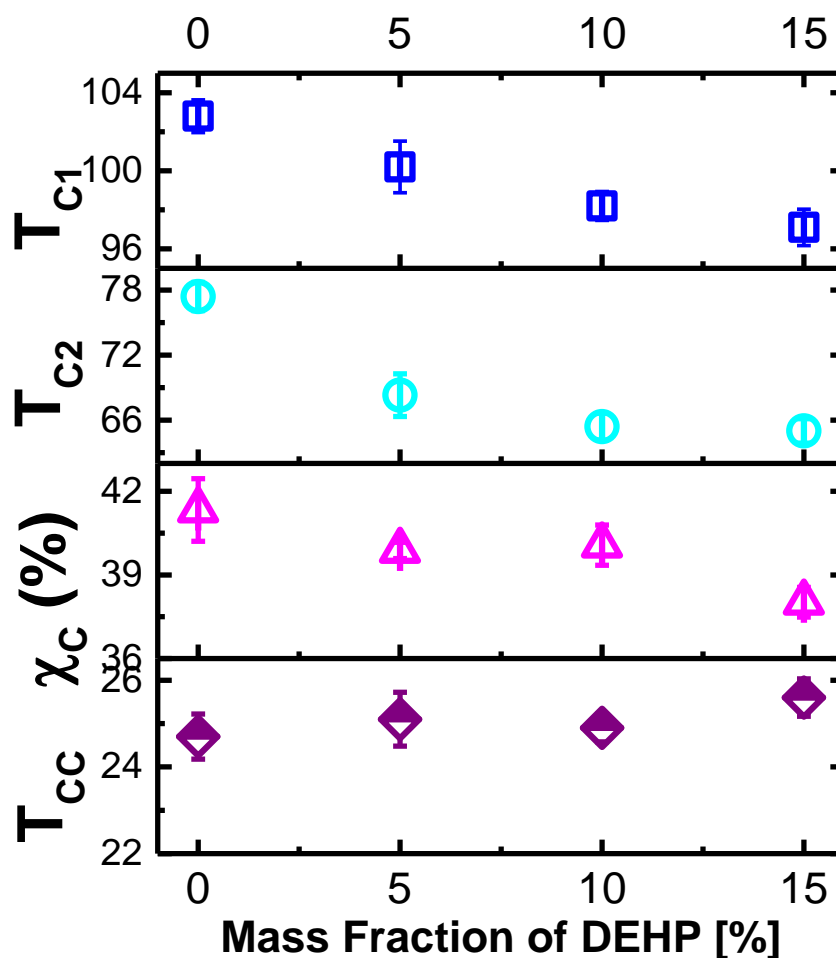


Figure IV. 3 Melt-recrystallization parameters upon DSC cooling as a function of mass fraction of DEHP plasticizer load, (a) the temperature (T_{c1}) of intensive melt-recrystallization peaks, (b)

temperature (T_{c2}) of weak satellite peaks of melt-recrystallization, (c) overall crystallinity fraction (χ_{cc}) originating from the reheating ramp and (d) Curie transition (T_{cc}) upon first cooling.

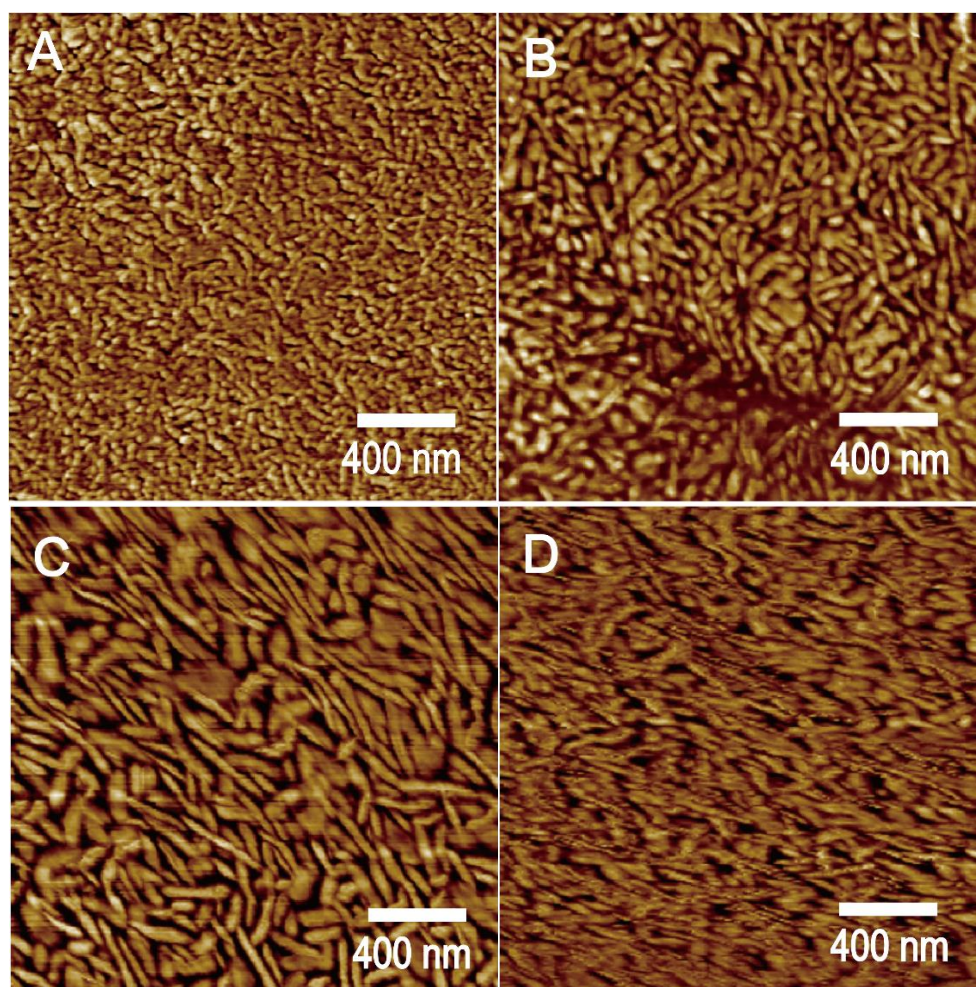
fraction were calculated by the fusion of enthalpy upon the reheating ramp. Consequently, the effects of DEHP were not pronounced in a non-isothermal crystallization processing since the degree of crystallinity was gently compressed by only 3% as increase in plasticizer mass fraction, in sharp contrast to an isothermal crystallization process at 80°C for 2h where a slight expansion of crystallinity fraction observed for terpolymer blends over the pristine. In addition, the effect of plasticizer on ferro-paraelectric phase transition in cooling was also compared. Curie transition during cooling (T_{cc}) at 24.7 °C of the pristine remained the similar value with that of 15% DEHP load terpolymer blend at 25.6 °C. We inferred that that the influence of the plasticizer molecules on para-ferroelectric phase transition was not discerned by using DSC technique. This Curie transition behavior of the ferroelectric polymer during the material forming and processing were an essential issue to the practical importance since the non-isothermal polymer processing were currently predominant in industrial area.

III. 2 Surface Morphology

In order to further manifest the miscibility of the PVDF-based terpolymers, the surface topological and microstructure of the pristine and DEHP modified blends were revealed by the AFM pattern profiles. As seen in Figure IV. 4, the surface characteristics of the samples in current study were presented in a phase mode, allowing to give the contrast phase properties. The bright worm and bumpy like parts, routinely referring to the crystal phase were densely stacked for the pristine annealed at 80 °C for 2h, resembling the surface morphological behaviors of preceding terpolymers in Chapter II as well as the crystal nanodomain size, gauging ca.150 nm length and 30 nm width. Note that the blurred interphase contrast displayed and such imperfect patterns suffered small crystallite size and preferred crystal orientation. And the crystal nanodomains were evolved in the terpolymers blends, exemplified by the low mass fraction of 5% DEHP content where the surface morphology was altered enormously. Although the worm and bumpy like crystal domain were retained consequently, the variation of the size was discerned. More interestingly, topological microstructure characterized a loosely packed crystal nanodomains. The sharp contrast between crystal and amorphous phases was clearly observed where the dark amorphous region considerably accounted in the profiles. We inferred this phenomenon was attributed to the dispersion of DEHP molecules in the amorphous region in the terpolymer blends, even for 15% DEHP load terpolymer blends where demonstrated the less packed crystal and sharp contrast interphase. Besides, the edge-on crystal orientation seen in the pristine was perfectly maintained in DEHP modified terpolymer blends according to the previous

patterns in Chapter II. This was further verified by the melt-recrystallization patterns, obtained via 10% DEHP terpolymer blends heated at 150°C for 2 min and then recrystallized. The surface topographies of melt-recrystallization was relatively smooth, absent from distinctive threadlike crystal domains and phase contrast. On basis of this surface microstructure referred to a flat-on crystal orientation with c-axis perpendicular to the supports rising from the melt-recrystallization process.

As a whole, it is observed that no macro-phase or phase separation was patterned with addition of DEHP molecules by the AFM phase profiles, reflecting rather good miscibility and compatibility between the compositions. The DEHP doping in the terpolymer simply modified the densification of the crystal lamellae packing and discerned interphase region characteristics rather than gave rise to the microphase separation within the limited DEHP concentration range.



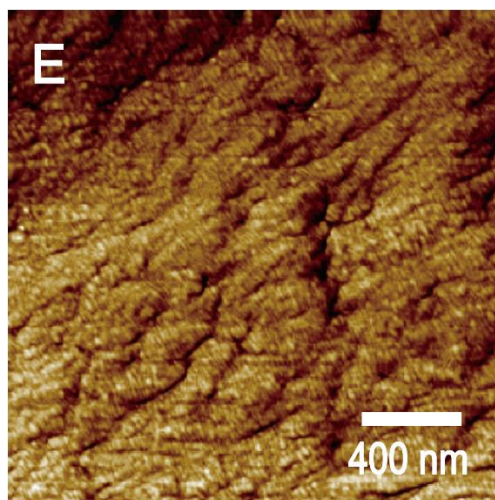


Figure IV. 4 Surface topography patterns (phase mode) of the isothermal crystallized neat terpolymer (A) and DEHP doped terpolymer blends, 5% (B), 10% (C) and 15% (D). Scale bar is marked in the profiles. The pattern of the neat sample undergoing melt-recrystallization showed smoothly topographic features in figure E.

III. 3 Tensile Test

The figure of merit of electrostrictive strain was certainly revealed in Chapter II when we analyzed the electrostrictive response to the thermal crystallization processing of neat terpolymers. A moderate Young's modulus consequently favored the large electric field-induced deformation, accompanying with the excellent free elastic mechanical energy density. However, the small molecules dispersing into the polymer materials, acted as a plasticizer, allowing the mechanical behavior of neat matrix declining. In current characterization, the plasticization effects on the mechanical behavior was manifested by the mechanical tensile strength versus strain and was performed by the ultrahigh precisely powered motor which is powered via a triangular wave form. The samples were uniaxially stretched in a rate of 30 mm/min, reaching to 1% strain of 50 mm effective length. The strain-stress mechanical curves were plotted in Figure IV. 5(a). The strain-stress curves satisfactorily followed a linear correlation in a stretch rate of 1% and the mechanical Young's modulus was given by the slope of the data curves. The efficacy of the DEHP molecules appeared significantly based on the pronounced slope of the data curves reduction. The derivative values of the curves were dotted in the Figure IV. 5(b) and slump down. The Young's Modulus, found at 107.35 MPa for pristine one in accordance with established value in Chapter II decreased to 60.95 MPa for 5% DEHP load, followed by a mild depression as the addition of DEHP reaching to 10% mass fraction. A Young's modulus of 34.23 MPa for 15% DEHP load represented the enormous modification in the mechanical behavior. And the strength values against DEHP mass fraction could follow an exponential decay decrease. However, the mechanical behavior of terpolymer blends with more than 15% DEHP was not conducted, considering that the possibility of unwanted phase separation occurred.

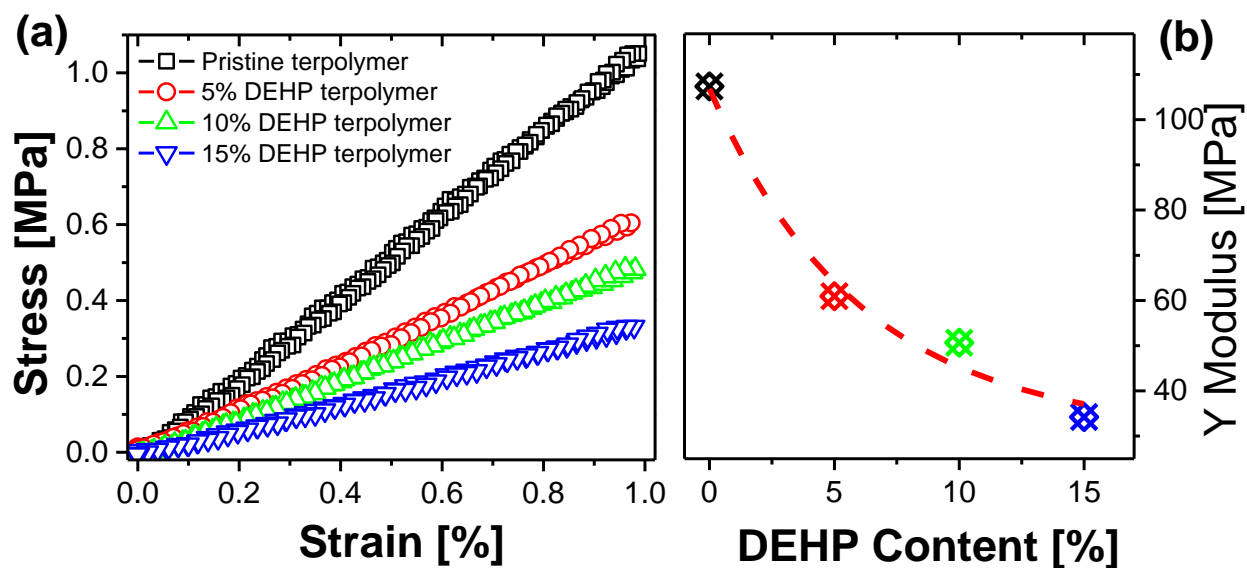


Figure IV. 5 Strain-stress mechanical strength curves of the pristine (\square) and 5% DEHP (\circ), 10% DEHP (Δ), 15% DEHP (∇) terpolymer blends (a). Solid lines are linear fits to the curves. (b) Y modulus values of the strain-stress curves as a function of mass fraction of DHEP load for pristine and terpolymer blends. Dash line is the exponential decay fit to the Y modulus values.

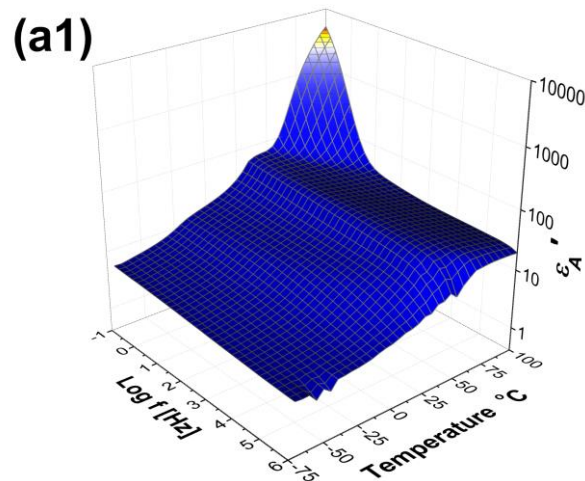
III. 4 Influence of DEHP Plasticizer on Molecular Mobility

In the previous section, studies have been dedicated to evaluate the effects of crystallinity on molecular mobility and electromechanical properties. The more fragile P(VDF-TrFE-CTFE) terpolymers were acquired thanks to the growth of degree of crystallinity. Because of the enhancement of crystal lamellae and interphase, dielectric permittivity increased by all most 2 folds, albeit on the expense of drastic increase in mechanical Young's modulus. The constrained terpolymers presented a decayed trend of field-induced transverse strain and depressed elastic mechanical energy density (recall the electromechanical behavior in Chapter II). In an attempt to overcome this undesired performances and side-effects from a practical point of view, in particular within the research field of miniaturized sensors and actuators, several modification approaches had been introduced, exemplified by a plasticized blend system [23, 24]. The excellent electromechanical performance was strongly attributed to by the multiple folds improvement of dielectric response of the DEHP plasticized terpolymers [7, 8]. On basis of these positive results, it is of significant interest to understand the dielectric behavior of terpolymer blends with presence of plasticizer. Therefore, the dielectric diffusion behaviors were preferred to be discussed in this current study since the absolute electromechanical properties, by the orders of magnitude, were enhanced in our previous reports [8].

Aiming at that, broadband dielectric spectroscopy technique was employed to track the trace of change in dielectric properties to the additives. Figure IV. 6 and Figure IV. 7 displayed the

overview of the temperature and frequency dependence of real part of complex permittivity ϵ'_i (a1, c1), dielectric loss ϵ''_i (a2, c2) and dielectric loss angle $\tan \delta$ (a3, c3) respectively, comparing between the pristine (a) and representative 10% DEHP load blend (c) which were fabricated under the identical cold-crystallization. Firstly, several dielectric anomalies were observed for the real part of complex permittivity of both pristine and 10% DEHP terpolymer blend as a function of both temperature and frequency. Towards the higher frequency whatever the temperature (isothermal) witnessed a progressive decreasing in dielectric permittivity values, in particular for the higher temperature regimes, where the dielectric values slumped from approximately 5000 to around 10 at frequency of 1MHz. On the other hand, a larger diminution by several orders of magnitude was observed from ca. 10000 to the similar level as pristine for 10% DEHP modified terpolymer blend. This abrupt variation was exclusively interpreted by the both decreasing effects of ions translational behavior and interfacial polarization which will be discussed later on. At isochronal broadband dielectric spectra level, the distinct contrast of dielectric constant was observed for the higher temperature in dielectric constant map of 10% DEHP load terpolymer blend comparable with the pristine. The lower frequency saw the large difference rather than the higher frequency where an overlapping of Curie relaxation and conductivity occurred. These modified characteristics could be more clearly reflected by the dielectric losses and loss angle $\tan \delta$ spectra.

As a whole, three distinctive dielectric relaxation anomalies over the temperature window in Figure IV. 6 (a2) were well articulated, in accordance with our established studies [25], which were also revealed in the representative BDS of the DEHP modified terpolymer blends. It is also worth noticing that ambiguous relaxation peaks hardly resolved at low frequency in Figure IV. 7



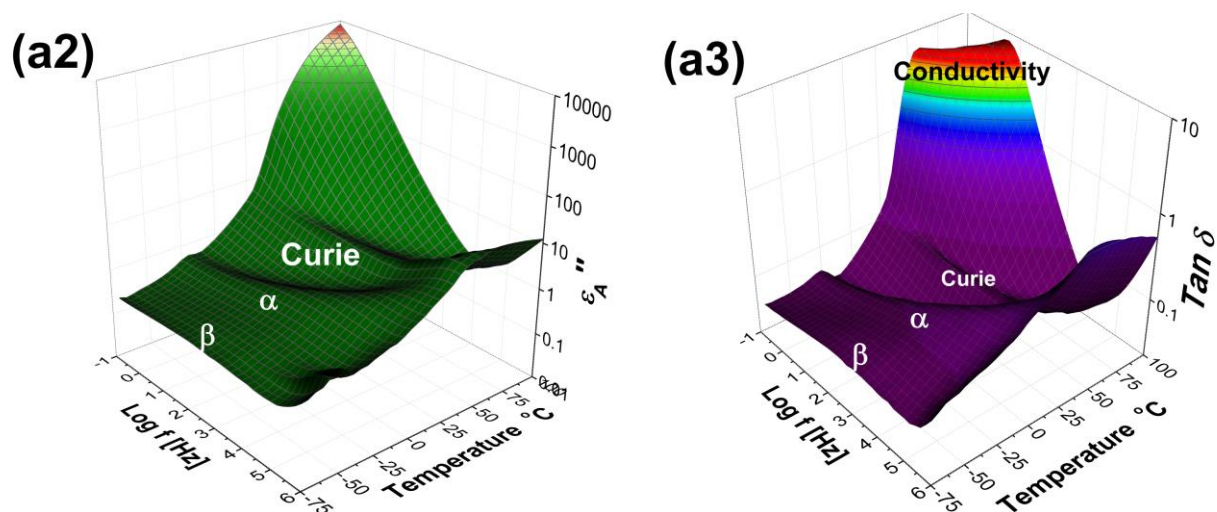
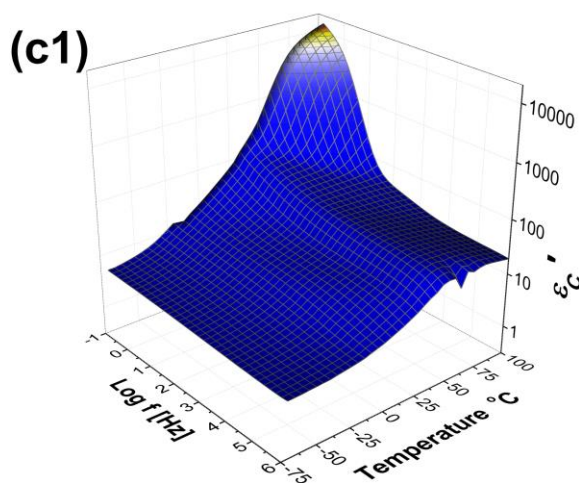


Figure IV. 6 Frequency and temperature dependence of real part of complex permittivity (a1), dielectric loss (a2) and dielectric loss angle $\tan \delta$ spectroscopy (a3) for the pristine terpolymer. The various relaxation processes, i.e. the β , α relaxation, Curie transition and ions DC conductivity were successively indicated in order of temperature increasing.

(c2) because the DC conductivity (or MWS) and Curie transition were superposed, with an abrupt increasing amplitude of relaxation strength. In case of the median frequency range, β relaxation in glassy state, α segmental relaxation in super-cooled liquid region and Curie transition were clearly identified. This suggests that DEHP molecules favored the significant influence on the dielectric behavior at lower frequency range instead of the higher. Correspondingly, the relaxation behavior was also visualized by dielectric loss angle $\tan \delta$. For both the pristine and 10% DEHP modified terpolymers, ions conductivity effects were dominant at lower frequency and higher temperature, where Maxwell-Wagner-Sillars (MWS) interfacial polarization superimposing with ions conductivity contribution and obscured.



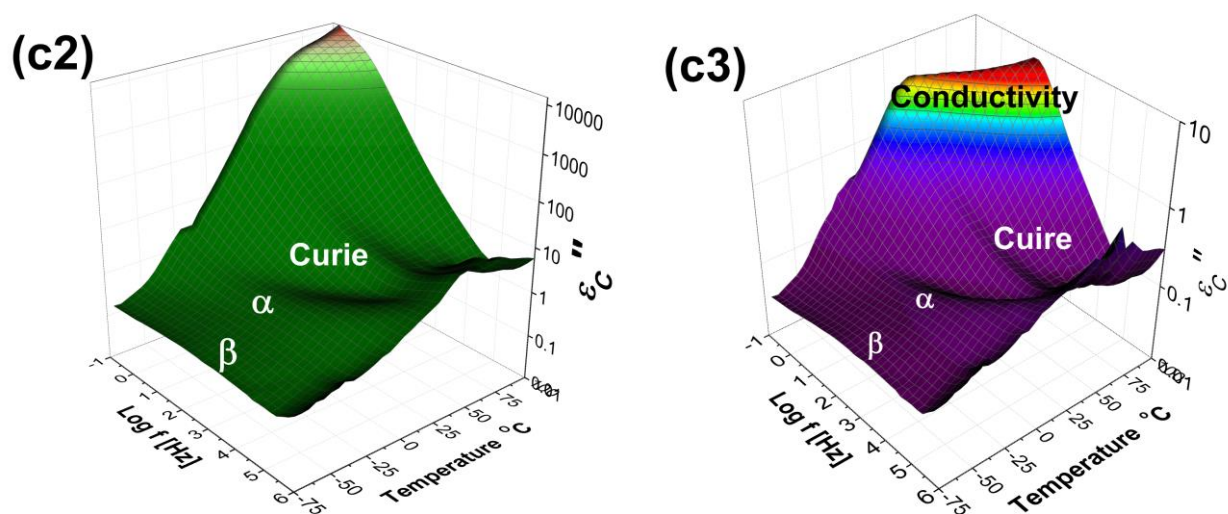


Figure IV. 7 Dielectric permittivity (c1), dielectric loss spectra (c2) and dielectric loss angle $\tan \delta$ (c3) as a function of frequency and temperature for the representative 10% DEHP doped terpolymer blend.

Plasticizing effects were also examined by the isochronal dielectric spectroscopy. Dielectric loss spectra, picked up from isothermal dielectric spectroscopy were plotted as a function of temperature at given frequency of 1581 Hz for the pristine and modified terpolymer blends with addition of various DEHP mass fraction, as shown in Figure IV. 8a. The dielectric loss spectra demonstrated the two discernible relaxation anomalies, respectively appearing at between 240K and 280 K, as well as range between 300 K and 340 K. The relaxation anomaly occurred at higher temperature, which has been identified as Curie transition [25], dispersed progressively towards the higher temperature, from 310.4 K for the pristine drift to 314.1K for 15% DEHP modified terpolymer blend, consisting with the diffusing behavior monitored by the DSC thermal curves. Previous investigation unveiled that Curie transition, associated with ferro-paraelectric phase transition, were likely to be activated by the lower ferroelectric crystal phase owing to the isothermal crystallization. In case of DEHP load terpolymer blends, Curie transition forcibly moved to the higher temperature range, implying a somewhat constraint behavior of the ferro-paraelectric phase transition as DEHP plasticizer doping. An amount of differences and several-folds expansion were discerned in the isochronal dielectric loss spectra at higher temperature, where the charge carrier ion motion and interfacial polarization were of significant responsibility rising from the addition of DEHP molecules. However, the less intensive peaks appearing at lower temperature range were certainly attributed to the α relaxation associated with the glass transition region, showing analogous position and amplitude characteristics. For the sake of essentially comparison, dielectric loss angle $\tan \delta$ for terpolymers against the temperature were plotted as Figure IV. 8b. The loss $\tan \delta$ peaks moved toward lower temperature by near 5 K

variation as the concentration of DEHP loaded increasing, although the peak drift were occasionally low referring to the literatures. Notwithstanding, this results implied that the glass transition in amorphous phase were affected more or less. Besides, no differences were witnessed for the dielectric strength for both ϵ'' and $\tan \delta$ spectra. It is reasonable to infer that the dipole polarization in the amorphous phase was altered. Last but not least, relaxation linked to the local motion of molecules in glassy state of the terpolymer and blends thereof shared the similar trend in terms of position and strength.

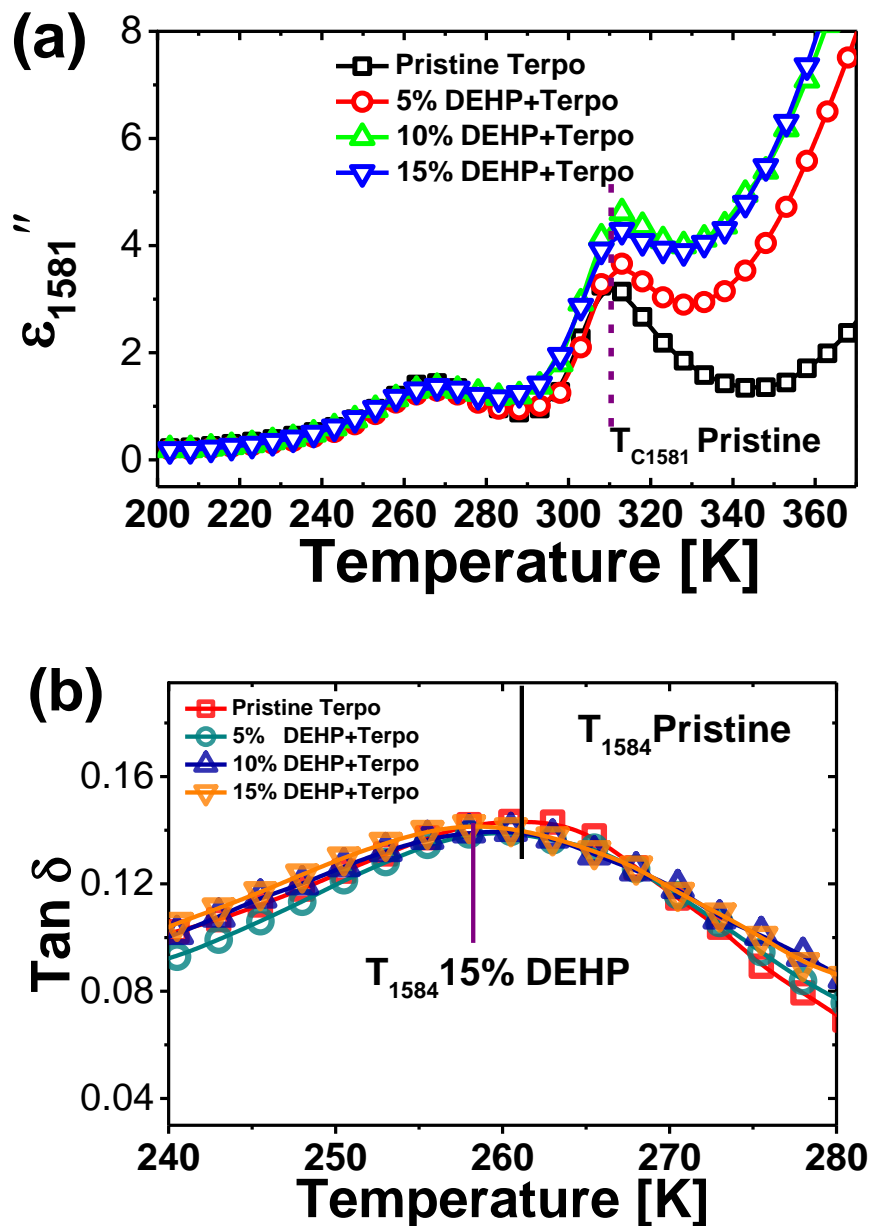


Figure IV. 8 (a) Isochronal dielectric loss spectra for pristine terpolymer and each plasticized film picked up from the isothermal BDS measurement over the temperature range between 203 and 373K at 1581 Hz (pristine, open square; 5% DEHP loaded, open circle; 10% DEHP loaded,

upward triangle; 15% DEHP, downward triangle). Dashed vertical line denotes the Curie transition peak of pristine terpolymer. (b) The fractional glass transition regions of the dielectric loss angle $\tan \delta$ where the relaxation peaks of the pristine and 15% DEHP terpolymer blends were marked by solid vertical line (denotation indicated by the context in the figure).

III.4.1 Segmental Relaxation- α Process

It is well-documented that by the addition of a plasticizer to the polymer matrix, the blend polymers showed the glass transition temperature declining, for instance the PEO oligomer doped PLA polymer blend system [26, 27]. These changes were mostly revealed by thermal or mechanical methods. Sparse researches have been handled to trace the underlying dynamics according to the molecular mobility point of view. Bao et al. [28] reported a novel DEP plasticized cellulose composite and observed a significant decrease of glass transition temperature in the terpolymer blends with the help of broadband dielectric spectroscopy analysis. The diminishing glass transition temperature was interpreted by a molecular level interaction between the molecules of the additive and polymer matrix. And research efforts have also been addressed to the intensively-examined plasticized PVC resins by the same technique [29, 30]. To best of our knowledge, broadband dielectric relaxation studies at least have rarely carried out to the plasticized PVDF-based dielectric polymer system. The DEHP, a family of phthalate plasticizer, has a similar chemistry with its homological phenyl plasticizer DEP, but is capped with the longer alkyl molecular chain. Thus comparable with DEP having melting point at -4°C , DEHP has a lower glass transition temperature at -76.3°C and melting temperature at -55°C . [10] These temperatures are rather good compatible with that of PVDF based dielectric polymers, most of which possessed the glass transition temperature far below ambient temperature but much higher than the melting point of the small molecules which is qualified acting as a plasticizer. At this level, the primary relaxation α''_{DEHP} of DEHP if existing was not likely to be present individually on the dielectric spectroscopy but mingled with the relaxation process of polymer matrix within the studied temperature range.

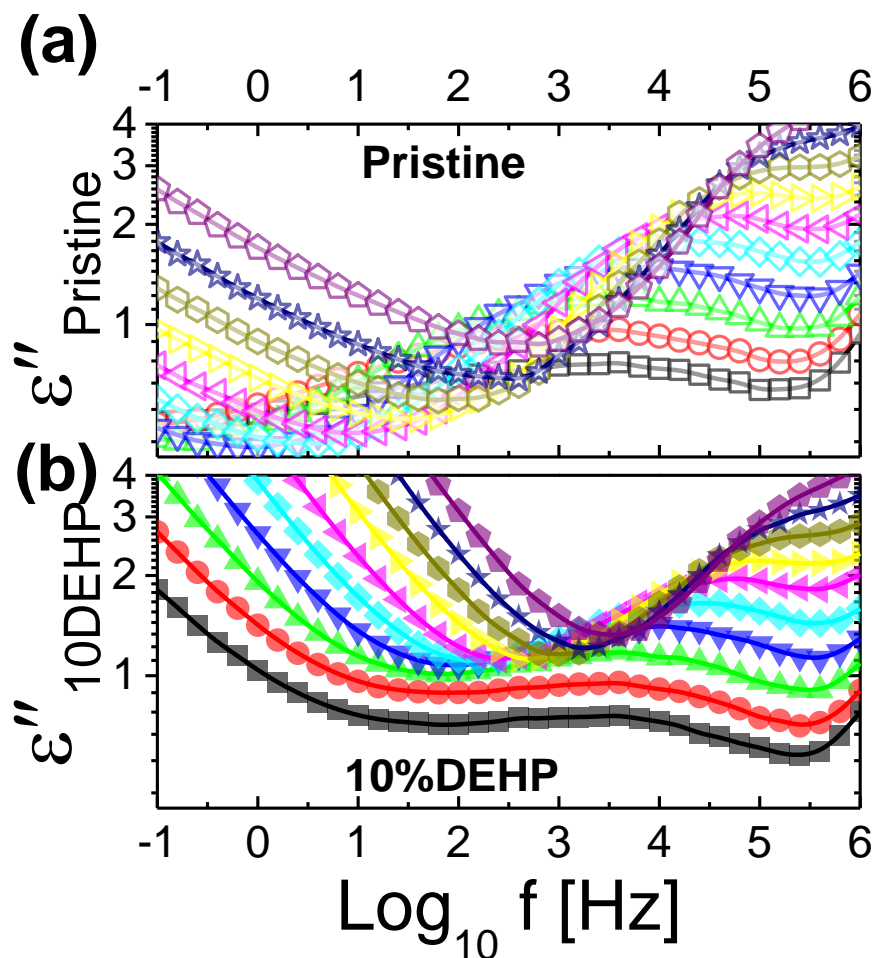


Figure IV. 9 Fraction of isothermal dielectric loss spectra as a function of logarithmic frequency at temperature range between 248 K and 293 K for pristine (a) and 10% DEHP modified terpolymer (b). The lines are guide to the eyes.

Previous dielectric spectroscopy analysis on relaxation behavior of P(VDF-TrFE-CTFE) terpolymer concluded that the main primary α process was fluctuated at temperature above approximately 25 °C (representative T_g of the terpolymers), extremely a large gap between the temperature where the α''_{DEHP} process of the DEHP plasticizer occurred. This process was subsequently masked by the dielectric relaxation of bulk terpolymer and had very limited influence on the molecular mobility of characteristic peaks. Here we thus mainly focused on the main relaxation peaks, associated with the segmental dynamics of P(VDF-TrFE-CTFE)/DEHP blends. In order to evaluate the DEHP plasticizing effects on the terpolymer matrices, isothermal dielectric spectroscopy of pristine and representative terpolymer blend containing 10% mass fraction of DEHP as a function of broadband frequency were firstly plotted in Figure IV. 9a and 9b at temperature between 248K and 298K, respectively. The observed differences upon the intensity of relaxation at low frequency demonstrated quite complexity and will be discussed later.

The intact relaxation peaks appearing at intermediate frequency, were ambiguously identified and attributed to the segmental relaxation of the molecular chain, linking to the glass transition region in terpolymer blends. The primary relaxation peaks for both systems featured the similar drift rapidly towards the higher frequency with increase in temperature. For the sake of good comparison, dielectric loss spectroscopy for pristine and each DEHP doped terpolymer blends at given temperature (253 K) were then plotted against the logarithmic frequency (f) in Figure IV 10a. The evolution behavior of dielectric peaks certainly depended upon the mass fraction of DEHP load before reaching the saturation of plasticizing effect, that is, with no more than 10% concentration. It is clearly revealed that the main relaxation peaks diffused to the high frequency by more than a half decade, accompanying with a moderate enhancement of the relaxation strength. As stated in previous investigation (recall Chapter III), intramolecular cooperativity or interaction is well-acknowledged as the origin of the main primary α relaxation, which described a long sequence of molecular chain backbone that was, the dipole involved in the molecular relaxation dynamics upon the variation of temperature surroundings. Generally, semi-crystalline polymers comprise amorphous phase and stiff crystal lamellae. The relaxation dynamics only originate from the randomly oriented molecular chains, dwelling in amorphous phase rather than the latter part where the α relaxation processes were shielded by the well-ordered crystal lamellae. The peak shift towards the higher frequency with increase in DEHP concentration suggested an activated behavior in the amorphous phase, a phenomenon as opposed to the constrained behavior, revealed in Chapter III. It has also been described that the acceleration behaviors of dielectric relaxation in amorphous phase were testified in many polymer systems with addition of small molecules or oligomers, i.e. cellulose/water [31], cellulose/DEP [28] lithium ionomers/PEG [32], P(VDF-TrFE)/PEO [33], TMBPA-PC/TEHP [34], etc. Those modification in polymer blends were reported by an interpretation of an effect of plasticization. Notwithstanding, this effect exhibited the large variances, heavily relying on the neat polymer matrices. For instance, DEP doped cellulose system witnessed a significant decrease in glass transition temperature by around 80 K with 20 wt% DEP addition, instead, only approximately 12.7 K loss was found for polyacrylic resin/DEP plasticized system [35] over the T_g values of the neat polymers. It is thus interesting to understand the origins behind these differences. Note that the cellulose molecules contained a large amount of H-bond functional groups pendant on the ring-like backbone and the Van der Waals force was predominant in the contribution to the influence on the molecular interaction. The disparities of plasticization effects implied that the segmental relaxation of amorphous phase was closely correlated to the intermolecular cooperativity, which strongly depended on the chemical structure of the backbone molecular chain, as reported by Ngai et al.[36]. Regarding the nature of the plasticizer molecules, the interaction between the soft alkyl segment of DEHP plasticizer molecules and VDF terpolymer backbone was somewhat disturbed the intermolecular cooperativity of the terpolymer molecule chain in amorphous phase, by an

indicative of the relaxation acceleration near the glass-rubber transition temperature (253 K) in Figure IV. 10 (a).

It is also worth mentioning that the amplitude of intact dielectric relaxation peaks were slightly enhanced with increasing the DEHP mass fraction as seen in Figure IV. 10 (a). This phenomenon can be explained by introducing a three phase mode microstructure of the semi-crystalline terpolymer materials. In Chapter III, the enhancement of the dielectric relaxation regimes was effectively ascribed to the enrichment of constrained amorphous interphase, aroused by the cold-crystallization in crystal lamellae region. On the basis of the exploration of the dielectric relaxation strength, the third layer, which was widely declaimed by many researchers [37-39], was identified. This amorphous layer, so-called interphase sandwiched between the amorphous phase and well-ordered crystal lamella, consists of the less-ordered molecular chain entanglement which stemmed from the neighboring ordered crystal lamellae, with its end embedded into the loosely packing and randomly orientated amorphous phase [38, 40]. Therefore, the interphase was in structure amorphous phase but rigid and more or less oriented. Considering at least 55% of constrained amorphous region accounted for the whole amorphous phase in PVDF-based polymer [38, 41], it is reasonable to assume that the interphase part had a strong effect on the molecular mobility. In previous study, P(VDF-TrFE-CTFE) terpolymer with the more fraction of crystallinity exhibited an enhanced dielectric relaxation strength due to the increasing amorphous interphase layer, and as a consequence, an intensified behavior in segmental relaxation was clearly observed. The equal trend witnessed in Figure IV. 10(a) was most possibly due to this assumption. Indeed, the crystalline fraction of the DEHP doped terpolymer blends were not undergoing a declining phenomenon, but a limited increment with addition of 15 wt% DEHP concentration verified via thermal analysis (recall Table IV. 2). This change in fraction of crystallinity counteracted the adverse influence of consumption of amorphous phase on the dielectric strength.

Subsequently, at lower frequency saw enormously dielectric relaxation strength for the terpolymer with the addition of DEHP molecules except the pristine terpolymer specimen as shown in Figure IV. 10a. The left wing of structural relaxation spectra were covered by the abrupt increase in dielectric losses which were unambiguous the effects of ions DC conductivity contribution. This is certainly confirmed via extrapolating the slope of the dielectric loss spectra- k values for DEHP doped terpolymer blends, as ions DC conductivity only accounted for the dielectric relaxation at low frequency range if k was equal to -1 sharp. And the influence of the DEHP on conductivity will be discussed later on. Moreover, one could not neglect the discernible

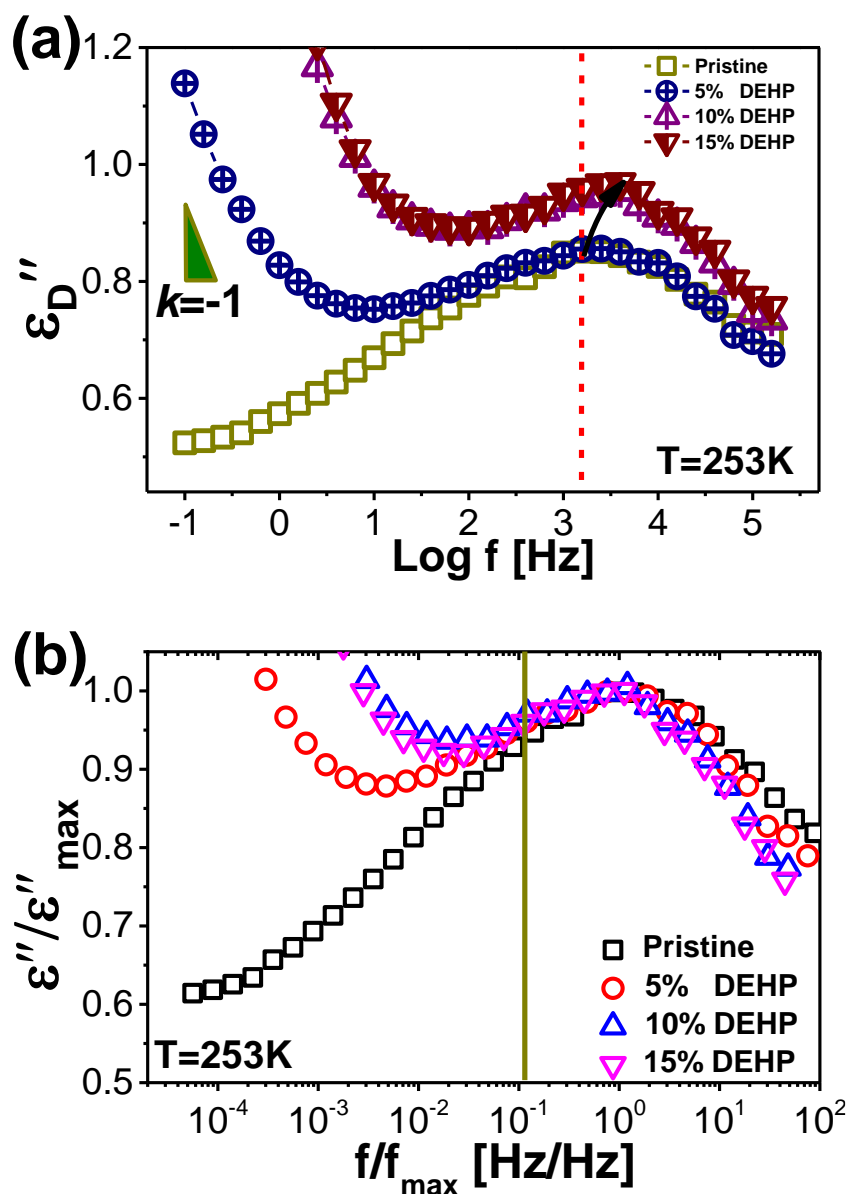


Figure IV. 10 (a) A comparison of the fractional dielectric loss spectra as a function of logarithmic frequency for pristine and modified terpolymer with various DEHP mass fraction at given temperature 253 K. Dashed vertical line denotes the peak position of the pristine terpolymer and curvature arrow oriented to the diffusion of the peak position for the DEHP doped terpolymer blends; a schematic of slope equal to -1 was depicted referring to the 100% contribution of ions DC conductivity. (b) dual normalized dielectric loss spectra against the logarithmic frequency at given 253 K; vertical line marked the normalized frequency below which the dielectric loss diverged obviously.

variation of broadness of segmental relaxation peaks. Figure IV 10 (b) displays the normalized dielectric spectra against frequency for each examined terpolymer. It is clearly observed that the broadness of the right wing of the dielectric relaxation peaks shrank as increasing DEHP concentration while the left arms of relaxation spectra showed the much complexity. The spectra

diverged at lower frequency below which a solid vertical line marked. Our previous studies revealed that the narrower shape of dielectric spectra were obtained for terpolymer containing higher content of crystalline fraction, suggesting an increasing average size of Cooperatively Rearranging Region (CRR). The increasing CRR size values only take place only if the number of neighboring dipole units participating in the structural relaxation process near to the glass transition temperature T_g . The structural dependence of the CRR sizes results from the external and internal hindrances imposed on the material at the critical glass transition temperature (253K) and this generally links to the dynamic inhomogeneity involved in relaxation domains. The Figure IV. 8b demonstrated a narrow trend of relaxation time distribution with increasing the DEHP concentration. Many researchers argued in the literatures that the relaxation time distribution broadens when the amorphous phase becomes constrained, revealed by the dynamic analysis techniques [42, 43]. In present study, the contribution of the crystalline phase to the cooperative length has been ruled out since the crystallinity fraction for each DEHP doped blends remains equivalent. The narrow relaxation distribution reflected the structural inhomogeneity of the systems induced by DEHP molecules.

In Chapter III, the remarkable differences in relaxation shape of dielectric loss spectra was only available on the left wing of segmental relaxation spectra (Figure III 4b). In current case, it is surprising to note that the dielectric losses split were more likely to appear at higher frequency at given temperature, showing a quite asymmetric behavior compared with the pristine terpolymer, absent of DEHP molecules. In order to quantitatively investigate, dielectric loss ε'' spectra were fitted to the HN function. The estimated breadth parameter α_{HN} values increased with the addition of DEHP concentration from 0.20 ± 0.02 of the pristine to 0.29 ± 0.02 of 15% DEHP load, concomitant with decrease of symmetric parameters from around 1.00 (symmetric) to ca. 0.68, in agreement with the values extrapolated previously. These asymmetrically experimental phenomena could not be described exclusively by an ideal Debye-like dielectric loss response. Therefore, Kohlrausch-Williams-Watts (KWW) equation $\phi_\alpha(t) = \exp[-(t/\tau_\alpha)^{\beta_{KWW}}]$ was then employed to characterize stretched exponential behavior of the relaxation time distribution, where β_{KWW} parameter was to describe the distribution of the relaxation time and can be empirically obtained from the HN fitting parameters via the following equation [44, 45]:

$$\beta_{KWW} = (\alpha_{HN}\beta_{HN})^{1/1.23} \quad \text{IV. 3}$$

The β_{KWW} parameters respectively were calculated as 0.27 and 0.38 for pristine and system with representative 15% DEHP doped terpolymer blend. A higher stretched exponential value β_{KWW} implied a narrow distribution of relaxation time, which is in good consistency with experimental dielectric relaxation spectra near glass transition temperature region.

In order to quantitatively investigate the DEHP plasticizing effect on segmental dynamics regime of terpolymer, the temperature dependence of the characteristic relaxation times for each studied sample was extrapolated by the structural dielectric regimes fitting to Havriliak-Negami (HN) function. The characteristic logarithmic relaxation times were then plotted against the reciprocal of the temperature $1/T$ individually in Figure IV. 11 within temperature range between 253 K ($1/T=3.95$) and 290 K ($1/T=3.45$). The relaxation time in any case increased orders of magnitude against temperature variation. Note that the relaxation times of α process τ_α are likely to split, depending on the addition of DEHP mass fraction as the temperature approaches to the dielectric defined glass transition temperature of the neat terpolymer which was marked by a vertical dash line in the figure and the changes in cooperative process near the glass transition region were clearly manifested instead of higher temperature. At comparatively low temperature, the relaxation times of DEHP doped terpolymer blends favored to be accelerated over the pristine one. This scenario was found inversely for the isothermal crystallized terpolymers underdoing a slowing down of relaxation times. According to the Adam and Gibbs theory [46], discrepancies in relaxation processes of the polymer systems originated from the changes in cooperatively conformational arrangement. In general, the cooperatively conformational arrangement relates to

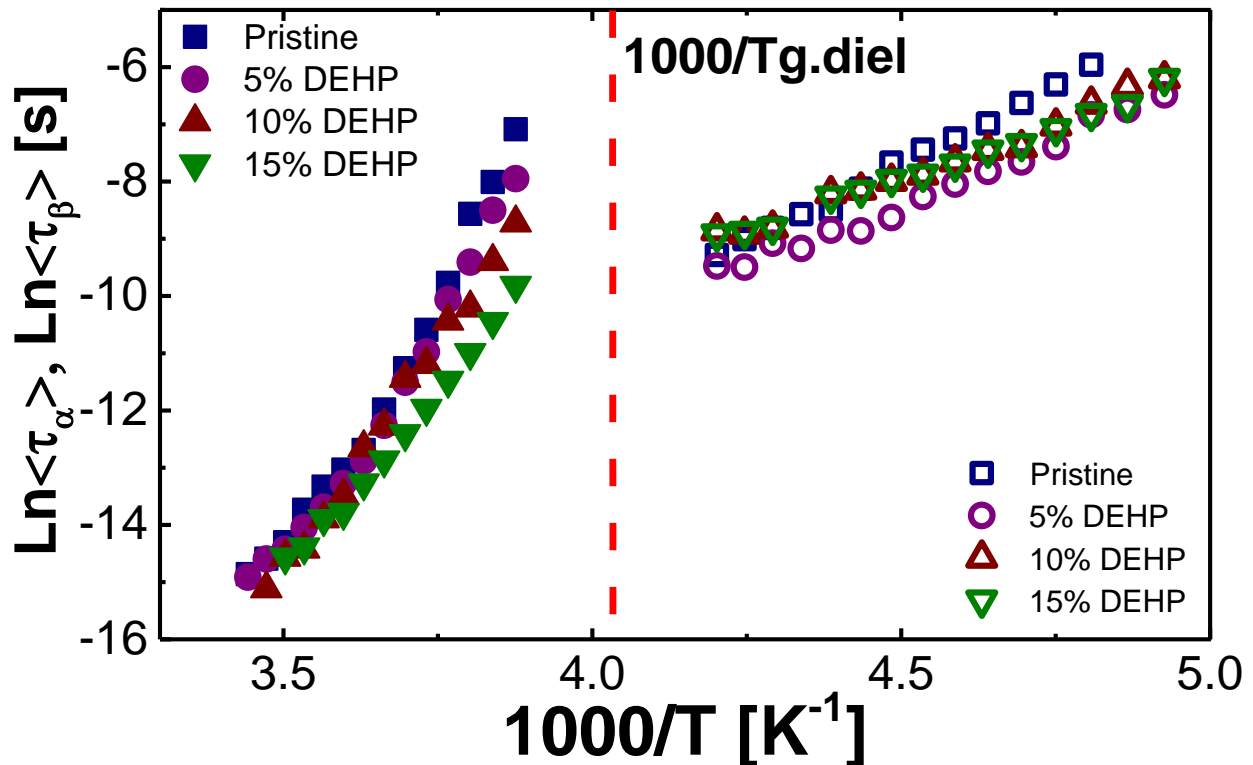


Figure IV. 11 Temperature dependence of structural relaxation times τ_α and secondary relaxation times τ_β plotted as a function of the reciprocal of temperature $1/T$ regarding the pristine and 148

DEHP doped terpolymer blends; filled symbols (for instance, ■, ●, ▲...) represent α relaxation times; open symbols (□, ○, △...) denote secondary relaxation times. Solid lines represent the VFT fitting to the curvature like relaxation times.

the thermodynamic variables such as temperature T as intramolecular reason proposed by Donth [47, 48], which is known that cooperative length increases when the temperature decreases from the crossover temperature (rubbery-glassy transition). On the other hand, cooperatively conformational arrangement could be affected by structural changes in the material assigned to the intermolecular aspect. Both actions are to induce the fluctuations in the glass transition region. The cold-crystallization, nanoparticle filler, drawn/reorientation, doped plasticizer and chemically cross-linked processing approaches were reported to alter the cooperative length. For example, Bao et al [28] reported that a jump of relaxation rate with increase of DEP load concentration was due to the breakdown of the intermolecular H-bonded for Cellulose/DEP plasticized system, which was also seen in a PLA/ATBC plasticized system [49].

Near the glass transition temperature, curvature-like temperature dependence of the structural relaxation times $\tau_\alpha(T)$ were satisfactorily described by Vogel-Fulcher-Tammann (VFT) function as applied in last chapter and VFT fitting parameters were then summarized in Table IV. 4. One can observe that the pre-exponential factor τ_∞ -relaxation times at infinite temperature of pristine terpolymer was in agreement with previous study on P(VDF-TrFE-CTFE) dynamics and also results for a large amount of semicrystalline polymer materials [50]. However, one decade shift towards the lower relaxation time occurred to the 15% DEHP load terpolymer blend. Vogel temperature T_0 where the relaxation times were infinite high also underwent a drastic decreasing from 230.9 K to 201.2 K. And estimated glass transition temperature $T_{g.diel}$ defined by dielectric approach with relaxation time τ_α equal to 100 s were extrapolated by VFT approach. In case of pristine terpolymer, the estimated $T_{g.diel}$ was reliable according to the previous dielectric, DMA and DSC study [51, 52]. The expected variation of estimated glass transition temperatures $T_{g.Fox}$ were also predicted with well-known Fox law (equation IV. 4):

$$\frac{1}{T_{g.Fox}} = \frac{\phi_i}{T_g^i} + \frac{1-\phi_i}{T_g^j} \quad \text{IV. 4}$$

Figure IV. 13 plotted the estimated glass transition temperature $T_{g.Fox}$ against DEHP concentration in together with estimated $T_{g.diel}$ and Vogel temperature T_0 . The Vogel temperature T_0 and $T_{g.diel}$ shared the same decreasing characteristic upon the addition the DEHP molecules, suggesting the enhanced molecular mobility in amorphous phase. As seen in Figure IV. 13, the decreasing behavior in Vogel temperature was strongly dependent upon the DEHP concentration over that of estimated $T_{g.diel}$ and the slope of latter was twice lower than the former, around 16.8 K diminution in $T_{g.diel}$ against 30 K reduction of T_0 . In this case, the Vogel temperature is a

rather sensitive parameter to evaluate the DEHP plasticizing effect on terpolymers. Note that the Fox estimated temperatures $T_{g,Fox}$ exhibited a slight deviation from the dielectric estimated temperature $T_{g,diel}$ defined by the dielectric relaxation spectra and this negative $T_{g,diel}$ deviation from the Fox equation has been reported in the literature [53]. The specific interaction or excess free volume formation of terpolymer blends were considered to interpret this consequence.

Glass transition temperature T_g of PVDF-based terpolymer, i.e. P(VDF-TrFE-CFE/CTFE), have been revealed by many authors and strongly determined by the chemical composition of each individual monomer. Our group reported [52] that the T_g of P(VDF-TrFE-CFE) with the mole ratio of 55.8/35/9.2% at 252 K and frequency of 1 Hz with the help of DMA measurement technique. Wang et al group [54] synthesized a series of P(VDF-TrFE-CTFE) terpolymer with variation of CTFE content range between 26.4% and 7.1% and reported the glass transition temperature varied between approximately 223 K and 245 K at 1 Hz thanks to the equivalent DMA measurement. Li Junjun et al [4] obtained a type of P(VDF-TrFE-CTFE) with 78.8/5.4/15.8% by copolymerization and subsequent dechlorination reactions and then observed the a T_g value of 245.5 K at 1Hz. Glass transition temperature can be also predicted by BDS technique, for instance, Zhang et al [51] disclosed that a P(VDF-TrFE-CFE) with molar ratio of 63/37/7.5% behaved the dielectric defined T_g of 251.2 K as structural relaxation time τ equal to 100 s. It is normally concluded that all the established T_g values of terpolymers somewhat consisted with the underlying $T_{g,diel}$ value estimated in this current work for the control pristine terpolymer. In a DEHP doped terpolymer blend system, good solubility of DEHP in the bulk terpolymer matrix is most possibly attributed to the long alkyl chain, characterizing very high hydrophobicity. Meanwhile, the interaction parameter χ between plasticizer molecules and P(VDF-TrFE-CTFE) terpolymer chain can be estimated by means of Hildebrand solubility parameters which were only based on hydrocarbon type solvents or additives, rather than the hydrogen-bonding (H-bonding) type. But it could be negligible since the H-bonding probability (δ_h of Hansen parameter) is only 3.1 and was not major contribution to the solubility parameter of DEHP molecules. Subsequently, the interaction parameter χ_{12} could be estimated by the following expression:

$$\chi_{12} = \frac{V}{RT} (\delta_1 - \delta_2)^2 \quad \text{IV. 5}$$

where V is the total volume of the terpolymer blends, δ_1 and δ_2 are solubility parameters of DEHP and terpolymer matrix as $16.2 (MPa)^{\frac{1}{2}}$ [55] and $14.3 (MPa)^{\frac{1}{2}}$ [56], respectively. Note that the solubility parameters of both components were close to each other and thus DEHP had a good interaction with the P(VDF-TrFE-CTFE) molecular chain in amorphous phase. On the other hand, relatively bulk phenyl ring capping in another end of DEHP molecules are likely to reduce the

density of molecule coils within the amorphous phase and thus increase the free volume of segmental relaxation of the terpolymer chain, giving rise to the molecule chain dynamics. As expected, T_g values were suppressed with addition of DEHP plasticizer. Dlubek et al. [57] reported a new approach to evaluate glass transition temperature of a PVC/DBP plasticized polymer blends thanks to the combined dilatometer and positron annihilation lifetime spectroscopy techniques. They inferred that with increase in DBP concentration, decrease in T_g values of doped PVC blends indeed caused by increase of specific free volume and molecular chain mobility in amorphous phase. Instead, the constrained molecular chain induced by forming properly rigid amorphous phase in semi-crystalline polymer observed the smaller specific free volume and high T_g values [58]. Inversely, the DEHP doped terpolymer blends were not the case as the constrained amorphous phase. As presented in Figure IV. 12, the addition of plasticizer weakens the main dispersion interaction between neighboring chains and eliminates the intermolecular hindrance. In this case, it is reasonable to assume that the addition of DEHP in PVDF-based terpolymer favored an increase specific free volume of segmental molecular chain. This intermolecular hindrance correlated to the geometrical restriction imposed by the modification such as confinement rising from the nanofillers which in turn could be released by the addition of DEHP molecules. The latter led to decreasing the cooperatively rearranging regions length scale [49].

In addition, it is interesting to note the negative deviation between the dielectric defined temperature $T_{g,die}$ and $T_{g,Fox}$ prediction. The researchers previously revealed that the estimation of glass transition temperatures $T_{g,Fox}$ had good accordance with DMA or DSC method in the

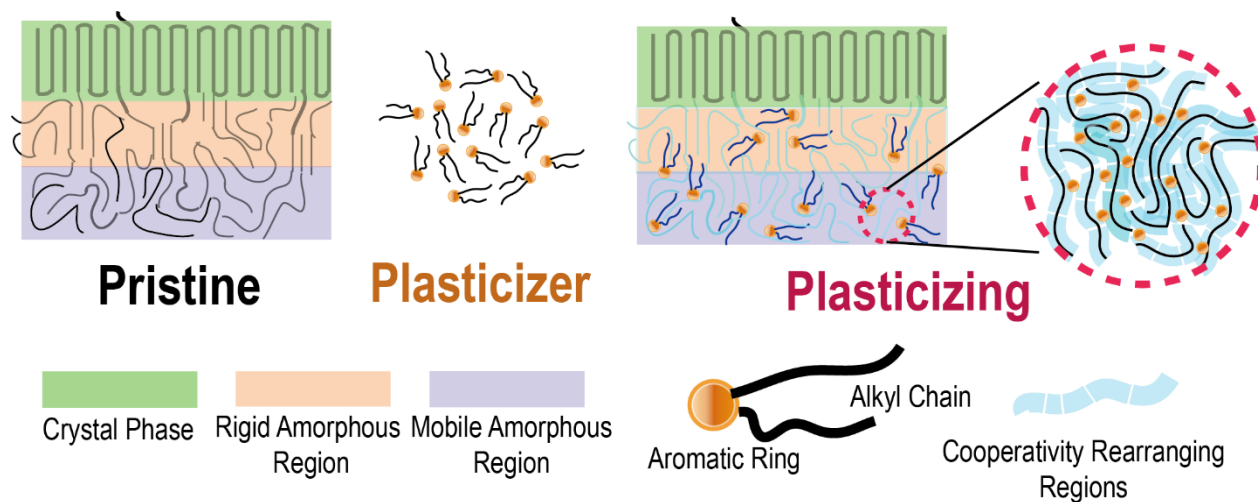


Figure IV. 12 Schematic representation of the three-phase model of plasticizer-free semi-crystalline polymer and microstructure of DEHP plasticized terpolymer blend. Color filled rectangle presents each possible phase of semi-crystalline polymer. Dash circle highlighted the

Cooperativity Rearranging Regions of the DEHP plasticized terpolymer system in amorphous phase.

plasticized polymer system where hydrogen-bonding was absent, i.e. PLA/TA(ATBC) [49], PVC/DEHP [10, 29], PVC/DBP [57] plasticizing systems etc. However, it has been reported previously in H-bonding rich polymer systems, i.e. cellulose, starch, and chitosan, appeared a poor consistency between $T_{g.Fox}$ and measured glass transition temperature (BDS, DMA, DSC, etc). Liu et al. [59] reported a hydrophilic polyols plasticized starch biopolymer system and mainly addressed the glass transition temperature T_g behaviors. The addition of polyols significantly decreased the T_g values of pure starch and only showed an approximately equally good fit to the “modified Fox equation”. The third component, water was employed to adjust the interaction strength between the polyols oligomer and bulk starch domains of the amorphous phase, based on the concept of the competitive interactions between starch-plasticizer pair and plasticize-water pair. The competitive interactions highly depended on the concentration/type of the plasticizer molecules. Bao et al [28] also found the experimental DMA glass transition showed a poor approximation to the Fox equation due to the strong hydrogen-bonding probability of the cellulose molecules. Water was also considered as a H-bonding rich plasticizer to polymer system, e.g. PLA [60] and cellulose [31], etc. In current study, H-bonding effects could be ruled out. The negative deviation of dielectric T_g is observed from the Fox function which fulfills the T_g -composition relationship of full amorphous polymer matrix. However, the terpolymer blends consisted of the considerable amount of crystalline phase (~40%) which enables the concentration values of terpolymer matrix taken for calculation of Fox temperature differ from the local concentration values [61, 62]. The estimated Fox temperatures with subtraction of crystalline phase were also plotted with mass fraction of DEHP and appeared a better approach to the dielectric glass transition temperature.

Table IV. 4 The VFT fitting parameters, estimated dielectric glass transition temperature at structural relaxation time $\tau_\alpha(T)$ equal to 100 s and strength indices values, estimated glass transition temperature thanks to the Fox glass transition temperature $T_{g.Fox}$ law.

Acronyms	$\tau_\infty(s)$	B_0 (K)	T_0 (K)	$T_{g.diel}$ (t=100 s)	D= B/T_0	$T_{g.Fox}$ (K)	$T'_{g.Fox}$ (K)	m
Pristine	2.13×10^{-10}	422.8	231.0	246.7 ± 3.8	1.83	246.7 ± 3.8	246.7 ± 3.8	183.3
P(VDF-TrFE-CTFE)/DEHP5%	2.91×10^{-11}	674.9	217.3	240.6 ± 5	3.11	243.6 ± 3.9	242.0 ± 4.1	129.5
P(VDF-TrFE-CTFE)/DEHP10%	1.12×10^{-11}	807.8	209.7	236.8 ± 3.7	3.85	240.6 ± 4.2	237.6 ± 4.4	113.1
P(VDF-TrFE-CTFE)/DEHP15%	2.16×10^{-11}	838.5	201.2	229.9 ± 5.1	4.17	237.7 ± 4.4	233.6 ± 4.8	101.8

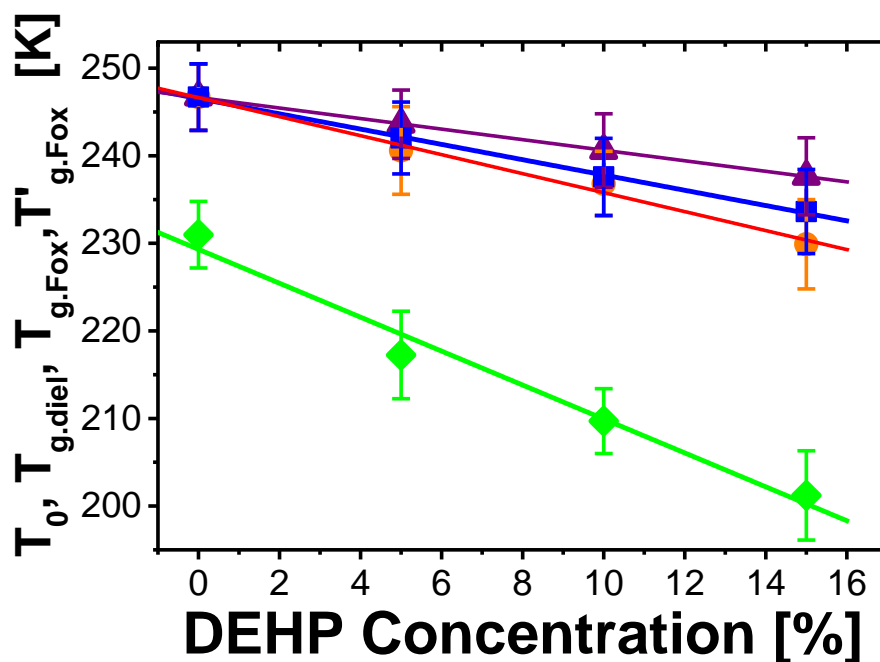


Figure IV. 13 Comparable between Vogel temperature T_0 (◆), dielectric glass transition temperature $T_{g,dielectric}$ (●), Fox glass transition temperature $T_{g,Fox}$ (▲) and estimated Fox temperature $T'_{g,Fox}$ in amorphous phase after subtraction of crystalline phase (■) for pristine and plasticized terpolymer blend systems as a function of DEHP concentration.

III.4.2 Strength & Fragility Index

Previous Chapter III pointed that the strength index parameter D is indicative of degree of deviation from Arrhenius-type relations defining the logarithmic relaxation time of the structural relaxation mode against the reciprocal of temperature near the glass transition region. The strength behavior of the polymer systems could be altered readily by the two kind conditions, thermodynamic and geometric contribution. A fragile polymer glass former can be obtained via isothermal crystallization since the D value is lowering progressively [25]. On basis of the VTF function, this fragile behavior in polymer can also be derived directly from the steep index m (also so-called fragility index) by following expression:

$$m = \frac{d \log \tau_g}{d(T_g/T)} \Big|_{T=T_g} = \frac{DT_0 T_g}{\ln 10 (T_g - T_0)^2} \quad \text{IV. 6}$$

The fragility index values reportedly range from 16 if the strength index parameter D of the glass former is enormously large, being up to maximal 200 when the temperature dependence of relaxation behavior is markedly far from Arrhenius-type correlation. The strong behavior of the polymer is acknowledged to be induced by dynamic inhomogeneity. Figure IV. 14 reported the

strength index D and corresponding fragility index values plotted with DEHP concentration. The strength index for the control pristine was calculated as 1.83, a value of good consistency with previous consequence and surged progressively to 4.17 for 15% DEHP load terpolymer blend

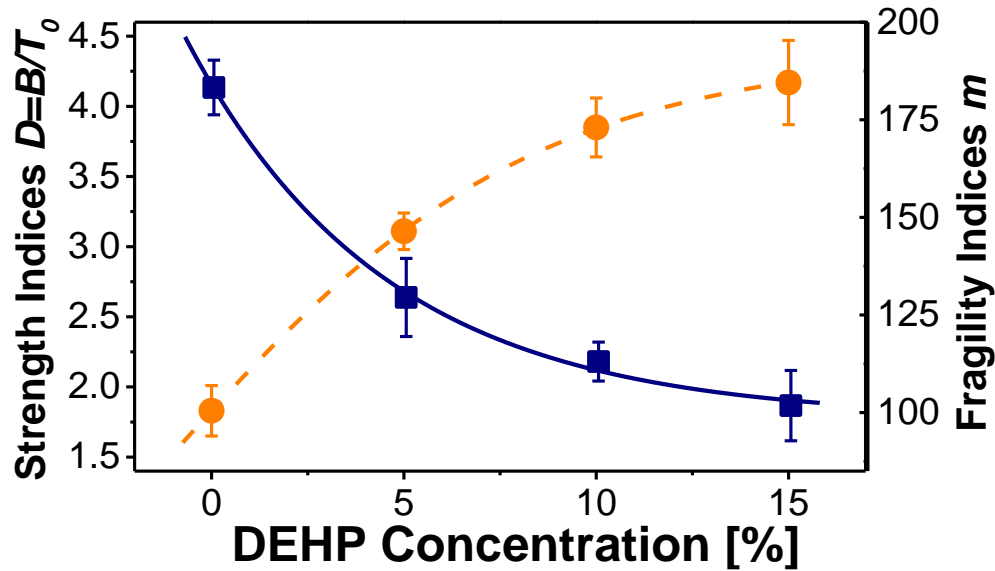


Figure IV. 14 Strength indices $D = B/T_0$ (●) and fragility indices m (■) values as a function of DEHP concentration for control pristine and DEHP doped terpolymer blends. Solid line and dash line were the exponential fit to the fragility and strength index values.

although the estimated D value via equation III.5 in Chapter III was slightly larger. As expected, the fragility indices m were compressed from 183.3 for pristine to 101.8 for 15% DEHP terpolymer blend.

III.4.3 Plasticizing Effect on the Sub-glass Relaxation Process- β Relaxation

β relaxation regimes generally characterize with a broader and less intense relaxation mode in sub-glass state of the glass former polymers at higher frequency over the dielectric spectroscopy. Some of this phenomenological relaxation evidently originated from the reorientation of side group such as methyl and phenyl pendants on the structural molecular backbone [45, 63, 64]. On the other hand, some secondary β relaxations evolve from the local motion of short length scale of repeated unites from the main molecular chain, either in a twisting mode with the certain angle or in an oscillation mode [65, 66]. And addition of DEHP molecules is likely to alter the relaxation rate at temperature approaching the glass transition region, hence it is interesting to identify the influence of DEHP molecules on the terpolymer in a secondary relaxation mode. Figure IV. 15 plotted the isothermal dielectric loss spectra as a function of

logarithmic frequency at temperature between 203 K and 233 K, below the estimated $T_{g,diel}$ for the pristine and 15% DEHP modified terpolymer blend. As a whole, the relaxation amplitude intensified with increase in temperature and a dispersion towards the high frequency were observed upon the dielectric relaxation spectra of both investigated terpolymers. However in Figure IV. 15 (b), the abrupt ridge at low frequency and temperature above 228 K was most possibly due to electrode polarization and undistributed process (most probably interfacial polarization) since the slope of dielectric loss extrapolated via conductive HN function was 0.34 (recall equation IV.1 in experimental section) [67], less than 1 which in theory corresponded to the full conductive contribution in Figure IV. 15.

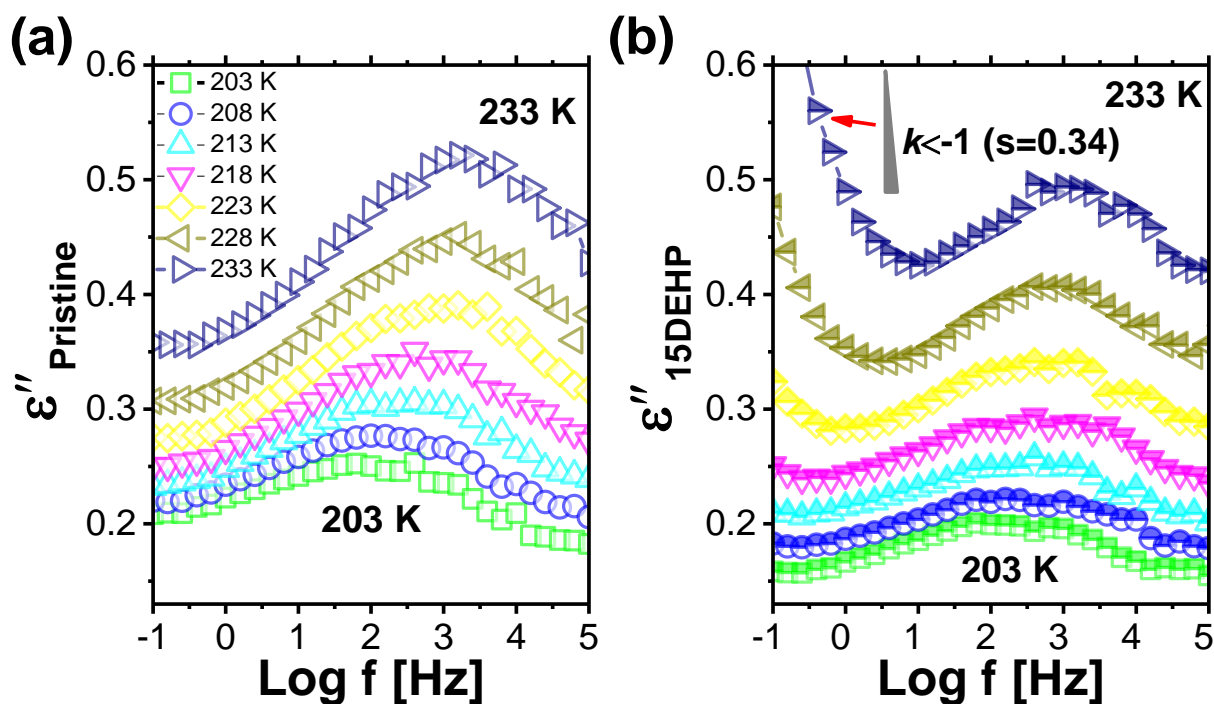


Figure IV. 15 Fractional isothermal dielectric loss as a function of logarithmic frequency with temperature range between 203 K and 233 K for pristine (a) and terpolymer with 15% DEHP mass fraction (b), respectively. k is the slope of the fractional dielectric loss spectroscopy at 233 K and low frequency. Lines are fits to the Havriliak-Negami function.

Similarly, multiple secondary relaxation components were contributed to the dielectric loss spectra at sub-glass region for plasticized terpolymer when the spectra were fitted to the well-known HN function. In this section the intact and dominant relaxation anomalies were mainly addressed. The characteristic relaxation times τ_β were then extrapolated and relaxation map, that was, the logarithmic values versus the reciprocal of temperature $1/T$ was displayed in Figure IV. 16 (a). It is evident that $1/T$ dependence of relaxation times τ_β values characterized a quasi-

linear relationship and satisfactorily followed the Arrhenius-type correlation, $\tau_\beta = \tau_0 \exp(-E_A/RT)$, where τ_0 is pre-exponential factor, E_A represents apparent activation energy and R is ideal gas constant. Note that the shape parameters for DEHP plasticized terpolymer blends were well maintained over the pristine terpolymer, and the rather good agreement with a broad and symmetric secondary relaxation was unambiguous. The shape parameters and calculated E_β were tabulated in Table IV. 5. The calculated E_A value was 39.1 ± 1.2 kJ mol⁻¹ for the pristine terpolymer, being consistent with the value found for crystallized terpolymer in previous section. Surprisingly, the E_A values were compressed with increase in the DEHP molecules concentration, which implies that the secondary relaxation is indeed thermally activated. This also suggested the energy barrier of the local motion of terpolymer molecular chain was likely to be changed. On the other hand, we can also infer that the plasticization effect on the local motion dynamics was corroborated since the moderate decrease in E_A values.

Table IV. 5 Havriliak-Negami function fitting parameters to the dielectric loss spectra of the pristine and DEHP modified terpolymer blends and apparent activation energy in sub-glass state.

Acronyms	α_{HN}	β_{HN}	τ_∞ (s)	E_β (kJ mol ⁻¹)
Pristine	0.20 ± 0.01	1.00	$3.64 \pm 0.93 \times 10^{-12}$	39.1 ± 1.2
P(VDF-TrFE-CTFE)/DEHP5%	0.19 ± 0.02	0.96 ± 0.04	$8.76 \pm 1.42 \times 10^{-12}$	35.8 ± 0.9
P(VDF-TrFE-CTFE)/DEHP10%	0.18 ± 0.02	1.00	$1.23 \pm 0.15 \times 10^{-11}$	31.8 ± 1.5
P(VDF-TrFE-CTFE)/DEHP15%	0.19 ± 0.01	0.99 ± 0.01	$2.14 \pm 0.26 \times 10^{-12}$	30.3 ± 0.6

It is interesting to investigate the origin of this local motion of the secondary process. Many researchers argue that the secondary relaxation is identified to involve motions of only small part of molecule structure, for example, the reorientation of side functional pendent on the backbone or small molecular unites such as methyl group [68]. Besides, the relaxation involved in local short sequence of the molecular chain was also the potential reason of a secondary process. However, Johari and Goldstein [69-71] found a universal secondary relaxation occurred in small molecule glass formers, which were composed of rigid backbone such as phenyl and ring-like element in organic molecules. Researchers have attributed this secondary relaxation to the fluctuation of the whole molecule instead of the relaxation regarding to the intramolecular reason. In case of present terpolymer studies, since the absence of flexible side group pendants on the C-C backboned molecular chain, it is reasonable to speculate the β relaxation process was the

fluctuation of rather short sequences, comparable with the cooperative segmental relaxation. Indeed, secondary relaxation mode in terpolymers has the very similar origins with structural relaxation, but involving over a short molecular length scale. We inferred that a Johari-Goldstein (J-G) like β relaxation, taken as the precursor of the α relaxation process, was transferred to the main segmental relaxation as the temperature approached glass transition region.

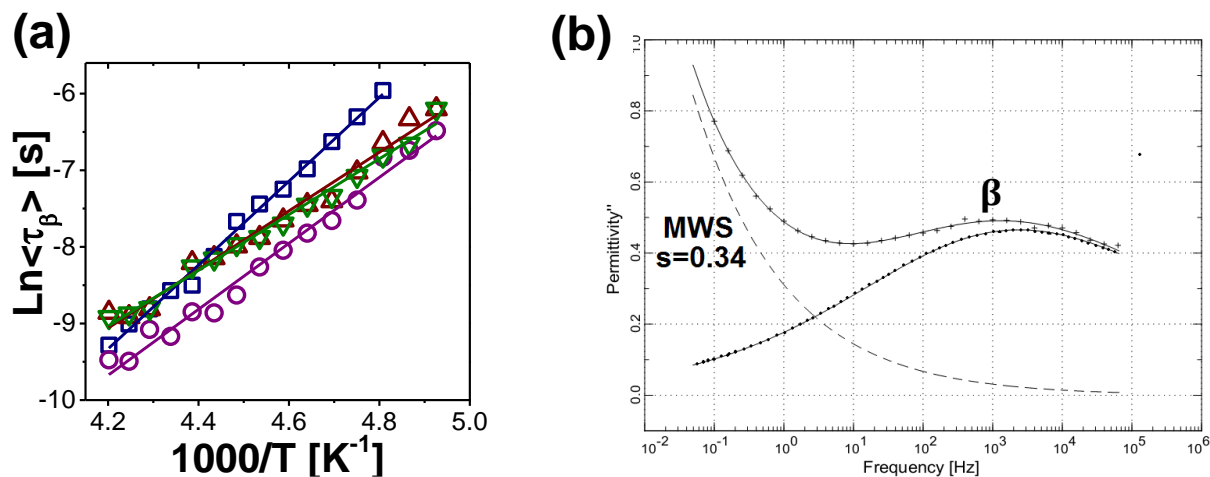


Figure IV. 16 Temperature dependence of β relaxation map plotted as a function of the reciprocal of temperature for the pristine and DEHP doped terpolymer blends (a); Dielectric loss spectra ($Permittivity''$) as a function of frequency in the temperature region of β relaxation at 238 K for representative 15% DEHP load terpolymer blend (b), dash line denotes the conductivity fitting component of the dielectric loss spectrum, here $s=0.34$ indicating the presence of interfacial polarization effect; dotted solid line was an individual HN fit to the measured dielectric loss spectrum.

III. 5 Mobility of Space Charge Carriers at High Temperature

3D dielectric loss spectra saw the several orders of magnitude stronger at higher temperature and low frequency for each terpolymer studied (recall Figure IV. 6), where the defined relaxation processes were overlapped with the conductivity. This was confirmed by the fact that the exponential parameter s of conductivity contribution in the right hand was equal to 1 via HN fitting to the dielectric loss spectrum at high temperature. Firstly, real part of complex conductivity were then calculated by $\sigma^* = \sigma' + i\sigma'' = \omega\epsilon_0\epsilon'' + \omega\epsilon_0\epsilon'$ and was plotted against logarithmic frequency for the representative terpolymer blend with 5% DEHP mass fraction as shown in Figure IV. 17 (a) accordingly. The DEHP modified terpolymer shared the equivalent features as that of pristine one (recall Figure III. 9 in Chapter III). As temperature increased, the conductivity values appeared less dependent upon the frequency, which was previously revealed

due to the contribution of charge carrier transportation in the polymer. In order to fully the influence of addition of DEBP molecules on the motion of charge carrier behavior, conductivity

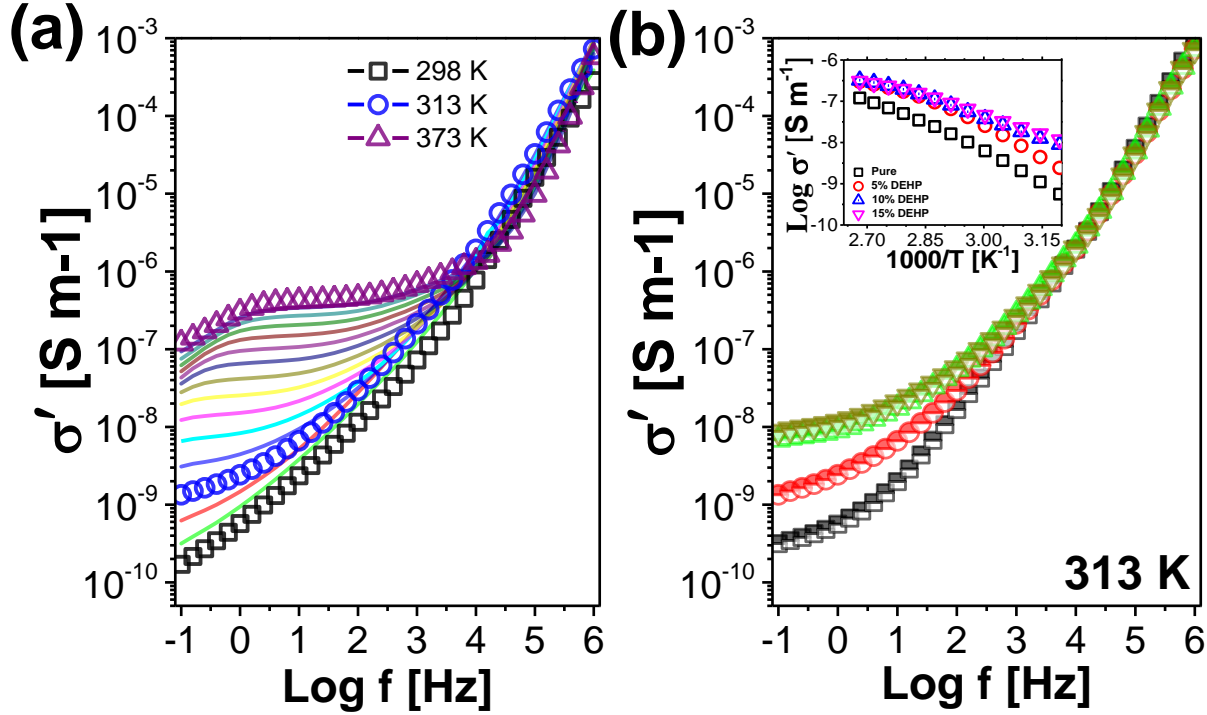


Figure IV. 17 Isothermal real part of complex conductivity as a function of log frequency over the wide temperature range between 298 K and 373 K for terpolymer blend with 5% DEHP concentration (a), Compared real part of conductivity against log frequency for pristine (■) and plasticized terpolymer with 5% (●), 10% (▲), 15% (▼) addition of DEHP at 313 K, inset figure represents the conductivity versus the reciprocal of the temperature ($1/T$).

values as a function of DEHP concentration at given temperature of 313 K were plotted in Figure IV. 17 (b). It is worthy to note that the conductivity were enhanced with more than one decade by the addition of 10% DEHP and was saturated even though the addition of the DEHP content reached as much as 15% mass fraction. Figure IV. 17 (b) inset plotted the respective logarithmic conductivity versus the reciprocal of the temperature and followed a monotonic and curvature fashion type, in good agreement with the conductivity behavior of the high conductive materials, implying the charge carrier transportation was thermally activated. And $1/T$ temperature dependence of the logarithmic conductivity can be fitted by using conductivity referred VFT function [72], namely:

$$\sigma = \sigma_0 \exp \frac{DT_0^\sigma}{T - T_0^\sigma}. \quad \text{IV. 7}$$

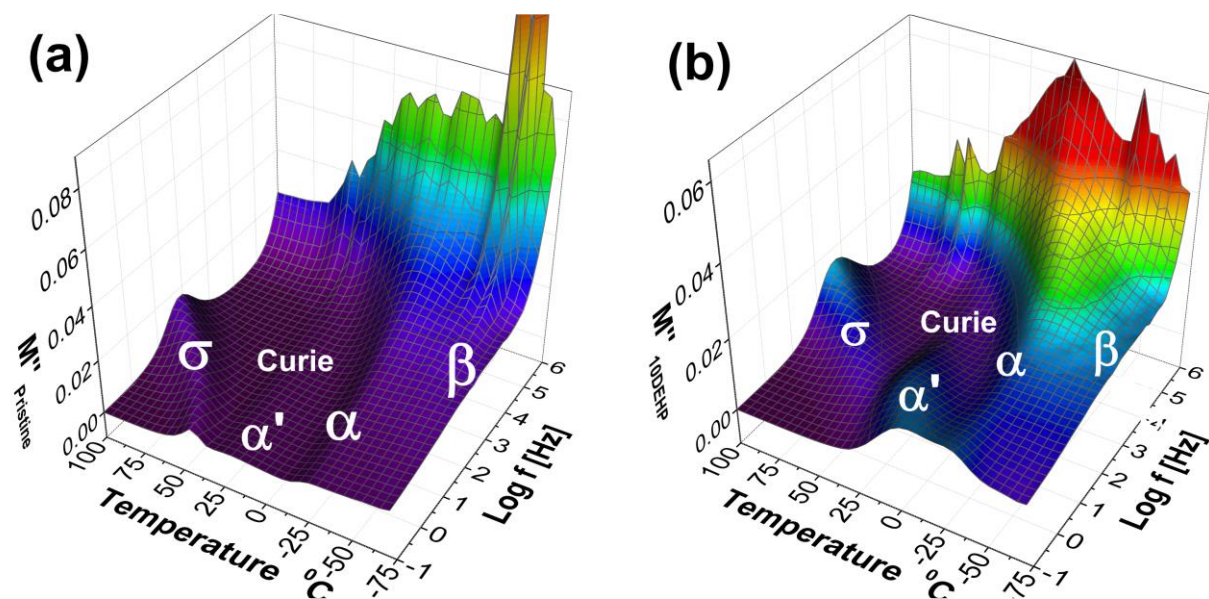


Figure IV. 18 Dielectric modulus spectra as a function of full temperature and frequency range for pristine (a) and representative modified terpolymer blends with 10% DEHP (b). The respective relaxation process was marked: σ , conductivity at high temperature; α' represents segmental relaxation of constrained amorphous phase; Curie process refers to the transition in crystal lamellae defects; α relaxation is segmental relaxation in mobile amorphous phase; β is secondary relaxation in subglass state of the terpolymer.

As stated in polymer system the influence of charge carrier motion on the electric conductivity behaviors were governed by two well-known approaches, proton-hopping theory and vehicle mechanism. In pure isothermal crystallized terpolymers, DC conductivity behavior was intimately associated with the motion of free ions charge carriers, which was thermally activated by the segmental relaxation in the amorphous region whatever the constrained or mobile. In DEHP doped terpolymer blend system, given that the conductivity behaviors increased enormously, it is interesting to insight into its origin. In order to precisely describe the translational motion behaviors of the free charge carriers in the DEHP modified terpolymer, an alternative approach of dielectric modulus M^* spectra were instead employed since the dielectric modulus transformation derived from the dielectric spectra enabled to compress and minimize the electrode polarization at low frequency. The conductivity behavior was then emphasized with the help of imaginary part of dielectric modulus spectra, being plotted as a function of temperature and frequency in Figure IV. 18. The quick drift towards the higher frequency occurred for the conductivity processes (marked as σ process) in both spectra as temperature proceeded. In case of 10% DEHP terpolymer blend, the constrained segmental relaxation process kinked with the conductivity process at higher temperature. The fractional isothermal dielectric modulus spectra

against frequency correlated with occurrence of conductivity relaxation for pristine and representative DEHP doped terpolymer blend were compared in Figure IV. 19. The typical

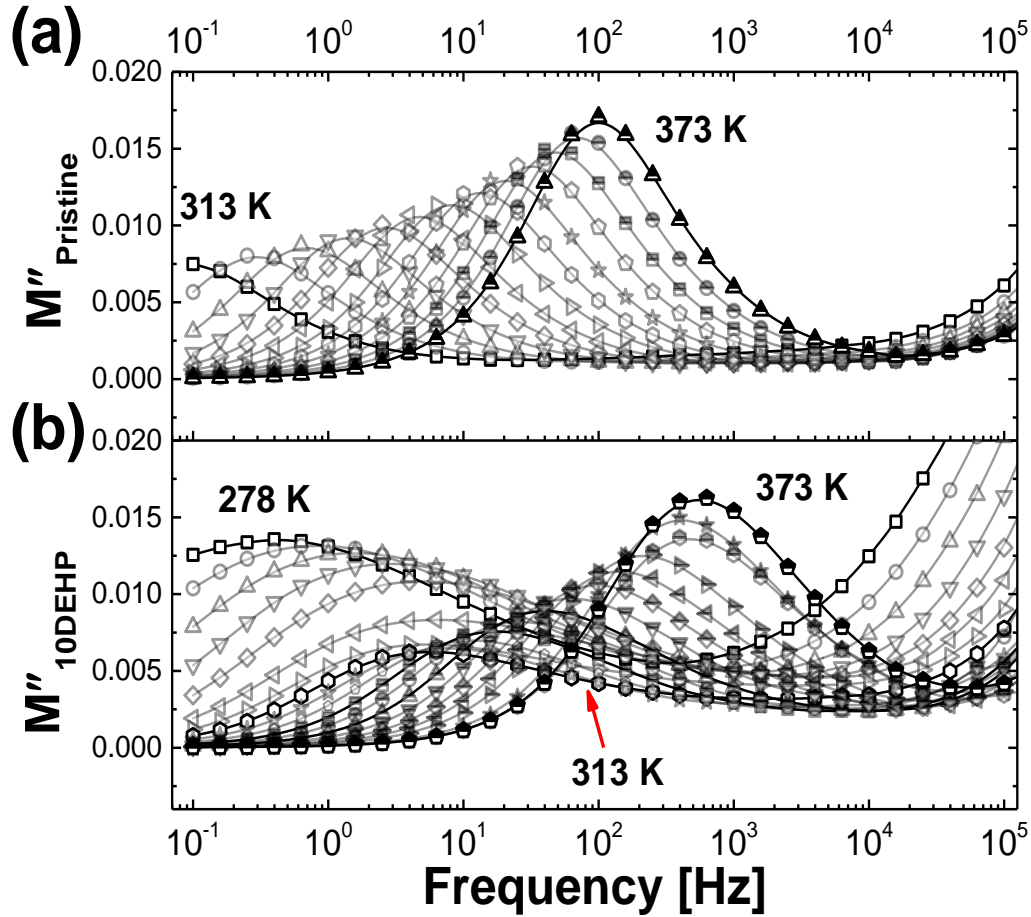


Figure IV. 19 Fractional isothermal dielectric modulus as a function of frequency with temperature range between 313 K and 373 for pristine terpolymer (a) between 278 K and 373 K for modified terpolymer with 10% DEHP concentration (b).

relaxation trend was observed for the M'' spectra of the pristine terpolymer in according with previous study. In case of modified terpolymer, a faster shift towards the higher frequency occurred to the isothermal M'' spectrum in contrast with pristine spectrum, suggesting the enhancement of the translational motion of charge carriers. In order to trace the conductivity behavior, the DC conductivity relaxation times τ_{con} had been reliably determined by the reciprocal values of angular frequency (ω) of electric modulus peaks, namely, $\tau_{con}=1/(2\pi f_{max})$. Temperature dependence of logarithmic relaxation times τ_{con} for each terpolymer system was compared in Figure IV. 20, featuring the large discrepancies. As illustrated, conductivity relaxation time τ_{con} of the pristine terpolymer was described as a curvature type correlation and was satisfactorily fitted to a single VFT power law. Similar fitting was observed to the 5% DEHP doped terpolymer blend. This is, however not the case for the terpolymer blends with 10% and 15%

DEHP. The both plots could not be fitted with a single power law, either VFT or Arrhenius-type correlation. Instead, the two compensations, VFT-type relaxation and Arrhenius-type were decoupled at 338 K and 343 K, respectively, below which the relaxation processes were assigned to the overlapping relaxation spectra of the primary relaxation, conductivity and Curie phase transition, examined via the three dimensional electric modulus spectra in Figure IV. 18b. The VFT fitting parameters of the respective conductivity relaxation were then tabulated in Table IV. 6. Not surprisingly, the Vogel temperature of conductivity relaxation T_0^σ were 230 ± 1.3 K and 203 ± 1.5 K for the pristine and 15% DEHP doped terpolymer blend, appearing quite close to the Vogel temperature T_0^α found for the mobile amorphous phase. Herein, it is reasonable to assume that the conduction process is controlled by the segmental molecular mobility of the terpolymer chain, which is highly consistent with the previous study.

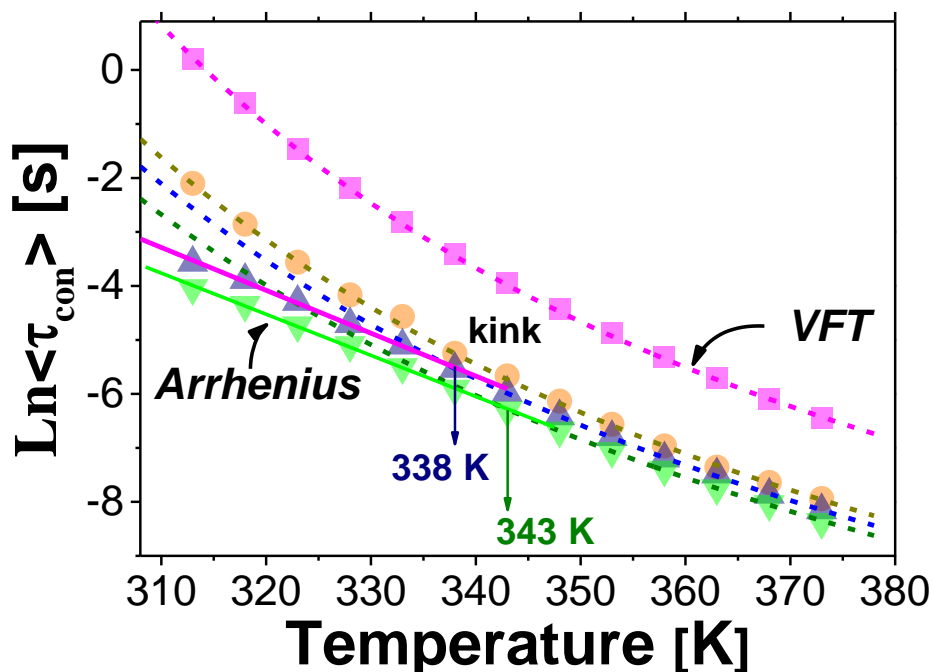


Figure IV. 20 Temperature dependence of the conductivity relaxation times τ_{con} for the pristine (■), 5% (●), 10% (▲) and 15% (▼) DEHP doped terpolymer blends. Dashed curvature lines are VFT fitting to the logarithmic conductivity relaxation times while linear lines represent the Arrhenius type fitting. The temperature at which Arrhenius type separated with VFT fits were visible for 10% DEHP and 15% DEHP plasticized terpolymers at 338 K and 343 K, respectively.

It is evident that the DC conductivity relaxation behavior was attributed to the translational motion of ions charge carrier, since in practice no polymer electrolytes or ionomers was present in DEHP doped terpolymer blends. It was acknowledged that In salt-containing PEO-based plasticized polymer system the electric conductivity was enhanced several orders of magnitude at ambient temperature, in concomitant with lowering the glass transition temperature [73]. The

excellent conductivity behavior was mostly possible due to a decrease in the grain-boundary resistance. Recent studies on polymer-based ionomers have revealed that the conductivity behavior was also strongly dependent upon the ions concentration and ions mobility [74, 75]. In this present work, free cations and anions were introduced during the polymerization process and the addition of the DEHP molecules. The free ions transferred in amorphous intermedium, at which the loose packing molecules mobility was accelerated by the DEHP plasticizer, accumulated near the interface between amorphous region and crystalline wall, where the latter had much higher electrical resistance [76]. On the other hand, in our previous statement the DEHP plasticizer molecule itself has a relatively high conductivity ($\sim 10^{-12}$ - 10^{-9} S cm⁻¹) over the ions-free polymer ($\sim 10^{-16}$ - 10^{-15} S cm⁻¹). The DEHP molecules were easy to be charged and polarized even under a low electric bias. As plasticized terpolymer blends were subjected to the electric field, charges were injected into the materials. The DEHP molecules acting as the charge carriers facilitated ions transportation to the phase boundary, resulting in high local space charge density, giving rise to the interfacial polarization. On the other hand, the remaining charges diffused towards the anode electrode ready for discharging and an expected high electric conductivity was then observed [77, 78].

Table IV. 6 The VFT-type fitting parameters for conductivity relaxation processes for pristine and DEHP doped terpolymer blends: Vogel temperature T_0^σ , VFT apparent activation energy B_0^σ and pre-exponential factor τ_0^σ .

Acronyms	τ_0^σ (s)	B_0^σ (K)	T_0^σ (K)	${}^bT_0^\alpha(t=100s)$
Pristine	1.68×10^{-7}	1308.3 ± 28.2	230.4 ± 3.1	231.0 ± 2.4
P(VDF-TrFE-CTFE)/DEHP5%	2.82×10^{-8}	1474.7 ± 15.4	216.4 ± 5.3	217.3 ± 1.9
P(VDF-TrFE-CTFE)/DEHP10%	1.98×10^{-8}	1560.3 ± 26.1	210.2 ± 2.4	209.7 ± 1.4
P(VDF-TrFE-CTFE)/DEHP15%	1.58×10^{-8}	1632.3 ± 33.5	203.2 ± 3.6	201.2 ± 2.6

Note: b, Vogel temperature obtained by VFT fitting to the segmental relaxation time against temperature in amorphous phase for isothermal crystallized terpolymers (recall Chapter III. IV. 1)

III. 6 Interfacial polarization and primary relaxation in constrained amorphous phase

In previous section, the DC conductivity behavior at higher temperature-low frequency range had been addressed, causing an abrupt surge of dielectric loss arising from the motion of ions charge carriers. We also unveiled the acceleration of translational motion of space charge carrier in DEHP doped terpolymer blends. Because of the multiphase microstructure, the semi-crystalline terpolymer shows the essence of structural inhomogeneity, which gives rise to the

unevenly distribution of free charge carrier in terpolymer matrices, particularly at the interfacial boundary adjacent to the crystal lamellae [53, 79]. The charged crystal lamellae, acting as the macroscopic dipoles, are locally polarized since applying electric field. Therefore, the polarization of macro-dipoles tremendously contributed to the dielectric spectra. This was reliably evidenced by a drastic enhancement of dielectric permittivity occurring at lower frequency than that of matrix segmental relaxation with the assistance of the real complex permittivity spectra, which was referred to the Maxwell-Wagner-Sillars (MWS) interfacial polarization. The relaxation region and strength of the MWS process acknowledgedly depend upon the contrast between the ions DC conductivity and dipolar polarization (orientational

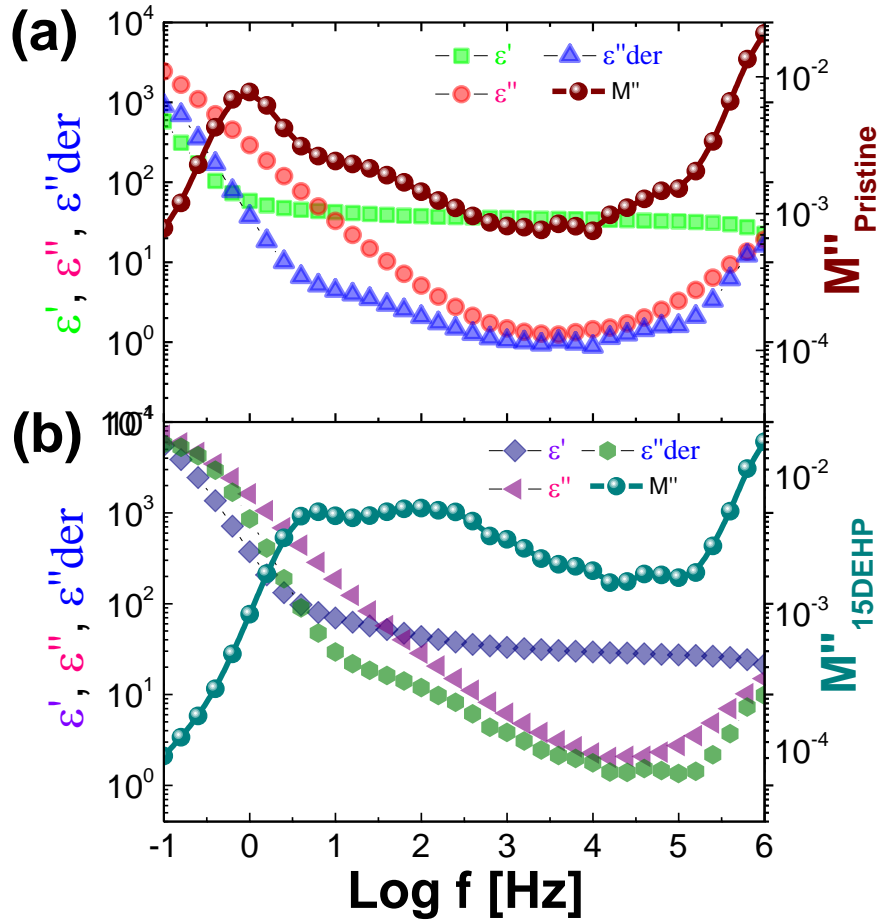


Figure IV. 21 Isothermal real ϵ' (green square) and imaginary ϵ'' (red circle) part of dielectric spectra, corresponding derivative dielectric loss ϵ''_{der} (blue upper triangle) and electric modulus M'' (wine filled ball) against the logarithmic frequency at temperature 343 K for the pristine (a); ϵ' (blue diamond), ϵ'' (purple triangle), ϵ''_{der} (green hexagon) and M'' (dark cyan filled ball) for 15% DEHP doped terpolymer blend (b).

polarization) of the polymer matrix. However, it is rather embarrassed that the MWS process was obscured by ions DC conductivity due to the ions translational motion. In order to eliminate the

conduction effects from the whole dielectric loss spectra, we resorted to the derivative dielectric loss (ε''_{der}) according to the Karmers-Kronig transformation [68, 80]:

$$\varepsilon''_{der} \approx -\frac{\pi}{2} \frac{\partial \varepsilon'(\omega)}{\partial \ln \omega} \quad \text{IV. 8}$$

where ω is the angular frequency. The picked up isothermal dielectric representative of the and 15% DEHP doped terpolymer blend along with derivative dielectric loss ε''_{der} spectra as a function of frequency at 343 K (70 °C) were plotted in Figure IV 21. The MWS, the one maintaining strong dielectric strength in lower frequency was disclosed with a broad and weak relaxation strength at intermediate-frequency, which the latter probably arose due to the dielectric manifestation of segmental relaxation in constrained amorphous phase (α'). For the sake of clear presentation, the dielectric relaxation processes were eventually resolved with the help of the dielectric modulus M'' formalism calculated by using dielectric loss derivatives (recall equation 4.8). As expected, the two intact relaxation peaks were discernible at low frequency for both the pristine and 15% DEHP doped terpolymer blend, assigned to the MWS interfacial polarization and α' process in order of increase in frequency.

Being benefit from the derivative electric modulus spectra, the respective relaxation processes were depicted as a function of frequency and temperature for the pristine and DEHP doped terpolymer blends in Figure IV. 22. The low frequency-high temperature spectra characterized with two curvature-type relaxation processes, representing very fast shift towards the high variables. Note that with increase in the addition of DEHP plasticizer content, the relaxation strength of the α' processes were significantly intensified, eventually resulting in a vague relaxation process display between both MWS and α' regimes. In order to have a better visibility, the isothermal electric modulus spectra of the representative terpolymer systems were picked up from the dual variables graphics in Figure IV. 23. As a whole, the typical and intensive relaxation assigned to MWS strongly depended upon the frequency for the pristine and DEHP modified terpolymer blend. A shift towards high frequency but less intense improvement in relaxation strength occurred to the broad constrained α' dielectric relaxation regimes. Notwithstanding for 10% DEHP doped terpolymer blend the MWS process characterized a progressive increase in dielectric strength and peak frequency, the α' process, which presented the remained relaxation strength initially, moved towards the higher frequency with a great enhancement of its relaxation strength, indicating the considerable plasticization effect. The relaxation behaviors of both regimes were consistent with the established findings [81-83].

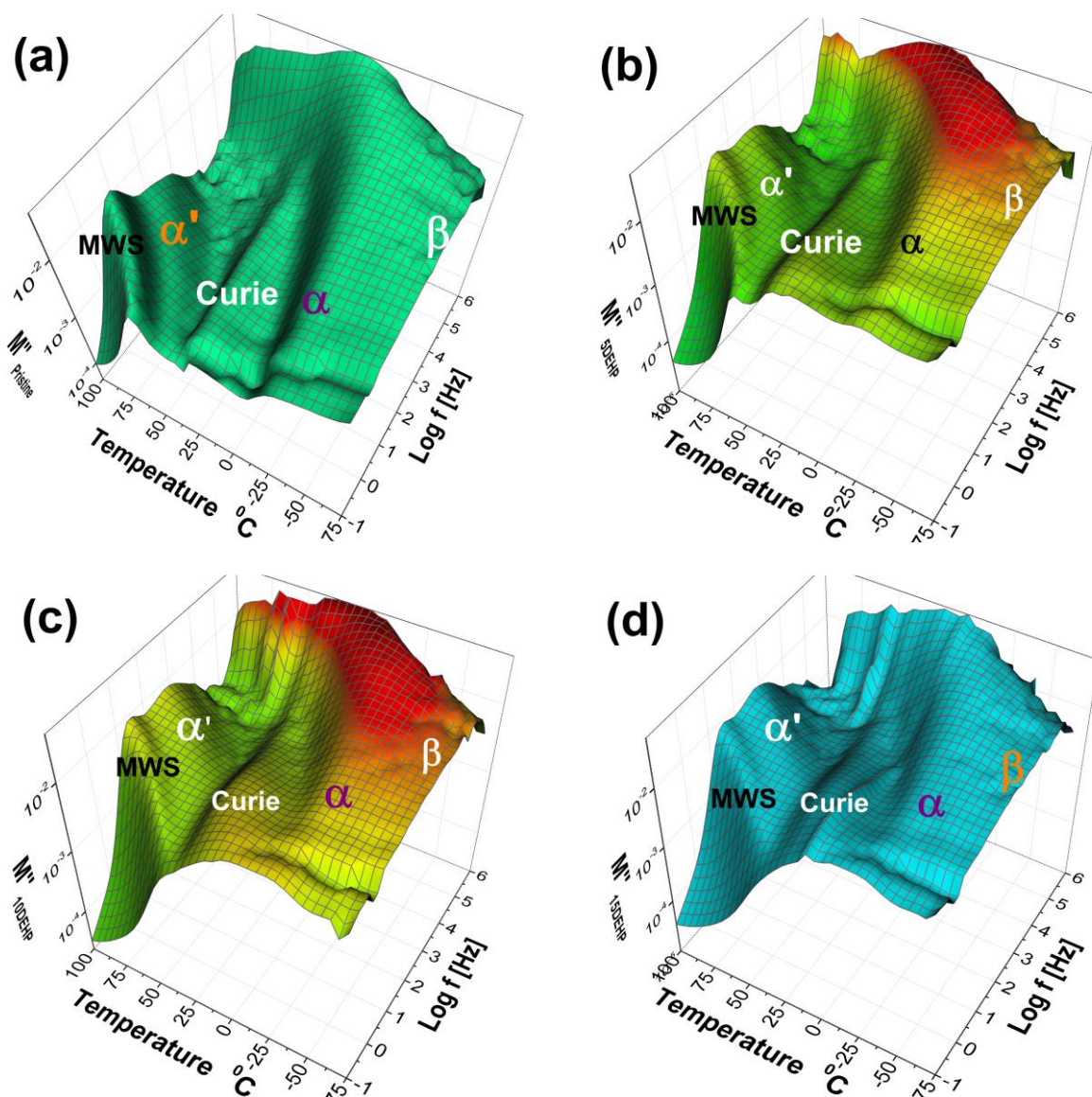


Figure IV. 22 Conductivity-free dielectric modulus derivative spectra M''_{der} for pristine (a), 5% DEHP (b), 10% DEHP (c) and 15% DEHP (d) as a function of frequency and temperature, the respective processes were marked by interfacial polarization (MWS), constrained structural relaxation (α'), Curie transition (Curie), segmental relaxation in amorphous phase (α) and secondary relaxation (β) in order of increase in temperature.

In order to evaluate the influence of DEHP concentration on both processes, the dielectric modulus for each studied terpolymer, pristine and DEHP doped, were compared in Figure IV. 24. At given temperature of 348 K, the relaxation peak frequency of MWS processes for DEHP doped terpolymer blends drifted almost one decade towards the higher value. The similar trend simultaneously appeared for the constrained α' process. In addition, one should not neglect the discernible compression of the relaxation strength of the MWS process instead of the enhancement of the amplitude of constrained α' relaxation process, in strength of MWS is

indicative of declining the phase contrast and improving the compatibility in anisotropic system, in other word, reducing the degree of the microphase separation [84]. In our case, with addition of DEHP molecules, the hypothesis that the constrained amorphous regions developed to behave similarly as the mobile amorphous phase, arose. This assumption was confirmed by the enhancement of peak intensity of the constrained α' process.

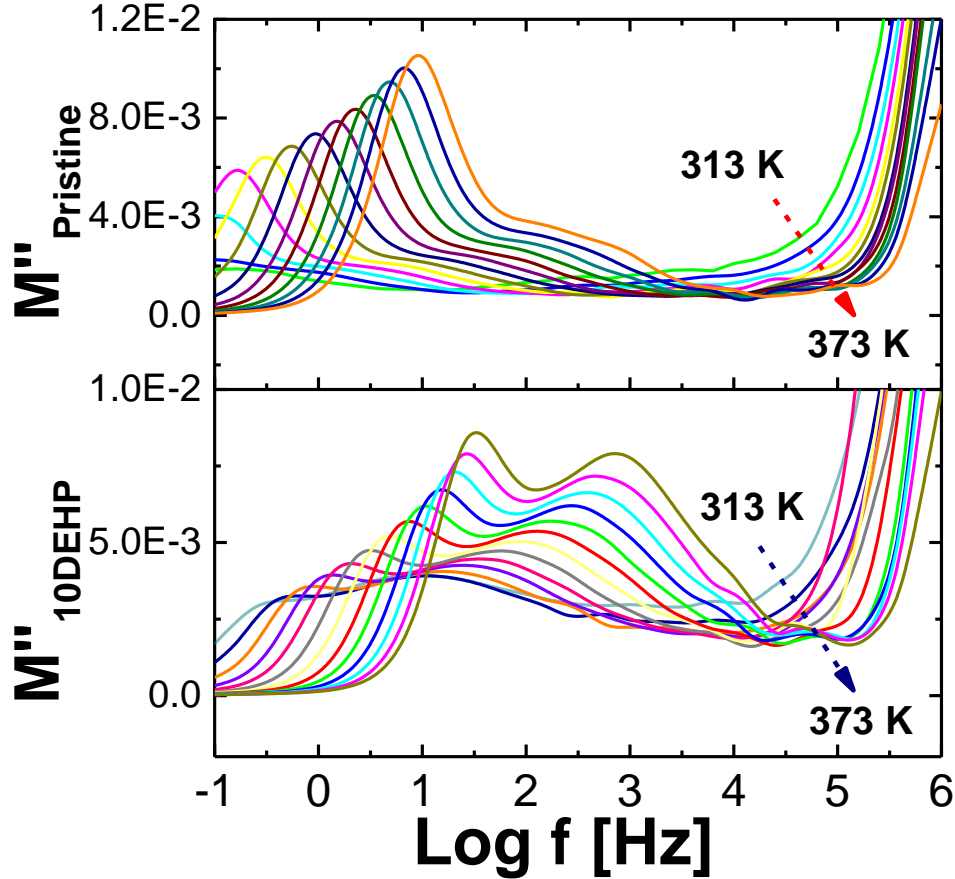


Figure IV. 23 Electric modulus spectra plotted as a function of frequency over temperature range between ambient temperature of 298K and 373K which derived from Karmers-Konig function for the pristine (top) and 10% DEHP load terpolymer blend (bottom). The spectra appeared the two distinctive relaxation regimes, being attributed to the interfacial polarization and primary α' -relaxation (α').

Aiming at quantitative evaluation of DEHP plasticization effect to the α' relaxation behavior, the peaks defined by electric modulus spectra were reliably described with Davidson-Cole formalism:

$$M^*(\omega) = M_{\infty} + \sum_j \frac{\Delta M_j}{(1+i\omega\tau_{Mj})^{\gamma}} \quad \text{IV. 9}$$

Where τ_M is the characteristic relaxation time, M_∞ is dielectric modulus at infinite frequency, ΔM_j is respective dielectric modulus of relaxation regimes at the index, τ_{Mj} represents the average characteristic relaxation time. γ is the shape parameter, describing the broadness of the relaxation regimes. The characteristic relaxation time for respective process was extrapolated by fitting the Davidson-Cole function to the electric modulus. Temperature dependence of the relaxation times for MWS process were plotted in Figure IV. 25, along with constrained α' relaxation time. In case of the MWS process, note that the relaxation times temperature T dependent for DEHP doped terpolymer blends split away from the pristine one to large extent. This separation was observed in particular at lower temperature, very similar behavior to a relaxation process arising due to dipole fluctuations. Indeed, the accumulating charges distribution induced by the inhomogeneity of the terpolymer microstructure was responsible for the occurrence of the MWS process. And it is also observed that an increase in DEHP concentration gave rise to the acceleration of the “macroscopic dipoles” relaxation rate. The dielectric permittivity behaved consequently the great enhancement at low frequency, appearing the observed dielectric strength up to the order of 10^2 - 10^4 magnitude.

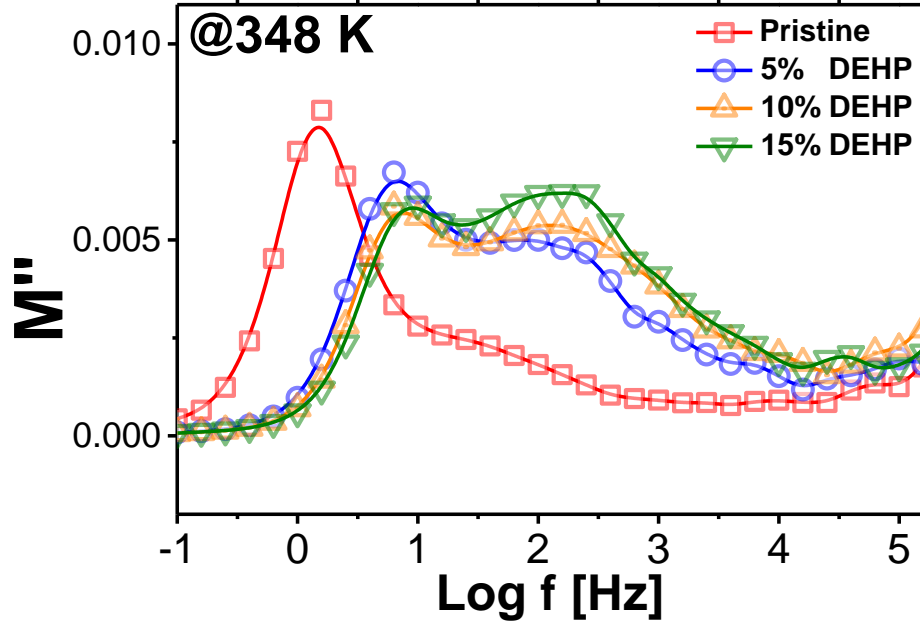


Figure IV. 24 A comparison of dielectric modulus M'' with variation of addition of DEHP content for the pristine and plasticized terpolymer systems as a function of logarithmic frequency at 348 K. M'' here was calculated using dielectric loss derivatives deduced from the Kramer-Kronig transformation.

Further, taking the terpolymer microstructure into consideration, it is worthy to note the relaxation behaviors of the constrained amorphous phase in Figure IV. 25, which in theory obstructs the transportation of space charges (recall the Chapter III), differ largely between the pristine and DEHP doped terpolymer blends, in particular at relatively low temperature. This observation was in rather good agreement with the relaxation process assigned to segmental relaxation in mobile amorphous phase. The plausible reason for this result was due to the presence of DEHP molecules in this constrained amorphous phase, enabling the terpolymer molecular chain less affinity and weak interaction. In this case, we inferred an equivalent plasticization mechanism as comparing with plasticizing effect in mobile amorphous phase. Then one could readily find a VFT-type correlation between the relaxation time and temperature. The fitting parameters and estimated glass transition temperature $T_{g.diel}^{\alpha'}$ as the relaxation time was equal to 100 s were summarized in Table IV. 7. As expected, the suppression of Vogel temperature $T_0^{\alpha'}$ occurred to the DEHP doped terpolymer blends which witnessed a monotonic decrease with the DEHP concentration. The pristine terpolymer with estimated glass transition temperature $T_{g.diel}^{\alpha'}$ of 301.8 K accordingly appeared the decreasing trend by almost 25 K upon the DEHP concentration. The plasticizing effect on the constrained/rigid amorphous phase was also reported in small molecules or oligomers doped P(VDF-CTFE) copolymer and PVDF blends [33, 41]. Based on the interpretation of the $T_{g.diel}^{\alpha}$ depression in mobile amorphous phase, the intermolecular interaction of the macromolecules weakened because of the substitution by the competitive interaction between DEHP molecules and macromolecular chains thanks to the excellent solubility of DEHP molecules with the terpolymer matrix. This led to a decreasing average length of cooperativity and increasing molecular free volume [85]. On the other hand, more than 50% of interphase accounting for the whole amorphous phase in terpolymer [38], allowed the plasticizing contribution as strong enough to jeopardize the estimated glass transition temperature $T_{g.diel}^{\alpha'}$. Since the constrained amorphous phase was somewhat “mobile and free”,

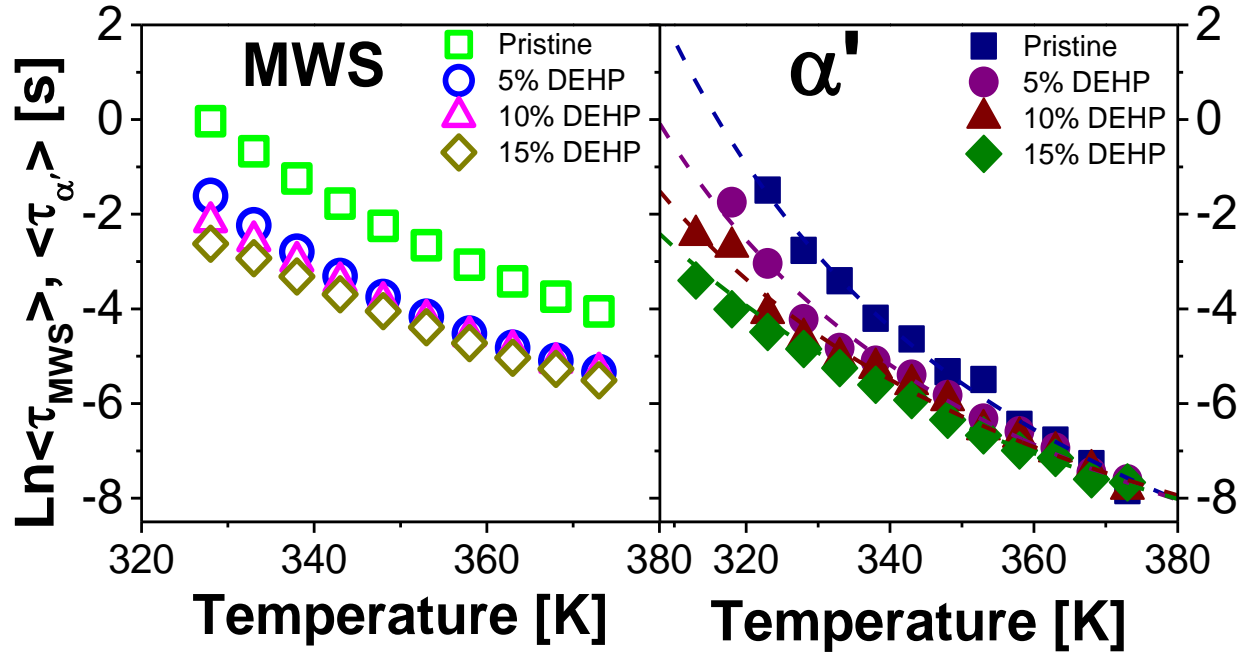


Figure IV. 25 Temperature dependence of relaxation time of the MWS processes (open symbols) and structural relaxation process of constrained amorphous phase α' (filled symbols) as a function of temperature for the pristine and DEHP doped blends. Dash lines in right graphic were the VFT fits to the curvature α' processes.

translational motion of the charge carriers in the interphase accelerated. According to the fact that the dipole relaxation governed the transportation of space free charges, the charges accumulating behavior was as expected altered. This hypothesis was in turn confirmed by the relaxation behavior of the MWS process.

Table IV. 7 VFT fitting parameters and estimated glass transition temperature $T_{g.diel}^{\alpha'}$, strength indices or fragility values for pristine and DEHP plasticized blends.

Acronyms	$\tau_{\infty}^{\alpha'} (s)$	$B_0^{\alpha'} (K)$	$T_0^{\alpha'} (K)$	$T_{g.diel}^{\alpha'} (t=100s)$	$D^{\alpha'}=B/T_0$	D^a Calcul.
Pristine	1.03×10^{-7}	1030.4 ± 37.4	252.0 ± 2.7	301.8 ± 1.5	4.09	7.74
P(VDF-TrFE-CTFE)/DEHP5%	6.03×10^{-7}	813.1 ± 21.6	250.7 ± 1.3	293.7 ± 2.1	3.24	6.71
P(VDF-TrFE-CTFE)/DEHP10%	7.97×10^{-7}	858.9 ± 18.9	239.3 ± 3.6	285.4 ± 1.9	3.50	7.54
P(VDF-TrFE-CTFE)/DEHP15%	4.44×10^{-7}	1039.2 ± 28.4	222.9 ± 1.9	276.9 ± 0.8	4.65	9.48

^a Note: values calculated from the equation: $T_{g.diel}^{\alpha'}/T_0^{\alpha'} = 1 + D / (2.303 \log \frac{\tau_g}{\tau_0})$.

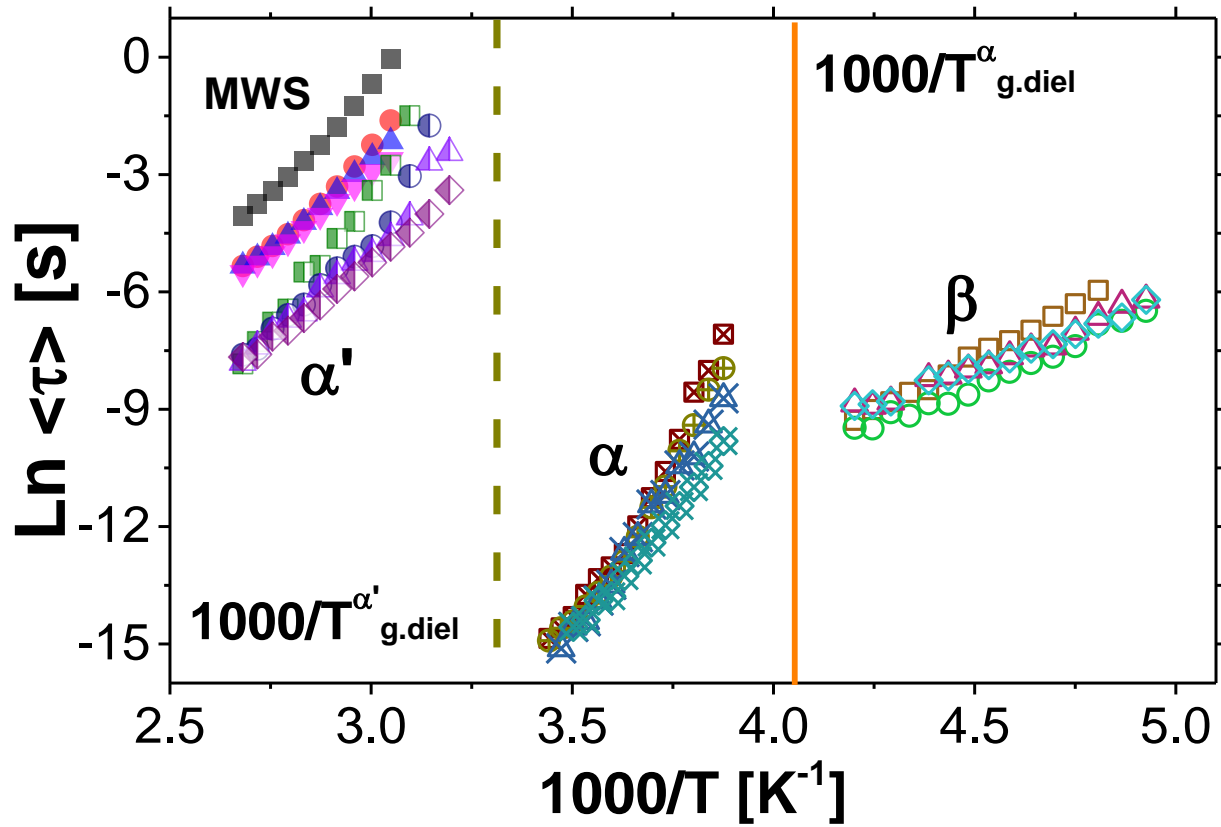


Figure IV. 26 Full dielectric relaxation map of the pristine and DEHP doped terpolymer blend systems, presenting all the relaxation processes covering the large scale of temperature range. Each process was designated as MWS (filled symbols), α' (left filled symbols), α (\times symbols) occurring in super-cooled liquid region and β (open symbols) in sub-glass state of the terpolymer material in the order of temperature proceeding. Solid vertical line and dash line were assigned to the reciprocal of estimated glass transition temperature $T^{\alpha'}_{g.diel}$ and $T^{\alpha}_{g.diel}$ s defined by the dielectric approach.

IV Conclusions

Several-fold improvements in the dielectric constant and electromechanical response of the all-organic polymer blends were readily achieved by simply adding commonly-used DEHP phthalate plasticizer into pure terpolymer matrix reported in our previous study. Around maximal 60 times increase in permittivity on expense of a half loss of the Young's modulus and mechanical energy density of plasticized terpolymer blends demonstrated 20 times higher over the pristine terpolymer. In this current chapter, an interpretation of this fundamental trend is given on a molecular level by means of broadband dielectric spectroscopy technique and thermal analysis. The main conclusions about this chapter are summarized as listed here:

First of all, AFM patterns were employed to evaluate the morphology structure and miscibility of the DEHP molecules load terpolymer blends. The regular surface morphology

manifested the absence of phase separation of the excellent miscibility of DEHP molecules in terpolymer. The bumpy-like crystal domains were however loosely packed, the size of which were likely to be somewhat intensified via addition of the plasticizer DEHP molecules, implying much inhomogeneity of size distribution over the pristine terpolymer matrix. And this was also evident by the DSC measurement technique which manifested that the addition of DEHP tended to suppress the growth of crystal phase and eventually lead to the smaller, but this was not the case for the overall crystallinity while undergoing an averaging fashion. Due to the presence of DEHP, the melting points of plasticized blends were dropped by the maximal 6 °C which also affected the non-isothermal recrystallization during the cooling. The recrystallization favored a retarded process eventually.

Influence of the plasticizer on molecule mobility covering a wide range of temperature was monitored by BDS technique by which the single segmental structure relaxation loss was first revealed. This manifested the good miscible behavior, due most probably to the compatible solubility parameters between both. The presence of the DEHP plasticizer expanded the specific free volume of the molecular chain, accelerated the relaxation rate of the structural relaxation process in rigid and mobile amorphous phase and enhanced dynamic heterogeneity near the glass transition region as well, as opposed to the results found in Chapter III; the estimated glass transition $T_{g,diel}$ slumped down from 246.7 K to 229 K and closely followed the Fox mode against the DEHP content; an increased strength indices implied the less fragility of the modified polymer blends. β secondary relaxation process was also identified and activated by almost 25% high in glassy state.

Furthermore, the ions conductivity of plasticized blend system was improved by around one order of magnitude higher. With the help of dielectric modulus spectra, the dynamic behavior of the translational charge carrier motions were carefully characterized at low frequency and high temperature. The curvature type was fitted to the motion behavior of ions charge carrier and fitting; and the ions conductivity behavior for plasticized blend was governed by structural relaxation in amorphous phase.

Finally, interfacial polarization was verified as a great dielectric strength mode which is usually assigned to the predominant dielectric relaxation process at low frequency and high temperature. After removal of the conductivity contributing part, although the MWS relaxation strength remained unaltered for the pure and plasticized blends, the relaxation had the peak drifted towards the high frequency by almost maximal one decade for terpolymers with 10% and 15% DEHP plasticizer content. Such results account for the several orders of magnitude enhancement of the dielectric properties in experimental measurement. On top of that, plasticizing effects for constrained amorphous phase were also identified.

References

1. Lu, Y., et al., *A modular approach to ferroelectric polymers with chemically tunable curie temperatures and dielectric constants*. Journal of the American Chemical Society, 2006. **128**(25): p. 8120-8121.
2. Tan, S., et al., *Controlled hydrogenation of P (VDF-co-CTFE) to prepare P (VDF-co-TrFE-co-CTFE) in the presence of CuX (X= Cl, Br) complexes*. Chemical Communications, 2011. **47**(15): p. 4544-4546.
3. Wang, Z., Z. Zhang, and T.M. Chung, *High dielectric VDF/TrFE/CTFE terpolymers prepared by hydrogenation of VDF/CTFE copolymers: synthesis and characterization*. Macromolecules, 2006. **39**(13): p. 4268-4271.
4. Li, J., et al., *Nanocomposites of ferroelectric polymers with TiO₂ nanoparticles exhibiting significantly enhanced electrical energy density*. Advanced Materials, 2009. **21**(2): p. 217-221.
5. Zhang, Q., et al., *An all-organic composite actuator material with a high dielectric constant*. Nature, 2002. **419**(6904): p. 284-287.
6. Wang, J.-W., et al., *Microstructure and dielectric properties of P (VDF-TrFE-CFE) with partially grafted copper phthalocyanine oligomer*. Macromolecules, 2005. **38**(6): p. 2247-2252.
7. Capsal, J.-F., et al., *Plasticized relaxor ferroelectric terpolymer: Toward giant electrostriction, high mechanical energy and low electric field actuators*. Sensors and Actuators A: Physical, 2014. **207**: p. 25-31.
8. Yin, X., et al., *Enhanced Electromechanical Performances in Plasticizer Modified Electrostrictive Polymers*. European Polymer Journal, 2016.
9. Wypych, G., *Handbook of plasticizers*. 2004: ChemTec Publishing.
10. Chiellini, F., M. Ferri, and G. Latini, *Physical-chemical assessment of di-(2-ethylhexyl)-phthalate leakage from poly (vinyl chloride) endotracheal tubes after application in high risk newborns*. International journal of pharmaceutics, 2011. **409**(1): p. 57-61.
11. Zhu, L., *Exploring strategies for high dielectric constant and low loss polymer dielectrics*. The journal of physical chemistry letters, 2014. **5**(21): p. 3677-3687.
12. Yin, H., S. Napolitano, and A. Schönhals, *Molecular mobility and glass transition of thin films of poly (bisphenol a carbonate)*. Macromolecules, 2012. **45**(3): p. 1652-1662.
13. Capsal, J.F., et al., *Enhanced electrostriction based on plasticized relaxor ferroelectric P (VDF - TrFE - CFE/CTFE) blends*. Journal of Polymer Science Part B: Polymer Physics, 2015. **53**(19): p. 1368-1379.
14. Schönhals, A. and F. Kremer, *Theory of Dielectric Relaxation*, in *Broadband Dielectric Spectroscopy*, F. Kremer and A. Schönhals, Editors. 2003, Springer Berlin Heidelberg. p. 1-33.

15. Choi, N.-S., et al., *Preparation and electrochemical characteristics of plasticized polymer electrolytes based upon a P (VdF-co-HFP)/PVAc blend*. *Electrochimica acta*, 2001. **46**(10): p. 1581-1586.
16. Lourdin, D., et al., *Influence of equilibrium relative humidity and plasticizer concentration on the water content and glass transition of starch materials*. *Polymer*, 1997. **38**(21): p. 5401-5406.
17. Barique, M. and H. Ohgashi, *Annealing effects on the Curie transition temperature and melting temperature of poly (vinylidene fluoride/trifluoroethylene) single crystalline films*. *Polymer*, 2001. **42**(11): p. 4981-4987.
18. Tanaka, R., K. Tashiro, and M. Kobayashi, *Annealing effect on the ferroelectric phase transition behavior and domain structure of vinylidene fluoride (VDF)–trifluoroethylene copolymers: a comparison between uniaxially oriented VDF 73 and 65% copolymers*. *Polymer*, 1999. **40**(13): p. 3855-3865.
19. Kim, K.J., et al., *Curie transition, ferroelectric crystal structure, and ferroelectricity of a VDF/TrFE (75/25) copolymer 1. The effect of the consecutive annealing in the ferroelectric state on curie transition and ferroelectric crystal structure*. *Journal of Polymer Science Part B: Polymer Physics*, 1994. **32**(15): p. 2435-2444.
20. Klein, R.J., J. Runt, and Q. Zhang, *Influence of Crystallization Conditions on the Microstructure and Electromechanical Properties of Poly (vinylidene fluoride-trifluoroethylene-chlorofluoroethylene) Terpolymers*. *Macromolecules*, 2003. **36**(19): p. 7220-7226.
21. Barendswaard, W., et al., *Crystallinity and microstructure of plasticized poly (vinyl chloride). A ¹³C and ¹H solid state NMR study*. *Macromolecules*, 1999. **32**(1): p. 167-180.
22. Saeidlou, S., et al., *Effect of nucleation and plasticization on the stereocomplex formation between enantiomeric poly (lactic acid) s*. *Polymer*, 2013. **54**(21): p. 5762-5770.
23. Ganet, F., et al., *Development of a smart guide wire using an electrostrictive polymer: option for steerable orientation and force feedback*. *Scientific reports*, 2015. **5**.
24. Le, M.Q., et al., *All-organic electrostrictive polymer composites with low driving electrical voltages for micro-fluidic pump applications*. *Scientific reports*, 2015. **5**.
25. Liu, Q., et al., *Influence of the crystallization on the molecular mobility and ionic DC conductivity behaviors of relaxor ferroelectric P (VDF - TrFE - CTFE) terpolymers*. *Journal of Polymer Science Part B: Polymer Physics*, 2016. **54**(16): p. 12.
26. Choi, K.-m., et al., *Plasticization of poly (lactic acid)(PLA) through chemical grafting of poly (ethylene glycol)(PEG) via in situ reactive blending*. *European Polymer Journal*, 2013. **49**(8): p. 2356-2364.
27. Liu, Y., et al., *Improved mechanical and thermal properties of PLLA by solvent blending with PDLA-*b*-PEG-*b*-PDLA*. *Polymer Degradation and Stability*, 2014. **101**: p. 10-17.
28. Bao, C.Y., D.R. Long, and C. Vergelati, *Miscibility and dynamical properties of cellulose acetate/plasticizer systems*. *Carbohydrate polymers*, 2015. **116**: p. 95-102.

29. Zorn, R., et al., *Plasticizer effect on the dynamics of polyvinylchloride studied by dielectric spectroscopy and quasielastic neutron scattering*. The Journal of chemical physics, 2006. **125**(15): p. 154904.
30. Xia, H. and T. Hirai, *Electric-field-induced local layer structure in plasticized PVC actuator*. The Journal of Physical Chemistry B, 2010. **114**(33): p. 10756-10762.
31. Jafarpour, G., et al., *Influence of water on localized and delocalized molecular mobility of cellulose*. Journal of Non-Crystalline Solids, 2009. **355**(34): p. 1669-1672.
32. Zhang, S., et al., *Glass transition and ionic conduction in plasticized and doped ionomers*. Journal of non-crystalline solids, 2005. **351**(33): p. 2825-2830.
33. Costa, C.M., et al., *Composition-dependent physical properties of poly [(vinylidene fluoride)-co-trifluoroethylene]–poly (ethylene oxide) blends*. Journal of Materials Science, 2013. **48**(9): p. 3494-3504.
34. Rizos, A.K., et al., *A dielectric relaxation study of the γ -relaxation in tetramethylbisphenol A polycarbonate plasticized by tris (2-ethylhexyl) phosphate*. Macromolecules, 1999. **32**(23): p. 7921-7924.
35. Lin, S.-Y., K.-S. Chen, and L. Run-Chu, *Organic esters of plasticizers affecting the water absorption, adhesive property, glass transition temperature and plasticizer permanence of Eudragit acrylic films*. Journal of Controlled Release, 2000. **68**(3): p. 343-350.
36. Ngai, K. and C. Roland, *Chemical structure and intermolecular cooperativity: dielectric relaxation results*. Macromolecules, 1993. **26**(25): p. 6824-6830.
37. Esposito, A., et al., *From a Three-Phase Model to a Continuous Description of Molecular Mobility in Semicrystalline Poly (hydroxybutyrate-co-hydroxyvalerate)*. Macromolecules, 2016. **49**(13): p. 4850-4861.
38. Yang, L., et al., *Semicrystalline Structure–Dielectric Property Relationship and Electrical Conduction in a Biaxially Oriented Poly (vinylidene fluoride) Film under High Electric Fields and High Temperatures*. ACS applied materials & interfaces, 2015. **7**(36): p. 19894-19905.
39. Bras, A., et al., *Influence of crystallinity in molecular motions of poly (L-lactic acid) investigated by dielectric relaxation spectroscopy*. Macromolecules, 2008. **41**(17): p. 6419-6430.
40. Álvarez, C., et al., *Structure-dynamics relationship in crystallizing poly (ethylene terephthalate) as revealed by time-resolved X-ray and dielectric methods*. Polymer, 2004. **45**(11): p. 3953-3959.
41. Yang, J., et al., *Understanding of versatile and tunable nanostructuration of ionic liquids on fluorinated copolymer*. Macromolecules, 2015. **48**(13): p. 4581-4590.
42. Delpouve, N., et al., *Cooperative rearranging region size in semi-crystalline poly (l-lactic acid)*. Polymer, 2008. **49**(13): p. 3130-3135.
43. Alves, N., et al., *Glass transition and structural relaxation in semi-crystalline poly (ethylene terephthalate): a DSC study*. Polymer, 2002. **43**(15): p. 4111-4122.

44. Alegria, A., et al., . *alpha.-Relaxation in the Glass Transition Range of Amorphous Polymers. 1. Temperature Behavior across the Glass transition*. Macromolecules, 1995. **28**(5): p. 1516-1527.
45. Vicioso, M.T., et al., *Confinement effects on the dynamic behavior of poly(D,L-lactic acid) upon incorporation in alpha-cyclodextrin*. J Phys Chem B, 2014. **118**(24): p. 6972-81.
46. Adam, G. and J.H. Gibbs, *On the temperature dependence of cooperative relaxation properties in glass - forming liquids*. The journal of chemical physics, 1965. **43**(1): p. 139-146.
47. Donth, E.-J., *The glass transition: relaxation dynamics in liquids and disordered materials*. Vol. 48. 2013: Springer Science & Business Media.
48. Donth, E., *Characteristic length of the glass transition*. Journal of Polymer Science Part B: Polymer Physics, 1996. **34**(17): p. 2881-2892.
49. Dobircau, L., et al., *Molecular mobility and physical ageing of plasticized poly (lactide)*. Polymer Engineering & Science, 2015. **55**(4): p. 858-865.
50. Bao, H.M., et al., *Phase transitions and ferroelectric relaxor behavior in P(VDF-TrFE-CFE) terpolymers*. Macromolecules, 2007. **40**(7): p. 2371-2379.
51. Zhang, S., et al., *Normal ferroelectric to ferroelectric relaxor conversion in fluorinated polymers and the relaxor dynamics*, in *Frontiers of Ferroelectricity*. 2006, Springer. p. 271-280.
52. Yin, X., J.-F. Capsal, and D. Guyomar, *A comprehensive investigation of poly (vinylidene fluoride-trifluoroethylene-chlorofluoroethylene) terpolymer nanocomposites with carbon black for electrostrictive applications*. Applied Physics Letters, 2014. **104**(5): p. 052913.
53. Choi, U.H., et al., *Influence of solvating plasticizer on ion conduction of polysiloxane single-ion conductors*. Macromolecules, 2014. **47**(9): p. 3145-3153.
54. Lu, Y., et al., *Structural Dependence of Phase Transition and Dielectric Relaxation in Ferroelectric Poly (vinylidene fluoride- chlorotrifluoroethylene- trifluoroethylene) s*. The Journal of Physical Chemistry B, 2008. **112**(34): p. 10411-10416.
55. Barton, A.F., *Solubility parameters*. Chemical Reviews, 1975. **75**(6): p. 731-753.
56. Chu, B., *PVDF-based copolymers, terpolymers and their multi-component material systems for capacitor applications*. 2008, The Pennsylvania State University.
57. Dlubek, G., et al., *Free volume in two differently plasticized poly (vinyl chloride) s: a positron lifetime and PVT study*. Polymer, 2003. **44**(6): p. 1921-1926.
58. Dlubek, G., et al., *Glass transition and free volume in the mobile (MAF) and rigid (RAF) amorphous fractions of semicrystalline PTFE: a positron lifetime and PVT study*. Polymer, 2005. **46**(16): p. 6075-6089.
59. Liu, H., et al., *Interactions of hydrophilic plasticizer molecules with amorphous starch biopolymer—an investigation into the glass transition and the water activity behavior*. Journal of Polymer Science Part B: Polymer Physics, 2011. **49**(14): p. 1041-1049.

60. Brás, A.R., et al., *Water effect in the thermal and molecular dynamics behavior of poly (L-lactic acid)*. Journal of thermal analysis and calorimetry, 2007. **88**(2): p. 425-429.
61. Painter, P. and M. Coleman, *Self-Contacts, Self-Concentration, and the Composition Dependence of the Glass Transition Temperature in Polymer Mixtures*. Macromolecules, 2009. **42**(3): p. 820-829.
62. Gaikwad, A.N., et al., *Two calorimetric glass transitions in miscible blends containing poly (ethylene oxide)*. Macromolecules, 2008. **41**(7): p. 2502-2508.
63. Dantuluri, A.K., et al., *Role of alpha-relaxation on crystallization of amorphous celecoxib above T(g) probed by dielectric spectroscopy*. Mol Pharm, 2011. **8**(3): p. 814-22.
64. Merino, E.G., et al., *Investigating the Influence of Morphology in the Dynamical Behavior of Semicrystalline Triton X-100: Insights in the Detection/Nondetection of the α' - Process*. The Journal of Physical Chemistry B, 2013. **117**(33): p. 9793-9805.
65. Ngai, K., *Relaxation and diffusion in complex systems*. 2011: Springer Science & Business Media.
66. Rodrigues, A., et al., *Molecular mobility of amorphous s-flurbiprofen: a dielectric relaxation spectroscopy approach*. Molecular pharmaceutics, 2013. **11**(1): p. 112-130.
67. Kremer, F., *Broadband dielectric spectroscopy*. 2003: Springer Science & Business Media.
68. Merino, E.G., et al., *Investigating the influence of morphology in the dynamical behavior of semicrystalline Triton X-100: insights in the detection/nondetection of the alpha'-process*. J Phys Chem B, 2013. **117**(33): p. 9793-805.
69. Ngai, K., et al., *Does the Johari–Goldstein β -Relaxation Exist in Polypropylene Glycols?* Macromolecules, 2015. **48**(12): p. 4151-4157.
70. Johari, G.P. and M. Goldstein, *Viscous liquids and the glass transition. II. Secondary relaxations in glasses of rigid molecules*. The Journal of chemical physics, 1970. **53**(6): p. 2372-2388.
71. Debenedetti, P.G. and F.H. Stillinger, *Supercooled liquids and the glass transition*. Nature, 2001. **410**(6825): p. 259-267.
72. Carvalho, T., et al., *Understanding the ion jelly conductivity mechanism*. The Journal of Physical Chemistry B, 2012. **116**(9): p. 2664-2676.
73. Pradhan, D.K., et al., *Effect of plasticizer on structure—property relationship in composite polymer electrolytes*. Journal of Power Sources, 2005. **139**(1-2): p. 384-393.
74. Fragiadakis, D., et al., *Molecular mobility, ion mobility, and mobile ion concentration in poly (ethylene oxide)-based polyurethane ionomers*. Macromolecules, 2008. **41**(15): p. 5723-5728.
75. Choi, U.H., et al., *Ionic conduction and dielectric response of poly (imidazolium acrylate) ionomers*. Macromolecules, 2012. **45**(9): p. 3974-3985.
76. Chu, B., et al., *A dielectric polymer with high electric energy density and fast discharge speed*. Science, 2006. **313**(5785): p. 334-336.

77. Ali, M. and T. Hirai, *Relationship between electrode polarization and electrical actuation of dielectric PVC gel actuators*. Soft Matter, 2012. **8**(13): p. 3694-3699.
78. Ali, M., et al., *Influence of plasticizer content on the transition of electromechanical behavior of PVC gel actuator*. Langmuir, 2011. **27**(12): p. 7902-7908.
79. Schönhals, A. and F. Kremer, *Analysis of dielectric spectra*, in *Broadband dielectric spectroscopy*. 2003, Springer. p. 59-98.
80. Choi, U.H., et al., *Dynamics of precise ethylene ionomers containing ionic liquid functionality*. Macromolecules, 2015. **48**(2): p. 410-420.
81. Ali, M., et al., *Dielectric and electromechanical studies of plasticized poly (vinyl chloride) fabricated from plastisol*. Polymer International, 2013. **62**(3): p. 501-506.
82. Kim, C.-H., et al., *Ion conductivities and interfacial characteristics of the plasticized polymer electrolytes based on poly (methyl methacrylate-co-Li maleate)*. Journal of power sources, 2001. **94**(2): p. 163-168.
83. Ramesh, S. and A. Arof, *Ionic conductivity studies of plasticized poly (vinyl chloride) polymer electrolytes*. Materials Science and Engineering: B, 2001. **85**(1): p. 11-15.
84. Yu, W., et al., *Influence of Dangling Chains on Molecular Dynamics of Polyurethanes*. Macromolecules, 2013. **46**(18): p. 7341-7351.
85. Sharma, M., G. Madras, and S. Bose, *Cooperativity and structural relaxations in PVDF/PMMA blends in the presence of MWNTs: an assessment through SAXS and dielectric spectroscopy*. Macromolecules, 2014. **47**(4): p. 1392-1402.

Chapter V

Enhanced Inkjet Printed Pseudo-piezoelectric Force Sensors based on Electrostrictive $P(\text{VDF-TrFE-CTFE})$ Terpolymer and Ferroelectric $P(\text{VDF-TrFE})$ Copolymer

I Introduction

A sensor is defined as a device that is capable of responding to some kinds of input physical excitations and converting these excitation into output electrical signals, compatible with signal processing circuits which ensure the signal readability. In particular, force sensor elements intend to switch the mechanical stress into readable output electrical signal with the conformal characteristics, involving frequency of excitation, phase and strength, etc. Accurately gauging and monitoring the mini- and large scale force stimuli, sometime in-situ could benefit the potential applications in fields of smart packaging [1], biological micromanipulation [2], acoustic transducer [3] and medical robot devices [4], etc. Meanwhile, challenges have also been rose in order to meet the specific needs in design and fabrication of the force sensor devices. For example, embedded sensors into the industrial microelectronics and flying objects are preferentially small but durability and flexibility, while the sensors for atomic force and microscale end-use demand the high sensitivity and reliability. Currently, sensors fabrication technology was booming thanks to the increasing development of large area printed polymer electronics. Simplified processing steps, reduced materials wastage, low fabrication cost and simple patterning techniques make the printing technology quite attractive. Generally, conventional approaches appear to apply the sensing material layers in a solution-processable ink transfer technique such as roll-to-roll gravure printing, screen printing, etc [5-7]. There is problematic of precise deposition of materials in a solution state. Inkjet printing technologies is an attractive method to overcome these drawbacks and benefit a minimizing quantity of material depletion [8-10]. On top of that, precisely controlled thickness of the sensing layer allows a highly performed sensitivity under low electric supply. In this present study, the inkjet printing protocol was optimized prior to the application of the patterned ferroelectric and electrostrictive sensing polymer layers on the flexible polyimide foils. The characteristics of morphology and dielectric features were then exploited and consequently, the dynamic impact force sensor piezoelectric behaviors of both inkjet printed force sensors were evaluated.

II Working Principle and Theoretical Consideration

Electromechanical coupling effect that has been revealed, is a common feature in ferroelectric and electrostrictive polymers. Their dimension changes in response to the external physical excitation such as electric field and dynamic impact force, give rise to the variation of the electrical displacement in combined underlying mechanisms of piezoelectric, electrostrictive and electrostatic effects. For ferroelectric polymer materials in a thickness mode, the tensor interactions between mechanical stress, strain, electric field and displacement can be written in the constitutive equations as follows [11, 12]:

$$S_{33} = s_{33}^E T_{33} + d_{33} E_{33} \quad \text{V. 1}$$

$$D_{33} = d_{33}T_{33} + \varepsilon_{33}^T E_{33} \quad \text{V. 2}$$

where S_{33} is mechanical strain out-of-plane of the polymer unimorph; s_{33}^E is elastic compliance; T_{33} is mechanical stress along the thickness direction; d_{33} is piezoelectric coefficient; E_{33} is electric field along the thickness direction; ε_{33}^T is dielectric constant under E_{33} and D_{33} is electric displacement. Under an out-of-plane electric field E , the dipoles aligning with the electric excitation results in a large polarization within a ferroelectric polymer, and thus a huge remnant polarization even though the electric excitation is switched off as presented in Figure V. 1a [13]. Likewise, when an dynamic force was applied to a capacitor-like ferroelectric device, the geometric change caused a variation in its capacitance, therefore accompanying with an altering electrical displacement D . This gave rise to an electric leakage current to be read out by a supplementary circuit. In this circumstance, it is possible to gauge the applied dynamic force by measuring the electric current output. However, relaxor ferroelectric material has a very slim D - E hysteresis loop and thus hardly detected remnant polarization (Figure V. 1b) [14, 15]. Since the electrostrictive effect predominates the origins of thickness contraction of terpolymer in response to the applied electric field, equation V. 1 and V. 2 can be rewritten as the constitutive expression [16, 17]:

$$S_{33} = s_{33}^E T_{33} + M_{33} E_{33}^2 \quad \text{V. 3}$$

$$D_3 = 2M_{33} E_{33} T_{33} + \varepsilon_{33}^T E_{33} \quad \text{V. 4}$$

where M_{33} is global electrostrictive coefficient across the thickness orientation. The cluster $2M_{33} E_{33}$ equivalent to the d_{33} factor is so-called *pseudo*-piezoelectric coefficient under electric field. Large polarization can also be induced with the help of electric field application for the relaxor ferroelectric terpolymers. In a similar mechanism to the ferroelectrics thickness deformation yields a change in electric displacement with a short-circuit leakage current I [18, 19]:

$$I = A \cdot \frac{\partial D_{33}}{\partial t} \quad \text{V. 5}$$

where A is the electrode area covering relaxor ferroelectric terpolymer and t is electrical displacement variation within a limited time. Equation V. 5 can be rewritten by a substitution of equation V. 4 for the $\frac{\partial D_{33}}{\partial t}$ cluster:

$$I = A \left[\frac{\partial E_{33}}{\partial t} \left(\varepsilon_{33}^T + \frac{2M_{33}S_{33} - 6M_{33}^2 E_{33}^2}{s_{33}^E} \right) + \frac{2M_{33} \frac{\partial S_{33}}{\partial t} E_{33}}{s_{33}^E} \right] \quad \text{V. 6}$$

herein the DC bias voltage applied on the thickness mode of electrostrictive terpolymers, the electric field variation rate $\frac{\partial E_{33}}{\partial t}$ was limited since the thickness change maintains within the restrictive scope. Hence, the short circuit current I can be simplified as [20-22]:

$$I = A \cdot [2M_{33}E_3Y \frac{\partial S_{33}}{\partial t}] \quad \text{V. 7}$$

The short circuit current is closely related to the *pseudo*-piezoelectric coefficient $2M_{33}E_3$ of the relaxor ferroelectric terpolymer and strain derivative $\frac{\partial S_{33}}{\partial t}$ across the thickness direction.

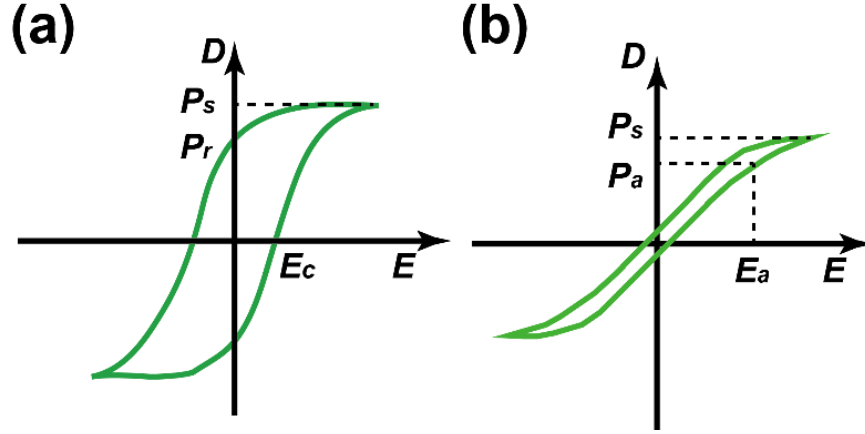


Figure V. 1 Schematics of displacement (D)-electric field (E) hysteresis loops for ferroelectric copolymer (P(VDF-TrFE)) (a) and relaxor ferroelectric terpolymer (P(VDF-TrFE-CTFE)) (b). Ferroelectric polymers exhibited fat hysteresis loop as well as a large remnant polarization (P_r) whereas relaxor one presented a narrow D - E hysteresis loop with a trace of remnant dipole polarization.

As motivated by using the theoretical model, outperformed ferroelectric P(VDF-TrFE) copolymer and relaxor electrostrictive P(VDF-TrFE-CTFE) terpolymer are employed as sensing materials of a parallel panel capacitor-like impact force sensor thanks to its high dielectric permittivity, low loss and excellent (pseudo)-piezoelectric coefficient which are expected to allow to achieve the outperformed electromechanical coupling phenomenon and elastic energy density. In addition, less rigid and low Young's modulus would benefit the large geometric deformation and its changing rate, in favor of an electric response to the mechanical excitation.

III Experimental Section

III. 1 Chemicals and Materials

Commercially passive and thermally resistant 50 μm -thick Polyimide foils (Dupont™ Kapton® HN, USA) served as the flexible substrate for inkjet printed dynamic force sensors [23]. Prior to the device fabrication, Kapton films were successively rinsed with acetone, ethanol and

isopropanol to ensure the fouling and discretion free of the reproducible and wettable surface of the flexible foils. Afterwards, in order to realize the excellent adhesion between the environmentally resistant substrate and inert metal electrode and, as well as solid sensing polymer layers, fresh Kapton film was subjected to the corona discharge plasma exposure by which the surface energy of plastic substrate were greatly improved. Then the surface tension of substrate in this way matched with the surface properties of non-parasitic elements.

The sensing layer polymer, P(VDF-TrFE) copolymer with molar ratio of 55:44/VDF:TrFE and P(VDF-TrFE-CTFE) terpolymer with a molar ratio of 61.0:30.1:8.9/VDF:TrFE:CTFE were purchased from the Piezotech S.A.S (Arkema, France) and used without further purification. The analytical grade solvents mentioned in the following substrate pretreatment and device fabrication were unexceptionally obtained from Sigma-Aldrich and harnessed as received. The two kinds of P(VDF-TrFE) and P(VDF-TrFE-CTFE) solution inks formula in 1 wt% concentration were prepared by dissolving the polymer granules in triethyl phosphate (TEP). Besides, the 10 wt% DEHP of total polymer residual modified terpolymer inks was also developed.

III. 2 Inkjet Printing Process and Device Fabrication

Freshly rinsed PI substrate films were firstly introduced into a conventional oven for 20 min at 150 °C. After heat stabilized, the substrate was subjected to the corona discharge exposure, and thus ink wettability and adhesion effect between the printed components were improved. Secondly, the patterned circular bottom Au electrode was sputtered using a customized shadow mask with a surface area of 78.54 mm². The thickness of the deposited could be precisely controlled through modulating the time and current of exposure application and was estimated as ~40 nm-thick. Prior to polymer deposition, the solution was filtered with a Teflon filter with 1 μ m-size customized pore. DEHP doped terpolymer inks without filter operation were also inkjet printed as a control process. The circular sensing polymer layer in 15 mm diameter was successively deposited on bottom metal electrode in rather good alignment using a specified droplet volume of 50 picoliter Dimatrix cartridge (SE-128 AA) [24] mounted on PiXDRO LP50 inkjet printer (Meyer Burger Technologies, Switzerland). In the meantime, PI substrate was continuously heated at 90 °C to favor the vaporization dynamics of the solvent possessing a high boiling point. Concretely, the printing protocol was opted to deposit the uniform and homogeneous polymer layers using jettable droplets with the stable morphology and 1m s⁻¹ falling velocity, firing frequency 1 kHz under optimized equilibrium ink pressure of 21.7 mbar. The print head was powered by a voltage of 120 Voltage, with a pulse width of 6 μ s raising, 8 μ s dwelling and 4 μ s falling steps for the ink droplet ejection protocol. In order to obtain the desirable sensing layer with the thickness of approximately 10 μ m, multiple repetitions of printing batch were employed. The freshly deposited polymer layers were dried over several minutes, subsequently moved into a conventional oven and followed by a tempering process at

140 °C for copolymer, at 110 °C for terpolymer overnight under vacuum to remove the solvent residual. This also allowed to enhance the degree of crystallinity and thus ferroelectricity. The force sensor was finalized by sputtering the custom-sized Au top electrode, similar to the bottom electrode.

III. 3 Characterization

Ferroelectric properties were characterized firstly. The two electrodes of the printed sensor were connected to the 20 kV AC high-voltage amplifier (Trek, New York) and the current amplifier (Stanford Research Systems, CA). In case of printed copolymer sensors, a 100 mHz sinusoidal wave was then applied upon the out-of-plane direction of the printed sensor with a maximum potential of 70 V/ μm from 20 V/ μm in an increment of 10 V/ μm since the printed sensors appeared electrical failure under an electric field slightly higher than 70 V/ μm . During each Current-Voltage cycle measurement, induced short-circuit current channel (peak-to-peak) was maintained to be stable. The polarization was obtained after extraction of leakage current which is contributed by conduction in materials.

Capacitance (C) and dielectric behaviors of copolymer sensors were checked by broadband dielectric spectroscopy before and after poling process, manipulated with the same specimens as in polarization process. The frequency range during the C and ϵ_r measurement was from 0.1 Hz to 1MHz. The sensors to characterize were selected according to a normal performance of dielectric spectroscopy; otherwise, both electrodes of the capacitor-like sensors were most probably interconnected during the Au deposition.

Piezoelectric property in response to the dynamic impact force was investigated subsequently. The well-prepared sensors with the top electrode stamped by Teflon belt were mounted manually on the large and thick PMMA panel via cyanoacrylate adhesive. The dynamic force impulse was applied upon the top of the printed sensors using an impact hammer (Dytran Instruments, Inc. CA), with a sensitivity of 1V/44.48N (100 mV/lbf) and measurement gauge of 0~4448 N scope. The applied force signal and readout current response of the sensors were recorded thanks to the Agilent oscilloscope. Afterwards, charges was obtained by integration of current curves with time and plotted against impact force pulse curve.

The sensitivity of the printed sensors in response to the sweep signal with frequencies range between 100 and 1000 Hz (covering the frequency range of a typical impulse force) of applied impact force were also investigated. In a typical experimental setup, the printed polymer sensors mounted to the free end of vibrator (LDS, Brüel & Kjær, UK), were stuck with the standard mass weight of 10 g on the top Au electrode of the printed sensors. The sensor was short-circuit connected and consequently, the induced current in response to the force was recorded by oscilloscope. Meanwhile, a MEMS-piezoelectric accelerometer (Brüel & Kjær) with concurrently

stuck onto the experiment setup panel in order to monitor the *in situ* acceleration of the experimental assemblies.

In case of relaxor ferroelectric terpolymer, owing to a very slim hysteresis D - E loop and poor remnant polarization, impact force application could not yield the vast change in its electric displacement. The impact force-induced charges would be reasonably ignored. Instead, so-called pseudo-piezoelectric d_{33eq} coefficient could be determined under applied electric field. A maximum of 240 V DC voltages was applied to the force sensor in across section in two step-wised increments of 5 V below 30 V and 30 V intervals above 30 V up to the maximum voltage value. d_{33eq} coefficient under respective electric field was extracted subsequently.

The electromechanical response of the printed terpolymer sensors were also characterized in terms of electric field-induced strain and displacement in thickness direction. Capacitor-like PI-based printed flexible sensor devices, with sensing layer thickness of approximately 10 μm were metallized with the help of shadow mask and a 100 mHz frequency sinusoidal AC voltage was applied upon the printed sensor devices. The displacement was recorded by using the OFV-5000 Vibrometer equipped with OFV-50x Sensor head (Polytec GmbH, Germany). A reflective paper was placed on the center of top electrode in order to measure the displacement *in-situ*.

IV Result and Discussion

IV.1 Design and Inkjet Printing of Two Types of Force Sensors

Continuous material deposition was realized by DOD inkjet printing technology in this current work. The individual ink droplet was generated by piezoelectric MEMS-modulated inkjet nozzle with the orifice dimension of 50 μm diameter. The desirable and patterned images of the polymer materials were printed by precisely controlled ink formula deposition on the demanded location. It has been well-recognized that the steady ink stream and normalized droplet size were responsible for the tailored application of polymer solution inks, otherwise, vacant and incomplete polymer solution patterns were yielded and thus affected the uniformity of the polymer residual layers. The printable ink formulation and microfluidic dynamics strongly determined the morphology and reproducibility of the droplets, in terms of viscosity η , useful physic constants such as Reynolds (Re) and Weber (We) numbers, etc. (see the-state-of-the-art Chapter I). The feasible solvent is the main factor reliably determining the printability of the polymer solution inks, rather than the polymer solute itself [25]. It has also been reported that the candidate solvents used successfully for dissolving the PVDF-based polymer involve Methyl Ethyl Ketone (MEK) [26, 27], DMF [28, 29], and TEP [30], with sharp contrast of boiling points.

Solvent evaporation to large extent, that is, vapor pressure occurred to the organic solvents owning a relatively low boiling point. This might on the other hand lead to severe problems, for instance, shrinking volume of the falling droplets, interruption of continuous ink ejection, nozzle clogging, etc. Otherwise, polymer solution deposited onto the substrate, successively evaporated for a quite long time span in case of solvent use with very high boiling point. There is a remarkable trade-off between customized ink ejection and highly efficient evaporation. Continuous single droplet was also a consequence of maneuverable viscosity of polymer ink solution, which would heavily adapt to the fluidic viscosity range of the nozzle during the operation of ink ejection. Table V. 1 summarized the physical specifications of the cartridge nozzle and two extensively-used solvent kinds, MEK and TEP, behaving a strong contrast of vaporization parameters. MEK is too much volatile to be employed as a jettable solvent, instead of TEP which characterizes an adaptable vapor pressure. TEP is also a solvent with very high quality which means the macromolecular chain can be stretched readily and does not favor to precipitate before reaching the very high critical polymeric concentration in an extensional fluidic flow [31, 32]. Afterwards copolymer and terpolymer inks were prepared in selected TEP solvent. And the viscosity of both polymer inks was measured as 2.16 cP and 3.26 cP, respectively, which were adapted to the nozzle characteristic nicely. Note that the measured surface tension of 32.7 mN m⁻¹ and 33.4 mN m⁻¹ for copolymer and terpolymer inks were in preferentially consistent with the referred value of pure TEP solvent and wettability of both inks were as expected almost the same than TEP solvent.

Table V. 1 Physic properties of Dimatix cartridge, solvents and polymer solution inks in TEP

Physical parameters	Dimatix Cartridge range [33]	MEK [34]	TEP [35]	Copolymer Inks (1%)	Terpolymer inks (1%)
Viscosity (mPa s)	8-20	0.43	1.46	2.16 ^a	3.26 ^b
Surface Tension (mNm ⁻¹)	28-33	24.6	30.6±3.0	32.7	33.4
Density (g cm ⁻³)	>1	0.805	1.072	1.081	1.082
Boiling point (°C)	--	79.6	215	As TEP	As TEP
Pressure vapor (Pa)	low	10500	100	As TEP	As TEP
Nozzle dimension (μm)	50				

^{a, b}Note: values measured by Brookfield viscometer according to ASTM D 1824-1995 [36].

In order to yield a printable droplet, it is an essence to understand the jettability mechanism. A successful ink droplet was closely related to the jet pulse waves and physico-chemical properties of the ink formula. The common dimensionless numbers, including Reynolds (Re), Weber (We), Capillary (Ca) and Z numbers, relevant to the droplet formation dynamics were governed by inertial force, viscosity, surface free energy, etc, of which were presented as follows [37-40]:

$$Re = \frac{\text{inertial force}}{\text{viscous force}} = \frac{\rho v d}{\eta} \quad \text{V. 8}$$

$$We = \frac{\text{inertial force}}{\text{surface tension}} = \frac{\rho v^2 d}{\sigma} \quad \text{V. 9}$$

$$Ca = \frac{\text{viscous force}}{\text{surface tension}} = \frac{\eta v}{\sigma} \quad \text{V. 10}$$

$$Z = \frac{\sqrt{\sigma \rho d}}{\eta} = \frac{1}{Ob} \quad \text{V. 11}$$

where σ , ρ and η symbolize surface tension, density and viscosity of the ink formula. v is the initial velocity of high shear rate ink flow pumped out of the nozzle with a diameter of d .

However, when piezoelectric-driven actuator is triggered by the voltage pulse waveform, polymer solution ink is then expelled out of the nozzle with a largely initial velocity. Its behavior during inkjet printing process presents the characteristics matching with the viscoelastic fluidic jets, according to the ejection behaviors of a Newtonian fluid ink [41, 42]. In order to verify the Newtonian behavior of ink ejection, the morphologies of droplets were analyzed as time processed. As shown in Figure V. 2, the series of photographic snapshots of ink solution were taken during the ink ejection with the help of stroboscopic video camera. The droplet formation maintained through a short and thick ink filament attached to the nozzle at the initial stage of ejection. The filament extended and thinned as the time elapsing. In several microseconds, the droplet detached when there was an occurrence of abrupt collapse of liquid ink ligament from the nozzle. The elongational tails remained attached to the heading bulk droplet through the thinning ink filament.

Alongside jettability of polymer solution inks regarding to the solvent aspect, it is also interesting to optimize the waveform of voltage pulse and ink chamber pressure for the various solvent system. The stable ejecting highly depends on the firing dwelling time for a given solvent system, which has to be matched to the superposition of the pressure wave propagation inside the ink reservoir chamber. The pressure is of the key issue which reliably determined the droplet

volume and viscosity within the matched dwelling time. In the current study, we also printed pure water, pure solvent based cyclopentanone inks and water-based silver nanoparticle inks on PI support and found a significant difference in the droplet velocity.

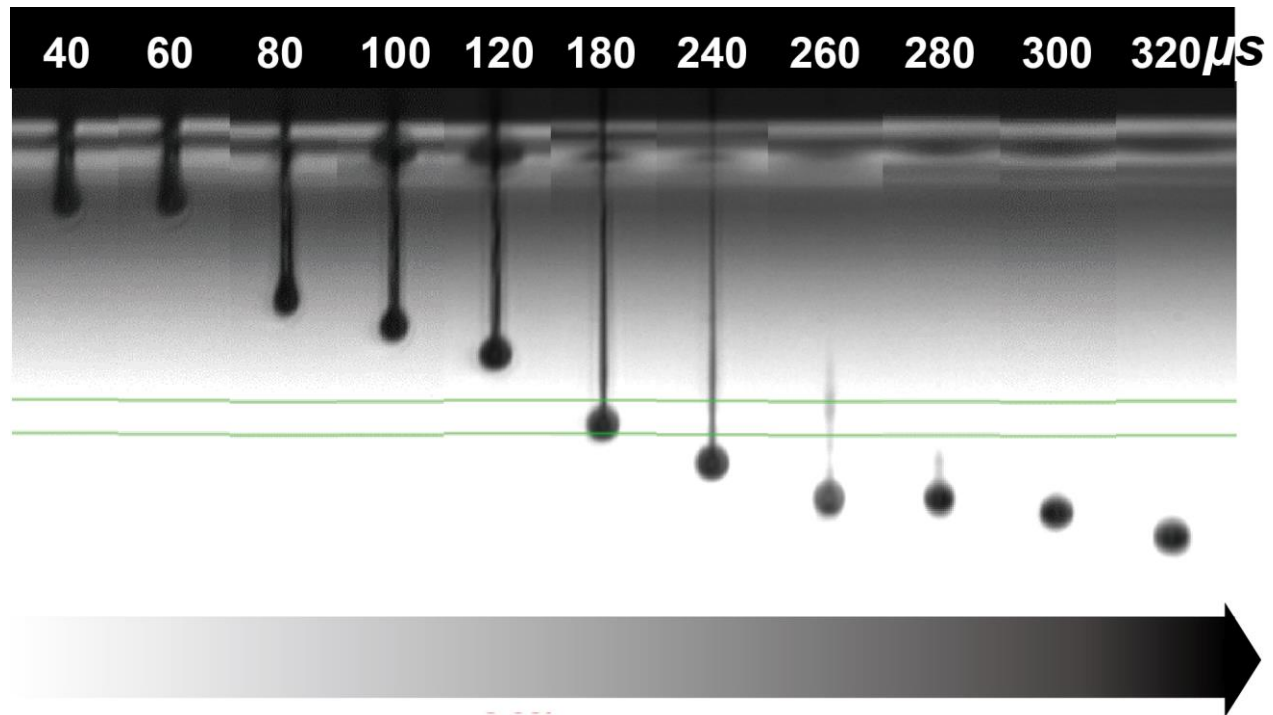


Figure V. 2 Snapshot graphics showing the droplet morphology evolution against time elapsing. 1% weight solution of P(VDF-TrFE-CTFE) in low volatile TEP solvent. The polymer solution droplet detached to the nozzle through inks liquid filament as time elapse beyond 260 μ s. Green horizontal lines marked the position of same altitude of the stroboscopic snapshots.

The scarce train of satellites behind the bulk droplets were observed for both copolymer and terpolymer solution inks which successively retracted into the heading bulk droplet bead during the time of flight at 260 μ s. The fusion of satellites with the heading droplet was acknowledged due to the surface tension, viscosity and density of the solution inks. [43] This scenario was very similar to the ejection behavior of pure TEP solvent, which suggested that the Newtonian behavior of TEP solvent sustained after the addition of a small quantity of high molecular weight polymer. However, this Newtonian behavior, that is, rare satellites accompanied with the primary droplets, is not seen any more if the polymer concentration reached its critical concentration threshold. In fact the concentration played a key parameter in the physics behavior of polymer solution inks. The disintegration of ligament was not likely to occur at relatively high polymer concentration, which corresponds to a typical Non-Newtonian behavior, having long tail of inks behind the primary bulk droplet [44]. In this circumstance thus a train of bead-line yielded

because surface tension of polymer solution inks was too weak to retract the free elongational ink flow. In this present study, the engineered copolymer and terpolymer inks exhibited the Newtonian behavior in a concentration of 1wt% and thus the viscosity measured at low shear rates were allowed to calculate the dimensionless parameters, Re , We , etc.

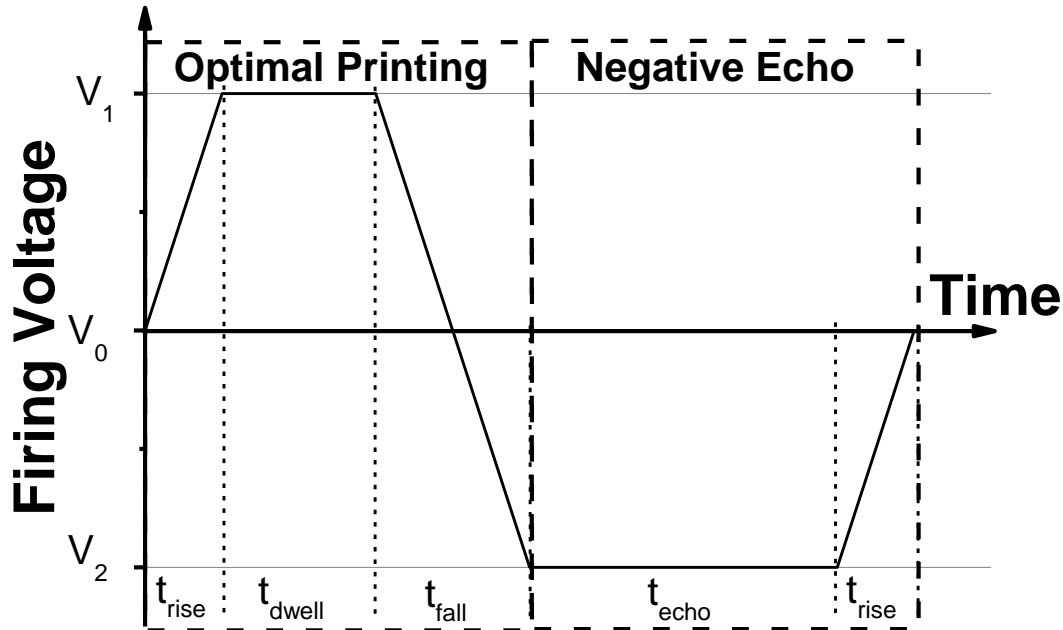


Figure V. 3 Optimal diagram of bipolar voltage pulse waveform for inkjet printing

The drop volume (size) and droplet velocity strongly differ from system to system. However, all ink systems have the similar behavior as if the pulse waves applied for the piezoelectric nozzle are kept unaltered. The droplets ejection intend to occur during the positive trapezoidal pulse (t_{dwell}), as shown in Figure V. 3. The droplet size could be determined by the time duration of the steady wave stage. The longer t_{dwell} , the larger the droplet size. And the rising ramp time span and falling ramp time spans were thought to be as short as possible because the longer ramp times would disturb the droplet formation and thus yield undesirable and inhomogeneous drop volume. Negative wave pulse (t_{echo}) was set in order to counteract the residual deformation waves whereby unwanted excessive liquid flows were sustained in the orifice right after the droplet ejection.

In fact, the inks physics, ink pressure, nozzle orifice diameters and voltage waveform pulse affected the droplet physics. The droplet velocity and volume were monitored via a stroboscopic vision system mounted on the inkjet printer. Table V. 2 marked the inkjet printing protocol which was optimally yielding the inkjet printable droplets. The generated drop velocity and size for both polymer solution inks were quite similar. However, the present drop velocity appeared to be

0.87±0.05 for copolymer inks, exhibiting the deviation far from the given calibration value of velocity specification as $\sim 8 \text{ m s}^{-1}$. The reasons for this behavior are unclear. The physical constants of the inkjet printing criterion were calculated according to equation V. 8-11. Since the parameters except viscosity did not vary from pure solvent based ink to the polymer solution inks, rheological behaviors of inks could be regarded as a key parameter for determining the jettability. The derived Z value is indicative of jettability where low Z value reflected that the satellites may yield in parallel with the main inks droplet [8, 45]. In case of copolymer inks possessing relatively low viscosity, a high Z value of 61.54 appeared to be out of the reported printability limits of $1 < Z < 60$ [44] previously although the rheological properties and printing protocol presently satisfied the requirement of a stable inkjet printing, whereas a higher viscosity of terpolymer inks demonstrated that Z value of 42.22 matched nicely to the defined printable limits and thus as expected a very stable jetting droplet was observed. It should also be noted that pure TEP solvent based inks presented rather matched printability under the optimal printing protocol even though the Z values reached as high as 91.04, being out of the defined printable window previously [39, 44, 46, 47]. This results suggested that pure TEP solvent and TEP based polymer solution inks were robust and extended parameter range of printability for the inkjet printing technology as well.

Besides, there raises the new challenges once the polymer ejection was deposited onto the substrate support. When the polymer solution drops on the substrate start to dry, the concentration of either the polymer solute or suspended particulate matters gradually increase during the solvent loss and then images are patterned until the solvent-free status of the polymer deposition. If the solvent drying process is not nicely controlled, well-known issues such as the coffee ring effect and unwanted inhomogeneous thickness inkjet printed films would occur. Although some researchers fabricated the functional devices with the help of this effect [48-51], uneven topological behavior of printed films have an enormously deleterious influence on the performance and lifetime of printed electronic and electroluminescent devices [52]. This issue also matters in our present inkjet printing process when the ink droplets drying. A quick and large portion of ink deposition results in a significantly uneven thickness distribution, giving rise to the topological wrinkles and uptilted inkjet printed electronics consequently. Hence it is interesting to deeply investigate the compatibility between the ejected materials and substrates, of which the wettability is playing a vital role.

Table V. 2 Optimal inkjet printing protocol used for generating a printable droplet formation of copolymer and terpolymer solution inks in this present study

dimension			Copolymer inks	Terpolymer inks	Note
Ink Pressure			-21.7	-21.9	
Number of active nozzles			25	20	
Wave form	t_{rise}	μs	8	8	
	t_{dwell}	μs	7	6	
	t_{fall}	μs	4	4	
Firing frequency			1000	1000	
Nozzle Temperature			70	70	
Droplet velocity			0.87 ± 0.05	0.77 ± 0.02	
Droplet size			49.8 ± 2.1	52.1 ± 1.8	Referred to Printed
Substrate temperature			90	90	
Number of printed layers			5	5	
Thickness			10	11	measured
Thickness per layer			2	2.2	
Reynolds Re			2351.2	1277.82	calculated
Weber We			1514.2	960.99	calculated
Ohnesorge Oh			0.01655	0.02426	calculated
$Z=1/Oh$			61.54	42.22	calculated

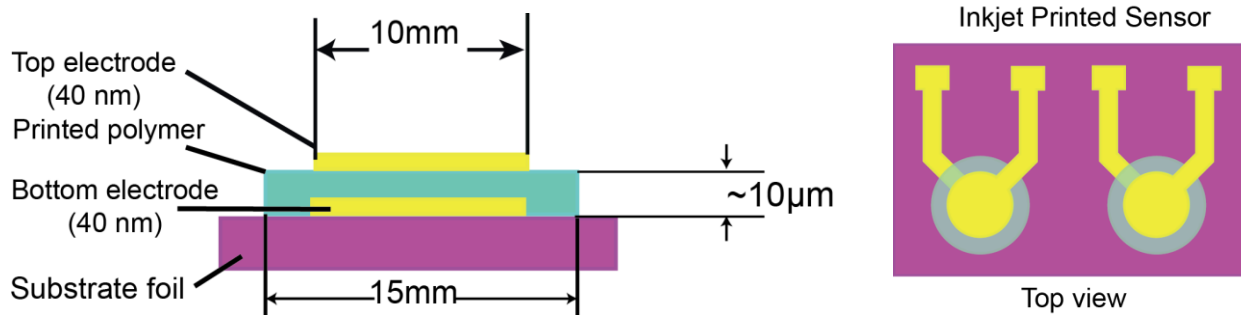


Figure V. 4 Schematic representations of layer by layer configuration of the inkjet printed force

The surface tension of solid substrate, serving as a quantitative reference of the wettability, would benefit the desirable patterns during the drying process. In this circumstance, the fabrication flow should be considered. Figure V. 4 represents a schematic diagram of inkjet printed sensors configuration, where the sensing polymer layer bounded to both the PI substrate

and sputtered Au electrodes. The measured surface tension values σ of the pristine PI foil were equivalent to the value of Au electrode, whereas the values were quite close to the solvent-free printed polymeric gelation layer. During the inks drying, here undergoes the σ values rising from the surface tension threshold of the polymer dilute solution inks. Excellent wettability was improved by application of corona discharge or UV-ozone treatment to the pristine PI foil. The treatment effect was visualized by the contact angle of water droplet on the PI foil. Figure V. 5 compared the UV-Ozone treatment effect of PI to the pristine PI foil. The contact angel significantly fell from 71.17° of the pristine to 24.58° of the treated foil with 30 min UV-Ozone exposure, by which the surface tension values were calculated as listed in Table V. 3. The surface

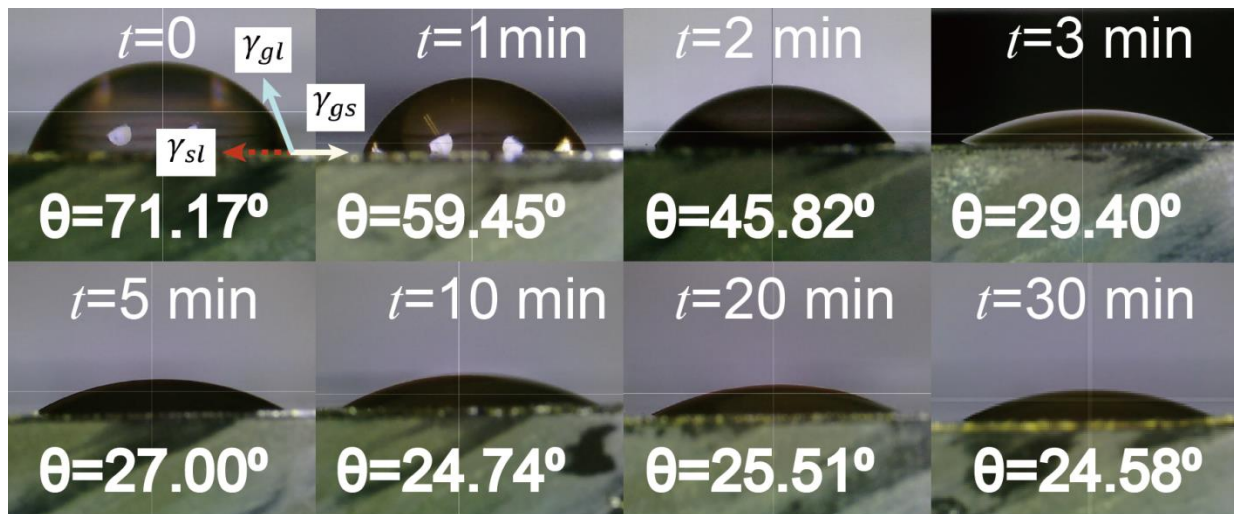


Figure V. 5 Photographics of the water droplet on the pristine PI against UV-Ozone treatment times. γ_{gl} represents the water surface tension vector; γ_{sg} symbolizes the PI foil surface tension veactor; γ_{sl} denotes the surface tension of PI foil and water interface. θ is the contact angle of the water drops on the untreated and treated PI substrate.

tension of UV-Ozone treated foil was then calculated as 71.38 mN m⁻¹ thanks to another inert organic solvent Diiodomethane, underlying the Owens-Wendt surface tension measurement mechanism. This is indicative of rather good wettability between the solid PI foil and gelling polymer during the volatilization of the solvent.

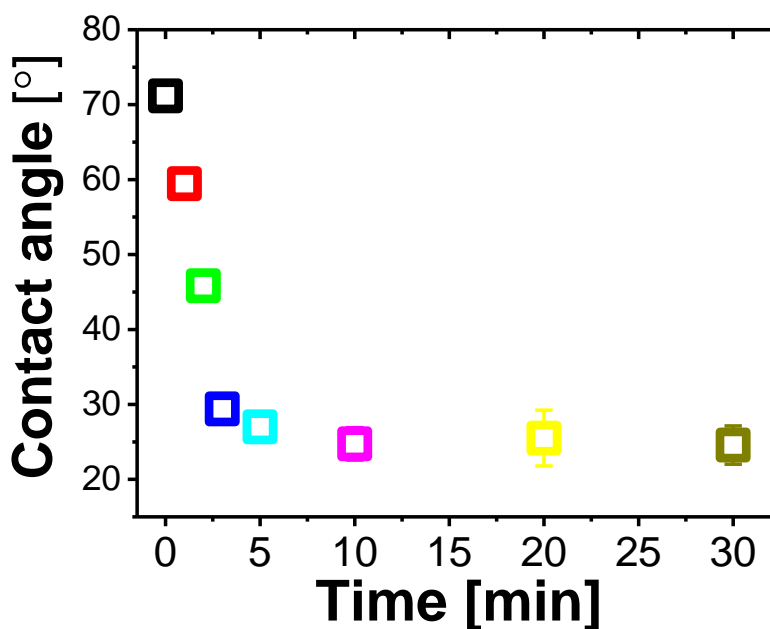


Figure V. 6 Water contact angle on the PI foil substrate as a function of UV-Ozone treatment time. Error bars are covered by the data symbols.

The aforementioned coffee ring effect is an ubiquitous phenomenon even though there was the excellent wettability [53]. In particular in case of present inkjet printing fabrication, a strong contrast of wettability between the corona treated PI foil and Au electrode exists. The evaporation rate of drying droplet rim exceeded the rate in the droplet center and thus this gave rise to the plenty of the solvent losing at the droplet edge near the contact line. It has also been well-acknowledged that the contact line of the drying drop is pinned so that the losing liquid must be replenished by outward capillary liquid flow from the interior to the pinning contact line. This convective flow carried dispersed polymers or nanoparticles and piled up at the contact ring line, being responsible for the coffee ring effect. This outward flow was however balanced by the inward Marangoni flow to the droplet interior center, driven by surface tension gradient between the periphery and the interior of the drying droplet. Several strategies have been developed to overcome the coffee ring effect such as ink formulation consideration, surfactant additives [54, 55] and baking condition [56]. The main approach is to engineer the inward Marangoni flow by a cosolvent strategy, with one minor component having a higher boiling point and a lower surface tension [57-59]. This strategy functioned very well for the printing patterns in some literatures [60, 61]. For consideration of sensor device application, additives into the formulation was ruled out.

Table V. 3 Surface tension properties of the pristine, plasma treated PI and Au sputtered PI substrate. Surface tension of the printed copolymer and terpolymer patterns were also compared with fluorinated fluid phobic Teflon films. Data listed here were also measured by Owens-Wendt- Kaelble method.

Acronyms	PI pristine	PI Plasma	Au on PI	Copolymer	Terpolymer	PTFE film
Surface tension (mN m ⁻¹)	59.24	71.38	55.12	39.4	58.01	24.55
Dispersive component mN m ⁻¹	43.29	47.05	45.93	35.23	54.75	20.29
Polar component mN m ⁻¹	15.95	24.33	9.19	4.17	3.26	4.26
Note	50 μ m - thick	50 μ m - thick	~40 nm- thick	Inkjet printed	Inkjet printed	1 mm-thick

Thanks to control of the printing drop-spacing and baking temperature, the coffee-ring effect was minimized with a single-solvent inkjet printing solution ink system. Subramanian et al. [62] reported a perfect morphology of inkjet printed PEDOT:PSS lines under the controlled printing and temperature condition in terms of drop spacing, firing frequency and substrate temperature and they also provided the explanation from the geometric point of view. Drop spacing, distance between the adjacent droplets center, corresponds to the pattern resolution. Decreasing the drop spacing is equivalent to an increase in the pattern resolution. For the compact inkjet printer employed in this current work, the low resolution was compensated by a large quantity of ink solution deposition in order to fully cover the printing patterns. Large portion of ink deposition prolongs the time duration of solvent evaporation serving as the main side-effect of a low printing resolution. This negative effect would exaggerate during the second repetition of inkjet printing process, leading to an severe coffee ring effect pattern. The best strategy is that as follows: in a certain drop spacing the ink droplet merges with the adjacent pinned beads and in parallel, the printed layer dries nearly when the upcoming repetition of printing application is to launch. As motivated in this case, the baking temperature would play a vital role during the pinned droplets drying. In the printing trials, substrate temperature was set to 70 °C and 90 °C. Baking time of 70 °C appeared almost 3 times longer than that of 90 °C baked. Decreasing the substrate temperature significantly undermined the evaporation rate at periphery of the landed drop more than the center. Hence, coffee ring effect was effectively minimized because of the weakening outward convective ink flow. In this regard, the liquid drop maintained on the substrate before next droplet

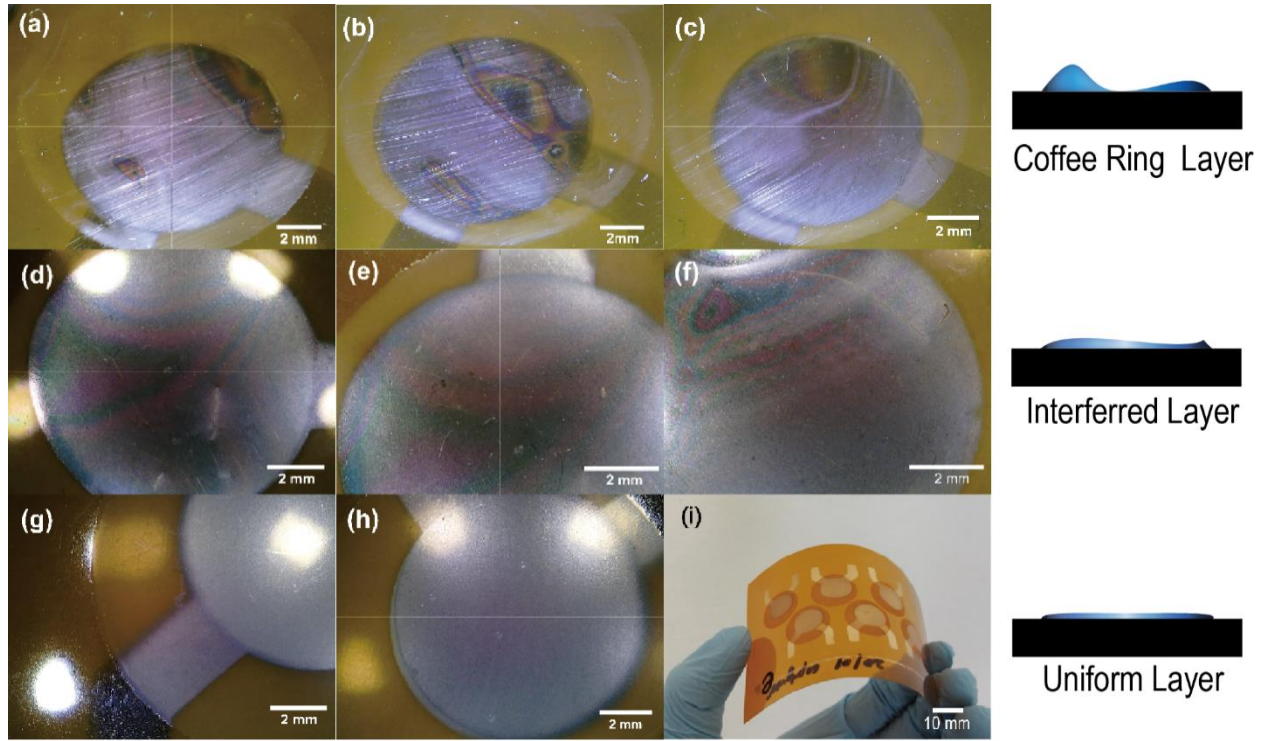


Figure V. 7 Optical photographs of inkjet printed terpolymer films on plasma treated Kapton substrate depending on the varying print speed at same pattern resolution of 2000×2000 (dpi, dots per inch). (a)-(c) void and incomplete terpolymer deposit layer upon 75 mm/s print speed; (d)-(f) colorful interplay strips due to the thickness discrepancies of the polymer layer at 40 mm/s printed speed; (g)-(h) strip-free and optically homogeneous topology at 30 mm/s print speed; (i) the monolithically inkjet printed force sensor array. Horizontal bar is respectively marked as the scale at bottom right.

falling. Implementation of ink ejection as a secondary repetition could give rise to the bulging because of ink overflowing. Whereas high substrate temperature favored to a high evaporation rate of pinned droplet, drop spacing needs to be optimized. The evaporation rate per area $J_{(r)}$ correlates to the $(R - r)^{-\lambda}$, where λ is from the contact angle (θ_c) between the drop the substrate via $\lambda = \frac{\pi - 2\theta_c}{2\pi - 2\theta_c}$; r represents the distance from the drop center to its periphery; R and θ_c are pinned drop radius and contact angle respectively. Both evaporation flux at pinned drop center and rim were enhanced so that the in situ viscosity of pinned drop multiplied before adjacent droplets to land. It is reasonable to assume that the onset of scalloping can be observed at relatively low drop spacing. And the correspondingly high pattern resolution would eventually in turn benefit the quantity of polymer deposit.

High pattern resolution does not witness a good quality of resultant polymer deposit in some cases. Notwithstanding the high substrate temperature is set to assist the solvent evaporation at given pattern resolution of 2000×2000 (high), drying time is insufficient to adapt the time

interval between two adjacent landing drops. For instance, Figure V. 7 (a)-(c) showed the resultant pattern deposits with a relatively high print speed of 75 mm/s (Y axis displacement). Discrete morphology of inkjet printed polymer layer is most probably due to the superimposition

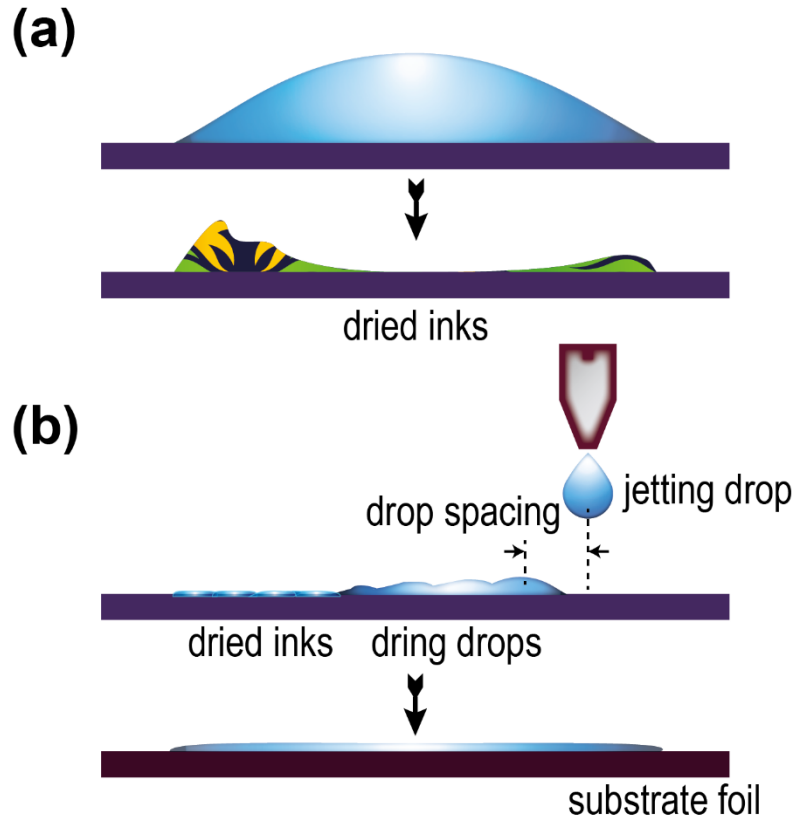


Figure V. 8 A schematic diagram of inkjet printing and pinned drops drying with a low (a) and high (b) quality factor numbers. Severe coffee ring like polymer residual pattern after inks dried due to a large amount of inks deposition per nozzle (a) whereas a small quantity of droplet volume applied by each nozzle favored to the indistinct coffee ring like polymer residual pattern.

of falling droplets and pinned liquid beads as presented in Figure V. 8. Although high substrate temperature somewhat enhanced the outward convective flow and eventually fragmentary deposit, at this print speed, the time duration between droplets landing is too short to nicely match the lifespan of a pinned drops drying. The dispersed polymers were carried to the plasma treated PI part of pattern rim. The print speed was thus optimized. The smaller value of print speed, the longer time interval between the adjacent landing drops application. Eventually, one layer inkjet printed terpolymer turn out as complete and homogeneous morphology at a print speed of 30 mm/s and a given resolution of 2000×2000 dpi.

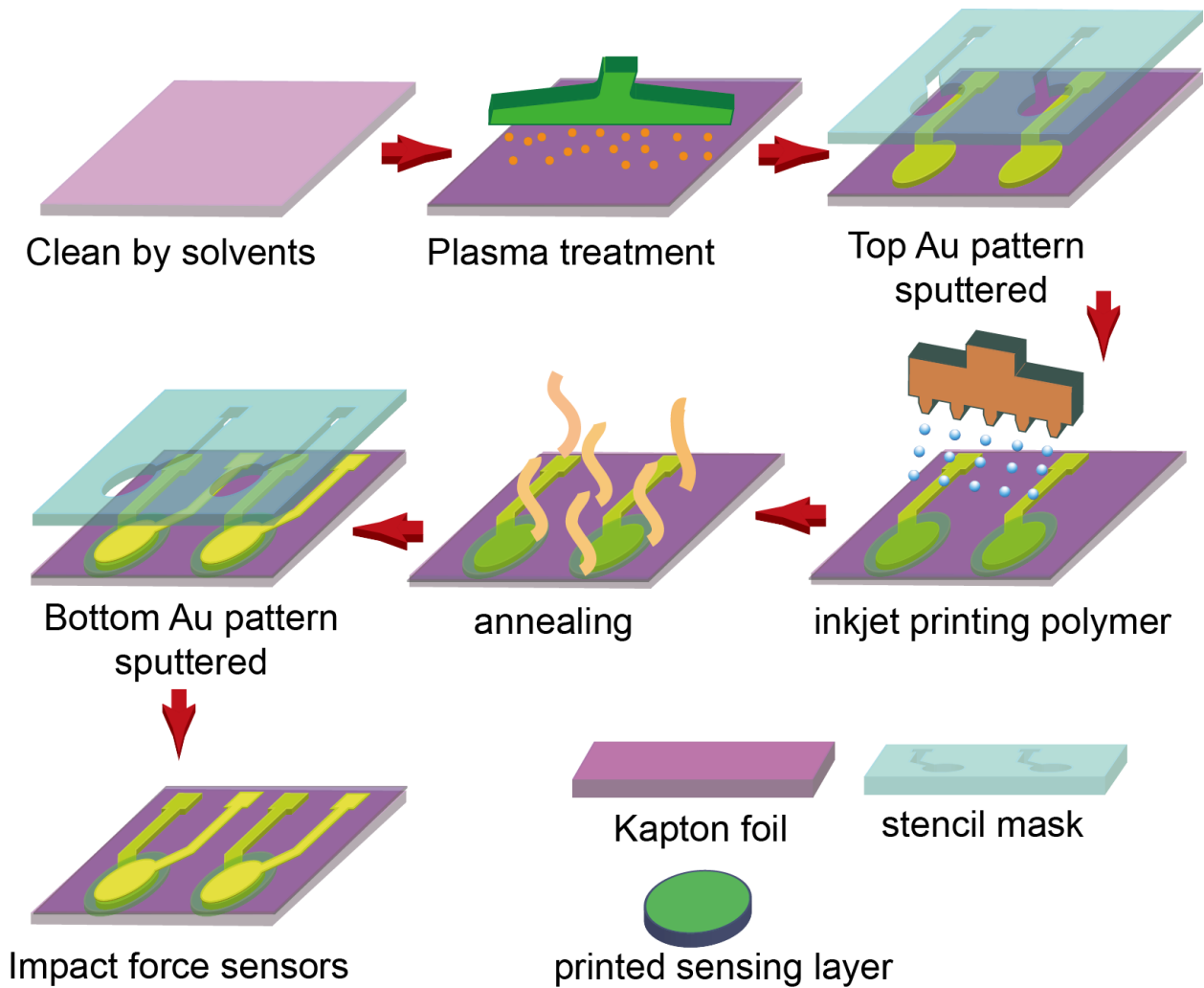


Figure V. 9 Fabrication flow of a typical inkjet printed force sensor

In summary, discussions here were divided into three main parts. The first part addressed the printable droplet generated by the inkjet protocol which was tuned to adapt the ink formulation physics and dynamics. Secondly, plasma surface treatment strategy eliminated the drop wettability issue to the fluidphobic PI substrate. Optimal baking substrate temperature and drop spacing would be a necessity to the inkjet printed ended with the millimeter-scaled pattern. The following statement, the sensor behavior to the dynamic impact force would be carefully characterized and several complementary parameters were jointly performed as well.

IV. 2 Ferroelectric Characteristics of Inkjet Printed Sensors

Ferroelectric properties of inkjet printed force sensors were characterized by displacement-bipolar electric field hysteresis loop measurement. High electric fields up to $70 \text{ V}/\mu\text{m}$ with increment of $10 \text{ V}/\mu\text{m}$ from $20 \text{ V}/\mu\text{m}$ were applied to the inkjet printed sensors in order to align the dipoles flipping with the normalized direction. The output of short-circuit current maintained stable during each poling cycle. The displacement of ferroelectric P(VDF-TrFE) copolymer

sensor under altering electric field as presented in Figure V. 10 showed a typical polarization curve as a ferroelectric material. The polarization reached its saturation state under a maximal poling electric field of around $70 \text{ V}/\mu\text{m}$, otherwise an electric field of $80 \text{ V}/\mu\text{m}$ usually caused an electrical breakdown failure. The remanent polarization P_r without an electric field supply and the coercive field appeared averaging at around 65 mC m^{-2} and $45 \text{ V}/\mu\text{m}$, respectively, which were closely to the values reported for a pressure-sensor based on P(VDF-TrFE) copolymer [63, 64]. Excellent reproducibility was manifested by the D - E hysteresis loop measurement on the batch fabrication, suggesting the high uniformity of sensor thickness and homogeneity via the inkjet printing technology. The D - E hysteresis loop behaviors of the relaxor ferroelectric P(VDF-TrFE-CTFE) terpolymer in the meantime were performed and incomplete hysteresis loop was obtained. This indicated considerable losses during the capacitor discharge.

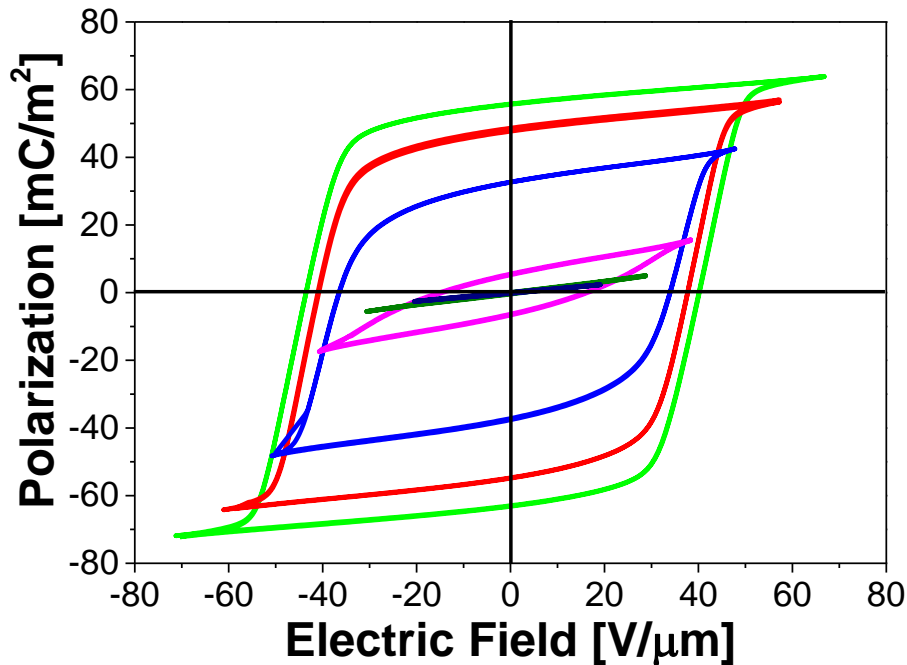


Figure V. 10 Polarization-Electric hysteresis loop measurements as a function of electric field with increasing poling electric field.

Capacitance C_p at low bias voltage ($\sim 0.1 \text{ V}/\mu\text{m}$) as a function of broadband frequency f was also measured by using an impedance analyzer for both poled ferroelectric copolymer sensor and relaxor terpolymer sensors. The representative spectra of the logarithmic f dependence of C_p value were plotted in Figure V. 11a. The mean value of C_p of ferroelectric copolymer fell very limited as a function of the frequency range, with a plateau appearing at $0.72 \pm 0.03 \text{ nF}$ at medium f . The values found for the inkjet printed copolymer sensors were close to the C_p values for the custom-sized sensors which were fabricated by spin coating and screen-printing ink deposition methodologies. Regarding to the relaxor ferroelectric terpolymer, capacitance surprisingly

reduced from 12.12 nF at low f to a level-off value of 3.30 ± 0.21 nF at the medium f , approximately 5 times higher than the C_p value of ferroelectric copolymer sensors. Dielectric behavior derived from expression $\varepsilon' = \frac{C_p \cdot d}{\varepsilon_0 \cdot A}$ shared the common features with their capacitance properties where d assigns to the thickness of electroactive polymer layer; A is the area covering

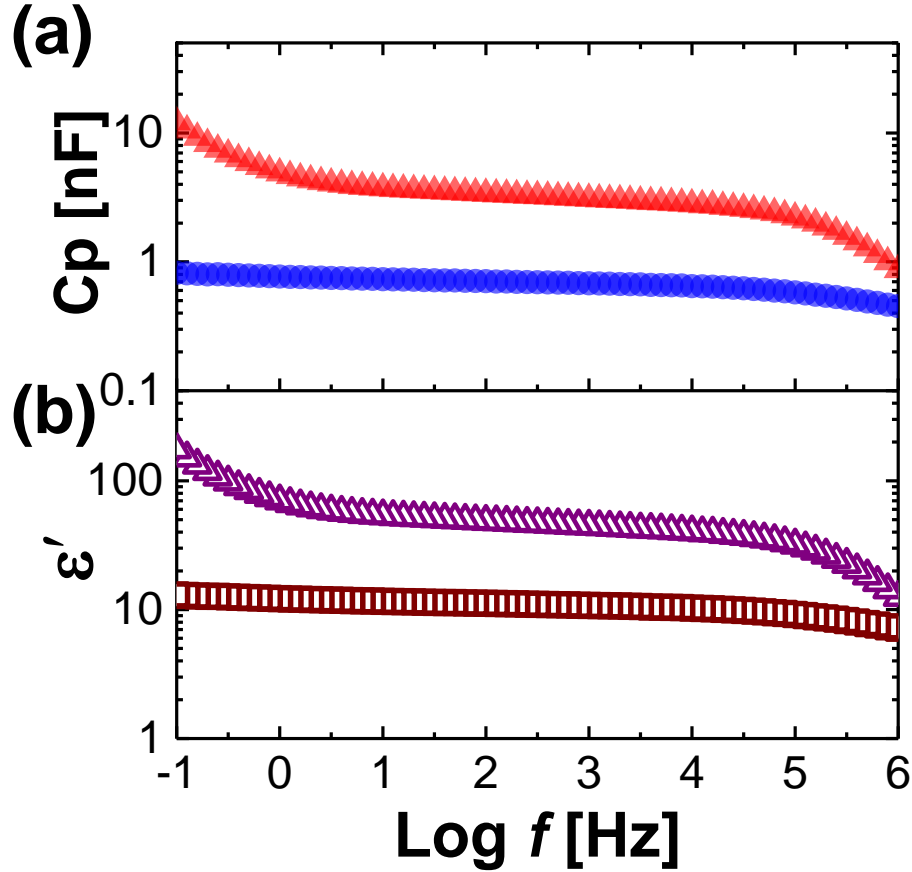


Figure V. 11 Logarithmic frequency dependence of capacitance behavior (a) and dielectric permittivity (b) for inkjet printed copolymer and terpolymer sensors. Filled square and open square were assigned to respective capacitance trace and dielectric spectrum of P(VDF-TrFE) copolymer sensors. Filled triangle and open triangle represented the obtained data of terpolymer sensors.

the electrodes; ε_0 is permittivity in vacuum. The ferroelectric sensor presented a typical dielectric spectra versus f as discussed in the established reports, dealing with the sensor devices fabricated by the versatile printing technologies, whereas for sensor based on electrostrictive terpolymer shown in Figure V. 12a saw an exceptional enhancement at low frequency as compared with the sensors based on spin coating solution process. In order to clear this exotic phenomenon, dielectric loss spectra were obtained after the subtraction of ions conduction contribution according to the well-known Kramer-Kronig method. The dielectric losses derivatives ε''_{der}

showed the discrepancies over spin coating at low frequency instead of medium and high f as presented in Figure V. 12b. In previous section Chapter IV, we revealed the high dielectric amplitude at low frequency was satisfactorily ascribed to the interfacial polarization. The surprisingly high dielectric loss for inkjet printed sensor implied an evolution of such relaxation over spin coated one. The evidence was further provided that a shift of peak by more than one decade towards the high frequency occurred to the dielectric modulus spectra of inkjet printed

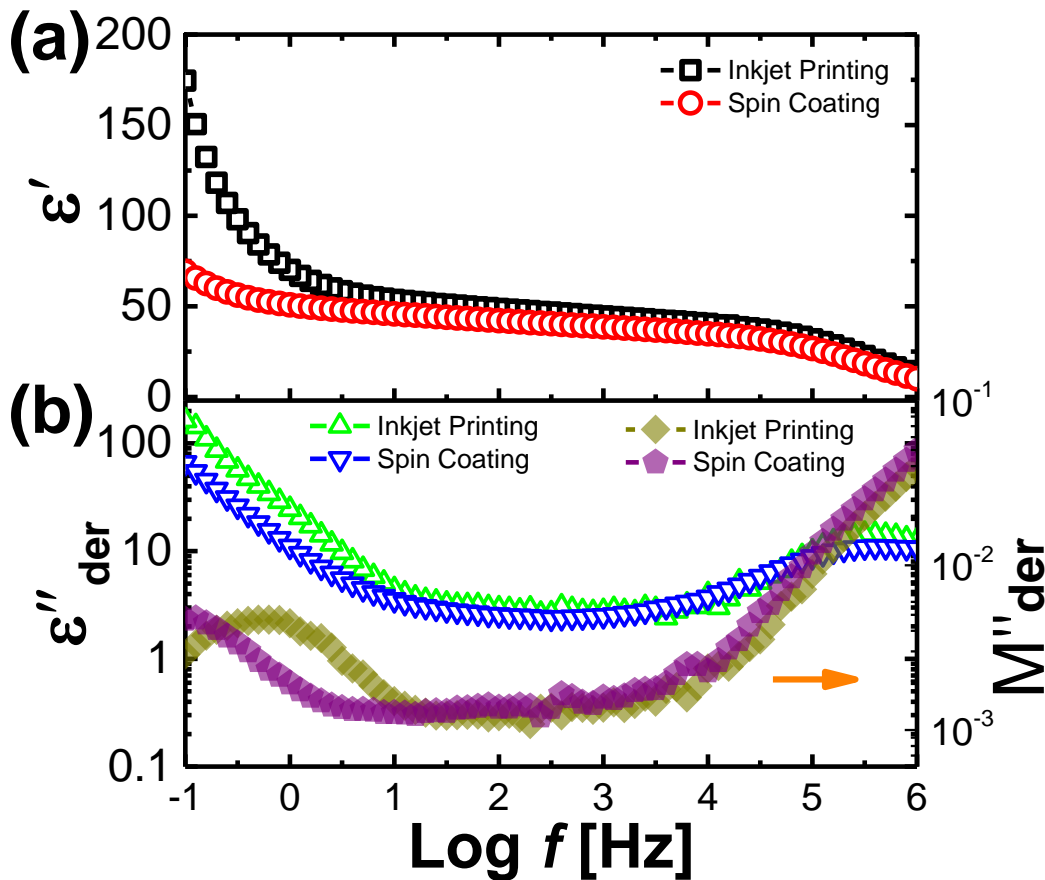


Figure V. 12 A comparison of inkjet printing and spin coating solution-process protocols with respect to broadband dielectric spectroscopy (a) and dielectric loss derivative ϵ''_{der} with dielectric modulus M''_{der} spectroscopy as a function of logarithmic frequency.

sensors. This might be due to a unique polymer ink deposition via inkjet printing technology, different to a conventional solution process in a continuous way (recall Figure V. 7). Scalloped or uniform patterns emerged more than bulging or overflow inks deposition so that the each pinned droplets dried individually. This led to the relatively isolated crystal domains which demonstrated a continuous polymer microstructure in non-optimized inkjet printing protocol. Each relatively isolated microstructure serving as the micro-capacitors would benefit the strong boundary interaction, that is, the MWS interfacial polarization.

IV.3 Electromechanical Coupling Behavior of Printed Electrostrictive Terpolymer

The studies in Chapter II showed that the electromechanical coupling behavior of the bulk terpolymers was performed via tip displacement of the unimorph cantilever beam. This is due to the thickness electrostrictive compression under electric field, which was expected to allow the discrepancies of geometric deformation over the both sides of bilaminar cantilever beam. In this current investigation, the deformation behavior of the inkjet printed terpolymers were investigated at the electrode center in a free mode with no fixation clip under an electric field supply up to 100 V/ μm at maximum, where the electric breakdown for the 10% DEHP plasticized printed terpolymers occurred sometimes. The reduced breakdown strength values were manifested in our previous study due to the DEHP dopant [65]. For the sake of noticeable comparison, the electric field was normalized as 100 V/ μm . By using a laser interferometer, electric field-induced displacement of each kind of inkjet printed terpolymer devices was characterized and was then plotted versus the electric field as shown in Figure V. 13. The three investigated inkjet printed terpolymers exhibited the “butterfly” displacement in response to the electric field. In a moderate electric field below 60 V/ μm , the three kinds shared the similar trend strength and the filtered printed terpolymer was slightly out-performed. This feature is not the case at high electric field where the 10% DEHP modified inkjet printed terpolymers appeared at maximum ca. 6 μm , almost three-fold higher than the pure one. In previous study, we suggested that the apparent electrostrictive strain of the terpolymer originated from both intrinsic electrostrictive effect and Maxwell effect [66, 67]:

$$S_{33} = S_E + S_M = Q(\epsilon_r - 1)^2 \epsilon_0^2 E^2 + \frac{1}{2} \frac{\epsilon_r \epsilon_0}{Y} E^2 (1 + 2\nu) = M_{33} E^2 \quad \text{V.12}$$

where ν is poisson ratio of the terpolymer material. The displacement of flexible capacitor-like device in a free mode is much more complex than the neat terpolymer films without a passive support. The contribution of passive PI substrate must be considered when analyzing the displacement in current case. Therefore, the quantitative evaluation of the apparent electrostrictive coefficient M_{33} seems not accessible. At a low electric field, the strain caused by electroactive terpolymer layer could not overcome the persistence of the passive PI substrate and only field-induced strain in printed terpolymer layer occurred rather than the whole sensor device.

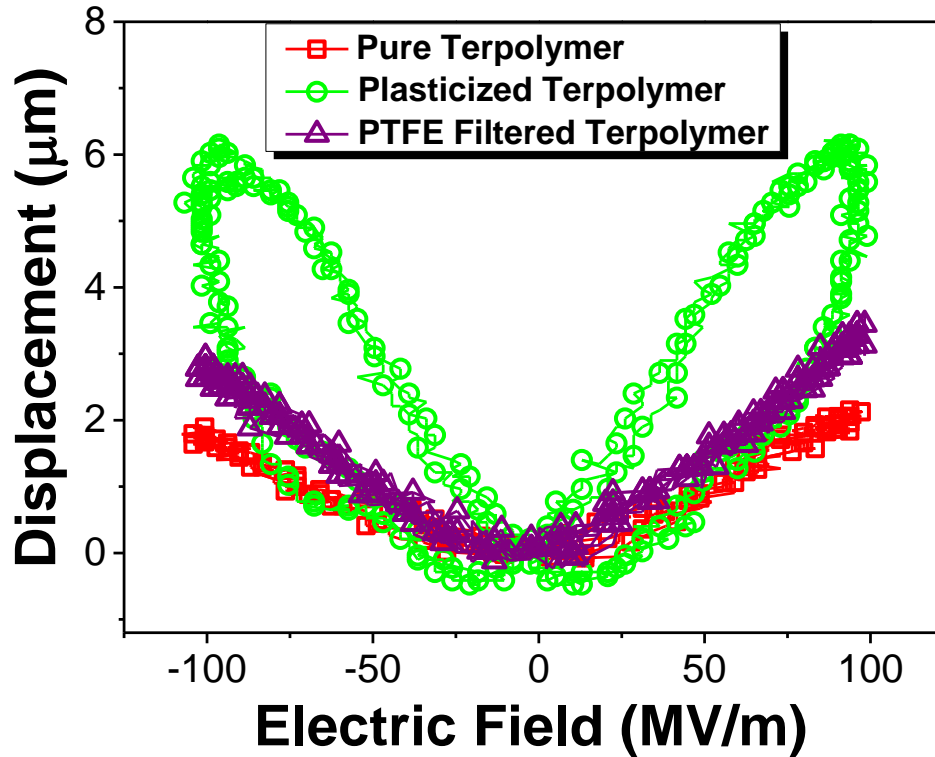


Figure V. 13 *In-situ* electric field-induced displacement by 2 cycles of the bipolar sinusoidal AC voltage up to 100 V/ μm for various inkjet printed terpolymers. Hollow rectangle (\square) symbolizes the printed terpolymer based on the pure terpolymer inks; triangle (Δ) represents 10% DEHP modified inks passed through the PTFE filter; circle (\circ) denotes the 10% DEHP modified inkjet printed terpolymer without the filter operation.

However, the response of pure and PTFE filtered DEHP modified terpolymer sensor devices both behaved the very slim hysteresis loops, suggesting very weak electromechanical losses. The low losses of pure terpolymer sensor device were in good agreement with the established results [68]. Surprisingly, large hysteresis loop was observed for the 10% DEHP plasticized inkjet printed sensor device. It is interesting to highlight the strong contrast between both. And this is explained by the fact that the amount of DEHP was absorbed by the micrometer-sized pore of the PTFE filter networks, making the trace remnant of DEHP molecules in the terpolymer ink. This can also be evident by a slump down dielectric behavior for filtered terpolymer sensor device, comparable with the plasticized one.

IV. 4 Piezoelectric Behavior of Ferroelectric Inkjet Printed Sensor

Piezoelectric properties of a single ferroelectric force sensor were investigated with varying dynamic force application. Prior to evaluation of force sensor performance, the sensitivity of the force sensor was characterized firstly. Different frequency of the dynamic force was conducted upon the top of sensor surface where the force was applied by using a frequency-modulated

vibrator. The acceleration of z axis was *in-situ* monitored by a MEMS-accelerometer stuck close to the inkjet printed sensor on the polycarbonate (PC) panel which was mounted on a z axis end free of a vibrator as depicted in Figure V. 14. The real-time force applied was defined by the normalized weight mass multiplying with the acceleration values of the z axis variation and could be modulated by the amplitude and frequency of an input signal. The sinusoidal signal with frequency of 100 up to 1000 Hz with increment of 100 Hz was applied to the vibrator. A representative output current of ferroelectric force sensor in response to the applied force at given frequency of 400 Hz was illustrated as Figure V. 15a. Note that the simultaneous output current in response to the applied force wave characterized a quasi-sinusoidal feedback signal. There was a clear phase shift between the applied force signal and the generated current. This phase drift was clearly visible in equation V.7 since the output current was proportional to the time derivative of the mechanical strain $\frac{\partial S_{33}}{\partial t}$ in cross-section mode [67]. The mechanical strain does not always align with mechanical excitation because of the viscoelasticity of the polymer nature [69].

Investigation of piezoelectric behaviors for copolymer dynamic sensor vs. applied force was also carried out at fixed frequency of 400 Hz. Note that the output current in Figure V. 15b was a quasi-linear relation with the applied force no more than 1 N. Since reliable setup for evaluation of sensing device in high accuracy was evidenced, peak-peak amplitude of acceleration and current response curves were both taken as data record for the sensitivity calculation of printed ferroelectric force sensor. In addition, the sensitivity of ferroelectric dynamic force sensor as a function of the frequency at fixed excitation amplitude of the input sinusoidal signal was then

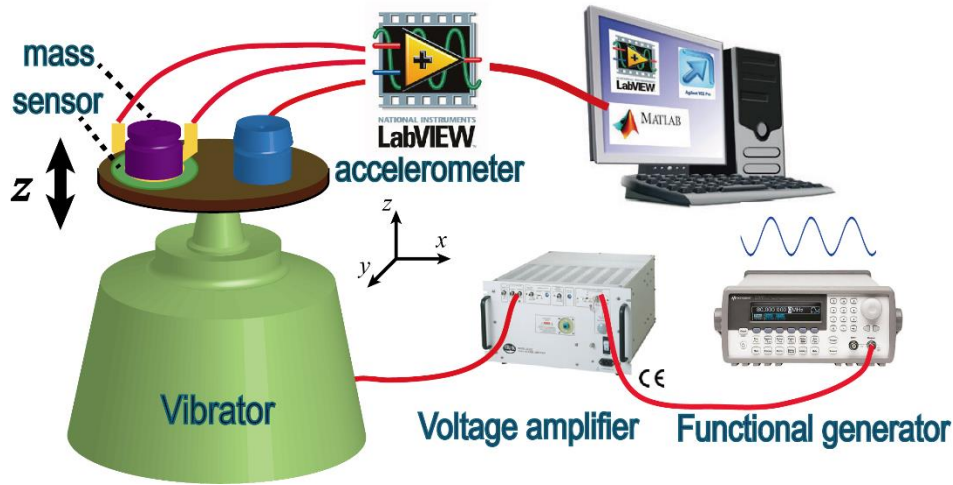


Figure V. 14 Schematic diagram of experimental setup for the sensitivity measurement of the inkjet printed ferroelectric force sensor.

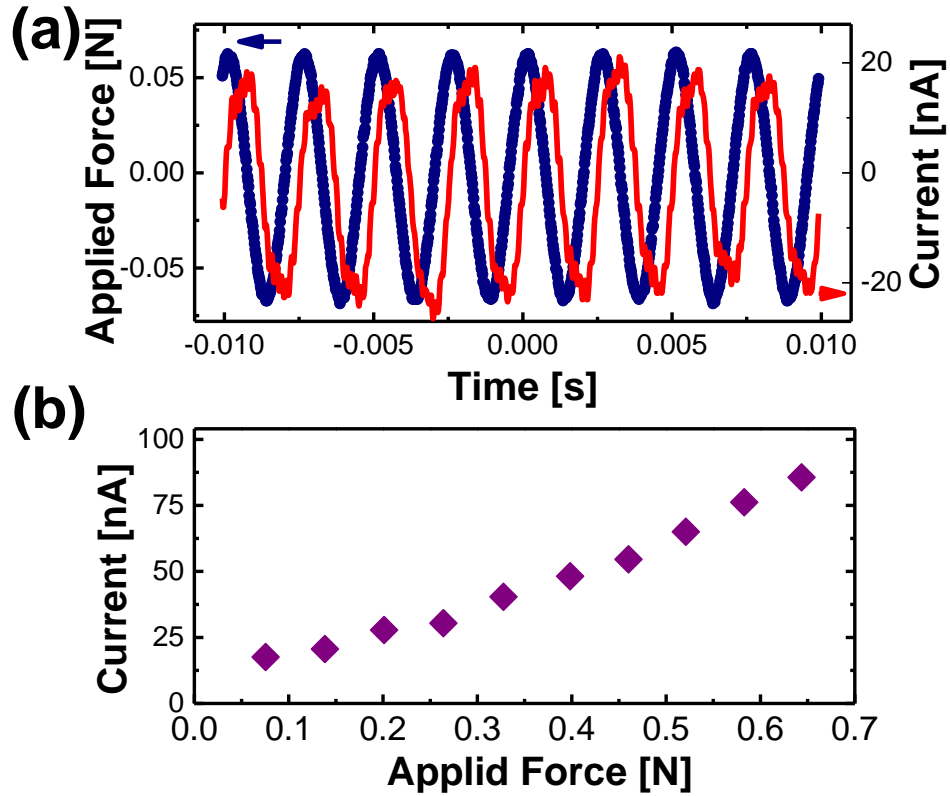


Figure V. 15 A representative output current in response to a given applied force of 400 Hz sinusoidal signal (a); output current I against varying dynamical force application for a single ferroelectric copolymer sensor at fixed 400 Hz (b).

plotted in Figure V. 16. It is clearly observed that the sensitivity, the specific ratio of readout current to the varying applied force values at each studied frequency, averaged at $11.8 \pm 1.1 \text{ nA g}^{-1}$ except an anomaly. The anomalous peak of the sensitivity appeared at frequency between 150 Hz and 250 Hz, which was unambiguously ascribed to the resonance frequency of the experimental setup. This corroborates that the sensitivity of ferroelectric dynamic sensor was independent of applied force frequency in a limited frequency range, simply being related to the strength of the excitation force.

Validation of the inkjet printed copolymer sensor was manifested by the dynamic force impulse application as presented in Figure V. 17. The applied force impulse waveform was monitored to be a Gaussian shape-like mechanical excitation signal as presented in Figure V. 17a. The force peak appeared at 5.76 Volts, corresponding to the force value of 255.78 N force excitation. The readout current and charge response of the printed ferroelectric sensors to such a force application were also illustrated. In the Figure V. 17b saw an incidence of the sinusoidal

current output and consequently, the charge yield of 4.77 nC was obtained according to the integration of output current curve versus the time elapsing. It was also worth noticing that common features of charge yield in shape and peak involved, were shared with the applied force impulse record and this indicated the fact that the yielding charge aligned simultaneously with the force applied. Hence, the piezoelectric coefficient d_{33} , defined as charge yield ratio to the applying force, was calculated as 18.7 pC N⁻¹, quite close to the values (~20 pC N⁻¹) found in the literature [6, 63, 70]. Varying force was then applied to the inkjet printed ferroelectric sensor within the force value range between 50 N and 305 N. The charge yield in response to such dynamic force applying was plotted in Figure V. 17b and was linear fitting with a slope of 18.9 pC N⁻¹. Note that the frequencies of applying forces were estimated at approximately 300 Hz which was not located within the proposed resonance scope (150~250 Hz). The replicate measurements were subsequently carried out with a batch of six sensors and the variation of d_{33} values among the individual sensor was negligible. In fact, a good reproducibility also implied the reliability and homogeneity of the inkjet printing technology.

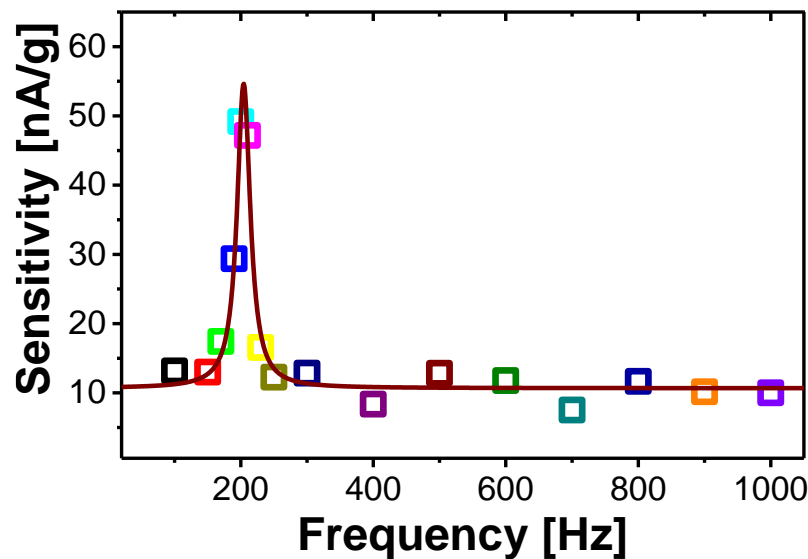


Figure V. 16 Sensitivity of the ferroelectric dynamic force sensor against force applying with a varying frequency range between 100 Hz and 1000 Hz. Solid curve is a peak fit by the Lorentz function.

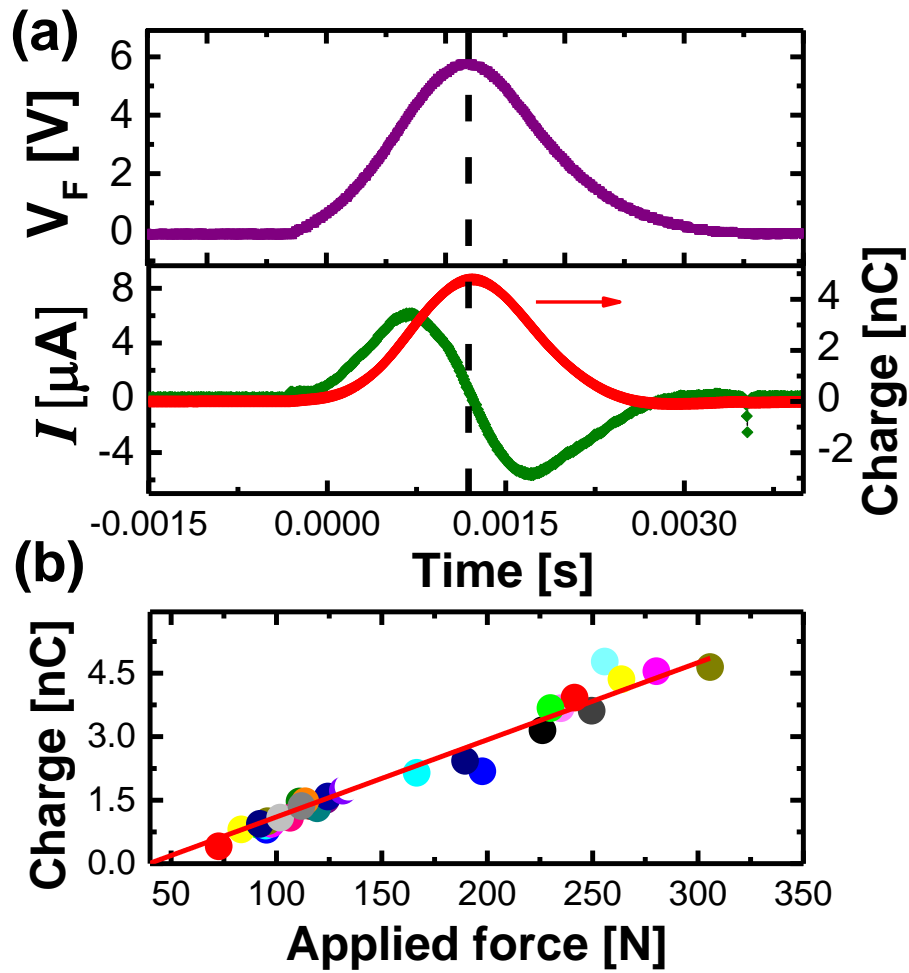


Figure V. 17 A representative of voltage trace of force applying impulse and readout current I with charge yield integration (a); Induced charge yield in response to the varying dynamic force impulse (b). Solid line was a linear fit to the data.

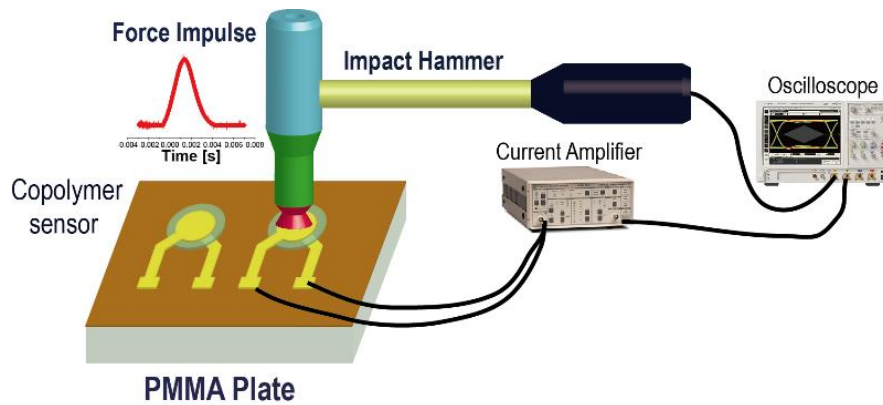


Figure V. 18 Schematic representation of the experimental configuration for impact force applying upon the inkjet printed ferroelectric P(VDF-TrFE) copolymer sensor devices.

IV. 5 Pseudo-piezoelectric Behavior of Electrostrictive Terpolymer

As motivated by the $D - E$ hysteresis loop behavior from the theoretical consideration point of view, the large electric polarization of the electrostrictive terpolymer could be induced under the bias electric field E . And so-called pseudo-piezoelectric coefficient d_{33eq} was linearly dependent on the external bias electric field E_{33} across the thickness. In order to validate such hypothesis, impact force excitations upon the inkjet printed sensors based on the electrostrictive terpolymer were characterized under varying electric field up to $33.33\text{V}/\mu\text{m}$, corresponding to a bias DC voltage supply of 300V as presented in Figure V. 19. The representatives of the output current and charge yield in response to the force excitation under a bias DC voltage of 10 V and 90 V were plotted in Figure V. 20. And the current and charge output curves in shape appeared quiet similar to the current and charge response of a printed ferroelectric sensor. It is interesting that terpolymer sensor under 90 V bias voltage presented the charge yield of 4.27 nC, nearly 9 times higher than the charge response of 0.46 nC under 10 V bias voltage supply although a similar impact force excitation (185.4 N) was applied under both bias voltage. Note that 9 times higher bias voltage resulted in nearly 9 folds charge yield response and thus it was reasonable to assume that the pseudo-piezoelectric coefficient d_{33eq} enormously benefited from the bias voltage supply. Individual d_{33eq} at each bias voltage supply was subsequently obtained and increased monotonically with the increment of electric field, which can be satisfactorily described with a quasi-linear compensation law as shown in Figure V. 21. d_{33eq} value under $33.33\text{ V}/\mu\text{m}$ equivalent to a 300V bias voltage supply reached a very high value of 81.64 pC N^{-1} , nearly 4 times larger than that of the printed ferroelectric force sensors. Considering that the terpolymer films possess a electric breakdown strength as high as ca. $300\text{ V}/\mu\text{m}$ in previous study, very high d_{33eq} value for the relaxor force sensors based on electrostrictive terpolymers would be expected. So was a greatly enhanced sensitivity under a high bias electric supply.

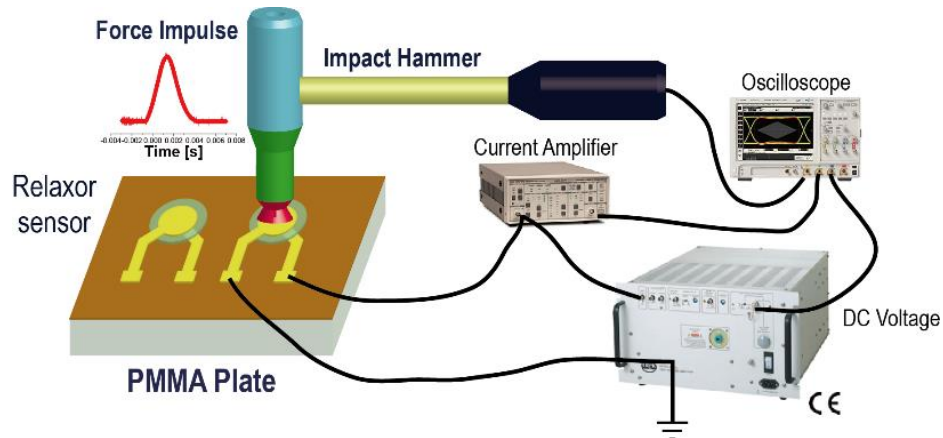


Figure V. 19 A schematic diagram of force impulse applying upon the relaxor inkjet printed sensor based on electrostrictive terpolymer and data acquisition circuit.

The key parameters playing the important roles in determination of the electromechanical properties were also compared with extensively investigated PZT ceramics in Table IV. 4. The high stiffness and heavy weight density of piezoelectric PZT ceramics with high cost limited its applications such as bendable and wireless wearable electronics, although PZT possessed a piezoelectric coefficient d_{33} as high as hundred orders, comparable with two polymer candidates. A high d_{33eq} value of 81.64 pC N⁻¹ for terpolymer was however considerably competitive to a d_{33} value of PZT ceramics only with a bias 33.33 V/ μ m supply, which was far below its electric failure breakdown strength. It should be also noted that in Figure V. 21 at 7.5V/ μ m bias electric field appeared the cross point between the electric field dependence of d_{33eq} and invariable d_{33} value of 18.9 pC N⁻¹. Such a low bias electric field compulsory for the electrostrictive terpolymer sensors gave rise to the equal piezoelectric coefficient value to the ferroelectric force sensors, equivalent to a 67.5 V bias voltage supply for a 9 μ m-thick inkjet printed force sensor, though such a bias voltage value was still relatively high for the wireless portable electronics and human safety reasons. In the perspective work, before sensor device fabrication, polymer ink formulation and inkjet printing protocol should be optimized in order to fulfill the requirement of printing less than 2 μ m-thick piezoelectric impact force sensor.

Table V. 4 A comparison of electromechanical properties of the sensing layer polymers in this present work and mostly investigated PZT ceramics

Acronyms	Printed Copolymer	Printed Terpolymer	PZT Ceramics
Young's modulus @ R.T	^a 3.3 GPa	182 MPa	^b 60.0 GPa
Density (g cm ⁻³)	1.78 [71]	~1.3 [72]	~7.80 [73]
Dielectric Permittivity	10.8 (1000 Hz)	44.5 (1000 Hz)	1200
Dielectric Strength (V μ m ⁻¹)	≤80 [74]	269 [65]	64 [75]
P_r (mC m ⁻²)	65 mC m ⁻²	--	--
P_s at 70 V/ μ m (mC m ⁻²)	72 mC m ⁻²	--	--
Capacitance of sensor (nF) (@1000 Hz, 78.59 mm ²)	0.68	3.08	--
Piezoelectric coefficient (pC N ⁻¹)	~18.9	18.9@7.5V/ μ m 81.64@33.33V/ μ m	223 [76]
^c Powder Cost (€ g ⁻¹)	7	9	15.2

Note: a, data value provided by reference [15]; b, value provided by the reference [76], c, Price referred to the Powder indicative Price List [77]

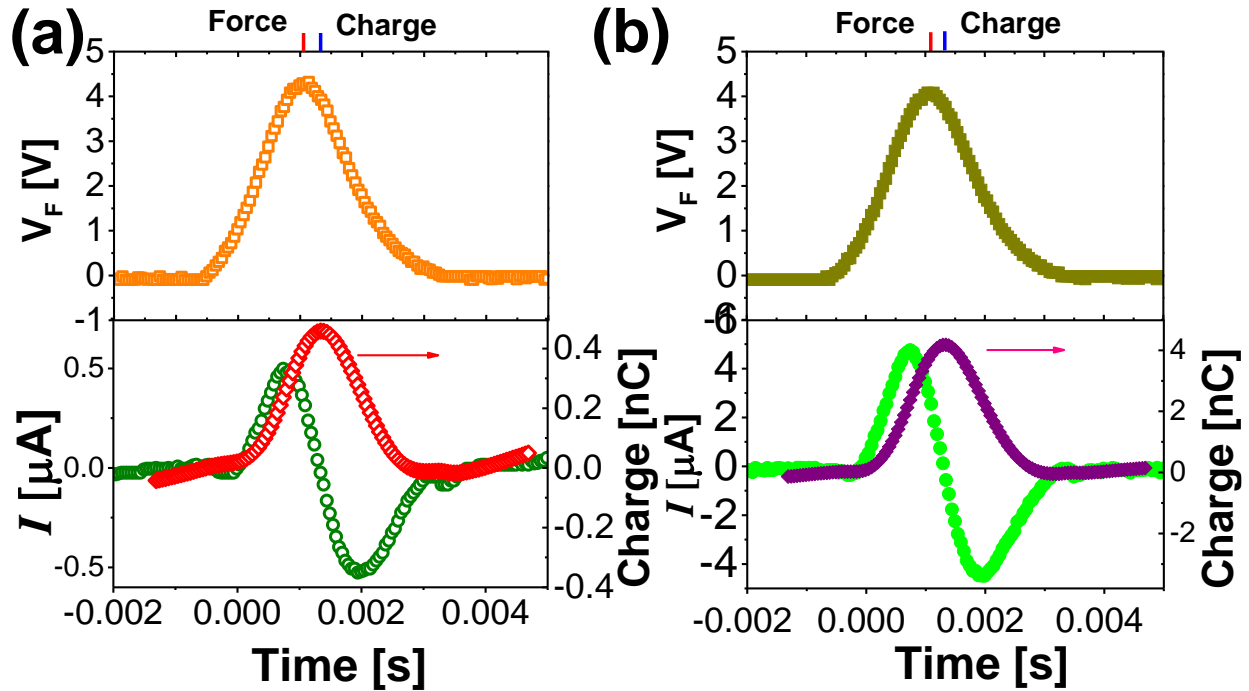


Figure V. 20 Representative readout current and integrated charge yield in response to an equal dynamic force applying under different bias electric field of 10V/9 μm (a) and 90V/9 μm (b).

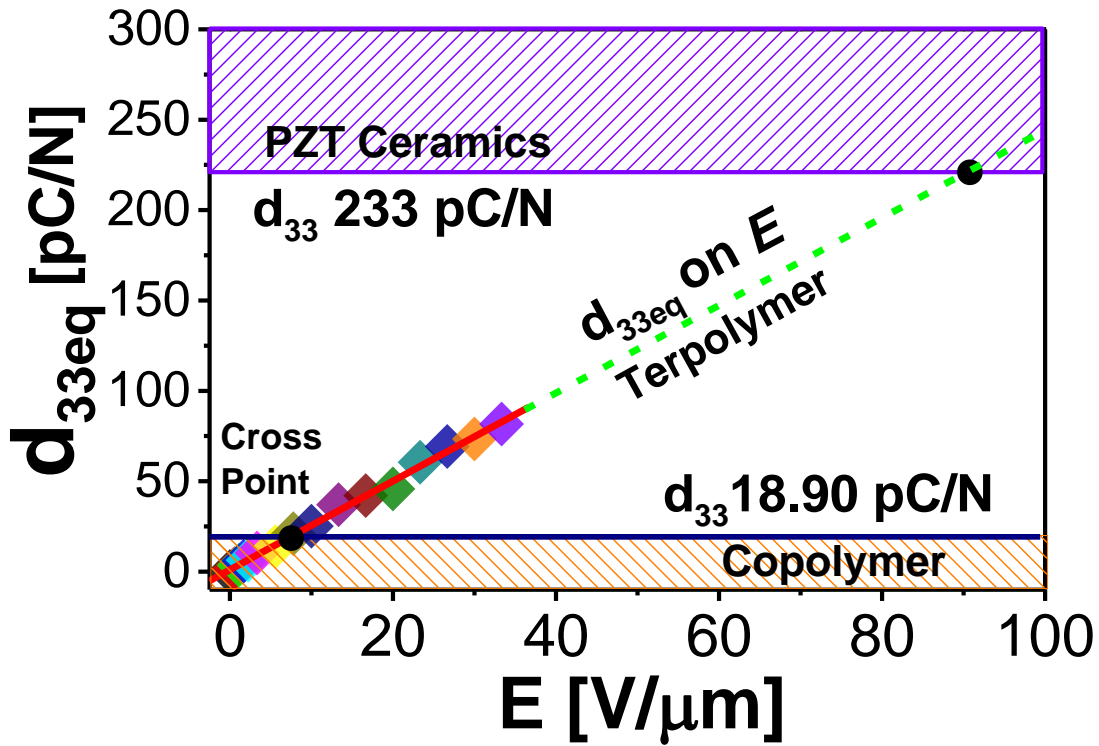


Figure V. 21 Pseudo-piezoelectric coefficient d_{33eq} as a function of the bias electric field E . Dash line is the linear fit and horizontal solid line is assigned to the electrically independent of measured piezoelectric coefficient d_{33} of inkjet printed ferroelectric copolymer force sensors.

V Conclusions

Printed electromechanical devices based on terpolymers are an alternative approach en route to fabricate piezoelectric force sensor networks. In this current chapter, the ink jettable parameters were firstly adapted to the polymer solution ink physics. The inkjet printing protocol for the ferroelectric P(VDF-TrFE) copolymer and electrostrictive P(VDF-TrFE-CTFE) terpolymer were then optimized. A piezoelectric copolymer force sensor has to be poled prior to its calibration or its use as an impact force sensor application. A large remnant polarization P_r is obtained resulting in the excellent piezoelectric coefficient. Inversely, a force sensor device made with an electrostrictive terpolymer do not exhibits any remnant polarization. In this regard, an indispensable electric field bias is compulsory. It is remarkable that for a given electromechanical performance the bias electric field for an electrostrictive terpolymer is much lower than the corresponding poling electric field for a copolymer. It is also observed that properties equivalent to the corresponding ferroelectric copolymer can be obtained for a bias as low as $7.5\text{V}/\mu\text{m}$.

These results show definitely the feasibility of low-cost inkjet printed terpolymer electromechanical devices with performances comparable to the ferroelectric copolymer once at the expense of only a fairly low electric field bias. These findings are rather promising for the moment, although future work goes to the all printed and multi-stack structured electronic devices with the aim at the enhanced mechanical energy density.

References

1. Schwizer, J., M. Mayer, and O. Brand, *Force sensors for microelectronic packaging applications*. 2006: Springer Science & Business Media.
2. Kim, K., et al., *Nanonewton force-controlled manipulation of biological cells using a monolithic MEMS microgripper with two-axis force feedback*. Journal of Micromechanics and Microengineering, 2008. **18**(5): p. 055013.
3. Crocker, M.J., *Handbook of acoustics*. 1998: John Wiley & Sons.
4. Merril, G.L., et al., *Apparatus for controlling force for manipulation of medical instruments*. 16 Nov. 2004, U.S. Patent
5. Subramanian, V., et al. *Printed electronics for low-cost electronic systems: Technology status and application development*. in *Solid-State Circuits Conference, 2008. ESSCIRC 2008. 34th European*. 2008. IEEE.
6. Khan, S., L. Lorenzelli, and R.S. Dahiya, *Technologies for printing sensors and electronics over large flexible substrates: a review*. IEEE Sensors Journal, 2015. **15**(6): p. 3164-3185.
7. Teichler, A., J. Perelaer, and U.S. Schubert, *Inkjet printing of organic electronics—comparison of deposition techniques and state-of-the-art developments*. Journal of Materials Chemistry C, 2013. **1**(10): p. 1910-1925.
8. Singh, M., et al., *Inkjet printing—process and its applications*. Advanced materials, 2010. **22**(6): p. 673-685.
9. de Gans, B.J., P.C. Duineveld, and U.S. Schubert, *Inkjet printing of polymers: state of the art and future developments*. Advanced materials, 2004. **16**(3): p. 203-213.
10. De Gans, B.-J. and U.S. Schubert, *Inkjet printing of well-defined polymer dots and arrays*. Langmuir, 2004. **20**(18): p. 7789-7793.
11. *IEEE Standard on Piezoelectricity*. , in *ANSI/IEEE Std 1988*. p. 176-1987.
12. Kawai, H., *The piezoelectricity of poly (vinylidene fluoride)*. Japanese Journal of Applied Physics, 1969. **8**(7): p. 975.
13. Nalwa, H.S., *Ferroelectric polymers: chemistry: physics, and applications*. 1995: CRC Press.
14. Zhang, Q., V. Bharti, and X. Zhao, *Giant electrostriction and relaxor ferroelectric behavior in electron-irradiated poly (vinylidene fluoride-trifluoroethylene) copolymer*. Science, 1998. **280**(5372): p. 2101-2104.
15. Xia, F., et al., *High electromechanical responses in a poly (vinylidene fluoride–trifluoroethylene–chlorofluoroethylene) terpolymer*. Advanced Materials, 2002. **14**(21): p. 1574-1577.
16. Liu, Y., et al., *Investigation of electrostrictive polymers for energy harvesting*. iee transactions on ultrasonics, ferroelectrics, and frequency control, 2005. **52**(12): p. 2411-2417.
17. Ren, K., et al., *An active energy harvesting scheme with an electroactive polymer*. Applied physics letters, 2007. **91**(13): p. 132910.

18. Cottinet, P.-J., et al., *Investigation of electrostrictive polymer efficiency for mechanical energy harvesting*. IEEE transactions on ultrasonics, ferroelectrics, and frequency control, 2011. **58**(9): p. 1842-1851.
19. Cottinet, P.-J., et al., *Analysis of AC-DC conversion for energy harvesting using an electrostrictive polymer P (VDF-TrFE-CFE)*. IEEE transactions on ultrasonics, ferroelectrics, and frequency control, 2011. **58**(1): p. 30-42.
20. Guyomar, D., et al., *Electrostrictive energy conversion in polyurethane nanocomposites*. Journal of Applied Physics, 2009. **106**(1): p. 014910.
21. Yin, X., et al., *Mechanical energy harvesting via a plasticizer-modified electrostrictive polymer*. Applied Physics Letters, 2016. **108**(4): p. 042901.
22. Ganet, F., et al., *Haptic feedback using an all-organic electroactive polymer composite*. Sensors and Actuators B: Chemical, 2015. **220**: p. 1120-1130.
23. <http://www.dupont.com/content/dam/dupont/products-and-services/membranes-and-films/polyimide-films/documents/DEC-Kapton-HN-datasheet.pdf>.
24. http://www.fujifilmusa.com/products/industrial_inkjet_printheads/print-products/printheads/general-purpose/sm-128-aa/index.html.
25. de Gans, B.J., et al., *Ink - jet Printing Polymers and Polymer Libraries Using Micropipettes*. Macromolecular Rapid Communications, 2004. **25**(1): p. 292-296.
26. Bhavanasi, V., D.Y. Kusuma, and P.S. Lee, *Polarization Orientation, Piezoelectricity, and Energy Harvesting Performance of Ferroelectric PVDF - TrFE Nanotubes Synthesized by Nanoconfinement*. Advanced Energy Materials, 2014. **4**(16).
27. Li, J. and F. Yan, *Solution-Processable Low-Voltage and Flexible Floating-Gate Memories Based on an n-Type Polymer Semiconductor and High-k Polymer Gate Dielectrics*. ACS applied materials & interfaces, 2014. **6**(15): p. 12815-12820.
28. He, F., et al., *Preparation and characterization of porous poly (vinylidene fluoride-trifluoroethylene) copolymer membranes via electrospinning and further hot pressing*. Polymer Testing, 2011. **30**(4): p. 436-441.
29. Chen, Y., et al., *Solution - Processed Highly Efficient Alternating Current - Driven Field - Induced Polymer Electroluminescent Devices Employing High - k Relaxor Ferroelectric Polymer Dielectric*. Advanced Functional Materials, 2014. **24**(11): p. 1501-1508.
30. Yeow, M., Y. Liu, and K. Li, *Morphological study of poly (vinylidene fluoride) asymmetric membranes: effects of the solvent, additive, and dope temperature*. Journal of Applied Polymer Science, 2004. **92**(3): p. 1782-1789.
31. Cathey, C.A. and G.G. Fuller, *The optical and mechanical response of flexible polymer solutions to extensional flow*. Journal of non-newtonian fluid mechanics, 1990. **34**(1): p. 63-88.
32. Somani, S., E.S. Shaqfeh, and J.R. Prakash, *Effect of Solvent Quality on the Coil- Stretch Transition*. Macromolecules, 2010. **43**(24): p. 10679-10691.

33. Specification, S.-A.P., *SM-128 AA Product Specification*,
<http://www.fujifilmusa.com/support/ServiceSupportProduct.do?prodcart=879638>.
34. *Methyl Ethyl Ketone Solvent Properties*.
<http://www.sigmaaldrich.com/catalog/substance/methylethylketone72117893311?lang=fr®ion=FR>.
35. *Triethyl phosphate solvent data sheet*.
<http://www.sigmaaldrich.com/catalog/product/aldrich/538728?lang=fr®ion=FR>.
36. 16, A.D.-. *Standard Test Method for Apparent Viscosity of Plastics and Organosols at Low Shear Rates*. 1995.
37. Dong, H., W.W. Carr, and J.F. Morris, *An experimental study of drop-on-demand drop formation*. *Physics of Fluids* (1994-present), 2006. **18**(7): p. 072102.
38. Fromm, J., *Numerical calculation of the fluid dynamics of drop-on-demand jets*. IBM Journal of Research and Development, 1984. **28**(3): p. 322-333.
39. Jang, D., D. Kim, and J. Moon, *Influence of fluid physical properties on ink-jet printability*. *Langmuir*, 2009. **25**(5): p. 2629-2635.
40. Migler, K.B., *String formation in sheared polymer blends: Coalescence, breakup, and finite size effects*. *Physical review letters*, 2001. **86**(6): p. 1023.
41. Derby, B., *Inkjet printing of functional and structural materials: fluid property requirements, feature stability, and resolution*. *Annual Review of Materials Research*, 2010. **40**: p. 395-414.
42. McIlroy, C., O. Harlen, and N. Morrison, *Modelling the jetting of dilute polymer solutions in drop-on-demand inkjet printing*. *Journal of Non-Newtonian Fluid Mechanics*, 2013. **201**: p. 17-28.
43. Christanti, Y. and L.M. Walker, *Surface tension driven jet break up of strain-hardening polymer solutions*. *Journal of Non-Newtonian Fluid Mechanics*, 2001. **100**(1): p. 9-26.
44. Nallan, H.C., et al., *Systematic Design of Jettable Nanoparticle-Based Inkjet Inks: Rheology, Acoustics, and Jetability*. *Langmuir*, 2014. **30**(44): p. 13470-13477.
45. Tai, J., et al. *Control of droplet formation in inkjet printing using Ohnesorge number category: materials and processes*. in *Electronics Packaging Technology Conference, 2008. EPTC 2008. 10th*. 2008. IEEE.
46. Derby, B. and N. Reis, *Inkjet printing of highly loaded particulate suspensions*. *Mrs Bulletin*, 2003. **28**(11): p. 815-818.
47. Meixner, R.M., et al., *Characterization of polymer inks for drop-on-demand printing systems*. *Microsystem technologies*, 2008. **14**(8): p. 1137-1142.
48. Tai, Y.-L. and Z.-G. Yang, *Flexible, Transparent, Thickness-Controllable SWCNT/PEDOT: PSS Hybrid Films Based on Coffee-Ring Lithography for Functional Noncontact Sensing Device*. *Langmuir*, 2015. **31**(48): p. 13257-13264.
49. Wong, T.-S., et al., *Nanochromatography driven by the coffee ring effect*. *Analytical chemistry*, 2011. **83**(6): p. 1871-1873.

50. Choi, S., et al., *Coffee-ring effect-based three dimensional patterning of micro/nanoparticle assembly with a single droplet*. Langmuir, 2010. **26**(14): p. 11690-11698.
51. Zhang, Z., et al., *Controlled inkjetting of a conductive pattern of silver nanoparticles based on the coffee - ring effect*. Advanced Materials, 2013. **25**(46): p. 6714-6718.
52. Tekin, E., et al., *Inkjet printing of luminescent CdTe nanocrystal-polymer composites*. Advanced Functional Materials, 2007. **17**(1): p. 23-28.
53. Rudawska, A. and E. Jacniacka, *Analysis for determining surface free energy uncertainty by the Owen-Wendt method*. International Journal of Adhesion and Adhesives, 2009. **29**(4): p. 451-457.
54. Still, T., P.J. Yunker, and A.G. Yodh, *Surfactant-induced Marangoni eddies alter the coffee-rings of evaporating colloidal drops*. Langmuir, 2012. **28**(11): p. 4984-4988.
55. Dua, V., et al., *All - organic vapor sensor using inkjet - printed reduced graphene oxide*. Angewandte Chemie International Edition, 2010. **49**(12): p. 2154-2157.
56. Valetton, J.J., et al., *Room temperature preparation of conductive silver features using spin-coating and inkjet printing*. Journal of Materials Chemistry, 2010. **20**(3): p. 543-546.
57. Lim, J.A., et al., *Self - Organization of Ink - jet - Printed Triisopropylsilylethynyl Pentacene via Evaporation - Induced Flows in a Drying Droplet*. Advanced functional materials, 2008. **18**(2): p. 229-234.
58. Park, J. and J. Moon, *Control of colloidal particle deposit patterns within picoliter droplets ejected by ink-jet printing*. Langmuir, 2006. **22**(8): p. 3506-3513.
59. Robin, M., et al., *Epoxy based ink as versatile material for inkjet-printed devices*. ACS applied materials & interfaces, 2015. **7**(39): p. 21975-21984.
60. Kim, D., et al., *Direct writing of silver conductive patterns: Improvement of film morphology and conductance by controlling solvent compositions*. Applied Physics Letters, 2006. **89**(26): p. 264101.
61. Wang, L., et al., *Inkjet printed colloidal photonic crystal microdot with fast response induced by hydrophobic transition of poly (N-isopropyl acrylamide)*. Journal of Materials Chemistry, 2012. **22**(40): p. 21405-21411.
62. Soltman, D. and V. Subramanian, *Inkjet-printed line morphologies and temperature control of the coffee ring effect*. Langmuir, 2008. **24**(5): p. 2224-2231.
63. Zirkel, M., et al., *An All - Printed Ferroelectric Active Matrix Sensor Network Based on Only Five Functional Materials Forming a Touchless Control Interface*. Advanced Materials, 2011. **23**(18): p. 2069-2074.
64. Khan, S., et al., *Flexible tactile sensors using screen-printed P (VDF-TrFE) and MWCNT/PDMS composites*. IEEE Sensors Journal, 2015. **15**(6): p. 3146-3155.
65. Yin, X., et al., *Enhanced Electromechanical Performances in Plasticizer Modified Electrostrictive Polymers*. European Polymer Journal, 2016.

66. Le, M.Q., et al., *All-organic electrostrictive polymer composites with low driving electrical voltages for micro-fluidic pump applications*. Scientific reports, 2015. **5**.
67. Ganet, F., et al., *Development of a smart guide wire using an electrostrictive polymer: option for steerable orientation and force feedback*. Scientific reports, 2015. **5**.
68. Garrett, J., et al., *Electrostrictive behavior of poly (vinylidene fluoride-trifluoroethylene-chlorotrifluoroethylene)*. Applied physics letters, 2003. **83**(6): p. 1190-1192.
69. Sperling, L.H., *Introduction to physical polymer science*. 2005: John Wiley & Sons.
70. Oliveira, F., et al., *Process influences on the structure, piezoelectric, and gas - barrier properties of PVDF - TrFE copolymer*. Journal of Polymer Science Part B: Polymer Physics, 2014. **52**(7): p. 496-506.
71. Lee, Y.-S., G. Collins, and T.L. Arinzeh, *Neurite extension of primary neurons on electrospun piezoelectric scaffolds*. Acta biomaterialia, 2011. **7**(11): p. 3877-3886.
72. Huang, C. and Q. Zhang. *High-dielectric-constant polymers as high-energy-density (HED) field effect actuator and capacitor materials*. in *Smart Structures and Materials*. 2004. International Society for Optics and Photonics.
73. Laurenti, M., et al., *Development of a flexible lead-free piezoelectric transducer for health monitoring in the space environment*. Micromachines, 2015. **6**(11): p. 1729-1744.
74. Dahiya, R.S., et al. *Deposition, processing and characterization of P (VDF-TrFE) thin films for sensing applications*. in *Sensors, 2008 IEEE*. 2008. IEEE.
75. Chen, H.D., et al., *Fabrication and electrical properties of lead zirconate titanate thick films*. Journal of the American Ceramic Society, 1996. **79**(8): p. 2189-2192.
76. Muralt, P., *PZT thin films for microsensors and actuators: Where do we stand?* IEEE transactions on ultrasonics, ferroelectrics, and frequency control, 2000. **47**(4): p. 903-915.
77. *Powder indicative Price List June 2016*, <http://www.piezotech.fr/fr/2-products-piezoelectric-polymers/>.

Chapter VI

General Conclusions and Perspectives

VI. 1 Conclusions

Ferroelectric materials have been paid emerging attraction due to their capability of converting external electric stimulus into other mainly available energy forms such as mechanical force, heat (electrocaloric effect), and magnetoelectric fields and vice versa. In particular, ferroelectric polymers have attracted great interests thanks to their flexibility, light weight, relatively low mechanical strength, ease of processability into large-area films, and the ability to be molded into a desirable dimension. Amongst those ferroelectric polymers, PVDF and the piezo-copolymers exhibit a high dielectric constant, a low dissipation factor, as well as rapid and excellent electromechanical response. Recently, e-beam irradiated poly(vinylidene fluoride-trifluoroethylene), P(VDF-TrFE) copolymer unimorph demonstrated rather high tip displacement[10], providing novel concepts of designing materials with maximal electric field-induced strain of 7% in thickness mode and high elastic free mechanical energy density E_{μ} . Inspiring from this method, chemical defects were introduced into molecular backbone by copolymerization of bulk-like ternary CTFE monomer and as a consequence, sub-micro crystal size broke into sporadic nano-sized crystallites. Due to presence of CTFE, β -form ferroelectric domains with all-Trans (T_m , $m>3$) conformation in copolymers transformed into non-polar α -form paraelectric crystallites and less-ordered γ ($T_3G^+T_3G^-$) ferroelectric phase. Hence interaction between neighboring crystallites was weakened. And spontaneous polarizations of the sporadic nano-sized crystallites in terpolymer were relatively independent and the dipole moment of each nano-sized crystallites were randomly distributed. Terpolymer exhibited diffusion phase transition frequently when subjected to the external electric stimulus. In this case, Terpolymers are ferroelectric with relaxor behaviors. Such diffusion ferro-paraelectric phase transition was responsible for the outstanding electrostrictive behavior.

In fact, two terms, Young's modulus (Y) and dielectric constant at working condition (ϵ_r) as revealed are the crucial essences governing the performance of the electromechanical properties in ferroelectric and relaxor PVDF-based polymers. In an attempt to enhancement the electromechanical behavior, the roadmap to manufacture the high performance terpolymer film were widely developed, such as spin-coating, cast, hot-pressing and stretching, etc. However, there still lacks the correlation of electromechanical properties with Y and ϵ_r of the terpolymer depending on the material processing. The current studies focused on the properties linked to the microstructure of terpolymer via processing and the molecular mobility in wide range of frequency and temperature were investigated by broadband dielectric spectroscopy technique. Besides, tremendous enhancement of ϵ_r and electrostrictive response were explained from molecule dynamics aspects. Finally, the electromechanical behavior were evaluated via the inkjet printed copolymer and terpolymer force sensors. The main conclusions of this thesis were briefly summarized:

1 Chapter II tends to provide as much as information on electromechanical properties of relaxor ferroelectric P(VDF-TrFE-CTFE) terpolymers. Its behaviors, strongly depending upon the terpolymer annealing effect, were systematically investigated in terms of thermal transition, dielectric property, electric breakdown strength and electrostriction response. Firstly in DSC thermograms, two stepwise variations were observed in both Curie transition and melting regions for isochronally annealed terpolymer from pristine film to fully crystallized film for 2h. Equivalently annealing temperature below its Curie transition point T_c for pristine terpolymer increased its T_c and ferroelectric crystal phase in crystal lamellae while decreasing T_c and Curie transition enthalpy observed for terpolymer annealed in hexagonal phase ($T_c < 80\text{ °C} \leq T_a$) were strongly attributed to less δ ferroelectric phase were involved in crystal lamellae. No distinct variation both in two values were seen for terpolymer annealed at temperature above 80 °C because of thermodynamic equilibrium. Melting regions inversely quite differed. Crystallinity fraction increased monotonically upon increase of annealing temperature. It is not the case for melting temperature for corresponding terpolymers where saw a two stepwise decrease with cross point at 90 °C . Annealing above 90 °C caused loose crystal stacks thickening and narrow distribution of crystal size. This was evidenced by a remarkably decreasing in FWHM values from ca. 15 °C to around 8 °C . Surface crystal morphology and microstructure were patterned by AFM techniques. Worm-like crystal nanodomains were observed in terpolymers. Coarse and loose bumpy-like topographic morphology observed for pristine was due to heterogeneous behavior and flat-on dominated orientated crystal lamellae. Regular needle-like nanocrystallites and distinct interfacial boundary suggested the edge-on crystal orientation lamellae in intermediate terpolymers induced by isothermal crystallization.

Two dielectric anomalies as function of temperature were strongly associated with two typical transitions where the peak at low temperature was ascribed to glass transition region in amorphous phase while the higher should be attributed to the Curie transition in crystal lamellae. Both regimes gave partial contribution to the dielectric permittivity at room temperature. An increase intensity of dielectric peak located at glass transition region was strongly due to enhancement of interphase where molecular chain more or less oriented. Electric breakdown strength E_b was strongly depended upon the dielectric and mechanical behaviors. Higher degree of crystallinity was in favor of high E_b values, for instance, maximal $340.4 \pm 38\text{ MV/m}$ for 45.3% as largest crystallinity content. Conductivity decreasing in higher crystal content films and charge carrier ion scattered by oriented interphase rationalized the high electric strength values. Finally, electromechanical response was evaluated by electrostrictive properties via an unimorph cantilever beam bend measurement. Although tip displacement D and transverse strain S_{31} for each annealed terpolymer followed quadratic-type with applied electric field, D maximized at 39.3% crystal content and S_{31} showed an exponential decay with increase of degree of

crystallinity. In order to generate out-performed electrostrictive behavior, relative dielectric constant ϵ' and elastic Young's modulus ratio should be seriously considered. The investigation were finalized by comparison of elastic free mechanical energy density E_μ . The decreasing E_μ values versus increment of crystal content were a result of electric permittivity ϵ' and Young's modulus combined factor. That is to say, one needs to compromise these two factors when the electroactive polymers were designed to practical implementation.

2 The purpose of **Chapter III** was focusing on frequency and temperature dependence of the dielectric relaxation behavior of semi-crystalline P(VDF-TrFE-CTFE) terpolymers. In order to evaluate the relaxation map, terpolymers containing different fractions of crystallinity were prepared by an isothermal crystallization process. Firstly, a slowing down of the segmental relaxation rate was found in the terpolymer with the highest crystallinity. The size of the cooperative rearranging region in the amorphous phase declined. The decrease of the strength index D indicated that the crystallized terpolymer had become more fragile with higher degree of crystallinity. However, a large interphase region led to an increase in dielectric strength as opposed to the non-ferroelectric polymer. Such a phenomenon was ascribed to the enhanced fraction of the interphase which was more or less well-orientated.

The Curie relaxation was accelerated by increasing the amounts of crystalline lamellae, which had a great influence on the segmental relaxation. Secondly, sub-glass β relaxation processes were also constrained and followed an Arrhenius-type mode. Considering the chemical composition of terpolymers, it is reasonable to assume that the β relaxation processes correlated with the segmental relaxation. Finally, the mobility of the space charge at high temperature was analyzed by an electric modulus method. A VFT-type mode revealed the DC conductivity vs. the relaxation at several temperatures, and suggested that segmental dynamics in the amorphous mode were responsible for the motion of the space charge carrier ions. A dielectric relaxation map provided a full picture of the dielectric behavior based on frequency and temperature. The results gave us an idea of the implementation of a point of view for the electromechanical system. The correlation of these behaviors with electromechanical properties is currently being studied.

3 Several folds improvements in the dielectric behavior and electromechanical response of the all-organic polymer blends were achieved by simply adding commonly used DEHP phalate plasticizer into pure terpolymer matrix reported in our previous study. Around maximal 60 times increase in permittivity on expense of half losses of the Young's modulus, mechanical energy density of plasticized terpolymer blends demonstrated 20 times higher over the pristine terpolymer. In current **Chapter IV**, an interpretation of this fundamental trend is given on a molecular level by means of broadband dielectric spectroscopy technique. The main conclusions about this chapter are summarized as listed here:

First of all, AFM patterns were employed to evaluate the morphology structure and miscibility of the DEHP molecules load terpolymer blends. The regular surface morphology manifested the absence of phase separation of the excellent miscibility of DEHP molecules in terpolymer. The bumpy-like crystal domains were however loosely packed, the size of which were likely to be somewhat intensified via addition of the plasticizer DEHP molecules, implying much inhomogeneity of size distribution over the pristine terpolymer matrix. And this was also evident by the DSC measurement technique which manifested that the addition of DEHP tends to suppress the growth of crystal phase and eventually leads to the smaller, but this is not the case for the crystallinity while undergoing a slightly increasing fashion. Due to the presence of DEHP, the melting points of plasticized were dropped by the maximal 6 °C which also affected the non-isothermal crystallization during the cooling. The crystallization favored a retarded process eventually.

Influence of the plasticizer on molecule mobility covering wide range of temperature was monitored by BDS technique by which the single segmental structure dielectric relaxation loss was first revealed. This manifested the good miscible behavior, due most probably to the compatible solubility parameters between both. The presence of the DEHP plasticizer expanded the specific free volume of the molecular chain and accelerated the relaxation rate of the structural process, enhanced dynamic heterogeneity near the glass transition region as well, as opposed to the results found in **Chapter III**; the estimated glass transition $T_{g,die}$ slumped down from 246.7 K to 229 K and closely followed the Fox mode against the DEHP content; an increased strength indices implied the less fragility of the modified polymer blends. β -secondary relaxation process was also identified and activated by almost 25% high in glassy state.

Furthermore, the ions conductivity of plasticized blend system was improved by around one decade higher. With the help of dielectric modulus spectra, the dynamic behavior of the translational charge carrier motions were carefully characterized at low frequency and high temperature. The curvature type was fitted to the motion behavior of ions charge carrier and fitting; and the ions conductivity behavior for plasticized blend was governed by structural relaxation in amorphous phase.

Finally, interfacial polarization was verified as a great dielectric strength mode which is usually assigned to the predominant relaxation process at low frequency at high temperature. After removal of the conductivity part, although the MWS relaxation strength remained unaltered for the pure and plasticized blends, the relaxation had the peak drifted towards the high frequency by almost maximal one decade for terpolymers with 10% and 15% DEHP plasticizer content. Such results account for the several orders of magnitude enhancement of the dielectric properties in experimental measurement. On top of that, plasticizing effects for constrained amorphous phase were also identified.

4 In **Chapter V**, inkjet printed electromechanical devices based on terpolymers are reported as an alternative way to fabricate piezoelectric and electrostrictive force sensor networks. In this current chapter, the ink jettable parameters were firstly adapted to the polymer solution ink physics. The inkjet printing protocol for ferroelectric P(VDF-TrFE) copolymer and electrostrictive P(VDF-TrFE-CTFE) terpolymer were then optimized. A piezoelectric copolymer force sensor has to be poled prior to its calibration or its use as an impact force sensor application. A large remnant polarization P_r is obtained resulting in the excellent piezoelectric coefficient. Inversely, a force sensor device made with an electrostrictive terpolymer do not exhibits any remnant polarization. In this regard, an indispensable electric field bias is compulsory. It is remarkable that for a given electromechanical performance the bias electric field for an electrostrictive terpolymer is much lower than the corresponding poling electric field for a copolymer. It is also observed that properties equivalent to the corresponding ferroelectric copolymer can be obtained for a bias as low as $7.5\text{V}/\mu\text{m}$.

These results show definitely the feasibility of low-cost inkjet printed terpolymer electromechanical devices with performances comparable to the ferroelectric copolymer once at the expense of only a fairly low electric field bias. These findings are rather promising for the moment, although future work goes to the all printed and multi-stack structured electronic devices with the aim at the enhanced mechanical energy density.

VI. 2 Future Work and Perspectives

Based on the results in this current thesis, the concepts of a possibly high dielectric constant and moderate reduced Young's modulus are adopted to enhance the electromechanical coupling factor and the elastic energy density for relaxor ferroelectric terpolymers. Here we only investigated these two factors linked to the microstructure via film solution-casting method by which a bulk terpolymer is thus obtained. The pure but nanoscale thin layers exhibit well-recognized differences of microstructure, as well as ferroelectric and dielectric behaviors because of existence of the nanoconfinement effect in PVDF-based copolymer. Thus it is worthy to investigate the electromechanical coupling performance of nanoscale thin terpolymer films. To realize this strategy, spin-coating method was recommended to elaborate the nanoscale thin films. And its dielectric relaxation and relaxor behavior are to be characterized over wide range of frequency of a low bias electric voltage and temperature in order to estimate properties from microstructure origins in nanoscale thin layer.

Secondly, DEHP is manifested as a good plasticizer for terpolymer matrix, allowing to strongly improve dielectric constant, compress the mechanical strength and thus enhance the electromechanical behavior. We have already explained the origins of this phenomenon and ascribed to the modification of free volume and molecular dynamics, mostly due to the interfacial polarization. Nevertheless, plasticizer DEHP is declared to be toxic and regarded as the carcinogenic health threat. And small DEHP molecules are facile to leach from the plasticized polymer matrix and thus are limited to be employed in low risk posed applications. To reach the environmental-friendly requirements, proper plasticizer with high plasticizing effect and low leaching from the matrix is encouraged to be investigated for terpolymer matrix. Alternatively, approaches to modify the electromechanical properties are also planned.

Metallized force sensors with sensing polymer layers were successfully fabricated via inkjet printing technology. And the results show the terpolymer electromechanical devices with performances comparable to the ferroelectric copolymer at the expense of only a low electric field bias. However, the deficiencies were faced and possible measures are forcibly taken to develop the inkjet printing technique and enhance the performance of products in the near future: 1, the challenge is the discrete fabrication due to the metallization of gold electrodes and this could increase the step complexity and high cost final products. To avoid metallization and overcome discrete printing, printable ink materials such as water-based nanoparticle silver inks and organic PEDOT:PSS inks are to be employed as electrode materials; 2, solvent based polymer solution inks are volatile and less eco-friendly. Water-based electroactive polymer inks will be developed to fulfill the rheological requirement of the inkjet printing technology; 3, polymer sensing layers' structure can be optimized to obtain the best electromechanical properties with less polymer material supply, such as multi-stacked sensing layer device.

Appendix:

Surface Energy Measurement

Owens-Wendt-Kaelble Method

Owens-Wendt-Kaelble method consists in determining the dispersive σ_{solid}^D and polar σ_{solid}^P components of the surface free energy σ_{solid}^T of a solid materials on the basis of the Betholt hypothesis. This hypothesis described that the interaction between both of the two substances was equal to the geometric mean of intermolecular interactions of each substance. The surface free energy of a solid materials usually relates to the contact angel of a liquid probe with expression:

$$\sigma_{liquid}^T(1+\cos \theta)=2\sqrt{\sigma_{solid}^D\sigma_{liquid}^D}+\sqrt{\sigma_{solid}^P\sigma_{liquid}^P} \quad A. 1$$

Where σ_{liquid}^T is the total surface free energy of the probe liquid; θ is the contact angel which varies upon the liquid probe; σ_{liquid}^D is the dispersive component while σ_{liquid}^P is the polar part. The polar component is defined as the sum of the polar, hydrogen, inductive and acid-base interactions.

To determine the surface free energy of the solid surface, a bipolar liquid, commonly used water and polar probe liquid are used whose dispersive and polar components are known. The roots of the constitutive equations A.1 can be obtained by the expressions:

$$\sqrt{\sigma_s^D} = \frac{\sigma_d(\cos \theta + 1) - \sqrt{(\sigma_d^P/\sigma_w^P)\sigma_w(\cos \theta + 1)}}{2\left(\sqrt{\sigma_d^D} - \sqrt{\sigma_d^P(\sigma_w^P/\sigma_w^D)}\right)} \quad A. 2$$

$$\sqrt{\sigma_s^P} = \frac{\sigma_w(\cos \theta + 1) - 2\sqrt{\sigma_s^D\sigma_w^D}}{2\sqrt{\sigma_w^P}} \quad A. 3$$

Where σ_s^D and σ_s^P are dispersive and polar components of the surface free energy of a solid material. For the sake of simple measurement, the second liquid probe has only dispersive

component and equation A.2 can be simplified as $\sqrt{\sigma_s^D} = \frac{\sigma_d(\cos\theta+1)}{2\sqrt{\sigma_d^D}}$. For that reason,

diiodomethane is used as a polar liquid probe which has a σ_d^D of 50.8 mN/m of total surface energy of 50.8 mN/m.

The water and probe liquid diiodomethane were dropped onto the substrate to measure and 10 replica measurement of water and diiodomethane liquid contact angel were recorded for each substrate. And surface free energy were then calculated in Table A.1.

Table A.1 Contact angel of water and diiodomethane probe on various substrate and induced surface free energy.

Supports	^a Contact angel (°)		Surface Energy Components	
	^b Water	^c Diiodomethane	Dispersive (mN m ⁻¹)	Polar (mN m ⁻¹)
PI substrate	51.13	32.20	43.29	15.95
Treated PI	32.24	22.35	47.06	24.33
Au electrode layer	62.35	25.61	45.93	9.19
Printed copolymer	80.66	66.04	35.23	4.17
Printed terpolymer	72.33	63.30	54.75	3.26

Note: a, average values; b, 21.8 mN m⁻¹ dispersive and 51 mN m⁻¹ polar components of the surface free energy of water; c, 50.8 mN m⁻¹ dispersive components of diiodomethane probe.

List of Figures

Figure I. 1 Schematic of a force system comprising sensing component array and signal processing circuit for readout.	7
Figure I. 2 Schematic of piezoresistive force sensor based on a strain gauge, showing the alloy wires bond to the plastic backing. Force normally was applied in aligned with longitudinal direction (a). Quarter wheatstone bridge circuit for precisely measuring resistance of the strain	9
Figure I. 3 A schematic diagram of cantilever beam with strain gauge piezoresistor mounted. Force F was applied upon its free end perpendicular to beam in-plane. The range of force measured is associated with size and shape of cantilever for a given beam materials	10
Figure I. 4 Schematic of cantilever beam integrated with the piezoresistor. (a) Fabrication process of paper based piezoresistive cantilever force sensor using a screen printing technique. (b) A diagram of paper cantilever beam mounted with a silver metalized carbon piezoresistor. (c) Dimensions of printed cantilever force sensor array.	11
Figure I. 5 Scanning electronic microscopy (SEM) graphic of a four-axial piezoresistive force sensor tethered on flexible platform[19] (a). Intact 3D piezoresistive force sensor prototype where the strain gauge mounted onto the Ti-foil cantilever beam. The schematics also show two rotational degrees of freedom of the device for eliminating cross-talk [34].	12
Figure I. 6 Parallel-plate capacitor with insulator gap sandwiched by two conductive electrodes (a); gap between two electrodes was compressed by Δd due to an applying normal force F_{normal} (b); ΔSA surface area variation when a lateral force $F_{lateral}$ is applied to a plate capacitor (c).	14
Figure I. 7 (a) Diagram of capacitive force sensor structure and monolithically fabricated element with cross-sectional view [39]. (b) Simplified illustration of three-axial capacitive force sensor and the components in reality.	15
Figure I. 8 Schematics and microscopies of MEMS-based capacitive force sensors. (a) and (b) Microgripper with dual-axial force sensor using two orthogonal comb-like electrode capacitors; (c) photographic of developed microtweezer bearing the compliant rotatory structure and linear guiding flexure joint with two comb-like capacitive force sensors. Adapted from the illustration provided by literature [41, 42].	16
Figure I. 9 (a) Photographic of encapsulated PZT piezoelectric force sensing elements device wrapped on a cylindrical support. Square-like force sensor array was collectively integrated with silicon metal oxide semiconductor field effect transistor. (b) Photographics of representative application of the piezoelectric force sensor mounted on human wrist and neck for monitoring the transient blood pressure waves. (c) Schematic illustration in tilted overview of soft tissue biomechanic force sensor. (d) Schematics of force sensor system in leftmost graphic [48]; figure in middle showing the large area of lesion of human skin with (lower) or without (upper) a mounted biomechanical force sensor device; a small lesion spot mounted with or without a nanoribbon force sensor system [49].	18
Figure I. 10 Schematic (a), microscopy (b) and photographic (c) of tactile piezoelectric force sensor integrated with metal oxide semiconductor field effect transistor.	20
Figure I. 11 Schematics of typical flexographic printing (a) and gravure printing technologies (b). Gear-like ink transfer system was zoomed. Adapted from the illustration provided by the literature [61].	24

Figure I. 12 Schematic of a flatbed screen printing process. Inks poured on the upper side of stencil, beneath which was placed the substrate. The inks (red) were squeezed to pass through blanket mesh which carrier the pattern information. Adapted from the illustration provided by literature [61].....	25
Figure I. 13 Roadmapping of two main kinds of inkjet printing technologies.....	26
Figure I. 14 Process flow of continuous inkjet printing technique, using a piezoelectric crystal electromechanical actuator. Adapted from illustration provided by Brian Derby [69].	27
Figure I. 15 Two main kinds of transduction principle for drop-on-demand inkjet printing, thermal actuation (a) and piezoelectric actuation (b). Adapted from illustration provided by Khan [61].....	28
Figure I. 16 Schematic diagrams of the piezoelectric printhead, (a) the ink-filled reservoir chamber and piezoelectric element prior to the imaging signal applied; (b) piezoelectric buckling induced by electric information; (c) high fluid pressure in the chamber as the displacement piezoelectric element recovered; (d) droplet left the nozzle orifice. Adapted from illustration provided by Khan [61].	29
Figure I. 17 (a) Capillary number (Ca)-Weber number two dimension coordinated space of the printability hydrophobic solvents based nanoparticle ink solutions. The hatched area defines the jettable bounds and within the polygon each data point represents jettable inks. Schemes inside the hatched area demonstrate the tailored drop morphology whereas outside the hatched area the drop ejection cannot give printable drop formation. (b) Inappropriate jetting condition causes the inks only a small perturbation in the meniscus. (c) Relatively inviscid fluid presenting wavelike instability of ink pillar, giving rising to satellites droplets. [81].....	32
Figure I. 18 (a) Diagram illustration of the maximum spreading factor β versus time evolution τ . The increasing trend plot over the whole window corresponds to the drop impact scenario on the wettable substrate ($\beta \ll \beta_\infty$) while the remaining one represents the spreading factor changes with time elapsed in case of non-wettable substrate. The predominated phenomena for the spreading angle occur with time proceeding after the drop collision with substrate. (b) photographics in initial stage (0~10 ms) of the drop impacting on the ITO-coated glass substrate as time proceeds. Adapted from the illustration reported by Jung et al [83].	34
Figure I. 19 Scheme illustration of droplet wetted on the support in equilibrium state. Contact angle θ describes thermodynamic equilibrium between the three phases: the liquid phase (l), the solid phase (s), and the gas or vapor phase (g).	35
Figure I. 20 Schematic illustration of the DoD inkjet printing water-based PEDOT:PSS solution on PVDF-graft-PEG membrane (a). SEM image of the cross-section of the inkjet printed actuator based on the surface grafting polymerization treatment (b). Adapted from the illustration provided in the literature [95].	36
Figure I. 21 Schematics of the contact line and two driving flows along with most ubiquitous obtained patterns morphologies including coffee-ring. Yellow curvature arrow represents the outward capillary flow while red one is the inward marangoni flow.	37
Figure I. 22 Unit cell of (A) α , (B) δ , (C) γ , and (D) β forms of PVDF crystals viewed along the c-axes and schematic chain conformations for (E) TGTG' (α/δ), (F) TTTGTTTG' (γ), and (G) all-trans (β) rotational sequences. Red, cyan, and blue spheres represent F (fluorine), C (Carbon), and H (Hydrogen) atoms. The projections of dipole directions are indicated by green arrows. Graphics adapted from the illustration in the literature [104].	39
Figure I. 23 Schematic diagrams of the comparison of hysteresis loops and microscopic crystalline structures for ferroelectric (a and c) and relaxor ferroelectric terpolymers (b and d).....	40

Figure II. 1 Processing flow schematics of preparation of terpolymer solution, film coating application and isothermal crystallization process.....	54
Figure II. 2 A schematic representation of measurement setups for mechanical strength properties	56
Figure II. 3 (a) Schematic representations of cantilever beam precursor multi-view for bending measurement, (b) configuration of cantilever beam and bending measurement setups	57
Figure II. 4 Schematic illustration of aluminum scaffold attached with cantilever beam sample holder.....	58
Figure II. 5 DSC thermogram traces of respective as-casted terpolymer films at various isothermal annealing temperature: pristine as-casted film (R.T.) (Film A), 60 °C for 12h (Film B), 70 °C for 12h (Film C), 80°C for 2h (Film D), 90 °C for 2h (Film E), 100°C for 2h (Film F), 110°C for 2h (Film G), 120 °C for 2H (Film H). Fully crystallized terpolymer Film I, with annealed at 120°C for 12h was also shown in the Figure. Vertical dash line in figure left marks the melting peak of the pristine Film A and dots line in figure right denotes melting peak of Film F (100°C2H).....	60
Figure II. 6 Plots of the degree of crystallinity (a), ΔH_c enthalpy of Curie transition (b), Curie transition temperature (c) and plots of ratio of heat of fusion ΔH_m , i for respective annealed terpolymer to the fusion of enthalpy ΔH_m of fully crystallized Film I (d), temperature values of melting peaks (T_m) (e) and full width at high maximal values (FWHM) of melting peak regions (f) on DSC heating curves over the temperature ramp.....	62
Figure II. 7 The solution casting films annealed in the hexagonal phase. TC – A and T_m – A are the phase transition temperature and the melting temperature, respectively, of the original SC film.....	63
Figure II. 8 The DSC thermogram curves of the terpolymer annealed at 90 °C for various time duration for neat and 10h processing terpolymer.	65
Figure II. 9 DSC thermogram curves of isochronal annealed terpolymer films, the vertical dash line designated as melting temperature of original Film A and inset figure showed normalized melting peak regions, which saw a distinct disparity. Dot plots of degree of crystallinity χ_C (a), Curie transition enthalpy ΔH_c (b) and Curie transition temperature TC (c) as a function of annealing time period at 90 °C.....	65
Figure II. 10 Surface topography (phase mode) of the AFM patterns for the isothermal crystallized P(VDF-TrFE-CTFE) terpolymer representatives of the pristine P(VDF-TrFE-CTFE) Film A (A), intermediate annealed Film E (B), fully crystallized Film I (C) and a schematic representation of flat-on and edge-on crystal lamellae orientation to the substrate (D).	67
Figure II. 11 Isochronal real part (a) of permittivity (ϵ') and dielectric loss $\tan \delta$ (b) spectra at different temperature for the representative terpolymer Film G. Temperature dependence of real permittivity ϵ' of annealed terpolymer containing various crystallinity fraction at given frequency of 100 Hz were also plotted (c). The rectangles in figure a marked the two phase transitions against temperature at various frequency, black for glass transition and red for Curie transition.	69
Figure II. 12 Dielectric permittivity of P(VDF-TrFE-CTFE) terpolymers under various annealing condition as function of logarithmic frequency (a) and real permittivity at selected frequency (0.1Hz and 1k Hz) against degree of crystallinity χ_C (b).....	71
Figure II. 13 (a)Weibull distribution probability of the breakdown strength E_b for each annealed terpolymer film; (b)experimentally measured E_b as a function of degree of crystallinity in bar chart; half right circles were estimated electric breakdown strength values as a function of the degree of crystallinity.	74

Figure II. 14 Mechanical behavior of annealed P(VDF-TrFE-CTFE) terpolymers: strain-stress curves in a sinusoidal functional mode (a), degree of crystallinity dependence of Young's modulus for the annealed films (b). The dash line was the sigmoidal growth fitting to the Y values.	76
Figure II. 15 Displacement (a) and transverse stain (b) curves versus applied electric field for each annealed terpolymer representatives; vertical (dash) line marks the 20 MV/m electric field.	78
Figure II. 16 Electromechanical response obtained by cantilever beam unimorph, (a) tip displacement and (b) transverse strain bar charts upon the 20 MV/m electric field as a function of degree of crystallinity of each annealed polymer unimorph. Red solid line is the peak fit to the saddle shape distribution of the δ values and dash dot line is the exponential decay fit to the transverse strain values.....	79
Figure II. 17 (a) ϵ'/Y , simplified electrostrictive coefficient parameter plotted against degree of crystallinity; (b) free elastic electric energy density over the degree of crystallinity.	80
Figure III. 1 isothermal dielectric loss spectra for each as-casted polymer thin films in a temperature range from -70 °C to 100 °C in step of 5 °C interval. Lines are guides to the eyes.	96
Figure III. 2 Frequency and temperature dependence of the dielectric loss (a) and dielectric loss angle $\tan\delta$ (b) for the representative as-processed Film C with a crystalline fraction of 36.40%.	97
Figure III. 3 Isochronal dielectric loss spectra picked up from isothermal dielectric relaxation.....	98
Figure III. 4 (a) The dielectric loss fraction as a function of frequency for isothermally crystallized films at 248 K. The vertical line denotes the relaxation peak position (frequency) for pristine terpolymer films and the dashed curve marks the shift trend of the relaxation position for each processed material; (b) normalized dielectric loss spectra as a function of frequency for isothermally crystallized terpolymers at 248 K.	101
Figure III. 5 (a) Dielectric strength $\Delta\epsilon$ as a function of the degree of crystallinity for as-treated semi-crystalline terpolymers at 248K (open squares) and 268K (open circles); (b) the temperature dependence of the dielectric strength $\Delta\epsilon$ for as-prepared terpolymers. The solid and dashed lines are linearly fitted to the $\Delta\epsilon$ values at 248K and 268K, respectively.	103
Figure III. 6 A schematic diagram of crystal-rigid amorphous phase-mobile amorphous phase mode for PVDF-based polymer.	104
Figure III. 7 (a) Temperature dependence of all relaxation anomalies for as-treated semicrystalline terpolymers regarding the amount of crystallinity: filled symbols (for instance, $\blacksquare, \bullet, \blacktriangle$...) represent the Curie transition; open symbols ($\square, \circ, \triangle$...) denote the α relaxation regimes; half-filled symbols ($\blacksquare, \circ, \blacktriangle$...) correspond to sub-glass relaxation processes. (b) Highlighted Curie relaxation time τ_C and (c) secondary relaxation times versus the reciprocal of temperature.	106
Figure III. 8 Strength index $D = BT_0$ as a function of the degree of crystallinity for each processed terpolymer.	108
Figure III. 9 Imaginary part of dielectric modulus spectroscopies as function of frequency and temperature for each as-cast terpolymer film	112
Figure III. 10 (a) The isothermal real part of the conductivity versus the full frequency scale for temperatures ranging from 203K to 373K for the as-treated terpolymer Film F; (b) the imaginary part of the electric modulus demonstrating a the shift towards higher frequency for the representative Film F. The lines are guides to the eye.....	113
Figure III. 11 Temperature-dependence of the relaxation time upon crystallization evolution as obtained from M'' maxima. The lines correspond to VFT-type fitting curves.....	114

Figure IV. 1 (a) electric field-induced transverse strain for the pure and 10% DEHP modified terpolymers under 0.1 Hz sinusoidal signal controlled tensile mode; (b) elastic mechanical energy density for pure and 10% DEHP modified terpolymers as a function of external electric field. Adapted from the graphics from the literature [8]	125
Figure IV. 2 DSC thermogram traces of heating (a) and cooling ramp (b) for the pristine and various DEHP doped terpolymer blends. Solid vertical line and dashed vertical line denote the melting and melt-recrystallization peak of the neat terpolymer, respectively.	130
Figure IV. 3 Melt-recrystallization parameters upon DSC cooling as a function of mass fraction of DEHP plasticizer load, (a) the temperature (T_{c1}) of intensive melt-recrystallization peaks, (b) temperature (T_{c2}) of weak satellite peaks of melt-recrystallization, (c) overall crystallinity fraction (χ_{cc}) originating from the reheating ramp and (d) Curie transition (T_{cc}) upon first cooling.....	133
Figure IV. 4 Surface topography patterns (phase mode) of the isothermal crystallized neat terpolymer (A) and DEHP doped terpolymer blends, 5% (B), 10% (C) and 15% (D). Scale bar is marked in the profiles. The pattern of the neat sample undergoing melt-recrystallization showed smoothly topographic features in figure E.	136
Figure IV. 5 Strain-stress mechanical strength curves of the pristine (\square) and 5% DEHP (\bigcirc), 10% DEHP (\triangle), 15% DEHP (∇) terpolymer blends (a). Solid lines are linear fits to the curves. (b) Y modulus values of the strain-stress curves as a function of mass fraction of DHEP load for pristine and terpolymer blends. Dash line is the exponential decay fit to the Y modulus values.	137
Figure IV. 6 Frequency and temperature dependence of real part of complex permittivity (a1), dielectric loss (a2) and dielectric loss angle $\tan \delta$ spectroscopy (a3) for the pristine terpolymer. The various relaxation processes, i.e. the β , α relaxation, Curie transition and ions DC conductivity were successively indicated in order of temperature increasing.	139
Figure IV. 7 Dielectric permittivity (c1), dielectric loss spectra (c2) and dielectric loss angle $\tan \delta$ (c3) as a function of frequency and temperature for the representative 10% DEHP doped terpolymer blend.	140
Figure IV. 8 (a) Isochronal dielectric loss spectra for pristine terpolymer and each plasticized film picked up from the isothermal BDS measurement over the temperature range between 203 and 373K at 1581 Hz (pristine, open square; 5% DEHP loaded, open circle; 10% DEHP loaded, upward triangle; 15% DEHP, downward triangle). Dashed vertical line denotes the Curie transition peak of pristine terpolymer. (b) The fractional glass transition regions of the dielectric loss angle $\tan \delta$ where the relaxation peaks of the pristine and 15% DEHP terpolymer blends were marked by solid vertical line (denotation indicated by the context in the figure).	141
Figure IV. 9 Fraction of isothermal dielectric loss spectra as a function of logarithmic frequency at temperature range between 248 K and 293 K for pristine (a) and 10% DEHP modified terpolymer (b). The lines are guide to the eyes.....	143
Figure IV. 10 (a) A comparison of the fractional dielectric loss spectra as a function of logarithmic frequency for pristine and modified terpolymer with various DEHP mass fraction at given temperature 253 K. Dashed vertical line denotes the peak position of the pristine terpolymer and curvature arrow oriented to the diffusion of the peak position for the DEHP doped terpolymer blends; a schematic of slope equal to -1 was depicted referring to the 100% contribution of ions DC conductivity. (b) dual normalized dielectric loss spectra against the logarithmic frequency at given 253 K; vertical line marked the normalized frequency below which the dielectric loss diverged obviously.	146
Figure IV. 11 Temperature dependence of structural relaxation times τ_α and secondary relaxation times τ_β plotted as a function of the reciprocal of temperature $1/T$ regarding the pristine and DEHP doped	

terpolymer blends; filled symbols (for instance, ■, ●, ▲...) represent α relaxation times; open symbols (□, ○, △...) denote secondary relaxation times. Solid lines represent the VFT fitting to the curvature like relaxation times.148

Figure IV. 12 Schematic representation of the three-phase model of plasticizer-free semi-crystalline polymer and microstructure of DEHP plasticized terpolymer blends. Color filled rectangle presents each possible phase of semi-crystalline polymer. Dash circle highlighted the cooperativity length of the DEHP plasticized terpolymer system in amorphous phase.....151

Figure IV. 13 Comparable between Vogel temperature T_0 (◆), dielectric glass transition temperature $T_{g, \text{diel}}$ (●), Fox glass transition temperature $T_{g, \text{Fox}}$ (▲) and estimated Fox temperature $T_{g, \text{Fox}}'$ in amorphous phase after subtraction of crystalline phase (■) for pristine and plasticized terpolymer blend systems as a function of DEHP concentration.....153

Figure IV. 14 Strength indices $D = B/T_0$ (●) and fragility indices m (■) values as a function of DEHP concentration for control pristine and DEHP doped terpolymer blends. Solid line and dash line were the exponential fit to the fragility and strength index values.154

Figure IV. 15 Fractional isothermral dielectric loss as a function of logarithmic frequency with temperature range between 203 K and 233 K for pristine (a) and terpolymer with 15% DEHP mass fraction (b), respectively. k is the slope of the fractional dielectric loss spectroscopy at 233 K and low frequency. Lines are fits to the Havriliak-Negami function.....155

Figure IV. 16 Temperature dependence of β relaxation map plotted as a function of the reciprocal of temperature for the pristine and DEHP doped terpolymer blends (a); Dielectric loss spectra (Permittivity'') as a function of frequency in the temperature region of β relaxation at 238 K for representative 15% DEHP load terpolymer blend (b), dash line denotes the conductivity fitting component of the dielectric loss spectrum, here $s=0.34$ indicating the presence of interfacial polarization effect; dotted solid line was an individual HN fit to the measured dielectric loss spectrum.157

Figure IV. 17 Isothermal real part of complex conductivity as a function of log frequency over the wide temperature range between 298 K and 373 K for terpolymer blend with 5% DEHP concentration (a), Compared real part of conductivity against log frequency for pristine (■) and plasticized terpolymer with 5% (●), 10% (▲), 15% (▼) addition of DEHP at 313 K, inset figure represents the conductivity versus the reciprocal of the temperature ($1/T$).....158

Figure IV. 18 Dielectric modulus spectra as a function of full temperature and frequency range for pristine (a) and representative modified terpolymer blends with 10% DEHP (b). The respective relaxation process was marked: σ , conductivity at high temperature; α' represents segmental relaxation of constrained amorphous phase; Curie process refers to the transition in crystal lamellae defects; α relaxation is segmental relaxation in mobile amorphous phase; β is secondary relaxation in subglass state of the terpolymer.159

Figure IV. 19 Fractional isothermal dielectric modulus as a function of frequency with temperature range between 313 K and 373 for pristine terpolymer (a) between 278 K and 373 K for modified terpolymer with 10% DEHP concentration (b).....160

Figure IV. 20 Temperature dependence of the conductivity relaxation times τ_{con} for the pristine (■), 5% (●), 10% (▲) and 15% (▼) DEHP doped terpolymer blends. Dashed curvature lines are VFT fitting to the logarithmic conductivity relaxation times while linear lines represent the Arrhenius type fitting. The temperature at which Arrhenius type separated with VFT fits were visible for 10% DEHP and 15% DEHP plasticized terpolymers at 338 K and 343 K, respectively.161

Figure IV. 21 Isothermal real ϵ' (green square) and imaginary ϵ'' (red circle) part of dielectric spectra, corresponding derivative dielectric loss ϵ'' (blue upper triangle) and electric modulus M'' (wine filled ball) against the logarithmic frequency at temperature 343 K for the pristine (a); ϵ' (blue diamond), ϵ'' (purple triangle), ϵ'' (green hexagon) and M'' (dark cyan filled ball) for 15% DEHP doped terpolymer blend (b).	163
Figure IV. 22 Conductivity-free dielectric modulus derivative spectra M'' for pristine (a), 5% DEHP (b), 10% DEHP (c) and 15% DEHP (d) as a function of frequency and temperature, the respective processes were marked by interfacial polarization (MWS), constrained structural relaxation (α'), Curie transition (Curie), segmental relaxation in amorphous phase (α) and secondary relaxation (β) in order of increase in temperature.	165
Figure IV. 23 Electric modulus spectra plotted as a function of frequency over temperature range between ambient temperature of 298K and 373K which derived from Karmers-Konig function for the pristine (top) and 10% DEHP load terpolymer blend (bottom). The spectra appeared the two distinctive relaxation regimes, being attributed to the interfacial polarization and primary α -relaxation (α').	166
Figure IV. 24 A comparison of dielectric modulus M'' with variation of addition of DEHP content for the pristine and plasticized terpolymer systems as a function of logarithmic frequency at 348 K. M'' here was calculated using dielectric loss derivatives deduced from the Kramer-Kronig transformation.	167
Figure IV. 25 Temperature dependence of relaxation time of the MWS processes (open symbols) and structural relaxation process of constrained amorphous phase α' (filled symbols) as a function of temperature for the pristine and DEHP doped blends. Dash lines in right graphic were the VFT fits to the curvature α' processes.	169
Figure IV. 26 Full dielectric relaxation map of the pristine and DEHP doped terpolymer blend systems, presenting all the relaxation processes covering the large scale of temperature range. Each process was designated as MWS (filled symbols), α' (left filled symbols), α (\times symbols) occurring in super-cooled liquid region and β (open symbols) in sub-glass state of the terpolymer material in the order of temperature proceeding. Solid vertical line and dash line were assigned to the the reciprocal of estimated glass transition temperature T_g , $diel\alpha'$ and T_g , $diel\alpha$ defined by the dielectric approach.	170
Figure V. 1 Schematics of displacement (D)-electric field (E) hysteresis loops for ferroelectric polymer (a) and relaxor ferroelectric terpolymer (P(VDF-TrFE-CTFE)) (b). Ferroelectric polymers exhibited fat hysteresis loop as well as a large remnant polarization (P_r) whereas relaxor one presented the narrow D- E hysteresis loop with a trace of remnant polarization	182
Figure V. 2 Snapshot graphics showing the droplet morphology evolution against time elapsing. 1% weight solution of P(VDF-TrFE-CTFE) in low volatile TEP solvent. The polymer solution droplet detached to the nozzle through inks liquid filament as time elapse beyond 260 μ s. Green horizontal lines marked the position of same altitude of the stroboscopic snapshots.	188
Figure V. 3 Optimal diagram of bipolar voltage pulse waveform for inkjet printing	189
Figure V. 4 Schematic representations of layer by layer configuration of the inkjet printed force.	191
Figure V. 5 Photographics of the water droplet on the pristine PI against UV-Ozone treatment times. γ_l represents the water surface tension vector; γ_{sg} symbolizes the PI foil surface tension vector; γ_{sl} denotes the surface tension of PI foil and water interface. θ is the contact angle of the water on treated PI substrate.	192
Figure V. 6 Water contact angle on the PI foil substrate as a function of UV-Ozone treatment time. Error bars are covered by the data symbols.	193

Figure V. 7 Optical photographs of inkjet printed terpolymer films on plasma treated Kapton substrate depending on the varying print speed at same pattern resolution of 2000×2000 (dpi, dots per inch). (a)-(c) void and incomplete terpolymer deposit layer upon 75 mm/s print speed; (d)-(f) colorful interplay strips due to the thickness discrepancies of the polymer layer at 40 mm/s printed speed; (g)-(h) strip-free and optically homogeneous topology at 30 mm/s print speed; (i) the monolithically inkjet printed force sensor array. Horizontal bar is respectively marked as the scale at bottom right.	195
Figure V. 8 A schematic diagram of inkjet printing and pinned drops drying with a low (a) and high (b) quality factor numbers. Severe coffee ring like polymer residual pattern after inks dried due to a large amount of inks deposition per nozzle (a) whereas a small quantity of droplet volume applied by each nozzle favored to the indistinct coffee ring like polymer residual pattern.	196
Figure V. 9 Fabrication flow of a typical inkjet printed force sensor.....	197
Figure V. 10 Hysteresis loop measurement as a function of electric field with increasing maximum values	198
Figure V. 11 Logarithmic frequency dependence of capacitance behavior (a) and dielectric permittivity (b) for inkjet printed copolymer and terpolymer sensors. Filled square and open square were assigned to respective capacitance trace and dielectric spectrum of P(VDF-TrFE) copolymer sensors. Filled triangle and open triangle represented the obtained data of terpolymer sensors.	199
Figure V. 12 A comparison of inkjet printing and spin coating solution-process protocols with respect to broadband dielectric spectroscopy (a) and dielectric loss derivative ϵ'' with dielectric modulus M'' spectroscopy as a function of logarithmic frequency.	200
Figure V. 13 In-situ electric field-induced displacement by 2 cycles of the bipolar sinusoidal AC voltage up to 110 V/ μ m for various inkjet printed terpolymers. Hollow rectangle (\square) symbolizes the printed terpolymer based on the pure terpolymer inks; triangle (Δ) represents 10% DEHP modified inks passed through the PTFE filter; circle (\bigcirc) denotes the 10% DEHP modified inkjet printed terpolymer without the filter operation.	202
Figure V. 14 Schematic diagram of experimental setup for the sensitivity measurement of the inkjet printed ferroelectric force sensor.	203
Figure V. 15 A representative output current in response to a given applied force of 400 Hz sinusoidal signal (a); output current I against varying dynamical force application for a single ferroelectric copolymer sensor at fixed 400 Hz (b).	204
Figure V. 16 Sensitivity of the ferroelectric dynamic force sensor against force applying with a varying frequency range between 100 Hz and 1000 Hz. Solid curve is a peak fit by the Lorentz function.....	205
.....	206
Figure V. 17 A representative of voltage trace of force applying impulse and readout current I with charge yield integration (a); Induced charge yield in response to the varying dynamic force impulse (b). Solid line was a linear fit to the data.....	206
Figure V. 18 Schematic representation of the experimental configuration for impact force applying upon the inkjet printed ferroelectric P(VDF-TrFE) copolymer sensor devices.....	206
Figure V. 19 A schematic diagram of force impulse applying upon the relaxor inkjet printed sensor based on electrostrictive terpolymer and data acquisition circuit.....	207
Figure V. 20 Representative readout current and integrated charge yield in response to an equal dynamic force applying under different bias electric field of 10V/9 μ m (a) and 90V/9 μ m (b).....	209

Figure V. 21 Pseudo-piezoelectric coefficient d_{33eq} as a function of the bias electric field E . Dash line is the linear fit and horizontal solid line is assigned to the electrically independent of measured piezoelectric coefficient d_{33} of inkjet printed ferroelectric copolymer force sensors.	209
--	-----

List of Tables

Table I. 1 Comparison of force sensor technologies based on three mainly reviewed transduction principles	21
Table I. 2 Comparison of the flexible polymer foil substrate. Adapted from review by Khan [55].	34
Table II. 1 Thermal parameters of Curie transition region and melting peak region for isothermally annealed terpolymer at various temperature for fixed 2h annealing time duration (from room temperature to 120 °C).....	64
Table II. 2 Thermal data collection of Curie transition region and melting peak region of terpolymer annealed at fixed temperature for various time period at given temperature of 90 °C.....	66
Table II. 3 Electric breakdown values E_b , Weibull fitting parameters (k) and the average thickness of the measured films with estimate errors for the isothermally annealed terpolymers	73
Table II. 4 Data collections of the transverse strain (S_{31}), Young's modulus (Y), free mechanical energy density ($E\mu$), fitted global electrostrictive coefficient (M_{31}) for each temperature treated terpolymer membrane.	81
Table III. 1 Degree of crystallinity (χ_c), VTF fitting parameters, VFT temperature (T_0), glass transition temperature ($T_{g,diel}$) defined for a relaxation time $\tau\alpha$ of 100s, merging temperature T_{me} and the activation energy EC of the Curie transition.	108
Table III. 2 Crystallinity dependence of the Havriliak-Negami fitting parameters and the apparent activation energy $E\beta$ for a terpolymer in the sub-glass state.	110
Table IV. 1 Summary of DEHP physico-chemical properties	126
Table IV. 2 Temperature and enthalpy parameters concerning Curie transition regimes and melting region monitored by a DSC heating ramp	132
Table IV. 3 Corresponding temperature and enthalpy parameters collection in a cooling ramp of DSC measurement.....	132
Table IV. 4 The VFT fitting parameters, estimated dielectric glass transition temperature at structural relaxation time $\tau\alpha(T)$ equal to 100 s and strength indices values, estimated glass transition temperature thanks to the Fox glass transition temperature $T_{g,Fox}$ law.	152
Table IV. 5 Havriliak-Negami function fitting parameters to the dielectric loss spectra of the pristine and DEHP modified terpolymer blends and apparent activation energy in sub-glass state.	156
Table V. 1 Physic properties of Dimatix cartridge, solvents and polymer solution inks in TEP	186
Table V. 2 Optimal inkjet printing protocol used for generating a printable droplet formation of copolymer and terpolymer solution inks in this present study	191
Table V. 3 Surface tension properties of the pristine, plasma treated PI and Au sputtered PI substrate. Surface tension of the printed copolymer and terpolymer patterns were also compared with fluorinated fluid phobic Teflon films. Data listed here were also measured by Owens-Wendt- Kaelble method.....	194
Table V. 4 A comparison of electromechanical properties of the sensing layer polymers in this present work and mostly investigated PZT ceramics.....	208

FOLIO ADMINISTRATIF

THÈSE SOUTENUE DEVANT L'INSTITUT NATIONAL
DES SCIENCES APPLIQUÉES DE LYON

NOM : LIU

DATE de SOUTENANCE : 29 Nov. 2016

Prénoms : QING

TITRE : **DEVELOPMENT OF ELECTROSTRICTIVE P(VDF-TRFE-CTFE) TERPOLYMER FOR
INKJET PRINTED ELECTROMECHANICAL DEVICES**

NATURE : **Doctorat**

Numéro d'ordre : **2016LYSEI126**

Ecole doctorale : **Mécanique, Energétique, Génie Civil, Acoustique**

Spécialité : **Génie Mécanique**

RESUME:

Electromechanical coupling effect has attracted the emerging attention due to ability to realize conversion between electric excitation and mechanical response and vice versa. Thanks to their flexibility, light weight, relatively low mechanical strength, ease of processability into large-area films, and ability to be molded into desirable geometric dimensions, polymers materials which possess an electromechanical coupling effect have been emerging recently. This thesis aims to systematically determine the electromechanical behavior of the P(vinylidene fluoride-trifluoroethylene-chlorotrifluoroethylene) [P(VDF-TrFE-CTFE)] terpolymers via crystallization and additive technology approaches and intend to extend such terpolymers to the electromechanical force sensor devices application. The influence of the thermal processing on the electromechanical response and microstructure of the terpolymers were firstly investigated. Cantilever unimorph bending measurement found the tip displacement δ and transverse strain S_{31} for each thermally treated terpolymer followed a quadratic correlation with the electric field. δ maximized at a 39.3% crystal content, instead of S_{31} peaking at lowest crystal content, showing an exponential decay against the crystal fraction increasing.

The dynamics of crystallized terpolymers were additionally studied via broadband dielectric spectroscopy. Constrained segmental dynamics was observed in the terpolymer containing the highest crystal fraction for which a narrow relaxation time distribution was found. Moreover, the enhanced dielectric and electromechanical response of DEHP doped terpolymer were interpreted via morphology microstructure and molecular mobility analysis. Interfacial polarization shifted to the high frequency by one decade because of dopant DEHP.

Finally, electromechanical devices based on ferroelectric P(VDF-TrFE) and electrostrictive P(VDF-TrFE-CTFE) towards the dynamic force sensor implementation were designed and fabricated via inkjet printing technology. The bias electric field for terpolymer sensor was much lower than the poling electric field for a copolymer sensor. And the piezoelectric properties equivalent to the corresponding copolymer sensor can be obtained for a bias as low as 7.5V/ μm .

MOTS-CLÉS : *Crystallinity fraction; Molecular mobility; Plasticized terpolymer blends, Interfacial polarization; Inkjet printing technique; Piezoelectric force sensor*

Laboratoire (s) de recherche : **Laboratoire de Génie Electrique et Ferroélectricité (LGEF) de l'Université de Lyon, INSA Lyon**

Directeur de thèse:

Pr. Claude RICHARD

Co-directeur de thèse :

Dr. Jean-Fabien CAPSAL

Président de jury :

Pr. Xavier BODDAERT

Composition du jury :

Président & Examineur :

Pr. Xavier BODDAERT

Rapporteur :

Pr. Zhiyong LIANG

Rapporteur :

Pr. Eric DANTRAS

Examineur :

Pr. Antoine MILLION

Examinatrice :

Pr. Qiuyu ZHANG

Co-directeur de thèse :

Dr. Jean-Fabien CAPSAL

CMP, Mines Saint-Etienne

HMPI, Florida State Univ.

CIRIMAT, Toulouse Univ.

Hospices Civiles de Lyon

Northwestern Polytech. Univ.

Maître de Conférences, INSA